



Universiteit
Leiden

The Netherlands

Applications of AdS/CFT to strongly correlated matter: from numerics to experiments

Chagnet, N.

Citation

Chagnet, N. (2024, June 11). *Applications of AdS/CFT to strongly correlated matter: from numerics to experiments*. Retrieved from <https://hdl.handle.net/1887/3762182>

Version: Publisher's Version

License: [Licence agreement concerning inclusion of doctoral thesis in the Institutional Repository of the University of Leiden](#)

Downloaded from: <https://hdl.handle.net/1887/3762182>

Note: To cite this publication please use the final published version (if applicable).

Applications of AdS/CFT to strongly correlated matter: from numerics to experiments

Proefschrift

ter verkrijging van
de graad van doctor aan de Universiteit Leiden,
op gezag van rector magnificus prof.dr.ir. H. Bijl,
volgens besluit van het college voor promoties
te verdedigen op dinsdag 11 juni 2024
klokke 12:30 uur

door

Nicolas Chagnet
geboren te Beaumont-Sur-Oise, France
in 1996

Promotor: Prof.dr. K.E. Schalm
Copromotor: Prof.dr. J. Zaanen

Promotiecommissie: Prof.dr. J. Aarts
Prof.dr. C.W.J. Beenakker
Dr. S. Cremonini (Lehigh University)
Prof.dr. B. Goutéraux (École Polytechnique)
Prof.dr.ir. H.T.C. Stoof (Universiteit Utrecht)

This thesis can be found electronically at <https://openaccess.leidenuniv.nl/>.
Cover art based on an original photo by Marek Piwnicki. Cover font: Eudoxus Sans.

To my wonderful wife, Martina.

Contents

Contents	i
Foreword	v
1 Introduction	1
1.1 Quantum critical points and strongly correlated electrons	1
1.2 The holographic AdS/CFT correspondence	7
1.3 Common holographic systems	11
1.4 This thesis	19
1.4.1 Chapters 2, 3, 4 — Metallic transport in an ionic lattice	19
1.4.2 Chapter 5 — Regulated Quantum Electron Star	20
1.4.3 Chapter 6 — Nielsen complexity of conformal field theories	21
2 Holographic lattices as local quantum critical metals	23
2.1 The Planckian dissipation mystery versus computational holography	23
2.1.1 Main observations and summary of the results.	25
2.2 Holographic strange metals, transport and translational symmetry breaking.	33
2.3 Umklapp hydrodynamics for weak lattice potentials.	37
2.4 The applicability of hydrodynamics and the imprint of local quantum criticality	42
2.5 DC vs Optical conductivities in explicit lattice (holographic) strange metals from Umklapp	45
2.5.1 Low temperatures: Drude transport	46
2.5.2 Intermediate temperatures: a mid-IR-peak in the optical response	50
2.5.3 Intermediate lattice strength: towards an incoherent metal	52
2.5.4 On the applicability of Umklapp hydrodynamics	53

2.6	Observations at strong lattice potentials: Planckian dissipation and incoherent metals	55
2.6.1	The remarkable ubiquity of Planckian dissipation	55
2.6.2	An incoherent metal explained with microscopic scrambling	57
2.6.3	Saturating behavior and Planckian dissipation	61
2.7	Discussion: is it relevant for condensed matter physics?	62
2.A	AdS RN and GR black holes	66
2.A.1	Reissner-Nordström	67
2.A.2	Einstein-Maxwell-Dilaton	67
2.A.3	Lattice Backgrounds	68
2.A.4	DC Conductivity	70
2.B	Semi-local criticality and an induced IR length scale	71
2.C	Four pole fitting formula	74
2.D	Memory matrix formalism	74
2.E	Scaling of hydrodynamical relaxation rates	74
2.F	Lorentz oscillator decoupling	76
3	Relativistic hydrodynamics in a periodic potential	79
3.1	Introduction	79
3.2	Hydrodynamics: Set-up and brief review of homogeneous fluctuations	81
3.2.1	Hydrodynamic fluctuations in a homogeneous background	84
3.3	Hydrodynamic fluctuations in a lattice background	86
3.3.1	Finite momentum aligned fluctuation spectrum	89
3.3.2	The $k = 0$ zero momentum perturbation	93
3.4	Bloch wave hydrodynamics emerging from holographic models: a comparison	97
3.5	Conclusion	101
3.A	Thermodynamics and susceptibilities	106
3.B	Onsager relations	107
3.C	Second order corrections in lattice strength	109
3.D	Numerical computations in strongly coupled field theories dual to Reissner-Nordström and Gubser-Rocha AdS black holes: set-up	112
3.D.1	Thermodynamics	112
3.D.2	Numerics	113
4	Quantization and thermodynamics of the Gubser-Rocha black hole solution	117
4.1	Introduction	117
4.2	Setup	119
4.3	Regularization, boundary terms and choice of quantization	120
4.3.1	Boundary action	120
4.3.2	Choice of quantization and thermodynamics	124
4.4	Deformed Gubser-Rocha black holes	128
4.4.1	Numerically constructed solutions	128

4.4.2	The holographic dual of the one-parameter family of solutions in different quantization choices	130
4.5	Conclusion	133
4.A	Validity of the boundary action	134
4.B	Matching of metric gauge choices	137
5	Emerging Fermi liquids from regulated quantum electron stars	139
5.1	Introduction	139
5.2	A confined Quantum Electron Star: set-up	142
5.2.1	Einstein-Maxwell-Dirac equations	144
5.2.2	Fermion densities and backreaction	146
5.2.3	Boundary conditions on the Einstein-Maxwell sector	147
5.2.4	Boundary conditions for the fermions	148
5.3	Regulated Quantum Electron Star: thermodynamics and spectrum . . .	152
5.3.1	Thermodynamics	153
5.3.2	Spectrum of the rQES	156
5.4	Towards a self-confining quantum electron star	160
5.4.1	Comparison to the holographic superconductor	160
5.4.2	Confinement in the rQES solution	161
5.5	Discussion and conclusions	162
6	Complexity for conformal field theories	165
6.1	Introduction	165
6.2	Preliminaries	167
6.3	Complexity in General Dimensions	167
6.4	Geometric Action and Coadjoint Orbits	170
6.5	Coherent State Generalization	171
6.6	Holography	172
6.7	Summary and Outlook	173
6.A	Relating the Euclidean and Lorentzian Conformal Generators	175
6.B	Expectation Values of the Conformal Generators in $d \geq 2$	177
6.C	Geodesic Trajectories in the Complexity Metric	179
6.D	Canonical Variables and Recombination Formula	181
6.E	Bounds on Complexity and its Time Evolution	184
6.E.1	Bounds on Complexity	184
6.E.2	Complexity of Time Evolved States	185
6.F	Comparison with Previous Results in $d = 2$	186
6.F.1	Expectation Values of the Conformal Generators in $d = 2$	188
6.G	Comments about Spinning States	189
6.H	Metric and Geometric Action in the Fundamental Representation of the Conformal Group	190
6.I	Root Space Decomposition	192
6.J	Holographic Interpretation	196
6.J.1	Background	196

6.J.2 Complexity in Holography	198
6.J.3 Geometric Interpretation of the Fubini-Study Metric	199
6.J.4 Example: Timelike Geodesics with Fixed Radius	200
Bibliography	201
Summary	223
Samenvatting	225
Résumé	227
Curriculum Vitae	229
Acknowledgements	231
List of publications	233

Foreword

This thesis will deal with the practical use of the AdS/CFT correspondence to shed some light on the properties of quantum matter. The first chapter will provide an introduction to the wider context in which this thesis is placed. This chapter will also introduce the key concepts required throughout the various later chapters. Chapters 2 to 6 consist of published papers I was an author on and are therefore rather self-contained. Due to their nature as publications, these chapters will each re-introduce the necessary notations and context although with a narrower focus.

Chapter 1

Introduction

1.1 Quantum critical points and strongly correlated electrons

Within the last century, Condensed Matter Theory (CMT) has emerged as one of the most successful areas of physics. The initial impetus behind it was the statistical mechanics underpinning of thermodynamics which opened the door to understanding the solid and liquid phases of matter made out of atoms and bound together through the electromagnetic force. With the advent of quantum mechanics, modern solid state physics was born, and the field grew to the more general study of quantum many-body systems.

A key pillar of CMT is *symmetries*; within Landau's framework, phases of matter are categorized by their symmetries and described by a low energy effective functional constrained by these symmetries. As an example, the effective quantum many-body description of up-down spins can be done through the following free energy functional

$$\mathcal{F}[\psi] = \frac{s(T)}{2}\psi^2 + \frac{u(T)}{4}\psi^4 + \dots, \quad (1.1)$$

where ψ is a real scalar field modelling the average number of up (positive) and down (negative) spins in some local area, also called *the magnetization*. A priori, the coefficients s and u depend on the temperature T and other physical parameters of the system. The symmetry under which the action (1.1) is invariant is \mathbb{Z}_2 inversion *i.e.*, when all spins simultaneously flip their signs $\psi \rightarrow -\psi$. When this symmetry is broken, either explicitly by interactions or spontaneously by the state, the physical system undergoes a *phase transition*. In our Ising example, the former can be done by coupling to an external magnetic field $\mathcal{F}_{\text{explicit}}[\psi] = \mathcal{F}[\psi] + h\psi$, which explicitly breaks the \mathbb{Z}_2

invariance. The case of spontaneous breaking can be understood as the deformation of the energy functional when tuning temperature. When $s(T) > 0$ and $u(T) > 0$, \mathcal{F} has a single minimum at $\psi = 0$ (the state is called a paramagnet) while when $s(T) < 0$ and $u(T) > 0$, two minima emerge at $\psi = \pm \sqrt{\frac{-s}{u}} \neq 0$ (the state is then a ferromagnet).¹ In the last case, since $\psi \neq 0$, the \mathbb{Z}_2 invariance is broken by the state while the functional remains invariant under the symmetry.

This scenario of spontaneous symmetry breaking presents a continuous transition where the system passes through a *critical point* at $s(T = T_c) = s_c$ ($s_c = 0$ for our Ising example). The self-induced change is driven by thermal fluctuations. At the critical point, the correlation length ξ diverges and the correlation functions showcase an emergent scale invariance — the system is then described by a conformal field theory (CFT). If the system depends on other physical parameters (e.g., pressure, chemical potential, etc.) collectively denoted by p , one can tune the transition at zero temperature to a critical point located at $s(p = p_c, T = 0)$. The system is now driven by quantum fluctuations instead of thermal fluctuations and the critical point is called a quantum critical point (QCP). It is this type of quantum phase transition (QPT) where the corresponding CFT exists at temperatures close to zero that will be of relevance to this thesis.

Most systems one encounters in CMT are generally perturbative in nature; they are usually related to a free system by a small deformation, an adiabatic deformation (e.g., the Fermi liquid is adiabatically connected to the Fermi gas) or by some duality (e.g., the bosonization of the Luttinger liquid). In these cases, the excitations of the systems are particle-like in nature and are called *quasiparticles*. For interacting systems, these quasiparticles generally acquire a finite yet large enough lifetime such that the quasiparticle manifests itself as a well-defined resonance peak in the spectrum of the correlation functions. The dynamics of the system can then be understood in terms of the collisions of these quasiparticles.

One of the most interesting properties of QCPs is that the excitations of the system at that point are generically not quasiparticles. Consider the following Euclidean action as a toy model [1]

$$S_{\text{QCP}}(\psi) = \int d^2x d\tau \left[(\partial_\tau \psi)^2 + (\nabla \psi)^2 + \frac{s}{2} \psi^2 + \frac{u}{4} \psi^4 \right], \quad (1.2)$$

This action is a generalization of the Ising functional (1.1) and will describe the Ising QPT between the previously described ferromagnetic and paramagnetic phases. Away from the QCP, both of these phases have quasiparticle excitations called *magnons*. How do we describe the theory *at criticality*, where there are no quasiparticles? In dimensions $d > 3$, one can still get away with a quasiparticle description (in a free field representation) even though formally there are no such excitations. In $2 + 1$ dimensions,

¹Note that the case of $u(T) < 0$ yields an unbounded energy functional as $|\psi| \rightarrow \infty$ and therefore signals an unphysical instability.

however, it is well-known that under Renormalization Group (RG) flow, the ψ^4 theory admits not only the trivial Gaussian fixed point $u = s = 0$ but also the Wilson-Fisher fixed point characterized by (s^*, u^*) — in that case this non-trivial fixed point will be the location of the Ising QCP. At this QCP, the two-point correlator for ψ will then take the conformal form [1]

$$G_{\psi\psi}(\omega, k) \sim \frac{1}{(k^2 - \omega^2)^{(2-\eta)/2}} \quad (1.3)$$

where $\eta \neq 0$ is some anomalous scaling exponent for ψ . Would $\eta = 0$ have been true, then the propagator would have poles at $\omega = \pm k$, and we would recover a quasiparticle description of the system.² However, for generic values of η , the propagator is not an analytic function and exhibits branch cuts instead of well-defined poles — this is the simplest example of ‘unparticle’ physics.

By definition, at the critical point, the correlation length ξ diverges as $\xi \sim |s - s_c|^{-\nu}$, defining the critical exponent ν . If we now add a small temperature, we still expect the system to remember its critical origin and therefore the correlator should take the scaling form

$$G_{\psi\psi}(\omega, k) \sim T^{\frac{\eta-2}{z}} \mathcal{F}\left(\frac{k}{T^{1/z}}, \frac{\xi^{-1}}{T^{1/z}}, \frac{\omega}{T}\right). \quad (1.4)$$

In the previous equation, we have allowed for a dynamical critical exponent z which accounts for a different scaling of time and space. Since the action (1.2) is manifestly Lorentz invariant, then $z = 1$. However, other theories can a priori show a non-trivial emergent $z > 1$.³ From the correlator (1.4), we can see that for temperatures $T > \xi^{-z}$, then the scaling ratio $T\xi^z$ remains large (and even grows with increasing T) and thus the physics of the system is controlled by the fluctuations of the QCP ground state. This is a special phase of the system called the quantum critical regime, which, remembering the scaling of ξ , is then defined at low temperatures by the region $T > |s - s_c|^{z\nu}$. In Fig. 1.1, we draw a schematic phase diagram for the system described by (1.2) where the quantum disordered phase is the paramagnet and the quantum ordered phase is the ferromagnet (which eventually transitions back to a classical paramagnet at high-enough temperature). A QCP without a quasiparticle description

²In this case, the poles have no imaginary part, so these quasiparticles do not decay.

³This is for instance the case for the Hertz-Millis model [2, 3] describing the coupling of a bosonic order parameter ψ passing through a QCP and coupled to fermionic excitations. After integrating out the fermions, we are left with an effective action for the critical boson of the form

$$S = \int d\omega d^d q \left[\left(\frac{|\omega|}{\gamma(q)} + q^2 \right) |\psi|^2 + m^2 |\psi|^2 + \dots \right] \quad (1.5)$$

where we ignored irrelevant terms for simplicity. If the critical boson describes a ferromagnetic order parameter, then $\gamma(q) \sim |q|$ and therefore the emergent dynamical critical exponent at this QCP is $z = 3$. Note that while the Hertz-Millis model predicts generic mean-field exponents below the upper-critical dimension $d_c = 1$, there are subtleties in two- and three-dimensional systems which may invalidate this simple Ginzburg-Landau description [4, 5, 6].

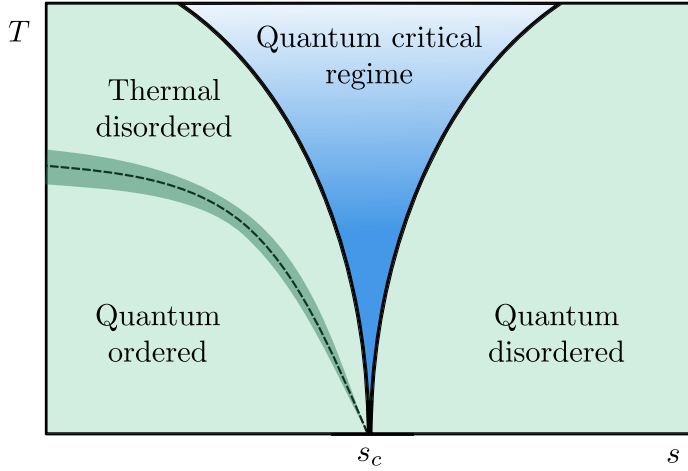
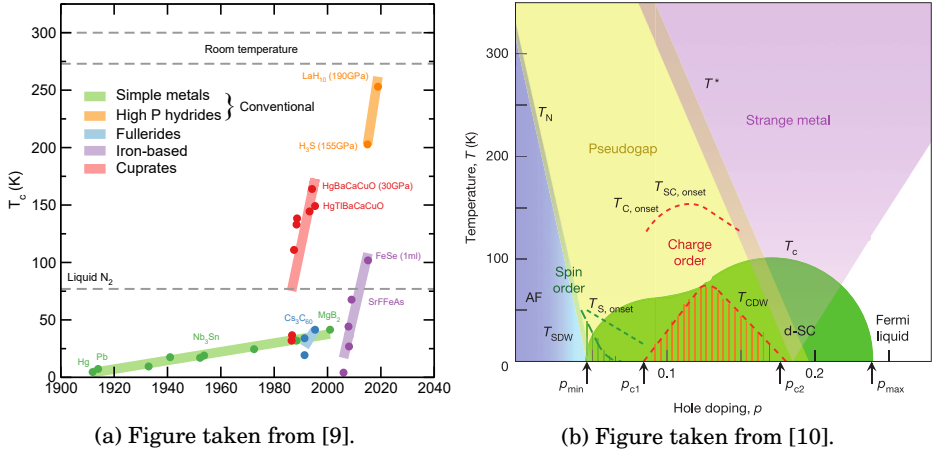


Figure 1.1: Schematic phase diagram of a system in the presence of a quantum critical point. On each side of the transition, there is a quantum ordered and disordered phase which can both be described by quasiparticles. The quantum ordered phase admits a classical phase transition to a thermal disordered phase. The shaded area indicates the area where fluctuations along the time direction are frozen, and the behavior is purely classical. At finite temperature, there is a region where the physics of the QCP remains dominant and the excitations of this region cannot be described perturbatively as quasiparticles.

is possibly the best example of a ‘strongly interacting’ or ‘strongly coupled’ system, as opposed to the perturbative systems mentioned at the beginning of this introduction which are dominated by quasiparticles.⁴

The explorations of this thesis are motivated by a variety of strongly coupled systems. Among them stands the mysterious ‘strange’ metallic phase of the copper oxides high- T_c superconductors (or *cuprates*) discovered in the 1980s [8]. Such cuprates are so-called Mott insulators. By tweaking their chemical composition, the number of available charge carriers per ionic site (electron or holes) can be changed (this is called electron or hole doping) and they can become conducting metals which superconduct at low temperature, where the temperature of onset of the superconducting phase changes with the doping parameter. The main characteristic of the cuprates is that for some optimal value of doping p^* , the transition temperature shows an anomalously high maximum, orders of magnitude larger than that predicted by the conventional Bardeen–Cooper–Schrieffer (BCS) theory (where $T_c^{\max} \approx 35\text{K}$, see Fig. 1.2). This, in essence, shows that such cuprates do not reflect the physics of conventional Fermi

⁴Note that this widely used nomenclature is not entirely exact. Adiabatically deformed systems can be strongly interacting and still have quasiparticle excitations. (see *e.g.*, for the Fermi liquid [7]). In this thesis we will follow this naming convention in spite of this technicality to match the rest of the literature.



(a) Figure taken from [9].

(b) Figure taken from [10].

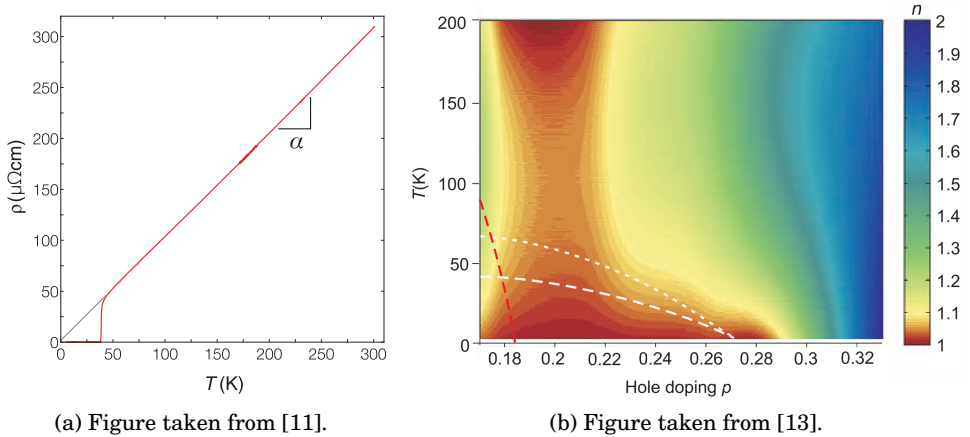
Figure 1.2: (a) Graph plotting the history of discovery of high- T_c superconductors. In green are the conventional superconductors described by BCS theory while in red are the cuprates. (b) Generic phase diagram of the cuprates parametrized by hole doping and temperature.

liquid quasiparticles.

The superconducting phase is not the only interesting part of these materials: the phase diagram of cuprates shows a remarkable number of exotic phases, with a pseudo-gap phase at low doping and a regular Fermi liquid phase at large doping. Yet the phase where the non-quasiparticle nature is most manifest is the *strange metal* phase at optimal doping, at temperatures above the superconducting transition. This phase is characterized by a variety of properties, the most prominent of which is the linear-in- T resistivity ρ — where a regular Fermi liquid metal would have $\rho \sim T^2$ at low temperatures. This linear-in- T resistivity is valid not only at low temperatures but also throughout a large range of temperatures where other interactions would usually take dominance (e.g., the $\rho \sim T^5$ electron-phonon contribution in regular metals is absent in strange metals). Moreover, at large enough temperature, the resistivity of a metal whose transport is mediated via quasiparticles should saturate at the Mott-Ioffe-Regel (MIR) bound [10]. Yet in strange metals, that bound is violated by the linear-in- T resistivity (Fig. 1.3a, see also [11, 12]) indicating again that the quasiparticle description of electronic transport should break down in those systems.

While early efforts were focused on attributing this behavior to the underlying high- T_c physics in cuprates, it was demonstrated that such strange metals can be found in more general strongly correlated electronic systems [14, 15]. It indicated that more universal physics could be at the root. One clear candidate for non-quasiparticle physics is the existence of a QCP, hidden by the superconducting dome, with the strange metallic physics originating from the quantum critical regime [16, 10].

In strange metals, experiments have shown, however, that if quantum critical



(a) Figure taken from [11]. (b) Figure taken from [13].

Figure 1.3: In-plane resistivity of the hole-doped $\text{La}_{2-p}\text{Sr}_p\text{CuO}_4$ (LSCO) cuprates. (a): We see the resistivity violates the MIR bound (located between 200 K and 300 K) at large temperature indicating transport is not mediated via quasiparticles. The hole-doping parameter is $p = 0.19$. (b): Exponent n of the resistivity $\rho \sim T^n$ as a function of hole-doping. The red region indicates the strange metallic phase where $n \approx 1$. The data within the superconducting dome is obtained via extrapolation of finite magnetic field data.

physics is at the origin of this phenomenon, it is not simply a QCP, but the even more exotic case of a quantum critical phase (QCPh), a continuous set of QCPs connected by a line. This is supported by measurements of the effective exponent n for the in-plane resistivity in cuprates $\rho \sim T^n$ [13] (in the presence of a high magnetic field such that the superconducting phase is suppressed and thus the hidden part of the resistivity can be extrapolated). This is represented in Fig. 1.3b where we see indeed that the strange metallic behavior does not seem to converge to a point but to a finite segment at zero temperature. Another argument in support of a QCPh can be found in ARPES measurements showing that the imaginary part of the electron-like non-quasiparticle self-energy⁵ takes the form $\Sigma(\omega) - \Sigma(0) \sim [T^2 + \omega^2]^\alpha$ with, crucially, α a non-integer value that varies continuously with hole doping p [17]. The key difference between a QCP and a QCPh is that in the latter case, some constraint must allow the emergent critical boson to be gapless within a finite range of parameter space instead of at a specific point.⁶ The coupling of this critical boson with a Fermi surface allows for non-Fermi liquid behavior in the photoemitted electron self-energy. This persistent gaplessness over a range of parameters is responsible for the continuous dependence of critical exponents to the tuning parameter instead of a fixed value but remains a big mystery from a theoretical point of view. A core objective of this thesis will be to show that, surprisingly, quantum critical phases naturally arise in the so-called ‘holographic’

⁵In the language of our toy model, the self-energy is just the correction to the dispersion relation of the quasiparticle pole due to interactions.

⁶We refer the reader to this excellent review for a more in-depth discussion of quantum critical phases [18].

description of quantum critical states [18] — which makes it a fertile ground to look for theories in the same universality class as observed strongly coupled non-quasiparticle and/or QCP-type physics, and will be the subject of our focus starting from now.

1.2 The holographic AdS/CFT correspondence

One of the breakthroughs in describing non-quasiparticle-like physics has been the discovery of the AdS/CFT correspondence, also known as holographic duality. Many books and reviews have been written on the topic already and more details can be found within those texts [19, 20, 1, 21]. Given the sizeable length such an in-depth introduction requires, it is not the goal of this section to exhaustively review the topic, but rather to introduce the main arguments and ideas behind applied holography through canonical examples whose details will also serve to highlight common notations and techniques.

The first example of the AdS/CFT duality was brought forth by Juan Maldacena in 1997 within the framework of string theory [22]. This result connects the physics of a very special quantum field theory (QFT) at strong coupling — a CFT which has no quasiparticles — with that of weakly-coupled gravitational physics. While a full derivation of the string theory background required to understand this specific example in details might be too intricate for the scope of this section, we will nonetheless attempt to extract the essential argument behind this matching.

To that end, let us first consider an $O(N)$ vector theory (see [23] for a more in-depth review). We consider a field ϕ_i in a vector representation of the symmetry group $O(N)$. Its dynamics are described by an action invariant under these transformations. Interaction terms inside the action must therefore be $O(N)$ scalars of the form $\phi^2 \equiv \phi \cdot \phi$, $\phi \cdot \partial_\mu \phi$, etc. to lowest orders in ϕ . We can thus build the following Euclidean action

$$S = \int d^d x \left[\frac{1}{2} (\partial\phi)^2 + \frac{m_0^2}{2} \phi^2 + \frac{g}{2N} (\phi^2)^2 \right]. \quad (1.6)$$

Why the quartic coupling has an extra N factor will become evident in the following derivation. The theory at $g = 0$ is a simple Gaussian free theory with partition function

$$Z_0 \equiv \prod_{i=1}^N \int \mathcal{D}\phi_i e^{-\frac{1}{2} \int d^d x [(\partial\phi_i)^2 + m_0^2 \phi_i^2]} \equiv e^{-NS_0(m_0^2)}, \quad (1.7)$$

where we defined the effective action $S_0(m_0^2) = -\frac{1}{2} \text{Tr} \log(-\partial^2 + m_0^2)$ of a single scalar field component ϕ_i . Keeping g finite, we apply a Hubbard-Stratanovitch transformation to this model such that we can rewrite the partition function $Z = \int \mathcal{D}\phi e^{-S[\phi]}$ into $Z' = \mathcal{N} \int \mathcal{D}\phi \mathcal{D}\sigma e^{-S'[\phi, \sigma]}$, where \mathcal{N} is an overall normalization term which has no effect on the correlations, with the new action

$$S' = \int d^d x \left[\frac{1}{2} (\partial\phi)^2 + \frac{m_0^2}{2} \phi^2 - \frac{N}{2g} \sigma^2 + \phi^2 \sigma \right]. \quad (1.8)$$

The action S' is again Gaussian in ϕ , and therefore we can apply the computation done previously at $g = 0$ with effective mass $m^2 = m_0^2 + 2\sigma$ such that, after integrating out the vector ϕ , the partition function is $Z_{\text{eff.}} = \mathcal{N} \int \mathcal{D}\sigma e^{-NS_{\text{eff.}}[\sigma]}$ with the effective action

$$S_{\text{eff.}}[\sigma] = S_0(m_0^2 + 2\sigma) - \frac{1}{2g} \int d^d x \sigma^2. \quad (1.9)$$

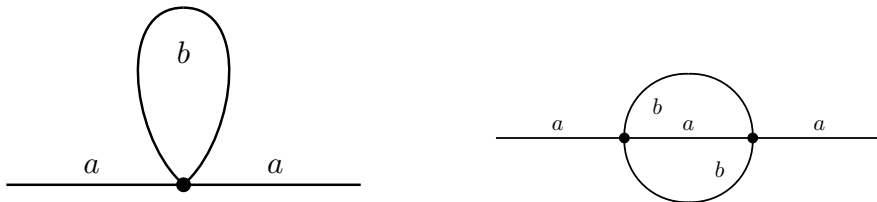
Due to the normalization of the quartic coupling in the action (1.6), the path integral now only depends parametrically on the number of vector components N through the overall normalization of the action. In the large- N limit, the path integral will then be dominated by the saddle-point $\sigma_{\text{cl.}}$ defined through the condition $\frac{\delta S_{\text{eff.}}}{\delta \sigma}(\sigma_{\text{cl.}}) = 0$. This condition is equivalent to the implicit (or gap) equation $G_0(x, x; m^2) = \frac{\sigma_{\text{cl.}}}{g}$ where G_0 is the propagator of a free scalar field with mass $m^2 = m_0^2 + 2\sigma_{\text{cl.}}$.

So far, we have shown that for this class of theories, taking a large- N limit can be an effective tool to achieve some semi-classical description where a saddle-point dominates the path integral. However, we see that the vector model is also entirely dominated by the Gaussian fixed point for any finite coupling g . A similar yet richer model can be considered by promoting the field ϕ_i from the vector representation to the adjoint representation of $O(N)$ — Φ_{ij} is now a real symmetric matrix with $\frac{N(N+1)}{2}$ components and the action (1.6) will then be promoted to

$$S = \int d^d x \left[\frac{1}{2} \text{Tr}(\partial\Phi)^2 + \frac{m_0^2}{2} \text{Tr}\Phi^2 + \frac{g}{\sqrt{N}} \text{Tr}\Phi^3 \right]. \quad (1.10)$$

In the new action (1.10), we only consider the relevant deformation $\text{Tr}\Phi^3$ (in $d = 4$) for simplicity, but there is a priori also a $\text{Tr}\Phi^4$ interaction — as there was in the vector model (the cubic interactions are not present in the vector model due to the $O(N)$ invariance condition). While in the vector model most loop diagrams get suppressed by powers of $1/N$ such that the only leading order effect is to renormalize the scalar mass (see Fig. 1.4), in the matrix model loop diagrams with increasingly high powers of the coupling g remain at leading order in N (see Fig. 1.5). The matrix model can therefore capture more non-trivial physics than the vector model [24]. It is then possible to take the semi-classical limit $N \gg 1$ while keeping the strongly coupled physics of the system. This interplay of limits is controlled by the so-called 't Hooft coupling $\lambda = gN$ such that $\lambda \ll 1$ is akin to a weak coupling limit (similar to the vector model) while $\lambda \gg 1$ is the strong coupling limit.

We can now briefly explain Maldacena's discovery. Within type-IIB string theory, solitonic 3 + 1-dimensional defects (so-called $D3$ -branes) have a zero-mode sector which is essentially the supersymmetric extension of (1.10). There, the strings connecting the branes are described by the matrix fields Φ_{ij} and the 't Hooft coupling is given by $\lambda \sim g_s N$ with g_s the string coupling constant. This is the low energy theory of a supersymmetric $\mathcal{N} = 4$ $SU(N)$ gauge theory which is a CFT. Maldacena observed that studying the system described by the supersymmetric extension of (1.10) at strong coupling $\lambda \gg 1$ and in the large- N limit $N \gg 1$ has a window $1 \ll \lambda \ll N^2$ within



- (a) The vertex brings a factor g/N while the loop over the index b yields a factor N . The overall order of this diagram is $\mathcal{O}(g)$.
- (b) The vertices bring a factor $(g/N)^2$ while the loop over the index b yield a factor N . The overall order of this diagram is $\mathcal{O}(g^2/N)$.

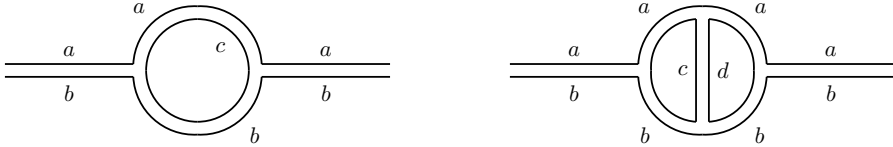
Figure 1.4: One-loop and two-loop 1PI diagram contributions to the vector model two-point function with equal input/output indices. We see that at two-loop order, the irreducible diagram is subleading in N and thus the leading contribution at every loop order will be the components of the geometric series associated with 1.4a.

perturbative string theory $g_s = \frac{\lambda}{N} \ll 1$ where the gravitational description is weakly coupled, and the gauge description remains strongly coupled. In this limit, the branes form an asymptotically hyperbolic geometry of 5-dimensional Anti-de Sitter (AdS) spacetime times a 5-dimensional sphere. As string theory is a theory of quantum gravity, the string coupling not only sets the coupling of the gauge theory $g_{\text{YM}}^2 = \frac{\lambda}{N}$, it also controls the dimensionless gravitational constant $\frac{G_N}{L^8} = \frac{1}{N^2}$, where L is the radius of curvature of the AdS spacetime. In this double limit, L is much larger than the Planck and string lengths *i.e.*, the curvature of the spacetime is weak. Thus, we have a *weakly coupled semi-classical gravitational* description of the system, which is *strongly coupled* from the brane perspective. This is the essence of the holographic principle: the duality maps strongly coupled CFT systems to weakly coupled gravitational systems.

Following on Maldacena’s seminal paper, a plethora of similar mappings were found within string theory (see *e.g.*, this review [25]) — this is called the ‘top-down’ approach. In order for the correspondence to be a practical tool, it is also necessary to find a mathematical formulation of the correspondence. This was put forward through the Gubser-Klebanov-Polyakov-Witten (GKPW) formula [26, 27] which relates the generating functional of a $d + 1$ -dimensional CFT to the gravitational partition function in AdS in one dimension higher

$$\int \mathcal{D}\mathcal{O} e^{iS_{\text{QFT}}[\mathcal{O}] + i \int d^{d+1}x h_i(x) \mathcal{O}_i(x)} = \int_{\phi_i(r=\infty, x) = h_i(x)} \mathcal{D}\phi e^{iS_{\text{grav.}}[\phi]}. \quad (1.11)$$

From this formula, we see that each operator \mathcal{O} of the CFT is dual to the asymptotic boundary value of some bulk field ϕ in a gravitational AdS spacetime with one extra dimension (named the radial direction and denoted by r). An AdS spacetime is different from flat spacetime where one usually requires fields vanish infinitely far away. Instead,



- (a) The vertices bring a factor $(g/\sqrt{N})^2$ while the loop over the index c yields a factor N . The overall order of this diagram is $\mathcal{O}(g^2)$.
- (b) The vertices bring a factor $(g/\sqrt{N})^4$ while the loops over the indices c, d yield a factor N^2 . The overall order of this diagram is $\mathcal{O}(g^4)$.

Figure 1.5: One-loop and two-loop irreducible diagram contributions to the matrix model two-point function with equal input/output indices. We see that by dividing the loops, we can build diagrams with arbitrarily large order in g but at leading order in N . This is how the matrix model remains strongly coupled in the large- N limit.

AdS is topologically a cylinder whose boundary, while spatially infinitely far away, is causally connected with any inertial observer inside the spacetime — signals travelling at lightspeed can reach the boundary in finite time. This therefore means that we must set meaningful boundary conditions on fields living inside AdS. Through the GKPW formula, we see that these boundary conditions translate into sources for each operator in the CFT. This is illustrated in Fig. 1.6. The GKPW formula (1.11) is most useful in its saddle-point approximation. We have seen that the weakly coupled limit of the gravitational description corresponds to the large- N limit of the gauge description. Hence, on the CFT, the interesting saddle point is the large- N saddle-point of the path integral — which at large 't Hooft coupling remains a strongly coupled theory. On the gravitational side in the weak coupling limit, we are interested in a bulk configuration of fields which solves the Einstein field equations with boundary conditions set by the sources $h_i(x)$. The variation of this gravitational action w.r.t. the boundary values of the bulk fields will then yield the expectation values and various n -point correlators of the CFT in the large- N limit. In this limit, we have seen before that diagrams can get suppressed such that only a subset (which can be infinite in the strongly coupled case) survives. This will mean that only the contribution of operators whose diagrams survive at leading order will be accounted for and thus included in the gravitational bulk description.

Importantly, the GKPW formula makes no reference to its string theoretic top-down origin. This invites us to generalize it to a larger class of strongly coupled CFTs and simply engineer 'bottom-up' models where we only consider a minimal set of fields which are generally chosen by symmetries and phenomenological considerations and which we expect to be dominant in the large- N limit. This is fully in the spirit of CMT as we introduced in the first few pages of this introduction. It is this perspective we take when attempting to model non-quasiparticle physics in a quantum critical regime such as that of strange metals. One can study the strong coupling physics of scalar,

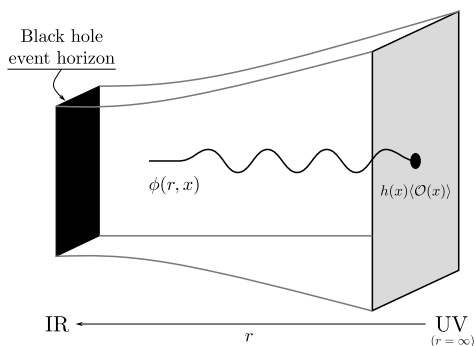


Figure 1.6: Schematic description of the AdS/CFT correspondence. We represent an asymptotically hyperbolic spacetime with a black hole event horizon in the interior in anticipation of finite temperature holography and with a bulk scalar field ϕ whose value at the conformal boundary $\phi(r = \infty, x) = h(x)$ sources a scalar operator $\langle O \rangle$.

fermionic, vector operators in such theories by simply looking at semi-classical scalar, fermionic and vector fields in AdS. Throughout the various chapters of this thesis, we will be making use of this bottom-up approach in order to distil some knowledge about the low energy sector of strongly coupled CFTs.

Pushing the generalization further, one can deform any of these CFTs by a relevant operator which translates into a deformation of the AdS spacetime due to some matter/energy content. Remarkably when doing so, one finds that such solutions often stay within the weak gravity regime where the geometry from the boundary to the interior can be interpreted as an RG flow to a new (but still strongly coupled) infrared (IR) fixed point that can be computationally controlled. The *working hypothesis* of this thesis is that the new IR of these deformed holographic theories is sufficiently universal such that the theory can be used as an effective field theory for real-world systems with similar low energy physics. By this we mean that we assume that the RG flow in real, experimentally observed materials, starting at some microscopic ultraviolet (UV) fixed point set by the material itself, ends at some unknown strongly coupled IR fixed point characterized by some critical exponents (thermodynamical and dynamical). We then attempt to find another flow from a different, controlled, theoretical holographic UV fixed point which ends at a strongly coupled IR fixed point with the same exponents and low energy properties. By RG universality of critical phenomena, it is reasonable to conclude that those IR fixed points are the *same* low energy effective theories and thus the two separate flows belong to the same universality class. If so, we can use the theoretical model to explain experimental observations. This is illustrated in Fig. 1.7 where we draw a canonical example of universality — the Ising universality class describing very different models such as spins or gas molecules on a lattice — as well as the projected analogy for the strange metals.

1.3 Common holographic systems

In the previous sections, we have introduced the GKPW formula which relates operators of a CFT with fields in a gravitational dual, and we have motivated what type

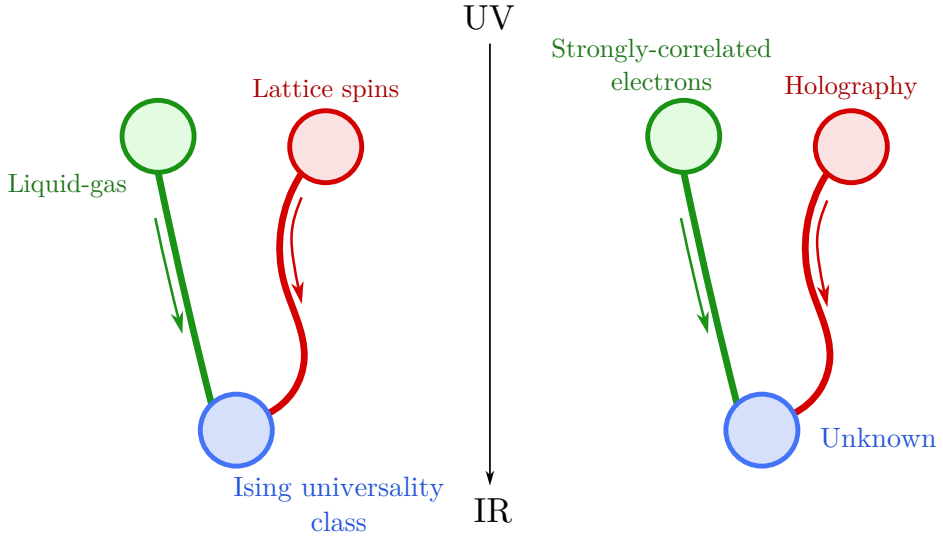


Figure 1.7: Left: Ising universality class describing the ferromagnet-paramagnet as well as the liquid-gas transitions. Right: Projected RG flow from the lattice UV fixed point describing the high-energy physics of strange metals (*e.g.*, cuprates) to some unknown IR theory. A holographic theory in the same universality class would flow to the same IR.

of CFTs should be studied with holography: CFTs deformed by a relevant operator that flow to a new yet still computationally accessible RG fixed point. We are now interested in detailing some common elements of bottom-up holographic models — these form a ‘dictionary’ of the duality (an excerpt of this dictionary can be found in Table 1.1).

The simplest AdS gravitational action one can write is the Einstein-Hilbert action with a negative cosmological constant Λ

$$S_{\text{EH}} = \frac{1}{2\kappa^2} \int d^{d+2}x \sqrt{-g} [R - 2\Lambda] , \quad \Lambda = -\frac{d(d+1)}{2L^2} , \quad (1.12)$$

where we have made explicit the relation between the cosmological constant and the AdS curvature scale L .⁷ The equations of motion for this action are solved by the AdS spacetime given by the metric⁸

$$ds^2 = g_{\mu\nu} dx^\mu dx^\nu = \frac{L^2}{z^2} (dz^2 - dt^2 + dx_i dx^i) , \quad (1.13)$$

⁷In general, we rescale Λ to set $L = 1$.

⁸The Poincaré patch described by this solution does not cover the full AdS spacetime. It is however very convenient to describe QFTs in infinite volume since its conformal boundary is $\mathbb{R}^{1,d}$. We will make extensive use of this patch throughout the various chapters of this thesis

Boundary QFT	Bulk semi-classical gravity
Global symmetry	Local symmetry
Scalar operator \mathcal{O}	Bulk scalar field ϕ
Conformal dimension Δ of \mathcal{O}	Mass of the field ϕ
Source h of \mathcal{O}	Value of the leading branch $\phi_-(z=0)$
Expectation value $\langle \mathcal{O} \rangle$	Value of sub-leading branch $\phi_+(z=0)$
Correlator $\langle \mathcal{O}\mathcal{O} \rangle(\omega, k)$	Ratio $\frac{\delta\phi_+(z=0)}{\delta\phi_-(z=0)}$ for a linearized perturbation $\delta\phi e^{-i\omega t + ikx}$
CFT vacuum state	AdS solution
Thermal state	Black hole solution
Finite density state	Charged solution with gauge field A_t
Temperature	Hawking temperature
Entropy	Bekenstein-Hawking entropy
Chemical potential	Boundary value of A_t
Charge density	Boundary radial derivative of A_t
Free energy	On-shell regularized Euclidean action

Table 1.1: Excerpt of the holographic ‘dictionary’ prescriptions for bottom-up models.

where $z = 1/r$ is the radial coordinate and the conformal boundary (also named the UV boundary) is located at $z = 0$. The local isometry group of this spacetime is $SO(d+1, 2)$, the conformal group in $d+1$ dimensions, which means that perturbations around this background will need to transform under representations of this group. Moreover, the AdS representations smoothly connect to conformal representations as one approaches the conformal boundary. Therefore, the CFT correlation functions we can compute out of this solution using the GKPW formula (1.11) transform covariantly under conformal symmetries and the state on the CFT-side of the duality will be the vacuum of a CFT_{d+1} .

Let us give an explicit example how to compute such GKPW correlation functions using a simple massive scalar field as a pedagogical model. In this example, we will only focus on the dynamics of the scalar field and ignore the metric, but everything we will show here is generally valid for all bulk fields, including the metric itself. The action on our bulk AdS_{d+2} is

$$S_{\text{scalar}} = - \int_M d^{d+2}x \sqrt{-g} \left[\frac{1}{2} (\nabla\phi)^2 + \frac{m^2}{2} \phi^2 \right]. \quad (1.14)$$

As we previously mentioned, we are interested in saddle-points of this action which can be found by varying the action w.r.t. ϕ

$$\delta S_{\text{scalar}} = \int_M d^{d+2}x \sqrt{-g} \delta\phi \left(\nabla^2 - m^2 \right) \phi - \oint_{\partial M} d^{d+1}x \sqrt{-\gamma} \delta\phi N^z \partial_z \phi. \quad (1.15)$$

In this computation, we have integrated by parts the bulk integral yielding the first term, proportional to the equation of motion. A saddle-point solution will therefore solve the Klein-Gordon equation of motion *i.e.*, $(\nabla^2 - m^2)\phi(z) = 0$ (from here on, we assume that the scalar field only depends on the radial coordinate, which in pure AdS is sufficient due to separation of variables). The second term is a remaining boundary integral after integrating by parts. In this boundary term, γ is the induced metric on the boundary and N^μ is an outward-pointing unit vector defining the boundary hypersurface⁹. Near the UV boundary, the Laplacian operator in the radial direction takes the form $\nabla^2\phi \sim z^2\partial_z^2\phi - d z\partial_z\phi$ such that the scalar field admits the follow expansion

$$\phi(z) \sim \phi_-(z)z^{d+1-\Delta} + \phi_+(z)z^\Delta + \dots, \quad (1.16)$$

where Δ is the larger solution of $\Delta(\Delta - d - 1) = m^2$ *i.e.*,

$$\Delta = \frac{d+1}{2} + \frac{1}{2}\sqrt{(d+1)^2 + m^2} > \frac{d+1}{2}. \quad (1.17)$$

The two independent branches ϕ_\pm then yield two degrees of freedom $\phi_\pm^{(0)} = \phi_\pm(z=0)$ whereas the higher order terms in their expansions are constrained by the equations of motion. Near the boundary, we will also be using that $N^z \sim -\sqrt{g^{zz}} \sim -z$ such that we can then compute the on-shell variation of the action (1.15)

$$\begin{aligned} \delta S_{\text{scalar}} &= \oint_{\partial M} d^{d+1}x z^{-d} \left(\delta\phi_-^{(0)} z^{d_\Delta} + \delta\phi_+^{(0)} z^\Delta \right) \left[d_\Delta\phi_-^{(0)} z^{d_\Delta-1} + \Delta\phi_+^{(0)} z^{\Delta-1} \right] \\ &= \oint_{\partial M} d^{d+1}x \left[d_\Delta\phi_-^{(0)}\delta\phi_-^{(0)} z^{d_\Delta-\Delta} + \left(\Delta\phi_+^{(0)}\delta\phi_-^{(0)} + d_\Delta\phi_-^{(0)}\delta\phi_+^{(0)} \right) + \dots \right]. \end{aligned} \quad (1.18)$$

Here we defined $d_\Delta = d + 1 - \Delta$. Since $\Delta > \frac{d+1}{2}$, then $d_\Delta - \Delta < 0$ and the first term diverges as $z \rightarrow 0$. To quell this divergence, we can add an extra boundary term to (1.14) which will not change the equations of motion and will only regularize the action in the boundary — we will discuss this topic in further generality in chapter 4. The extra boundary term¹⁰ we consider is then

$$S_{\text{bdy,scalar}} = \oint d^{d+1}x \sqrt{-\gamma} \frac{m_0^2}{2} \phi^2, \quad (1.19)$$

whose variation leads to an extra contribution

$$\delta S_{\text{bdy,scalar}} = m_0^2 \oint_{\partial M} \phi_-^{(0)}\delta\phi_-^{(0)} z^{d_\Delta-\Delta} + \phi_+^{(0)}\delta\phi_-^{(0)} + \phi_-^{(0)}\delta\phi_+^{(0)} + \dots \quad (1.20)$$

⁹In the coordinate system (1.13), the normal vector to the boundary hypersurface N^μ can be chosen such that only the component N^z is non-zero.

¹⁰A priori we could consider other boundary terms which might simply not contribute at leading order *i.e.*, irrelevant deformations or, depending on the value of the mass m^2 , we can use a boundary term which would reverse the roles of $\phi_-^{(0)}$ and $\phi_+^{(0)}$ *i.e.*, a Legendre transformation. Chapter 4 has an in-depth discussion of this point.

By choosing $m_0^2 = -d_\Delta$, the leading divergent term vanishes and we are left with a finite contribution proportional to $\phi_+^{(0)}\delta\phi_-^{(0)}$ plus terms that vanish as $z \rightarrow 0$. The total finite variation becomes

$$\delta S_{\text{scalar}} = (2\Delta - d - 1) \oint_{\partial M} d^{d+1}x \phi_+^{(0)} \delta\phi_-^{(0)}. \quad (1.21)$$

This term can be written as $\delta S = \oint \langle \mathcal{O} \rangle \delta h$ where we identify $\delta h = \delta\phi_-^{(0)}$ as the source of the bulk scalar field following the GKPW description.¹¹ Through the GKPW formula (1.11) and in the saddle-point approximation, computing the variation of the action S_{scalar} is the same as computing the expectation value of the associated QFT operator

$$\frac{\delta S_{\text{scalar}}}{\delta h} = -i \frac{\delta}{\delta h} \log Z_{\text{QFT}} = \langle \mathcal{O} \rangle. \quad (1.22)$$

So we deduce here that the expectation value of the QFT scalar operator associated with the bulk field ϕ is $\langle \mathcal{O} \rangle = (2\Delta - d - 1) \phi_+^{(0)}$. This relation between the falloffs of the bulk field and the boundary source and expectation value of the associated operator is at the core of the AdS/CFT duality. Pushing this reasoning further, we can similarly compute the n -point correlation functions of the QFT operator \mathcal{O} . Taking the two-point correlator as an example, we use that within linear response theory and in Fourier space, $\langle \mathcal{O}(\omega, k) \rangle = G_{\mathcal{O}\mathcal{O}}(\omega, k) \delta h(\omega, k)$. So to obtain the two-point function, one must simply add to the saddle-point solution ϕ a plane wave perturbation $\delta\phi(z)e^{-i\omega t + ikx}$, solve the linearized equations of motion for this model with Dirichlet boundary conditions and finally read off the Green's function through the ratio

$$G_{\mathcal{O}\mathcal{O}}(\omega, k) = (2\Delta - d - 1) \frac{\delta\phi_+^{(0)}}{\delta\phi_-^{(0)}}. \quad (1.23)$$

We can now build on the knowledge of how to compute correlation functions in the conformal vacuum to deduce how to generalize this computation to other states. As we have just seen, the choice of sources of operators on the QFT fixes the boundary conditions on the bulk fields in the UV region. The boundary conditions deep in the interior can still be chosen freely. This allows for multiple solutions which we will consider as different states of the theory. An intuitive way to see this is to remember that the radial coordinate encodes for the RG flow such that the IR of the theory corresponds to the low energy sector of the dual QFT where state specific aspects become important. For instance, the Anti-de Sitter-Schwarzschild (AdS-Schw) black hole solution can be obtained by allowing for a more general metric ansatz and requiring that g_{tt} vanishes for some value $z = z_h$, which defines the black hole event horizon.

¹¹In the initial section of this chapter, we have mentioned that the correspondence maps the source to the boundary value of the bulk field, whereas we now show that it is actually given by the coefficient of the term scaling as $z^{d+1-\Delta}$. In practice, one often works with rescaled fields $\varphi = z^{\Delta-d-1}\phi$ such that the sourcing is done by imposing Dirichlet boundary conditions on φ .

This solution takes the following form

$$ds^2 = \frac{L^2}{z^2} \left(\frac{dz^2}{f(z)} - f(z) dt^2 + dx_i dx^i \right), \quad f(z) = 1 - \left(\frac{z}{z_h} \right)^{d+1}. \quad (1.24)$$

What states could this encode in the QFT? Black holes naturally introduce a notion of thermodynamics in the system with their Hawking temperature T [28] and Bekenstein-Hawking entropy S [29], and it is thus reasonable to conclude that the dual state to this AdS-Schw solution is a CFT thermal state. The thermodynamic quantities can be read off from the geometry near the horizon; the temperature is given by the slope of the emblackening factor f at the horizon $T = \frac{-f'(z_h)}{4\pi}$ while the entropy density is given by the area density of the event horizon $s = 4\pi \sqrt{\prod_i g_{ii}(z_h)}$ (where the product is defined on the d spatial coordinates). Many subsequent tests have verified that this identification is correct [30].

Two different solutions to the same equations of motion will yield two different holographic states, yet in general we are interested in the thermodynamically preferred state of a system. In this case, we select the solution which minimizes the free energy of the system. By definition, the free energy is related to the Euclidean partition function through $F = -T \log Z_{\text{QFT}}^E$ which, when using the GKPW formula (1.11) and when the collective bulk fields ϕ are taken on a saddle-point ϕ_0 , can be related to the Euclidean on-shell gravitational action

$$F = TS_{\text{grav.}}^{E,\text{reg.}}[\phi = \phi_0]. \quad (1.25)$$

This notion of thermodynamics is fully compatible with the black hole thermodynamics of the AdS-Schw solution such that the integrated first law of thermodynamics is obeyed $F = E - TS$ (where E is the internal energy of the solution obtained by reading the expectation value of the boundary quantity dual to the bulk metric field).¹²

To construct another state which we will use heavily, we need to introduce the electromagnetic charge. These are associated with a local $U(1)$ symmetry (this is notably the case for the ordinary electric charge). In condensed matter applications however, one can usually ignore the dynamics of the electromagnetic field and only think of the symmetry as a global $U(1)$ describing conserved particle flows. An important feature of holography is that it maps global symmetries to local symmetries. The argument behind this statement can be readily understood by considering some local gauge symmetry in the bulk — the diffeomorphism invariance of general relativity

¹²In the expression (1.25), an extra regularization constraint was imposed on the Euclidean gravitational action. The reason behind this is that bulk actions in holography are usually supplemented with two kinds of boundary integrals — the first kind, which we previously discussed, is required to make the variational problem on the boundary well-defined while the second kind consists of counterterms to regularize UV divergences. These additions only have support on the boundary, and therefore they do not affect the bulk equation of motions and their solutions. However, they play a vital role when varying the action around a saddle-point as we will see shortly. These two types of contributions will be thoroughly reviewed for a specific holographic model in chapter 4.

for instance. Variations of the total action — meaning (1.12) and additional boundary terms — can formally be written as¹³

$$\delta S = \int d^{d+2}x \sqrt{-g} \left(R_{\mu\nu} - \frac{2\Lambda}{d} g_{\mu\nu} \right) \delta g^{\mu\nu} + \oint d^{d+1}x \sqrt{-\gamma} T^{\mu\nu} \delta g_{\mu\nu}, \quad (1.26)$$

where the bulk term is proportional to the equations of motion which vanishes on-shell and γ is once again the induced metric determinant on the boundary. Applying the same logic we previously used for the scalar field action, we can conclude that $T_{\mu\nu}$ is the boundary expectation value associated with the QFT source $\delta g^{\mu\nu}$. Let us now consider a diffeomorphism transformation on the metric variation $\delta g_{\mu\nu} \rightarrow \delta g_{\mu\nu} + \nabla_\mu \xi_\nu + \nabla_\nu \xi_\mu$ for some vector ξ . Requiring that δS is invariant under such gauge transformation is equivalent to the condition

$$\oint d^{d+1}x \sqrt{-\gamma} T^{\mu\nu} \nabla_\mu \xi_\nu = - \oint \sqrt{-\gamma} \xi_\nu \nabla_\mu T^{\mu\nu} = 0. \quad (1.27)$$

To obtain this equality, we used that $\sqrt{-g} \nabla_\mu X_\nu = \partial_\mu (\sqrt{-g} X_\nu)$, and we integrated by parts. The condition (1.27) must be valid for every vector ξ and thus is equivalent to the conservation equation $\nabla_\mu T^{\mu\nu} = 0$. A more detailed argument shows that $T^{z\mu}$ can also be set to zero and, noting that the AdS metric is flat at the conformal boundary, we therefore have on the boundary theory $\partial_i T^{ij} = 0$ — thus indicating that T_{ij} is the boundary stress-tensor.¹⁴

This feature tells us that in order to introduce a conserved $U(1)$ current in the boundary, we must add a local $U(1)$ gauge field A_μ in the bulk. The minimal extension to the Einstein-Hilbert action with such a gauge field is the Einstein-Maxwell action

$$S_{\text{EM}} = S_{\text{EH}} - \frac{1}{4e^2} \int d^{d+2}x \sqrt{-g} F_{\mu\nu} F^{\mu\nu}, \quad F_{\mu\nu} \equiv \partial_\mu A_\nu - \partial_\nu A_\mu. \quad (1.28)$$

The canonical black hole saddle-point for this action is the Reissner-Nordström (RN) charged black hole solution which uses the same metric ansatz as (1.24) but with a different emblackening factor as well as a non-trivial gauge field

$$f(z) = \left(1 - \frac{z}{z_h} \right) \left(1 + \frac{z}{z_h} + \frac{z^2}{z_h^2} - \frac{\mu^2 z^3}{4z_h} \right), \quad A = \mu \left(1 - \frac{z}{z_h} \right) dt \quad (\text{in } d=2). \quad (1.29)$$

This family of solutions is parametrized by (μ, z_h) where now μ is the boundary value of A_t and therefore the source of the charge density operator $\mathcal{J}^t = n$ on the boundary

¹³Here we see immediately why boundary terms must be supplemented to (1.12). In this specific example, we consider Dirichlet boundary conditions on the metric, and therefore we must eliminate any leftover variations proportional to $\partial_z \delta g_{\mu\nu}$ which naturally arise when varying the Ricci scalar. This can be done using the Gibbons-Hawking-York term [31]. Counterterms are also needed to tame the divergences in the volume element $\sqrt{-g} \sim z^{-(d+2)}$ near the boundary.

¹⁴An important consequence of this statement is that the bulk stress-energy tensor in the gravitational system, defined as the r.h.s. of the Einstein equations $R_{\mu\nu} - \frac{1}{2}(R - 2\Lambda)g_{\mu\nu} = \kappa^2 \hat{T}_{\mu\nu}$, is fundamentally different from the boundary stress-energy tensor.

theory — μ can thus be identified as the chemical potential of the boundary theory. This allows us to deduce that this solution encodes for a thermal finite density QFT whose thermodynamics will now obey the first law of thermodynamics $F = E - TS - \mu N$, where the free energy F can once again be obtained by the Euclidean on-shell regularized gravitational action.

Such a solution, parametrized only by a temperature and a finite density, has garnered a lot of interest over the years for condensed matter applications, as its near-horizon geometry encoding for low energy physics shows a novel heretofore unknown IR anchored on an emergent $\text{AdS}_2 \times \mathbb{R}^2$ geometry [32, 33]. This was immediately recognized as the dual of a quantum critical sector in the spectrum of the theory, with curiously an infinite dynamical critical exponent $\mathbf{z} = \infty$.¹⁵

More generalized types of scaling can be found from the infrared geometry of more complicated black hole solutions [32, 34, 35, 36]. The most general family of such solutions are saddle-points of the Einstein-Maxwell-Dilaton (EMD) action

$$S_{\text{EMD}} = \int d^{d+2}x \sqrt{-g} \left[\frac{1}{2\kappa^2} (R - 2\Lambda) - \frac{Z(\phi)}{4e^2} F_{\mu\nu} F^{\mu\nu} - \frac{1}{2} (\partial\phi)^2 - V(\phi) \right], \quad (1.30)$$

where V and Z are arbitrary functions of ϕ . These solutions will yield a near-horizon geometry of the form

$$ds^2 = r^{2\theta/d} \left[-\frac{dt^2}{r^{2\mathbf{z}}} + \frac{dr^2 + dx_i dx^i}{r^2} \right] \quad (1.31)$$

where we have set $L = 1$ and the horizon is now located at $r \rightarrow 0$. The exact choice of scalar potentials V, Z will determine the value of the exponents θ, \mathbf{z} . We have already encountered \mathbf{z} , identified as the dynamical critical exponent of a quantum critical theory, and θ can be identified as the hyperscaling violation exponent.¹⁶ Since the scalings control the IR geometry of the theory where the event horizon lies, they will directly affect the low temperature thermodynamic scalings, with in particular the entropy density obeying a scaling form $s \sim T^{\frac{d-\theta}{\mathbf{z}}}$.

As we mentioned previously, the near-horizon geometry of the RN solution is $\text{AdS}_2 \times \mathbb{R}^2$. We can deduce from Eq. (1.31) that for the RN black hole, the two exponents take the values $(\theta, \mathbf{z}) = (d, \infty)$. An immediate consequence of this scaling is that for the RN solution, $S(T \rightarrow 0) = S_0 > 0$. This finite ground state entropy signals that the RN solution is a fine-tuned point in the large- N limit and will carry artifacts of such limit. By the usual arguments, it should be unstable. Let us set aside that matter for a second and focus on the intriguing property of an infinite dynamical critical

¹⁵The existence of such a state has later been verified for SYK-type models, confirming that this feature is not a holographic artifact.

¹⁶While the dynamical critical exponent relates scaling properties of space and time, the hyperscaling violation exponent sets an effective dimensionality $d_{\text{eff}} = d - \theta$ for the system at low energies. A typical example of such property can be found in theories with a Fermi surface which are effectively one-dimensional and whose physics is set by a non-decoupling dimensionful energy scale: the Fermi energy.

exponent $\mathbf{z} = \infty$. Remembering the physics of QCPs of the previous section, an infinite dynamical critical exponent means that the system remains in the quantum critical regime throughout a large portion of parameter space (this is akin to having a flat cone for the quantum critical regime). This suggests that the RN solution is closer to describing a quantum critical phase rather than a quantum critical point. Moreover, in that limit, lengths and spatial momenta do not scale away at low energies and thus any momentum can contribute to low energy fluctuations. This seems to hint that, in spite of its fine-tuning, the RN solution demonstrates relevant physics to that of strange metals. Other solutions were later found which also displayed an infinite critical dynamical exponent $\mathbf{z} = \infty$ while preserving the third law of thermodynamics. This is made possible when the hyperscaling violation exponent also diverges while keeping the ratio $-\frac{\theta}{\mathbf{z}} \equiv \eta$ fixed. The near-horizon geometry is then *conformal-to-AdS₂* *i.e.*, it is related to the near-horizon RN geometry by a conformal factor as [37]

$$ds^2 = y^{-\frac{2\eta}{\eta+d}} \left[a^2 \frac{-d\tilde{t}^2 + dy^2}{y^2} + dx_i dx^i \right], \quad a = \frac{d}{\eta+d} \mathbf{z}^{-1}, \quad (1.32)$$

where we used the coordinate transformation $r \rightarrow y^a$ and $t \rightarrow a\tilde{t}$ on (1.31) and used that $a-1 \sim -1$ as $\mathbf{z} \rightarrow \infty$. Such near-horizon geometries will then lead to entropy scalings $S \sim T^\eta$ which will vanish at low temperatures for $\eta > 0$. Among this family of solutions, we will be interested in this thesis in the Gubser-Rocha (GR) model [38] which has $\eta = 1$ and therefore an entropy $S \sim T$, the same scaling behavior observed in a Fermi liquid (which has $(\mathbf{z}, \theta) = (1, d-1)$). Note that in practice, while these more refined solutions provide a less artificial starting point to study $\mathbf{z} \rightarrow \infty$ physics than the RN solution, they are also generally more complicated. For that reason, it is still common to study the RN solution as a simpler toy model and eventually consider a conformal-to-AdS₂ model as a refinement — which is what we will do in chapter 2.

1.4 This thesis

In this introduction, we have presented a pedagogical review of the tools and ideas behind the AdS/CFT correspondence with a strong emphasis on its application to study strongly correlated quantum matter at novel QCPs and QCPh's. In the following chapters of this thesis, we will apply these methods to various holographic models built in order to produce varied physics, showcasing the universal power of our holographic methods for such cases, either in the direction of experimental strange metals or to address more fundamental theoretical puzzles. These applications can be grouped in three parts.

1.4.1 Chapters 2, 3, 4 — Metallic transport in an ionic lattice

We will follow this introduction with chapter 2 in which we will numerically construct black hole solutions with modulated boundary charge densities in order to simulate the effect of a lattice made of background ions on the holographic QCPh of

the RN and GR models. Chapter 2 will further feature a detailed introduction of the wider condensed matter context and will situate our findings within that context. Our numerical data will allow us to measure electrical and thermal conductivities, thus probing flows of charge and thermal carriers in such a modulated potential, both at small *i.e.*, perturbative, and at large lattice potential strength. These observables can be directly compared with laboratory experiments and are thus of great interest.

The holographic data in the perturbative regime at small wavelength and frequencies will then be thoroughly compared with the theoretical predictions of a purely hydrodynamic flow of electric charges with perturbatively small spatial modulation of their chemical potential. The general framework of the underlying hydrodynamic theory will be developed in chapter 3 where we present a novel, standalone hydrodynamic calculation. The benefit of such theories comes from the wide range of systems they can describe. However, as effective theories, they lack predictive power without microscopic model-specific input. We will thus further see in chapter 3 that holography doubles as a great set of microscopic models to probe interesting hydrodynamic behavior. Why hydrodynamics gives additional theoretical leverage to describe QCP's will be explained.

The question of the quantization procedure on the QFT side of the duality for the GR solution (with or without a lattice modulation) is a subtle but important detail of the GKPW formula that we have so far not addressed and can often be ignored. However, for the GR model which we considered for experimental reasons, one cannot ignore this subtlety. In particular, one must carefully understand the role of the scalar field in the action (1.30) under the flow of the Renormalization Group in order to interpret the boundary theory, as well as to understand its influence on the choice of sources imposed as boundary conditions when computing correlation functions. In chapter 4, we will derive the various interpretations of the boundary theory and a posteriori justify the choices of boundary conditions made in chapter 2.

1.4.2 Chapter 5 — Regulated Quantum Electron Star

An interesting feature of black holes in AdS is that they can be ‘hairy’ *i.e.*, they can be labelled by more than just their mass, charge and angular momentum. This was rather unexpected and counter to much of the conventional flat space gravitational wisdom at the time but proved to be an essential feature of the AdS/CFT correspondence. It was shown that scalars readily condensate around a black hole. This is the dual to some scalar order parameter condensating in the boundary QFT and indicating a phase transition to some broken symmetry phase. When the scalar is charged under the $U(1)$ local gauge symmetry, the condensed state is similar to a superconducting state¹⁷ around a quantum critical metal; in other words, the holographic superconductor [39, 40, 41].

¹⁷Formally it is only a superfluid as the broken $U(1)$ symmetry is a global symmetry of the boundary.

Fermions proved more difficult. Due to the Pauli principle, they do not condensate and thus initially, all that was observed was an instability of the black hole solution under light fermionic perturbations. By considering the density of fermions to be high enough, it was possible to treat them as an effective charged fluid — similar to a neutron star but with charge — leading to an AdS electron star solution [42]. While it was hoped that this solution would shed some light on the physics of strongly interacting fermionic systems, it also displayed some artifacts of the holographic origin of this theory, therefore failing the hypothesis of universal emergent low energy features. In more detail, the electron star showed an infinite amount of Fermi surfaces in its spectrum, a remnant of the large- N limit saddle-point approximation. Further attempts were then made to study this question in more sophisticated ways in order to shield the IR from purely holographic effects [43, 44, 45, 46] until eventually the assumption of large density was found to be the cause of these spurious Fermi surfaces. New attempts were made [47, 48, 49, 50] at reaching the other end of the spectrum, characterized by a small density of fermions where quantum corrections might be required. These new models were free of the holographic effects but lost the semiclassical gravitational stability of the electron star. In chapter 5 of this thesis, we will provide a new model attempting to bridge these two concepts — a model of a quantum electron star which is both gravitationally and thermodynamically stable while only displaying a single Fermi surface — at the price of introducing some external regulator in the form of a non-dynamical scalar field.

1.4.3 Chapter 6 — Nielsen complexity of conformal field theories

The last chapter of this thesis will look at strongly coupled systems from a different point of view. A crucial observation is that there seems to be a deep connection between the notions of strong coupling in QFTs and long-range entanglement, see *e.g.*, [51]. The main idea behind this statement is that when interactions are weak, it is expected that each part of the system only overlaps with its neighbors and the resulting entanglement pattern should be short-range. However, with strong interactions, a small part of the system can reach further away from its local support which leads to long-range densely entangled states. The QCPs we have been discussing are themselves examples of such states; since they are described by CFTs, the entanglement structure of a given subregion will diverge logarithmically in the length of the subregion [52]. This observation was the impetus behind the search for a holographic quantity encoding this property of strongly interacting systems. The first result of this kind was the discovery by Ryu and Takayanagi of a geometric quantity matching the entanglement entropy of a CFT subregion [53]. This result was inspired by the Bekenstein-Hawking entropy formula, yet instead of equating the entanglement entropy to the area of the event horizon of a black hole, it is given by the area of an extremal surface anchored at the UV boundary on the subregion.

However, the interior region of a black hole is never probed by such extremal surfaces and therefore a priori not accounted by this subsystem entanglement entropy.

It was then an affirmation that entanglement entropy (and the various analogous proposals for mixed states of bipartite systems) is not enough to account for the entire entanglement structure of a system [54, 55].

Recent efforts have been made to bridge that gap from the boundary side by finding another quantity which would probe deeper into the entanglement pattern of QFTs. One such attempt is called ‘Nielsen complexity’ [56, 57, 58]. This was inspired by the field of quantum computing wherein the complexity of a given unitary operation is measured by the minimal number of elementary operations required to build it. In quantum systems and more generally QFTs, Nielsen proposed that this discrete measure should generalize to a distance in the space of unitaries. While there is no doubt that such a quantity can be a useful measure, many ambiguities in its definition remain (such as the choice of gate set and cost functions). In chapter 6, we study one such possible measure on CFTs in various dimensions, and, through the holographic duality, directly and unambiguously connect it to the dynamics of massive semiclassical particles in AdS.

Chapter 2

Holographic lattices as local quantum critical metals

Attribution

This chapter was published as a journal article under the title “ T -linear resistivity, optical conductivity, and Planckian transport for a holographic local quantum critical metal in a periodic potential” in the journal *Physical Review B* (PRB), volume 108, issue 12 (2023), together with Floris Balm, Sam Arend, Joost Aretz, Kevin Grosvenor, Martijn Janse, Ole Moors, Jonah Post, Vladimir Ohanesjan, David Rodriguez-Fernandez, Koenraad Schalm and Jan Zaanen.

2.1 The Planckian dissipation mystery versus computational holography

Are there states of matter that are governed by physical principles of a different kind from those identified in the 20th century? This question arose in the study of strongly interacting electron systems realized in condensed matter, starting with the discovery of superconductivity at a high temperature in copper oxides. Their metallic states exhibit properties that appear to be impossible to explain with the established paradigm explaining normal metals – the Fermi-liquid theory – and these were accordingly called “strange metals” [10, 12].

An iconic signature is the linear-in-temperature electrical resistivity [15], an exceedingly simple behavior that is at odds with transport due to the quasiparticle physics of normal metals. A linear temperature dependence of the resistivity does occur

naturally in conventional metals due to scattering of the quasiparticles against thermal disorder of the lattice above the Debye temperature. The problem in the cuprates and related systems is that the resistivity is linear all the way from the lowest to the highest temperatures where it has been measured. One anticipates some powerful principle of a new kind to be at work protecting this unreasonable simplicity.

The measured optical conductivities reveal at lower temperatures a Drude response [59, 60, 61, 62], signaling that the electrical conduction is controlled by a current relaxation time. Intriguingly, this time is very close to the “Planckian dissipation” timescale $\tau_{\hbar} = \hbar/(k_B T)$. Planck’s constant \hbar plays a special role in dimensional analysis, as for instance the Planck scale of quantum gravity. Since \hbar carries the dimension of action, τ_{\hbar} is a timescale associated with the thermal physics property of dissipation, the conversion of work into heat [63, 64]. The case was made based on DC data that this Planckian time is remarkably universal also involving a variety of non-cuprate unconventional metals exhibiting the linear resistivity [65, 66, 1].

However, upon raising temperature further, in the “bad metal” regime above the Mott-Ioffe-Regel bound optical conductivity studies show that the dynamical response changes drastically. Instead of a Drude response, a mid-infrared resonance develops with a characteristic energy that appears to increase with temperature, leaving a rather incoherent response at low energy [67]. Remarkably, there is no sign of this radical reconfiguration of the dynamical response in the DC resistivity that continues to be a perfectly straight line, seemingly controlled by τ_{\hbar} .

The occurrence of this universality of electrical conduction poses quite a problem of principle. On the one hand, considerable progress has been made in the understanding of dissipative phenomena in terms of quantum thermalization, explaining it in terms of unitary time evolution and the collapse of the wave function (e.g. [68]). An early result is the identification of τ_{\hbar} as the characteristic universal dimension for the dissipation time of non-conserved quantities associated with densely many-body entangled quantum critical states [69] realized at strongly interacting bosonic quantum phase transitions [70, 71].

This was very recently further clarified using both holographic duality (AdS/CFT correspondence) as well as studies in the closely related SYK models that connect macroscopic transport in such strange metals to microscopic quantum chaos. The central issue is that thermalization leading to local equilibrium may proceed very rapidly in densely entangled systems compared to quasiparticle systems. Using out-of-time-order correlators (OTOC’s) one can identify a quantum Lyapunov time τ_{λ} characterizing the microscopic time associated with the onset of quantum chaos that turns out to be bounded from below by τ_{\hbar} . In strongly correlated strange metals this microscopic timescale together with the chaos propagation “butterfly” velocity v_B can set the natural scale for the charge/heat and momentum diffusivities controlling the dissipative properties of the macroscopic finite temperature hydrodynamical fluid [72, 73, 74].

However, in ordinary metals electrical conduction is controlled by total momentum conservation, as a ramification of translational invariance: any finite density system in the Galilean continuum *has* to be a perfect conductor. A finite resistivity is therefore rooted in the breaking of translation invariance. But how can this ever give rise to a universal resistivity controlled by τ_h ? This is the core of the mystery – all explanations we are aware of rely on accidental, fine-tuning circumstances, e.g. [75, 1, 76].

Holographic duality is now widely appreciated as a mathematical machinery that has a remarkable capacity to shed light on general principles associated with densely entangled matter [77, 19, 1, 69], the “scrambling” that we just discussed being a case in point. It achieves this by dualizing the densely entangled quantum physics into a gravitational problem in one higher dimension that is computable with (semi-)classical General Relativity. However, this is only a relatively easy mathematical affair for a homogeneous translationally invariant space. When one breaks the spatial translation symmetry the Einstein equations become a system of highly non-linear partial differential equations. If one wishes to have a full view on what holography has to say about transport in the laboratory systems one has to confront this challenge. Invariably a very strong effective potential due to the background of ions is present in the laboratory strange metals, and it is even believed to be a *necessary* condition to obtain strongly correlated electron behavior [78, 79, 80]. But what has holography to tell about the effects of strong lattice potentials on strange metal transport?

This can only be accomplished numerically. Although relatively efficient numerical relativity algorithms are available, the computations are demanding. Proof of principle was delivered that it can be done [81, 82, 83, 84, 85] and we set out to explore this more systematically. We focused specifically on the so-called Gubser-Rocha (GR) holographic strange metal [38]. This is unique in the regard that it is characterized by “local quantum criticality” (a dynamical critical exponent $z \rightarrow \infty$) as well as a Sommerfeld entropy $s \sim T$ in the regime $T \ll \mu$, generic properties that appear to be realized by the cuprate strange metals [69]. In such strongly coupled systems this then also predicts a linear-in- T resistivity [86]. For comparison we also include results for the elementary Reissner-Nordström holographic strange metal. This also exhibits local quantum criticality, but it has a (pathological) finite zero temperature entropy.

2.1.1 Main observations and summary of the results.

We consider a 2+1-dimensional strongly interacting strange metal holographically dual to the Gubser-Rocha model in the presence of a harmonic square ionic lattice background encoded in the chemical potential

$$\mu(x, y) = \bar{\mu} \left[1 + \frac{A}{2} \cos(Gx) + \frac{A}{2} \cos(Gy) \right]. \quad (2.1)$$

We numerically compute the full set of DC thermo-electrical transport coefficients — electrical conductivity σ , thermal conductivity $\bar{\kappa}$, the thermo-electrical coefficient α — up to very large potentials ($A \simeq 8$) and temperatures as low as $T \simeq 0.005\mu$. For stronger

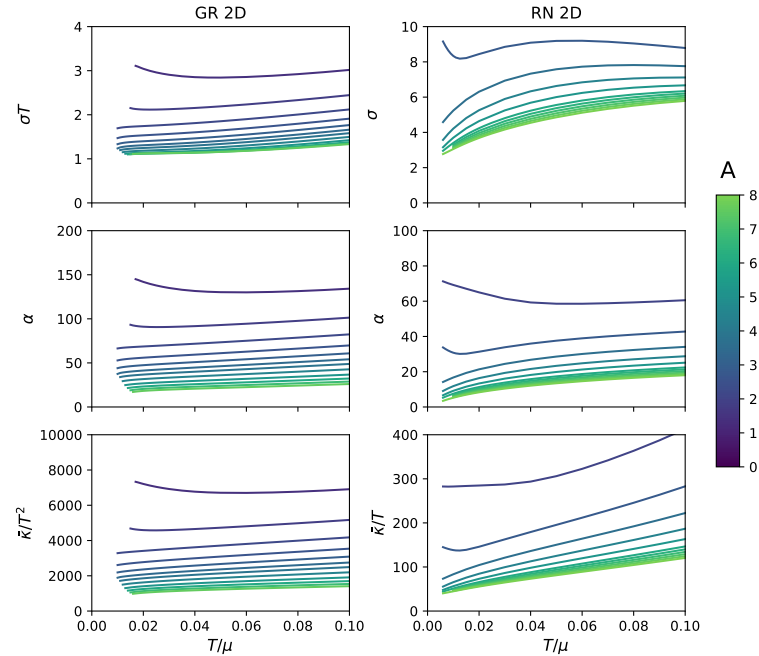


Figure 2.1: The thermo-electrical DC transport coefficients as functions of temperature T in units of the chemical potential μ for the Gubser-Rocha (GR, left column) and Reissner-Nordström (RN, right column) metals in a 2D square lattice harmonic background potential with wave vector $G = 0.1\sqrt{2}\mu$ and a strength $0 < A < 8$. σ , α and $\bar{\kappa}$ are the electrical conductivity, thermo-electrical cross conductivity and the overall thermal conductivity respectively. The electrical conductivity of the GR metal (top-left panel) shows for all potentials a nearly linear in temperature resistivity ($\rho = 1/\sigma \sim T$) with a slope that shows saturating behavior for large potentials.

potentials we sometimes resort to uni-directional 1D potentials to maintain numerical control. In addition, we also compute the optical conductivities. Because of numerical difficulties we encountered this is limited to intermediate potential strength ($A \lesssim 1-2$) and 1D lattices.

From this computational experiment we make three remarkable observations:

1. The DC electrical resistivity of the Gubser-Rocha metal becomes to good approximation linear in temperature at low temperatures, see the upper left panel in Fig. 2.1. Strikingly, we find the slope of this linear resistivity to saturate for an increasing potential strength after correcting for a spectral weight shift. This suggests a connection with the universal Planckian dissipation bound: using the optical conductivity to deconvolve this in a total spectral weight and a current lifetime, the saturation value for the latter is close to $\tau_{GR} = \frac{1}{2\pi} \hbar / (k_B T)$ (see Fig. 2.13).

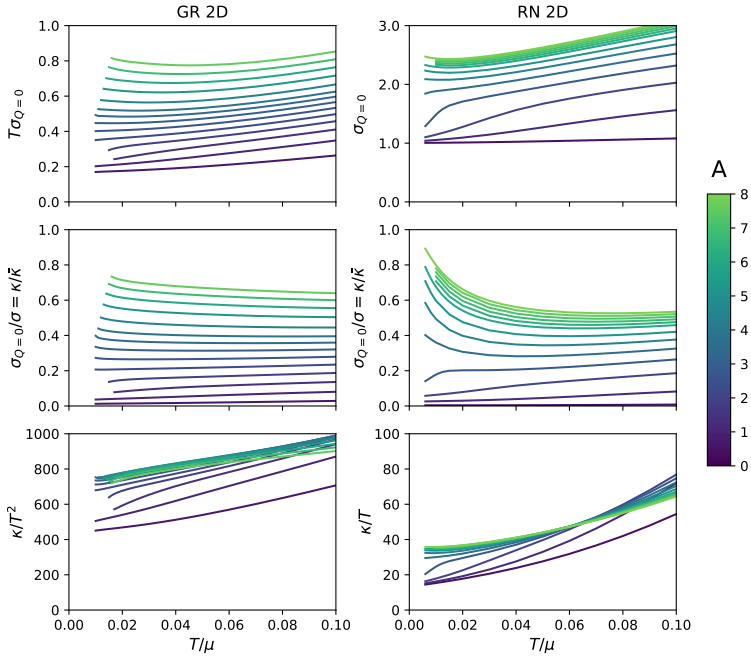


Figure 2.2: The electrical conductivity at zero heat current $\sigma_{Q=0}$ shows that as the lattice strength is increased the non-convective current anchored in charge diffusion becomes the dominating conduction channel. At the largest lattice strength where $A = 8$, the ratio of non-convective to convective transport $\sigma_{Q=0}/\sigma$ reaches up to 80%, signalling that momentum conservation is nearly completely destroyed. By definition, the fraction $\sigma_{Q=0}/\sigma$ is equal to the ratio $\kappa/\bar{\kappa}$. The open boundary thermal conductivity κ anchored in thermal diffusion is rather independent of the lattice strength, barely changing after a moderate value of $A = 1$ has been reached. Parameters are the same as in Fig. 2.1.

The electrical conductivity of the Reissner-Nordström (RN) metal also saturates for large potential strength at a roughly temperature independent value, although less perfect. The gross differences in temperature dependencies of the GR and RN metals between the electrical conductivity appear to reflect the different temperature dependencies of the entropies. We will discuss below why this is not so. Despite first appearances, the thermo-electric (α) and heat ($\bar{\kappa}$) conductivities do not saturate at larger lattice potentials, but vanish as $1/A$ (see Fig. 2.12).

2. We can separate out the convective overall transport from more microscopic diffusive transport by considering the heat conductivity with zero electrical current $\kappa = \bar{\kappa} - T\alpha^2/\sigma$, also known as the open boundary heat conductivity. Similarly, one can define an electrical conductivity without heat transport $\sigma_{Q=0} = \sigma - T\alpha^2/\bar{\kappa}$ that is a (non-perfect) proxy for transport anchored in charge diffusion — it is pro-

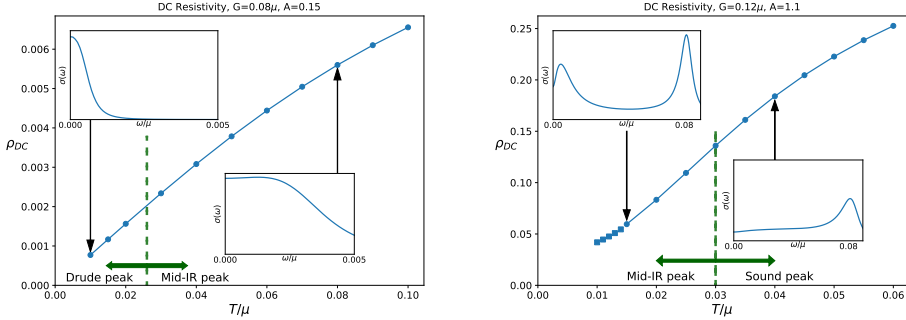


Figure 2.3: The DC resistivities for the small- ($A = 0.15$, left panel) and intermediate ($A = 1.1$, right panel) lattice potential of the Gubser-Rocha metal are in both cases (nearly) linear in temperature. However, in both cases the optical conductivity (insets) undergoes radical changes when temperature increases. At the lowest temperatures in the small potential case (left panel) this consists of a simple Drude peak that gradually turns into an incoherent “flat top” low frequency response terminating at a developing “mid-IR peak”. The characteristic temperature where this happens decreases for increasing potential strength. In the right panel, a full fledged mid-IR peak has already developed at a low temperature $T \sim 0.015\mu$ (left inset), while it is accompanied by a high energy peak at $\omega = c_s G = \frac{1}{\sqrt{2}}G$ that is identified to be the “Umklapped sound peak”. Upon further raising temperature, the mid-IR peak moves up in energy to eventually merge with the sound peak (right inset).

portional to charge diffusion, but its thermodynamic scaling is also determined by cross-terms with the convective part. These are shown in Fig. 2.2. The $\sigma_{Q=0}$ is also (nearly) inversely proportional to temperature up to the largest potentials, similar to the overall σ . Most importantly, however, we see that for large potentials this diffusion-anchored contribution to the conductivity dominates the transport (middle panels): up to $\sim 80\%$ of the electrical currents is anchored in the diffusive sector. Similarly, the diffusion-anchored open boundary thermal conductivity (κ , lowest panels) accounts for almost the full heat conductivity $\bar{\kappa}$ of Fig. 2.1 in the large potential regime. This signals that for the strongest potentials the system approaches closely the incoherent metal regime addressed by Hartnoll [64] where there is no longer a sense of momentum conservation; It is governed instead by a “hydrodynamics” that only relies on energy- and charge conservation. A key observation is that this is the regime which displays the “Planckian saturation” of the electrical resistivity highlighted above in Fig. 2.1. In other words, this is the regime that should contain the clue behind the saturation phenomenon.

3. Computing the optical conductivities, we find for small lattice potential at the lowest temperature a perfect Drude peak (left panel Fig. 2.3). Strikingly, upon raising temperature this evolves into a mid-IR peak, reminiscent of what is seen in experiment. Although the dynamical response shows such drastic changes,

these do not imprint *at all* on the linearity in temperature of the DC resistivity remarkably. This finding is repeated in the intermediate potential case. There, the electrical DC resistivity can even stay linear-in-T through a second change in relaxational dynamics from the mid-IR-peak regime to a fully incoherent metal. Just within reach of our numerics, the spectrum at the lowest temperature (left inset) now already displays the mid-IR peak, and we have good reasons to expect that at even lower temperatures, outside of our numerical reach, a Drude response should still be present. There is also a second peak at higher frequencies that can be identified with the “Umklapp copy” of the sound mode at an energy $\omega = c_s G$ where c_s is the speed of sound and G the lattice wavevector (Section 2.5). Upon raising temperature the mid-IR peak moves to higher frequency to eventually merge with the “Umklapped sound” peak, transitioning to a fully bad incoherent metal regime (right inset), while the DC resistivity stays essentially linear-in-T throughout.

These observations are reminiscent of the experimental observation that the linear-in-T DC resistivity appears to be completely insensitive to the change from “good metal” to “bad metal” behavior when temperature increases. This transition can be defined using the absolute value of the resistivity crossing the Mott-Ioffe-Regel limit but perhaps a better way is to identify it through the dynamical response, associating the good metal regime with a Drude response while the bad metal has the incoherent “mid-IR peak” type of behavior as in our computations.

To dissect these numerical results is an intensive exercise. We therefore provide an executive summary of the paper here. The reader interested in the details may proceed directly to Section 2.2 and skip the remainder of this Introduction.

The local quantum critical strange metals of holography and hydrodynamical transport

Transport in holographic strange metals is governed by hydrodynamics (Section 2.2). Holographic strange metals originate in the quantum critical state of a non-trivial IR fixed point and the GR metal is singled out as the one with the right scaling properties to reproduce both the local quantum criticality and Sommerfeld entropy of the cuprate strange metals. The non-trivial fixed point is of a special kind in that it still has an intrinsic correlation length $\xi \sim 1/\mu$ ([33] and Appendix 2.B). Hydrodynamics has long been utilized to describe transport in such densely entangled critical states, and holography is no different; though it is still an important open question whether transport in cuprate strange metals is hydrodynamical. In the Galilean continuum hydrodynamics is governed by (near) *momentum conservation* captured by the Navier-Stokes equations describing *convective* currents, also called “coherent” in the condensed matter- and holographic communities. However, there are also transport channels that are controlled by only *diffusive* (or “incoherent”) transport. The overall electrical (σ) thermo-electric (α) and thermal ($\bar{\kappa}$) transport coefficients are set by the sum of both

convective and diffusive transport channels. The open boundary thermal conductivity $\kappa = \bar{\kappa} - T\alpha^2/\sigma$ and the charge-without-heat transport $\sigma_{Q=0} = \sigma - T\alpha^2/\bar{\kappa}$ can be used to disentangle these. These zero out the dominant convective contribution. If Planckian dissipation occurs, the natural channel is this diffusive channel which can reflect universal microscopic dynamics. The convective channel is controlled by the way translational symmetry is broken and therefore unlikely to be universal. However, the convective channel dominates when translational symmetry is only broken weakly, and Planckian dissipation is therefore most natural in systems with strong translational symmetry breaking.

Convective hydrodynamics in the presence of a weak lattice potential

The presence of a lattice potential plays an important role in cuprate strange metals and this is the obvious way translational symmetry is broken. Placing the holographic strange metals in a background lattice with a perturbatively small potential strength the nature of the linear response of hydrodynamical transport is in fact familiar (Section 2.3). Hydrodynamic fluctuations must be decomposed in Bloch modes that Umklapp at Brillouin zone boundaries. This holds for purely diffusive as well as propagating modes. Well known is that the translational symmetry breaking by the lattice makes momentum relax due to shear drag with a lifetime $\Gamma_{\text{shear}} = \eta G^2/(\epsilon + P)$ (ϵ and P being the energy density and pressure and η the shear viscosity). However, a careful analysis reveals that the Umklapp potential gives rise to a mode coupling between this relaxational mode and the Umklapped charge diffusion mode characterized by a relaxation rate $\Gamma_{\text{charge}} = D_c G^2$, where D_c is the charge diffusivity. For weak lattices $A \ll 1$ the result of this generic mode coupling problem is an optical conductivity of the form (cf. Eq. (2.18) & Eq. (2.31)),

$$\sigma(\omega) \sim \frac{\Omega - i\omega}{(\Gamma - i\omega)(\Omega - i\omega) + \omega_0^2} \quad (2.2)$$

where ω_0 is related to the strength of the mode coupling and Γ and Ω are combinations of Γ_{shear} and Γ_{charge} . Taking the DC limit gives an overall current relaxation rate $\Gamma_{\text{DC}} = \Gamma + \omega_0^2/\Omega$ controlled by two separate dissipative channels.

The above hydrodynamic analysis is only valid for lattice sizes $a = G^{-1}$ greater than the earlier emphasized retained correlation length $\xi \simeq 1/\mu$ of the IR fixed point or equivalently $G \ll \mu$ (Section 2.4). This length $\xi \simeq 1/\mu$ where hydrodynamics provides the better perspective on transport than the quantum critical power law response set by the near horizon geometry as elucidated by Hartnoll and Hofman [87]. In a lattice background this reflects itself in a strong change in the transport properties when the lattice momentum G crosses this scale. The results in the above are all associated with the hydrodynamical regime ($G \ll \mu$); for large lattice momenta ($G \gtrsim \mu$) the additional Umklapp contribution to the dissipation of the currents is strongly suppressed (Fig. 2.11).

This Umklapp hydrodynamics can explain our observations at weak lattice potential (Section 2.5). When $|\Gamma - \Omega| > 2\omega_0$ the AC conductivity displays a single peak, explaining the low temperature Drude-like result of Fig. 2.3. Only for the lowest temperatures is this a pure Drude peak controlled by a single pole, however. In detail it originates in two diffusive poles, the Drude $k = 0$ sound pole and the Umklapped charge diffusion pole; for each we fully understand their temperature dynamics from the underlying hydrodynamic computation and the thermodynamical properties of the holographic strange metal.

At higher temperatures (and/or at stronger lattices) generically $|\Gamma - \Omega| < 2\omega_0$ and a *real*, propagating part develops in modes controlling the AC conductivity. This pole collision explains the emergence of the mid-IR-peak in the dynamical response – the numerical results are perfectly fitted by this form.

The same two-relaxational-current response was identified in the context of a hydrodynamical fluid coupled to the fluctuations of a damped pinned charge density wave [88]. There the peak emerges as the temperature is lowered as it can be identified as a pseudo-Goldstone mode of spontaneous translational symmetry breaking, that is absent at high temperatures.¹ Our discovery is that Umklapp hydrodynamics gives the right temperature evolution necessary to have a mid-IR-peak appear as temperatures increase. As emphasized in the introduction, this same development of a mid-IR peak in the optical conductivity as temperatures increase is observed in the strange metal phase of the high T_c cuprates.

As emphasized, the DC resistivity can remain linear throughout this transition. This can be explained by the fact that the scaling properties of the hydrodynamic parameters are inherited from the underlying non-trivial quantum critical IR fixed point. For the GR strange metal both relaxation rates scale as T , whereas for the RN metal one scales as T^0 and the other as T^2 . This manifestation of the differing detailed expressions for both relaxation rates shows that a simple interpretation of the scaling of the resistivity in terms of the entropy fails. Instead their scaling is determined at a deeper level by the quantum critical IR fixed point. It behooves us to point out at this stage that we are considering a rigid lattice only. We are at this stage not taking lattice vibrations or phonons into account. The underlying assumption is that in these intrinsically densely entangled system the strongly self-interacting degrees of freedom dominate all the physics and any phonon contribution is negligible. We comment on this further in the conclusion.

At intermediate lattice strengths a similar scenario can take place. Now the transport response is determined by four modes, the two modes above and two Umklapped sound modes at $\text{Re } \omega = \pm c_s G$. Upon raising temperature the pole responsible for the mid-IR peak moves up with temperature to approach close to the Umklapped sound

¹Because the lattice is ultimately irrelevant in the deep IR, at the lowest temperatures the pseudo-Goldstone boson mid-IR peak from spontaneous translational symmetry breaking will move again to $\omega = 0$ or equivalently disappear as the temperature is lowered; see e.g. [89].

pole, such that it gets obscured and only one peak remains in the AC conductivity (right inset of Fig. 2.3). From this temperature onward the low frequency AC spectrum becomes roughly temperature independent. We can track this in terms of the quasnormal modes (Fig. 2.9) although we can no longer rely on the perturbative expansion to enumerate it. For a large part of this intermediate lattice regime, the DC resistivity is still effectively captured by the expression $\sigma_{DC} = \omega_p^2 / (\Gamma + \omega_0^2 / \Omega)$, though one needs a careful AC-fit to extract the values. Again, its temperature scaling is set by the non-trivial IR fixed point and can remain unaffected by the change in dissipative dynamics in the AC conductivity.

The incoherent hydrodynamics at large lattice potential

At large lattice potentials momentum is strongly broken and we enter a qualitatively different regime (Section 2.6). Observationally this is where the numerically extracted relaxation rate of the DC conductivity of the GR metal saturates at about the Planckian value $\Gamma_{\text{corrected}} \simeq 2\pi T$ (Fig. 2.13). Because momentum is strongly broken, the framework to understand whether this can be verified is the one where transport is governed by only two conserved quantities, energy and charge [64]. Their fluctuations consist of two coupled diffusive modes with diffusion constants that are not the same as they are in the homogeneous system. At strict $T = 0$, charge and energy transport formally decouple and the electrical conductivity is governed by one of these modes $\sigma = \chi D_+$ with χ the charge susceptibility, while the thermal conductivity $\kappa = c_n D_-$ is governed by the other with c_n is the specific heat at constant charge density. At low but finite temperature they mix perturbatively, but are still dominated by their $T = 0$ scaling. From our numerics we conclude that $D_+ \sim T^{-1}$ whereas $D_- \sim T$ for the GR metal; similar behavior has been established in homogeneous holographic strange metals with strong momentum relaxation (GR metal in a Q-lattice) where the homogeneous geometry allows analytical solutions [90]. It has been argued that the temperature dependence of the thermal diffusivity empirically defined as $D_T \equiv \kappa / c_n$ should be insensitive to the breaking of translations and reduces to one of the incoherent diffusivities D_- at low temperature and strong lattices. Moreover, it can be related to microscopic chaos through a butterfly velocity v_B^2 times a maximal Lyapunov rate $\lambda = 2\pi T$ that embodies Planckian dissipation $D_T = \frac{1}{2} v_B^2 / (2\pi T)$ [72, 73, 74]. Provided we can extrapolate from the homogeneous result that in the non-trivial IR fixed point of the GR metal in a strong lattice the butterfly velocity still scales as $v_B^2 \sim T^2$, this is consistent with our findings. The puzzle is the DC-conductivity and charge response. We conjecture that the Planckian relaxation set by the maximal Lyapunov rate should still govern charge transport as well. Given that on dimensional grounds $D_+ \sim (v^{\text{charged}})^2 / (2\pi T)$, this can be only so if the velocity appearing in charge diffusion is not set by the universal butterfly velocity. In other words scrambling depends on the quantum numbers of the operators probing chaos; there are hints that this is true [91, 92, 93, 94]. If it can be shown that $v^{\text{charged}} \sim T^0$ this could explain not only the observed linear-in-T resistivity at strong lattice potentials in the GR metal, but also its saturation to the Planckian value.

We will end with a short discussion in Section 2.7 of these results with a focus on the possible relevance to experiment. We also include a number of Appendices where we discuss various technical details.

2.2 Holographic strange metals, transport and translational symmetry breaking.

In the absence of a lattice, the homogeneous finite density strange metals [77, 19, 1, 69] of holography are characterized by a non-trivial IR fixed point. These are specified by a handful of anomalous scaling dimensions: the dynamical critical exponent z , the hyperscaling violation dimension θ and the charge exponent ζ , expressing the scaling of time with space, the scaling of the thermodynamically relevant degrees of freedom with volume, and the running of the charge, respectively. Experimental evidences suggest that the cuprates are “local quantum critical” [95, 96, 97], referring to $z \rightarrow \infty$, while electronic specific heat measurements in the high temperature strange metal regime exhibit a Sommerfeld entropy, $s \simeq k_B T/\mu$ (see e.g. [98]) where μ is the chemical potential taking the role of the Fermi energy. Though the notion that cuprate strange metals are explained by a non-trivial IR fixed point was put forth independently of holography, the fixed point that shares the rough qualitative characteristics was first discovered using AdS/CFT. Amongst the holographic strange metals this is the so-called Gubser-Rocha strange metal [38], being the only holographic strange metal in the general classification that reconciles $z \rightarrow \infty$ with Sommerfeld entropy. Within the larger class of holographic strange metals, the critical scaling at the IR fixed point insists that the entropy should scale as $s \sim T^{(d-\theta)/z}$. For $z \rightarrow \infty$ and $d - \theta$ finite the entropy should therefore be temperature independent, implying a zero temperature entropy. This is the case for the holographic strange metal dual to the Reissner-Nordström black hole and the closely related SYK systems. The GR metal is characterized by a double scaling limit such that $z, -\theta \rightarrow \infty$ while $-\theta/z = 1$. This reconciles a low temperature Sommerfeld entropy $s \sim T + \dots$ with local quantum criticality. For comparison we will also present results for the Reissner-Nordström strange metal [19, 1, 99]. For a qualitative understanding of our results nothing more than the thermodynamics of the fixed point are required (summarized in Table I). The precise details RN and GR holographic strange metal and the duality map are discussed in Appendix 2.A.

The motivation for this study is that all experimental strange metals are known to occur in the presence of an excessively strong effective ionic background potential felt by the electron system, the Mottness of the cuprates being case in point (see e.g., [78, 79, 80]). The commonality of this lattice potential suggests an importance in observed systems of which the effects on the holographic strange metals have not yet been systematically investigated. We shall study the GR and the RN AdS black holes dual to 2+1 dimensional strange metals where we break translations by either a one dimensional or two-dimensional explicit periodic square ionic lattice potential encoded

	IR Scaling	RN ($\theta = d, z = \infty$)	GR ($-\theta, z = \infty$)
Entropy	$s/\mu^2 \sim (T/\mu)^{(d-\theta)/z}$	$s/\mu^2 \sim (T/\mu)^0$	$s/\mu^2 \sim (T/\mu)^1$
Charge Density	*	$n/\mu^2 \sim (T/\mu)^0$	$n/\mu^2 \sim (T/\mu)^0$

Table 2.1: IR scaling behavior in holographic strange metals of the entropy density s and the charge density n in terms of the chemical potential μ and the temperature T . The first column highlights the general formula of holographic scaling geometries. The last two columns focus on the two holographic models with local quantum criticality ($z \rightarrow \infty$) of interest in this paper: the Reissner-Nordström and the Gubser-Rocha model. (*): For a discussion on this, see section 4.2.4 of [1].

in the local chemical potential

$$\begin{aligned}\mu_{1D}(x, y) &= \bar{\mu} \left(1 + A \cos(Gx) \right), \\ \mu_{2D}(x, y) &= \bar{\mu} \left(1 + \frac{A}{2} (\cos(Gx) + \cos(Gy)) \right).\end{aligned}\tag{2.3}$$

The parametrization is such that the maximal deviation from the average is $\pm A$ in both cases.

The above explicit lattice condition appears as boundary conditions in the dual holographic gravitational description of the strange metal system in question. The difficulty is that studying such explicit translational symmetry breaking is only possible numerically outside perturbation theory. We solve the full set of spatially dependent Einstein-Maxwell-Dilaton equations of motion for the GR and RN strange metals using the DeTurck gauge in a Newton-Raphson scheme [100, 101, 102]. A summary is given in Appendix 2.A.3. DC transport is computed by numerically solving for the Stokes flow problem at the horizon [103, 104, 105, 106]. All numerical computations employ a higher-order finite difference scheme where the radial coordinate is discretized on the Chebyshev-Lobatto nodes (Appendix 2.A.3).

We treat the numerical data obtained as the outcome of an experiment. However, the framework in which to analyze this data is known. As we already emphasized, the dense entanglement of the quantum many body system described holographically by its dual gravity theory drives a very rapid quantum thermalization. This implies that local equilibrium sets in very rapidly, which in turn implies that, in the homogeneous background with no lattice, transport at macroscopic times and lengths is governed by hydrodynamics. Different from the quasiparticles in Fermi-liquid metals, a strange metal flows like water. It is a general hydrodynamical principle that it can be decomposed in convective- (also called “coherent”) and diffusive (“incoherent”) flows. The former refers to the motion of the fluid as a whole as protected by the conservation of total momentum in the translationally invariant homogeneous background. When the

translational symmetry is weakly broken — introduced by hand through a momentum decay rate $\Gamma_{\text{mom.rel.}} = \tau_{\text{mom.rel.}}^{-1}$ as the largest relaxation time — a straightforward hydrodynamic analysis yields²

$$\sigma(\omega) = \frac{n^2}{\chi_{\pi\pi}} \frac{1}{\Gamma_{\text{mom.rel.}}} + \sigma_{\text{inc}} , \quad (2.4a)$$

$$\alpha(\omega) = \frac{ns}{\chi_{\pi\pi}} \frac{1}{\Gamma_{\text{mom.rel.}}} + \alpha_{\text{inc}} , \quad (2.4b)$$

$$\bar{\kappa}(\omega) = \frac{s^2 T}{\chi_{\pi\pi}} \frac{1}{\Gamma_{\text{mom.rel.}}} + \bar{\kappa}_{\text{inc}} . \quad (2.4c)$$

Here n, s of the convective terms are the charge and entropy density respectively, and $\chi_{\pi\pi}$ is the momentum susceptibility. For non-relativistic hydrodynamics $\chi_{\pi\pi} = nm$ with m the constituent quasiparticle mass and one recognizes the Drude model. For relativistic hydrodynamics appropriate to strange metals where a linear dispersion relation of charged constituents induces an emergent Lorentz symmetry, and for holographic strange metals studied here the momentum susceptibility equals $\chi_{\pi\pi} = \epsilon + P$, the sum of the energy and pressure density respectively. The Lorentz symmetry also demands that the incoherent contributions are related to each other by $\sigma_{\text{inc}} = \sigma_Q$, $\alpha_{\text{inc}} = -\frac{\mu}{T}\sigma_Q$ and $\bar{\kappa}_{\text{inc}} = \frac{\mu^2}{T}\sigma_Q$ in terms of a transport coefficient σ_Q .³

Writing $\sigma_{\text{inc}} = \frac{T}{\mu^2}\bar{\kappa}_{\text{inc}}$, $\alpha_{\text{inc}} = -\frac{1}{\mu}\bar{\kappa}_{\text{inc}}$ instead, this reveals that in a Galilean invariant system where both $c \rightarrow \infty$ and $\mu = m_e c^2 + \dots \rightarrow \infty$, only the incoherent heat contribution survives. It is a highlight of non-relativistic finite temperature Fermi-liquid theory that such a diffusive heat conduction is present even dealing with spin-less fermions, mediated by the Lindhard continuum. This $\bar{\kappa}_{\text{inc}} = c_n D_T$, where the specific heat at constant density (equal to the specific heat at constant volume) $c_n \sim T$, while the thermal diffusivity $D_T \simeq v_F^2 \tau_{\text{col}}$ where $\tau_{\text{col}} \simeq \frac{E_F}{k_B T} \tau_{\hbar}$; therefore $\bar{\kappa}_{\text{inc}} \sim 1/T$ as verified *e.g.*, in the ³He Fermi liquid. In contrast in the non-relativistic limit $\epsilon + P \rightarrow \mu n \sim n m c^2$ the electrical conductivity becomes purely convective and one recognizes the familiar Drude weight expressed in the plasma frequency as $\omega_p^2 = n e^2 / m$.

The incoherent contributions to transport are in principle measurable in the laboratory by zeroing out the coherent part. This can be done by measuring heat transport in the absence of charge transport (open circuit thermal conductivity) κ or charge transport without heat, $\sigma_{Q=0}$ equal to

$$\kappa = \bar{\kappa} - \frac{T\alpha^2}{\sigma} , \quad \sigma_{Q=0} = \sigma - \frac{T\alpha^2}{\bar{\kappa}} . \quad (2.5)$$

²see *e.g.* the review [107].

³There is one exception. If the translational symmetry breaking happens in only one of the spatial dimensions α_{inc} and κ_{inc} vanish [108]. In that particular case a subleading term in the numerator of the convective term precisely cancels the incoherent term in the thermo-electric and heat conductivity.

Note that in the Galilean limit when there is only an incoherent heat conductivity $\kappa = \bar{\kappa}_{\text{inc}}$; note therefore that in ordinary metals the thermal conductivity consists completely of the incoherent contribution in this language (see [109]).

These incoherent contributions are diffusive. The open boundary combinations Eq. (2.5) are therefore a mixture of diffusive and convective transport. Nevertheless, it is useful and conventional to define the charge and thermal diffusivities $D_c \equiv \sigma/\chi$ and $D_T \equiv \kappa/c_n$, where χ is the charge susceptibility, and c_n the heat capacity. In the remainder of this text, we will see that when translational symmetry is strongly broken and the convective part is strongly suppressed, these diffusivities are directly related to diffusion constants in transport. These “incoherent metal” diffusivities and diffusion constants should not be confused with the well-known diffusion of charge D_ρ and energy D_π in weak or vanishing translational symmetry breaking. As we shall see in the Gubser-Rocha metal the latter are both linear-in- T at low temperature while they are T -independent at low temperature in Reissner-Nordström. In the incoherent metal, in contrast, we will see that $D_T \sim T$ while $D_c \sim T^{-1}$.

Will the real Planckian dissipating channel make itself known?

The point of this brief hydrodynamical exposition is to highlight the fundamental issue we address in this article. The above illustrates that even in the simplest Drude hydrodynamics there are two dissipative channels: the convective coherent Drude term encoding the way translational symmetry is broken, and the incoherent term related to a diffusion of microscopic origin. For weak lattice potentials, or more generally for weak translational symmetry breaking, the convective Drude term is much larger than the incoherent term. With the conjecture that in strongly correlated critical points the shear viscosity is bounded by the entropy $\eta \geq s/4\pi$, two of us, together with R. Davison, proposed that in disordered strange metals the usual shear viscosity based momentum relaxation rate $\Gamma_{\text{mom.rel.}} \sim \eta \sim s$ can explain a linear-in- T resistivity for a system with Sommerfeld entropy [86]. The connection between the resistivity and the entropy would explain the universality and the minimal viscosity would be the encoding of Planckian dissipation. Moreover, this argument is also consistent with a Drude response in the optical conductivity. The counterargument is that this only holds in detail for marginal disorder. Relevant or irrelevant disorder would significantly limit the regime of applicability of this argument [110, 111].

Taking a step back, it actually is difficult to argue that a universal phenomenon such as Planckian dissipation should manifest itself through the convective channel, as this coherent channel will generically depend on the details of translational symmetry breaking [72, 112]. The far more natural channel for Planckian dissipation would be the incoherent diffusive channel. But if one takes this point of view, one can no longer use it to explain the universal linear-in- T DC resistivity in strange metals. These all show strong Drude behavior in the optical conductivity, and the DC conductivity is therefore set by the coherent response in the context of weak translational symmetry breaking.

It appears to be a Catch-22.⁴ Either a Planckian dissipation can set the universally observed linear-in-T resistivity in strange metals, but then the AC conductivity ought to be Drude, or weak translational symmetry breaking sets the resistivity, but then it is hard to see how it can be universal.

We will resolve this conundrum by showing explicitly that in weak lattice near a non-trivial IR fixed point, the thermodynamics of the fixed point together with a fixed-point-controlled scaling of transport coefficients can set the DC resistivity in a universal sense, independent of the dissipative channel shown in the AC conductivity. Qualitatively this is an extension of the Davison-Schalm-Zaanen $\Gamma_{\text{mom.rel.}} \sim \eta \sim s$ result. At the same time, for large lattice strengths the incoherent part becomes dominant and indeed shows universal Planckian dissipation as surmised by Blake and others [72, 73, 74]. For good measure we state that there may still be a deeper way to also understand the weak lattice results in terms of Planckian dissipation. Even though they appear non-universal, the observed scaling, together with the way the Sommerfeld entropy is a natural bounding behavior at low temperatures, leaves this possibility open.

2.3 Umklapp hydrodynamics for weak lattice potentials.

As we emphasized, in the low frequency limit at macroscopic long wavelengths holography reduces to hydrodynamics albeit with specific transport coefficients [113]. A fundamental principle behind the theory of hydrodynamics is local equilibrium. The state of the fluid can be described by a slowly spatially varying energy-momentum tensor $T_{\mu\nu}(x)$ and in the presence of a $U(1)$ charge, a current $J^\mu(x)$. In turn the local equilibrium condition implies that one can also describe fluid behavior in the presence of a slowly spatially varying external potential whether temperature $T(x)$, pressure $P(x)$, or chemical potential $\mu(x)$ [114, 115, 116]. Suppose this background is periodic in the coordinate x . The hydrodynamical problem of relevance is nothing else than that of a hydrodynamical fluid like water that is flowing through a periodic “array” of obstacles weakly perturbing the flow, characterized by a microscopic “lattice constant”. This is a rather unusual circumstance in standard hydrodynamics and we are not aware of any literature addressing the role of Umklapp in the AC structure of the correlators, though a beginning was made in [117].

But it represents an elementary exercise, and the answer is readily understood. From elementary solid state physics it is well known that a quantum mechanical wave function in a periodic background experiences Umklapp. This is purely a wave phenomenon and the principle therefore also applies to classical waves as described by hydrodynamics. Both a quantum mechanical wave function and linearized hydrodynamic fluctuations around equilibrium are described by a differential equation of the

⁴A Catch-22 is a paradoxical situation which cannot be escaped by design. It originates from the eponymous novel written by Joseph Heller and published in 1961.

form

$$(\partial_t + M(x))\phi(x) = 0. \quad (2.6)$$

If $M(x)$ is periodic $M(x + \frac{2\pi n}{G}) = M(x)$, then $\phi(x)$ can be decomposed in Bloch waves $\phi(x) = \frac{1}{2\pi G} \int_{-G/2}^{G/2} dk \sum_n \phi_n(k) e^{i(k+nG)x}$. Taking $M(x) = -M_0 \partial_x^2 + A \cos(Gx)$ as canonical example, one can solve Eq. (2.6) perturbatively in A . Defining $\phi_n(k) = \phi_n^{(0)}(k) + A \phi_n^{(1)}(k) + \frac{A^2}{2} \phi_n^{(2)}(k) + \dots$, the solution to first order A is

$$\phi_n(k) = \phi_n^{(0)}(k) + \frac{A}{2G(G-2k)M_0} \phi_{n-1}^{(0)}(k) - \frac{A}{2G(G+2k)M_0} \phi_{n+1}^{(0)}(k) + \dots \quad (2.7)$$

This mixing between the different Bloch waves is Umklapp. In hydrodynamics these Umklapped responses have already been observed several years ago in numerical computations of holographic metals in explicit periodic lattices in [82, 118, 84]. Fig.4 in the article [84] shows an Umklapped sound mode at $\omega = v_s G$ in the optical conductivity with G the lattice momentum. However, a full treatment has been lacking.

For $U(1)$ charged relativistic hydrodynamics the fluctuation equations in the longitudinal sector in a spatially constant background are the coupled equations [119]

$$\begin{pmatrix} -i\omega & ik & 0 \\ ik\beta_1 & D_\pi k^2 - i\omega & ik\beta_2 \\ -D_{n_1} k^2 & ik\beta_3 & D_{n_2} k^2 - i\omega \end{pmatrix} \begin{pmatrix} \delta\epsilon \\ \delta\pi_x \\ \delta n \end{pmatrix} = 0. \quad (2.8)$$

Here $\delta\epsilon, \delta n, \delta\pi_x$ are the fluctuations in energy-, charge-, and longitudinal momentum density respectively. The upper two-by-two block is the sound sector with $\beta_1 = \left(\frac{\partial \bar{p}}{\partial \bar{\epsilon}}\right)_n$. At finite density this interacts with a charge diffusion mode in the bottom one-by-one block through the interactions $\beta_2 = \left(\frac{\partial \bar{p}}{\partial \bar{n}}\right)_\epsilon$, $\beta_3 = \frac{\bar{n}}{\bar{\epsilon} + \bar{p}}$ and the diffusion constant D_{n_1} . The diffusion constants equal

$$\begin{aligned} D_\pi &= \left(2 \left(1 - \frac{1}{d}\right) \eta + \zeta\right) \left(\frac{\partial v_x}{\partial \pi_x}\right)_\epsilon = \frac{2 \left(1 - \frac{1}{d}\right) \eta + \zeta}{\bar{\epsilon} + \bar{p}}, \\ D_{n_1} &= \sigma_Q \bar{T} \left(\frac{\partial(\bar{\mu}/\bar{T})}{\partial \bar{\epsilon}}\right)_{\bar{n}} = -\sigma_Q \frac{\left(\frac{\partial \bar{n}}{\partial \bar{T}}\right)_{\bar{\mu}} + \frac{\bar{\mu}}{\bar{T}} \left(\frac{\partial \bar{n}}{\partial \bar{\mu}}\right)_{\bar{T}}}{\left(\frac{\partial \bar{n}}{\partial \bar{\mu}}\right)_{\bar{T}} \left(\frac{\partial \bar{\epsilon}}{\partial \bar{T}}\right)_{\bar{\mu}} - \left(\frac{\partial \bar{n}}{\partial \bar{T}}\right)_{\bar{\mu}} \left(\frac{\partial \bar{\epsilon}}{\partial \bar{\mu}}\right)_{\bar{T}}}, \\ D_{n_2} &= \sigma_Q \bar{T} \left(\frac{\partial(\bar{\mu}/\bar{T})}{\partial \bar{n}}\right)_{\bar{\epsilon}} = \sigma_Q \frac{\left(\frac{\partial \bar{\epsilon}}{\partial \bar{T}}\right)_{\bar{\mu}} + \frac{\bar{\mu}}{\bar{T}} \left(\frac{\partial \bar{\epsilon}}{\partial \bar{\mu}}\right)_{\bar{T}}}{\left(\frac{\partial \bar{n}}{\partial \bar{\mu}}\right)_{\bar{T}} \left(\frac{\partial \bar{\epsilon}}{\partial \bar{T}}\right)_{\bar{\mu}} - \left(\frac{\partial \bar{n}}{\partial \bar{T}}\right)_{\bar{\mu}} \left(\frac{\partial \bar{\epsilon}}{\partial \bar{\mu}}\right)_{\bar{T}}}. \end{aligned} \quad (2.9)$$

In the last two equations, the last equality leads to a seemingly more complicated form, but each of these derivatives is much simpler to compute. Barred quantities

denote the (spatially constant) equilibrium background, and η, ζ, σ_Q are the microscopic transport coefficients: the shear- and bulk-viscosity and the momentum-independent contribution to the conductivity. As discussed, the holographic models we consider have $d = 2$ with an underlying conformal symmetry for which the equation of state $\bar{\epsilon} = 2\bar{p}$ implies that $\zeta = 0$, $\beta_2 = 0$ and $\beta_1 = c_s^2 = 1/2$; we will limit our focus to conformal hydrodynamics in the remainder.

Placing such a system in a spatially varying chemical potential $\mu(x) = \bar{\mu} \left(1 + A \cos(Gx) \right)$ the Umklapp interactions follow from a re-derivation of the fluctuation equations in this background. A detailed derivation for both conformal and non-conformal hydrodynamics and discussion with a natural generalization to a two-dimensional lattice $\mu(x) = \bar{\mu} \left(1 + \frac{A}{2} \cos(Gx) + \frac{A}{2} \cos(Gy) \right)$ is given in a companion article [120]. In summary, to maintain equilibrium with spatially constant temperature also requires a spatially varying charge density $n(x) = \bar{n} + \bar{\mu} A \left(\frac{\partial \bar{n}}{\partial \bar{\mu}} \right)_T \cos(Gx) + \dots$ and pressure $p(x) = \bar{p} + A \bar{\mu} \bar{n} \cos(Gx) + \dots$ to leading order in A . The exact equation of state $\bar{\epsilon} = 2\bar{p}$ in a conformal fluid means the energy density follows the pressure. By viewing the lattice as a small perturbation on the thermal equilibrium, we can express the perturbations in terms of the chemical potential modulation and the thermodynamic susceptibilities of the background. These corrections to the background are responsible for the Bloch decomposition and Umklapp interactions mixing them. To first order in the lattice strength A the three modes of the longitudinal sector⁵ mix with their six Umklapp copies. Our interest in this article is how this Umklapp affects the response at low frequencies $\omega \ll G$ and zero momentum $k = 0$. At $k = 0$ the un-Umklapped charge diffusion mode decouples, and the remaining eight modes decompose into four parity-odd-in- G ones and four parity-even modes. The latter include the $k = 0$ sound mode $\delta\pi^{(0)}$, two Umklapped sound modes built on $\delta\epsilon^{(S)} = \int dx \sin(Gx) \delta\epsilon(x)$, $\delta\pi^{(C)} = \int dx \cos(Gx) \delta\pi(x)$; and one Umklapped charge diffusion mode built on $\delta n^{(S)} = \int dx \sin(Gx) \delta n(x)$ that interact as

$$(\partial_t + M) \cdot \delta\phi = R \quad (2.10)$$

with

$$M = \begin{pmatrix} 0 & \frac{1}{2}AG\bar{\mu} & \frac{1}{2}AG\bar{\mu} & -\frac{3}{2}i\omega A\bar{\mu}\beta_3 \\ -\frac{AG\bar{\mu}}{(\bar{\epsilon}+\bar{p})\alpha_n} & D_\rho G^2 & 0 & 0 \\ -2AG\bar{\mu}\beta_3^2 & 0 & 0 & -G\beta_3 \\ -3i\omega A\bar{\mu}\beta_3 & 0 & \frac{G}{2\beta_3} & D_\pi G^2 \end{pmatrix} \quad (2.11)$$

⁵Substituting this spatially varying background into the defining conservation equations of hydrodynamics and expanding in fluctuations, they no longer decompose in a longitudinal and transverse sector. It can be shown, however, that in the presence of an orthogonal lattice the naively longitudinal sector along one of the lattice directions is self-contained.

and

$$\delta\phi = \begin{pmatrix} \delta\pi_x^{(0)} \\ \delta n^{(S)} - \beta_3 \delta\epsilon^{(S)} \\ \beta_3 \delta\epsilon^{(S)} \\ \delta\pi_x^{(C)} \end{pmatrix}, \quad R = \begin{pmatrix} \bar{n} \\ \bar{\mu} A \beta_3 \frac{D_\rho G}{\alpha_n} \\ -\bar{\mu} A \beta_3 \frac{D_\rho G}{\alpha_n} \\ \bar{\mu} A \left(\alpha_n^{-1} + \frac{\bar{n}^2}{(\bar{\epsilon} + \bar{p}) c_s^2} \right) \end{pmatrix} \delta \bar{E}_x \quad (2.12)$$

where we have defined $D_\rho = D_{n_2}$ the charge diffusion constant and where we used the coefficient $\alpha_n \equiv \bar{T} \left(\frac{\partial(\bar{\mu}/T)}{\partial \bar{n}} \right)_{\bar{\epsilon}}$ which entered the definition of D_{n_2} . It is purely thermodynamic and has a universal scaling behavior determined by the scaling of entropy, as we will later highlight. We have added to our system a perturbatively small time-varying electric field $\delta E_x(t) = -\delta \bar{E}_x e^{-i\omega t}$ which will externally source a longitudinal current δJ^x . This term will also enter the hydrodynamic system as an extra term in the current constitutive relation through $\partial_x \mu \rightarrow \partial_x \mu + \delta E_x(t)$.

We can now therefore linearize the constitutive relation $\delta J^x = n \delta v^x - \sigma_Q \left[\partial^x (\delta \mu - \frac{\mu}{T} \delta T) + \delta E_x \right]$ for the current density defined as

$$\delta J^x(t) = \left(\frac{\partial J^x}{\partial \phi} \right)^\top \cdot \delta \phi(t) + \sigma_Q \delta \bar{E}_x e^{-i\omega t} \quad (2.13)$$

with $\left(\frac{\partial J^x}{\partial \phi} \right)^\top = \left(\beta_3, \quad -\bar{\mu} A \frac{D_\rho G}{2} \beta_3, \quad \bar{\mu} A \frac{D_\rho G}{4 \bar{n} \alpha_n}, \quad \bar{\mu} A \left(\beta_3 + \frac{1}{2 \bar{n} \alpha_n} \right) \right)$.

We make use of the dynamical system (2.10), to obtain the time-evolution of the dynamical fields $\delta \phi(\omega) = (-i\omega I_4 + M(\omega))^{-1} \cdot \left(\delta \phi(t=0) + R \delta \bar{E}_x \right)$. Since we have turned on the external electric field, we are not interested in explicitly sourcing any of the hydrodynamical variables and therefore we set $\delta \phi(t=0)$ as an initial condition such that $\delta \phi(\omega) \propto \delta \bar{E}_x$ and by extension so will be δJ^x . Finally, the optical conductivity can be computed as [120]

$$\sigma(\omega) = \frac{\delta J^x}{\delta \bar{E}_x}. \quad (2.14)$$

The inverse $(-i\omega I_4 + M)^{-1}$ is dominated by the vanishing of its determinant. These zeroes show up as poles in the conductivity. Expanding the determinant⁶ to order A^2 ,

⁶Strictly speaking, there are terms at order $\mathcal{O}(A^2)$ in the lower-right 3×3 sub-block of M that are ignored in Eq. (2.11) but will contribute to the eigenvalues at that order. However, as we show in detail in [120], these contributions to the poles (2.15) are also higher order in G . They contribute at order $\mathcal{O}(A^2 G^2)$. Crucially, moreover, these corrections will not affect ω_1 but only correct the diffusion constants and sound velocities of ω_2 and ω_\pm . They will not qualitatively change the pole structure (2.15) therefore, nor the decomposition (2.19). Since $A^2 G^2$ will typically be very small compared to the finite position of these poles, we ignore these corrections here. Figure 2.7 illustrates that this assumption is justified in the numerical range we consider.

there are four poles at

$$\begin{aligned}
 \omega_1 &= -i(\Gamma_\eta + \Gamma_d) + \mathcal{O}(A^4), \\
 \omega_2 &= -i(D_\rho G^2 - \Gamma_d) + \mathcal{O}(A^4), \\
 \omega_\pm &= \pm \frac{G}{\sqrt{2}} \left[1 - \bar{\mu}^2 A^2 \beta_3^2 + \mathcal{O}(A^4) \right] - i \frac{1}{2} \left[D_\pi G^2 - \Gamma_\eta + \mathcal{O}(A^4) \right] + \mathcal{O}(G^3)
 \end{aligned} \tag{2.15}$$

with

$$\begin{aligned}
 \Gamma_d &\equiv A^2 \frac{\bar{\mu}^2}{2(\bar{\epsilon} + \bar{p}) D_\rho \alpha_n}, \\
 \Gamma_\eta &\equiv 2\bar{\mu}^2 A^2 \beta_3^2 D_\pi G^2 = 2A^2 \frac{\bar{\mu}^2 \bar{n}^2}{(\bar{\epsilon} + \bar{p})^2} D_\pi G^2.
 \end{aligned} \tag{2.16}$$

At low frequency $\omega \ll c_s G$, the contribution from the two sound poles ω_\pm should be negligible in the conductivity. By expanding the expression (2.14) as a quadruple Laurent series

$$\sigma(\omega) = \sigma_0 + \sum_{i=1,2,\pm} \frac{Z_i}{\omega - \omega_i} \tag{2.17}$$

and truncating the two sound modes, one finds that it takes the form⁷

$$\sigma_{\text{no sound}}(\omega) = \sigma_0 + \frac{Z_1}{\omega - \omega_1} + \frac{Z_2}{\omega - \omega_2} = \sigma_0 + Z_{\text{eff}} \frac{\Omega - i\omega}{(\Gamma - i\omega)(\Omega - i\omega) + \omega_0^2} \tag{2.18}$$

with

$$\begin{aligned}
 \Omega &= \overbrace{D_\rho G^2}^{\mathcal{O}(1)} - \overbrace{2D_\rho^2 G^2 \Gamma_d + \mathcal{O}(G^3)}^{\mathcal{O}(A^2)} + \mathcal{O}(A^4), \\
 \Gamma &= 2D_\rho^2 G^2 \Gamma_d + \Gamma_\eta + \mathcal{O}(G^3) + \mathcal{O}(A^4), \\
 \omega_0^2 &= D_\rho G^2 \Gamma_d \left[1 - 2D_\rho^2 G^2 + \mathcal{O}(G^3) \right] + \mathcal{O}(A^4), \\
 Z_{\text{eff}}/\omega_p^2 &= 1 + 4\bar{\mu}^2 A^2 \beta_3^2 D_\pi^2 G^2 - D_\rho \Gamma_d \left[4 + D_\rho (D_\rho - 4D_\pi) G^2 \right] + \mathcal{O}(G^3) + \mathcal{O}(A^4), \\
 \sigma_0 &= \sigma_Q + \mathcal{O}(A^4),
 \end{aligned} \tag{2.19}$$

where the plasmon frequency is $\omega_p^2 = \frac{\bar{n}^2}{\bar{\epsilon} + \bar{p}}$.

The form Eq. (2.18) is well known from studying the hydrodynamics of decaying charge density waves or other pseudo-spontaneously broken $U(1)$ superfluids [67, 121,

⁷An attempt to formally decouple the sound modes by taking the limit $c_s^2 \rightarrow \infty$ requires that $\Gamma_\eta \sim \frac{1}{c_s^2}$ and will therefore shift the poles. The truncated Laurent expansion keeps the poles in the right location.

122, 89, 123, 124, 125]. This is not surprising as the underlying physics is that of two damped currents cross-coupled with an interaction ω_0 (see Appendix 2.F). Both a decaying (*i.e.*, damped) pseudo-Goldstone boson, as well as an Umklapp hydrodynamics interaction belong to this class.

Given an appropriate temperature scaling of Γ, Ω, ω_0 or equivalently $Z_{1,2}, \omega_{1,2}$ it was already proposed that such a conductivity could explain the emerging mid-IR peak at high temperature in the cuprates. We will argue below that this Umklapp hydrodynamics in a holographic AdS₂ metal with Sommerfeld specific heat provides precisely the right scaling.

2.4 The applicability of hydrodynamics and the imprint of local quantum criticality

Despite the fact that the interplay between holography and hydrodynamics has been formidable, it is not a given that a hydrodynamical understanding as given above applies directly to holographic strange AdS₂ metals in explicit lattices. Even though holography describes strongly coupled systems which implies a large hydrodynamical regime, this regime is finite as has been emphasized in several recent articles [126, 127, 128, 129, 130], and bounded by $\omega = 2\pi\Delta T$ where Δ is the scaling dimension of the lowest irrelevant operator from the strange metal fixed point. This argument against hydrodynamics can be sharpened by the fact that momentum dependent longitudinal DC-conductivities at zero frequency $\sigma(\omega = 0, k \neq 0)$ vanish [131].⁸ This is an unavoidable consequence of $U(1)$ current conservation: $\omega \rightarrow 0$ implies $G \cdot J = 0$. Naively considering Umklapp as the mixing of the $\sigma(\omega, 0)$ and $\sigma(\omega, k = G)$, would argue that the amplitude of the mixed-in Umklapp wave is thus very small. This is illustrated by a memory matrix computation [87, 131]. The momentum-dependent density correlation function G_{J^t, J^t} in a homogeneous AdS₂ metal, which is the operator to consider for our choice of lattice, scales as a function of the temperature as

$$\text{Im} G_{J^t, J^t}^{\text{homogeneous}}(\omega = 0, k) \sim T^{2\nu_k} + \dots, \quad (2.20)$$

$$\nu_k = \frac{1 + \hat{\eta}}{2\sqrt{2 + \hat{\eta}}} \sqrt{10 + \hat{\eta} + 4(2 + \hat{\eta})\bar{k}^2 - 8\sqrt{1 + (2 + \hat{\eta})\bar{k}^2}}$$

where $\hat{\eta} \equiv -\theta/z$ characterizes the near-AdS₂ region and \bar{k} is a wavevector renormalization that correctly rescales to the emergent near horizon AdS₂ geometry in a lattice [131, 84]. For GR $\hat{\eta} = 1$ and for RN, $\hat{\eta} = 0$ while in both cases, $\bar{k} = \frac{k}{\mu}$. This scaling of

⁸Recall that momentum-dependent conductivities at finite momentum need not be in the hydrodynamic regime. Within hydrodynamics, longitudinal diffusive conductivities obeying $\sigma(\omega, k) = \frac{i\omega D\chi}{i\omega - Dk^2}$ give an exactly vanishing DC conductivity at finite momentum, but a finite DC conductivity at zero momentum obeying Einstein's relation $\sigma = D\chi$.

$G_{J^t J^t}$ follows from a near-far matching method in the AdS₂ bulk which shows that a generic Green's function takes the form

$$G = \frac{A + B\mathcal{G}}{C + D\mathcal{G}} \quad (2.21)$$

with A, B, C, D purely real and \mathcal{G} the AdS₂ Green's function [32]

$$\mathcal{G}(\omega, k) \propto T^{2\nu_k} \frac{\Gamma(1 - \nu_k) \Gamma\left(\frac{1}{2} + \nu_k - \frac{i\omega}{2\pi T}\right)}{\Gamma(1 + \nu_k) \Gamma\left(\frac{1}{2} - \nu_k - \frac{i\omega}{2\pi T}\right)}. \quad (2.22)$$

The imaginary part of the density correlator is proportional to the imaginary part of the AdS₂ correlator as $\text{Im} G_{J^t J^t} \sim \text{Im} \mathcal{G}$. Though this scaling as a function of the temperature is exact, it ignores the possibility that there can still be a large amplitude as a function of the other parameters. This is in fact what happens when one extrapolates the exact answer for the momentum-dependent transverse conductivity $\sigma_{\perp}(\omega, k)$ to the hydrodynamic regime $k \ll \mu$ [132]. The momentum dependent current-current correlation function in an AdS₂ metal behaves as

$$G_{J_{\perp} J_{\perp}}(\omega, k) = -\frac{k^2 \mathcal{G}(\omega)}{\omega^2 + \frac{k^2}{2r_0} \mathcal{G}(\omega)}. \quad (2.23)$$

Although the scaling is indeed captured by the Hartnoll-Hofman result Eq. (2.20) one also sees that for small k the hydrodynamic pole at $\omega = -iDk^2$ becomes far more important than the $(\omega/T)^{2\nu}$ -suppression. For $k \leq \mu$ the hydrodynamic pole captures the physics far better than the AdS₂ power-law.

As is clear from the mathematical expressions this is not a sharp transition, but a smooth crossover. Nevertheless there is a clear transition between dominant physics regimes (AdS₂ vs hydrodynamics) that can be made visible through the holographic dynamics. A finite momentum conductivity is better viewed as the response when the system is placed in a fixed spatially oscillating but static electric field background. The spatial oscillation imprints a lattice structure in the finite density system. The conventional RG perspective is that this lattice is irrelevant in the RG. This is the physics behind the power-law dependence on temperature in Eq. (2.20). The AdS₂ fixed points of the holographic metals that we study, either RN or GR, are so-called semi-local quantum liquids [33], however. This means that while for $T < \mu$ the two-point correlation function displays power-law behavior between two time-like separated points, it is exponentially suppressed between two space-like separated points. This exponential suppression is so strong that two points separated spatially by a distance $|x| \gtrsim \frac{1}{\mu}$ have no causal contact [33]. In momentum space this implies that the coupling between modes with $k \lesssim \mu$ is exponentially small. This decoupling means that for modes $k \lesssim \mu$ or equivalently a spatially oscillating but static electric field with $G \leq \mu$ the RG-flow becomes strongly suppressed once T decreases below μ . One can think of it as that the d -dimensional RG-flow at $T = \mu$ decomposes into individual RG-flows for each

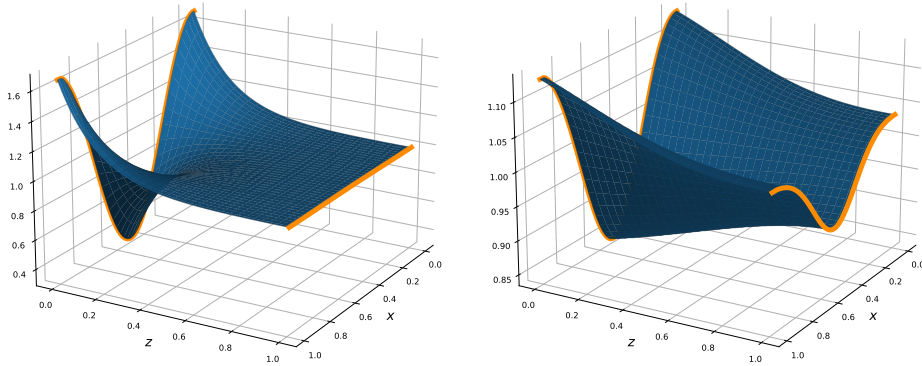


Figure 2.4: A holographic visualization of the cross-over in response functions between $G > \mu$ (left) and $G < \mu$ (right). Plotted is the bulk electric field F_{tz} (whose boundary value is dual to the charge density) in the presence of a 1D spatially varying chemical potential $\mu(x) = \bar{\mu} + A \cos(Gx)$ as a function of position and the AdS radial direction z . For $G > \mu$ ($G = 4\mu$) one sees the lattice amplitude decrease smoothly as one moves from the AdS boundary to the horizon at $z = 1$. For $G < \mu$ ($G = 0.05\mu$) on the other hand, one sees that the RG flow is much slower and “halts” around $z \sim 0.5$. This is due to the exponential suppression of the coupling between different momentum modes at the AdS₂ IR fixed point. The results are for a RN black hole at $T/\mu = 0.15$.

momentum mode. Recalling that in holography the radial direction encodes the RG-flow, we can visualize this. In Fig. 2.4 we plot the charge/current density as a function of location for a modulated chemical potential. For a lattice momentum $G \gg \mu$ the lattice irrelevancy towards the IR is uninterrupted. However for an oscillating chemical potential with periodicity $G \ll \mu$, the RG flow “halts” around the AdS radius value $r \sim \mu$ corresponding to $T \sim \mu$. For such values of $G \ll \mu$ the lattice thus remains quite strong in the IR and certainly much stronger than one would naively expect. The way to understand this is that precisely in this regime it is the proximity of the hydrodynamic pole that dominates the response rather than the RG scaling suppression. Ultimately the RG wisdom does hold for any lattice perturbation and even for $G \ll \mu$ the lattice will eventually turn irrelevant in the IR (Sec 3.4 in [84]), and scaling again becomes the pre-eminent physical effect but this only happens at the lowest of temperatures.

For Umklapp hydrodynamics this is relevant because it implies that the regime where the hydrodynamics results capture the physics is appreciable. Below we shall verify that near an AdS₂ fixed point Umklapp hydrodynamics is the better way of understanding the physics for $G < \mu$, whereas AdS₂ Hartnoll-Hofman scaling is the better way for $G > \mu$. For the sake of clarity, we emphasize that strictly speaking at a mathematical level both can be, and often are, valid simultaneously as is evidenced by (2.23). However, the physical response is generically dominated by one or the other,

and relying on only one of them is not sufficient.

There is a second reason why hydrodynamics is the more appropriate perspective for $G \ll \mu$. A more precise analysis of the momentum-dependent density correlator in an AdS₂ metal shows that it has multiple characteristic scaling contributions [131]

$$\text{Im} G_{J^t J^t}^{\text{homogeneous}}(\omega = 0, \mathbf{k}) \sim c_- T^{2\nu_k} + c_0 T^{2\nu_k^0} + c_+ T^{2\nu_k^+} \quad (2.24)$$

with the additional scaling exponents

$$\begin{aligned} \nu_k^0 &= \frac{1 + \hat{\eta}}{2} \sqrt{1 + 4\bar{k}^2}, \\ \nu_k^+ &= \frac{1 + \hat{\eta}}{2\sqrt{2 + \hat{\eta}}} \sqrt{10 + \hat{\eta} + 4(2 + \hat{\eta})\bar{k}^2 + 8\sqrt{1 + (2 + \hat{\eta})\bar{k}^2}}. \end{aligned} \quad (2.25)$$

For $k = G \ll \mu$ as one needs for Umklapp between $\text{Im} G_{J^t J^t}^{\text{homogeneous}}(0, k')$ for $k' = 0, \pm G$, all these three exponents take values that are very close to each other. For such small differences in the exponents there is observationally no clean scaling regime. For low lattice strengths A this is the reason that the observed weak lattice DC conductivities in Fig. 2.3 do not scale exactly inversely-linear-in- T as noted in the Introduction. Through Umklapp, the lattice DC conductivity is related to the homogeneous density correlator (which we will review in more details in the next section)

$$\sigma_{\text{DC, lattice}} \sim \left(\lim_{\omega \rightarrow 0} \frac{\text{Im} G_{J^t J^t}^{\text{homogeneous}}(\omega, k)}{\omega} \right)^{-1} \sim \frac{1}{c_- T^{2\nu_k - 1} + c_0 T^{2\nu_k^0 - 1} + c_+ T^{2\nu_k^+ - 1}}. \quad (2.26)$$

Fig. 2.5 shows that the deviation from linearity is exactly due to the contribution of the additional exponents.

2.5 DC vs Optical conductivities in explicit lattice (holographic) strange metals from Umklapp

Having argued that hydrodynamics should dominate the response in holographic strange metals, we now exploit our ability to do computational experiments to confirm that Umklapp hydrodynamics applies when such holographic strange metals are placed in an explicit periodic lattice with a small amplitude A . Then we shall describe the surprising phenomenological conclusions for electrical DC and optical electrical conductivity.

To verify the applicability of Umklapp hydrodynamics in AdS₂ metals, we can study the location of the poles in linear response functions. Fig. 2.6 shows the poles in the optical conductivity $\sigma(\omega)$ in a GR strange metal in a 1D ionic lattice background $\mu(x) = \bar{\mu}(1 + A \cos(Gx))$. There are multiple poles on the negative imaginary axis and two poles with real part at the location $\omega = \pm v_s G$. The latter are the ones already noted by

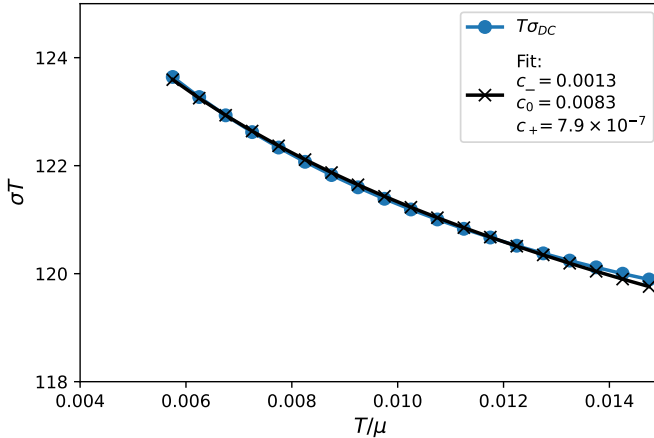


Figure 2.5: The DC conductivity of the GR metal in a weak lattice potential $A = 0.05$ is not perfectly inversely linear-in- T . This is due to subleading scaling contributions computable from the AdS_2 fixed point. Shown is a three parameter fit of the DC conductivity for c_-, c_0, c_+ to the functional form $\sigma_{DC} = 1/\left(c_- T^{2\nu_G-1} + c_0 T^{2\nu_G^0-1} + c_+ T^{2\nu_G^+-1}\right)$ at low temperature with ν_G, ν_G^0, ν_G^+ given by Eq. (2.20) and Eq. (2.25), with $k = G$, for $G/\mu = 0.1$. The values of the exponents ν_G, ν_G^0, ν_G^+ at this wave vector are 1.00015, 1.0198 and 2.53, respectively. Therefore according to this fit, one expects the exponent ν_G to be the dominating one only at temperatures $T/\mu < \mathcal{O}(10^{-50})$.

[82, 118, 84] and identified as Umklapp sound modes [84]. That Umklapp is at work is confirmed by tracing the behavior of the poles as a function of temperature. Compare the behavior of the two poles on the negative imaginary axis closest to the origin to the analytically computed values Eqs. (2.15), we see that the match is very good; see Fig. 2.7. Moreover, if one also studies the response functions at finite momentum k , then one observes the characteristic Umklapp level repulsion at the edge of Brillouin zone $k = G/2$ (Fig. 2.6).

2.5.1 Low temperatures: Drude transport

We have claimed Umklapp Hydrodynamics explains the remarkable finding summarized in Fig. 2.3 that the DC conductivity of a strange metal in a weak lattice remains linear-in-temperature while the mechanism governing the AC-response appears to change. We can now show this.

The DC conductivity from Umklapp Hydrodynamics to lowest order in the lattice

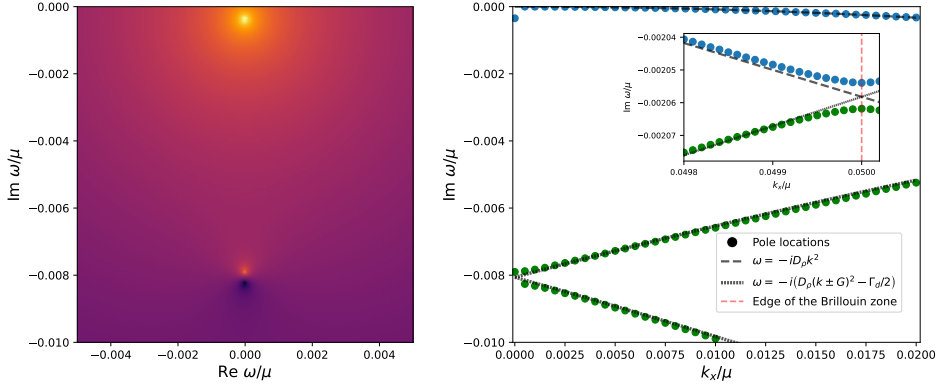


Figure 2.6: Umklapp hydrodynamics. The left panel shows the presence of both the Drude (upper) pole and the Umklapped charge diffusion (lower) pole and associated zero in the complex frequency plane at $k_x = 0$. The right panel shows the motion of both poles as a function of longitudinal momentum k_x . The Umklapp is confirmed by matching this motion to the diffusion coefficients of the un-Umklapped hydrodynamics computed in Eqs. (2.23). The inset shows the level splitting near the Brillouin zone boundary at $k = G/2$. The results are computed in the GR black-hole lattice at $T/\mu = 0.1, G/\mu = 0.1$ with a 1D ionic lattice potential $\mu(x) = \mu(1 + 0.05 \cos(Gx))$. The deviation at low k finds its origin in the next order level splitting in Umklapp which our formula does not account for, similar to the level splitting near the Brillouin zone.

strength A equals

$$\sigma_{DC} = \frac{Z_{\text{eff}}}{\Gamma + \frac{\omega_0^2}{\Omega}} + \sigma_Q = \underbrace{\frac{\omega_p^2}{\Gamma_\eta + \Gamma_d}}_{\mathcal{O}(A^{-2})} + \underbrace{\sigma_{\text{offset}} + \sigma_Q}_{\mathcal{O}(1)} + \mathcal{O}(A^2) \quad (2.27)$$

where, in the last equality, the first term is the leading order and the offset term σ_{offset} comes from the higher order terms in Eqs. (2.19). The first contribution in the DC from the sound part of the Laurent expansion (2.17) only comes at order $\mathcal{O}(A^2)$ and is therefore negligible here. These expressions already suggest that two physical mechanisms are at play in the DC result. At first sight this may appear contradictory to the conventional explanation of weak lattice DC conductivity in terms of Drude momentum relaxation $\sigma = \frac{\omega_p^2}{\Gamma_{\text{mom.rel.}}}$. The momentum relaxation rate $\Gamma_{\text{mom.rel.}}$ can be computed in the memory matrix formalism [133, 87] to equal

$$\Gamma_{\text{mom.rel.}} = \frac{g^2 G^2}{(\bar{\epsilon} + \bar{p})} \lim_{\omega \rightarrow 0} \frac{\text{Im} \langle \mathcal{O} \mathcal{O} \rangle(\omega, k = G)}{\omega} \quad (2.28)$$

where $\mathcal{O}(G)$ is the operator that breaks translation invariance with coupling g . In the case of an ionic lattice with a cosine potential as we consider, there are two operators

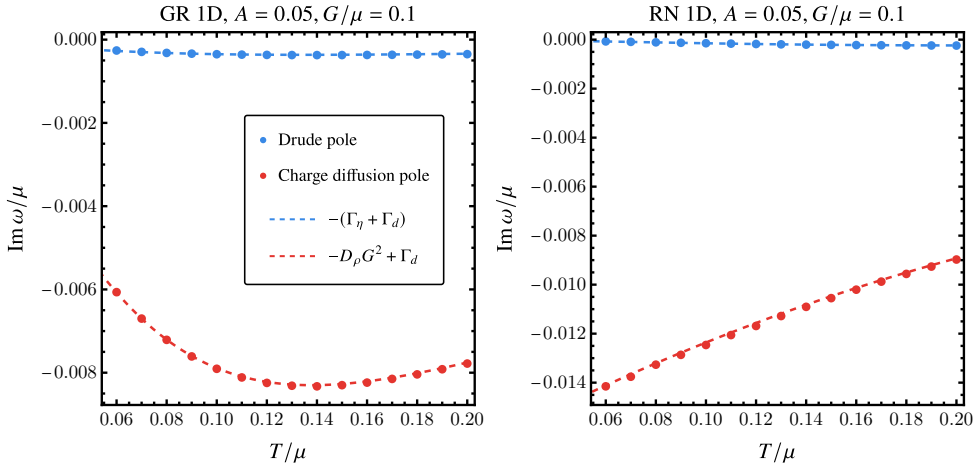


Figure 2.7: The motion of the poles (points) as one increases temperature compared to hydrodynamics (dashed). As the temperature is increased further the Drude pole eventually collides with the Umklapped charge diffusion pole and gains a real part. At low temperatures where a perturbative Umklapp analysis is valid the behavior of the poles can be understood from the un-Umklapped hydrodynamic analysis. Results are in the GR and RN 1D lattices with $G/\mu = 0.1$, $k_x = 0$ and potential strength $A = 0.05$.

$\mathcal{O}(G) = J^t$, one inserted at wavevector G and one at $-G$ each with coupling strength $g = \bar{\mu}A/2$. Therefore the memory matrix momentum relaxation rate for the ionic lattice is

$$\Gamma_{\text{mom.rel.}} = \frac{\bar{\mu}^2 A^2 G^2}{2(\bar{\epsilon} + \bar{p})} \lim_{\omega \rightarrow 0} \frac{\text{Im} G_{J^t J^t}(\omega, k = G)}{\omega}. \quad (2.29)$$

Inserting its correlation function computed in a homogeneous background into (2.29) one in fact finds the exact same answer as computed by Umklapp hydrodynamics $\Gamma_{\text{mom.rel.}} = \Gamma_\eta + \Gamma_d$ (see Appendix 2.D for a derivation of this result). Theoretically this can be understood through the observation that there are two possible dissipative channels in hydrodynamics. There is sound attenuation controlled by the shear viscosity η (and bulk viscosity ζ) and there is charge diffusion controlled by the microscopic conductivity σ_Q . Both are at the same order in the lattice strength $\Gamma_{d,\eta} \sim A^2$. This is the expansion parameter in the memory matrix computation and explains why they both show up.

The phenomenologically important characteristic is the temperature scaling of the DC resistivity. Implicitly the lattice scaling implies a scaling with temperature as the effective lattice strength should become irrelevant in the deep IR. This must be encoded explicitly in the scaling of both Γ_η and Γ_d , and not in the UV-strength A . However, there is a priori no requirement that both Γ_d and Γ_η will scale the *same* as a function of T . Generically they ought not. However, in holographic strange metals

without a ground state entropy they do. For these systems at low temperatures

$$\Gamma_\eta \sim \eta(T) \sim s \sim T^{(d-\theta)/z}, \quad (2.30a)$$

$$\Gamma_d \sim \frac{T^2}{\sigma_Q(T)} \left(T \frac{\partial s}{\partial T} \right)^2 \sim \left(\frac{d-\theta}{z} \right)^2 T^{(d-\theta)/z}. \quad (2.30b)$$

The derivation requires a mild assumption about the low temperature equation of state and is given in Appendix 2.E. Thus for the GR strange metal $\Gamma_\eta \sim T$ and $\Gamma_d \sim T$, whereas for the RN metal which has a ground state entropy $\Gamma_\eta \sim T^0$ but the first non-vanishing order for Γ_d is $\Gamma_d \sim T^2$. Over the range of validity, usually one of them will dominate, though it is conceivable that one dissipative momentum relaxation process switches dominance with the other. If this coincides with a change in scaling this would show up as a change of temperature scaling of the DC resistivity.

Two observations follow. The first is that despite the numerical results supporting the inference from disordered translational symmetry breaking that the momentum relaxation rate scales as the entropy, this is not true for the contribution from Γ_d .

The more important observation here and in the following is that which term dominates does not matter. In holographic strange metals the momentum-relaxation rate is set at a deeper level by the non-trivial locally quantum critical IR fixed point. As pointed out by Hartnoll-Hofman and briefly reviewed in the previous Section 2.4, in the regime where Eq. (2.29) holds, the frequency scaling enforced by local quantum criticality also sets the temperature scaling of the DC result. For the RN strange metal it is only Γ_η that is responsible for this, whereas in the Gubser-Rocha strange metal both obey the appropriate scaling. Since Γ_η also scales as G^2 , whereas Γ_d does not, one can tune the GR response to be dominated by Γ_d for $G \ll 2\mu$, and Γ_η to dominate for $G \gg 2\mu$. This coincides with the applicability of hydrodynamics as we discussed in the previous section, confirming a correlation with a physically observable change (see also section 2.5.4 below). This very difference between $\Gamma_\eta \sim G^2$ and $\Gamma_d \sim G^0$ actually causes the order of importance to be opposite in disordered systems. Because disorder can be viewed as an average over an infinite set of lattices, in the decay rate in a disorder system $\Gamma_{\text{disorder}} \sim \int G^{d-1} dG (\Gamma_d + \Gamma_\eta)$ the Γ_η term will generically dominate the integral [86]. Since $\Gamma_\eta \sim \eta \sim s$, this explains why in disordered systems entropy does directly control the dissipation timescale in contrast to a lattice with a fixed lattice momentum G_L as we explained above.

Independent of the dissipative mechanism, both leading in A momentum-relaxation rates Γ_η and Γ_d become vanishing small at low temperatures suggesting Drude transport. This is readily confirmed in the AC conductivity. Its real part displays a characteristic Drude peak. Mathematically, however, the peak is not exactly a (half-)Lorentzian, but follows from the two-pole expression Eq. (2.18).

2.5.2 Intermediate temperatures: a mid-IR-peak in the optical response

We have just argued that the DC resistivity can remain the same while the physical regime controlling dissipation changes, because it is set at a deeper level by the underlying AdS₂ fixed point. Though we have just noted this fact by analyzing the analytic expressions, it is in fact dramatically made clear at an intermediate higher temperature, as we already summarized in the Introduction.

In the regime of interest the conductivity computed from Umklapp hydrodynamics is controlled by two poles. In the parametrization

$$\sigma(\omega) = \sigma_Q + Z \frac{\Omega - i\omega}{(\Gamma - i\omega)(\Omega - i\omega) + \omega_0^2} \quad (2.31)$$

these are the Drude and Umklapp charge diffusion poles at

$$\begin{aligned} \omega_{\text{Drude}} &= \frac{-i}{2}(\Gamma + \Omega) + \frac{i}{2}\sqrt{(\Gamma - \Omega)^2 - 4\omega_0^2} = -i(\Gamma_\eta + \Gamma_d) + \mathcal{O}(A^4), \\ \omega_{\text{Um.Ch.Diff.}} &= \frac{-i}{2}(\Gamma + \Omega) - \frac{i}{2}\sqrt{(\Gamma - \Omega)^2 - 4\omega_0^2} = -i(D_\rho G^2 - \Gamma_d) + \mathcal{O}(A^4). \end{aligned} \quad (2.32)$$

At low temperatures, the second pole (let alone the two already ignored Umklapped sound poles) has a small effect. Increasing the temperature changes this fundamentally, however. Both poles move as one increases the temperature. However, they do not move in unison. When the argument under the square root $(\Gamma - \Omega)^2 - 4\omega_0^2$ becomes negative, the poles collide. For temperatures higher than the pole-collision temperature, the poles can now acquire a real part and move off the imaginary axis symmetrically; see Fig. 2.8. Initially this “microscopic pole collision” has little effect on the optical conductivity. In a formal sense it slightly broadens the peak around $\omega = 0$ and without an insight into the complex frequency response it is essentially indistinguishable from a conventional Lorentzian Drude peak. However, as one increases temperature further and the poles move further away from the imaginary frequency axis, the peak will split into two, symmetrically arranged around $\omega = 0$. For the positive half-line $\omega > 0$ one would thus see a peak emerge in the near IR whereas the DC value at $\omega = 0$ continues to decrease.

This collision point is controlled by a combination of temperature, lattice strength and lattice periodicity. Already at moderate lattice strengths, this emergence of the mid-IR peak in the AC conductivity happens at temperatures $T < T_{\text{strange}}$ where the DC response is still set by the critical scaling behavior of the underlying AdS₂ strange metal. In other words, despite the qualitatively drastic change in the AC-vs-T conductivity, the DC-vs-T response is unaffected.

What is striking is that this emergence of mid-IR peak in the optical response as temperature increases while the DC-resistivity stays linear in T is precisely what is

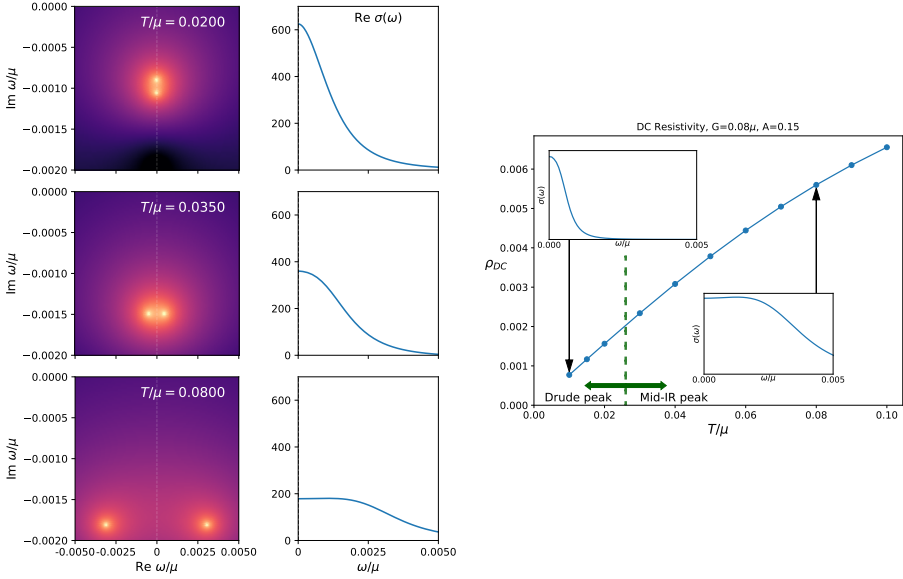


Figure 2.8: Emergence of mid-IR peak in the optical conductivity $\sigma(\omega)$ from pole collision. At low temperatures the Umklapp has negligible consequences as the response is strongly dominated by the conventional Drude pole. At intermediate temperatures the Umklapp pole causes an additional broadening. When the temperature increases to the point where the poles collide and gain a real part the peak still looks Drude to the eye even though it arises from two poles symmetrically arranged on both sides of the real axis. At even higher temperatures these two poles move so far apart that the peaks separate and a mid-IR peak at finite ω appears in the optical response. For this figure the parameters are $A = 0.15, G = 0.08\mu$, the same as in Fig. 2.3.

observed in high T_c cuprates and other strange metals as explained in the introduction. Given the earlier hypothesis reviewed there that transport in the high T_c -cuprates is hydrodynamical, it is conceivable that this is the explanation of this observed experimental finding.

The mechanism we just explained is tantalizing given its minimalistic nature. It is in fact *ubiquitous* for any hydrodynamical fluid exposed to a microscopic Umklapp potential where the effective potential strength is rising more rapidly than the momentum diffusivity. Notice that it does *not* apply to a Fermi liquid in metallic background potentials. The onset of equilibration is set by the quasiparticle collision time, but typically a substantial fraction of the center of mass momentum is absorbed by the Umklapp impeding the total momentum conservation required for hydrodynamics including the mechanism in the above.

2.5.3 Intermediate lattice strength: towards an incoherent metal

Our computational experiments on holographic strange metals can also provide us insight in what happens at larger lattice strengths beyond the applicability of perturbative Umklapp hydrodynamics. This is best quantified by tracking the behavior of the complex frequency poles in the AC conductivities. In Fig. 2.9 we show typical quasi-normal mode spectrum computed for lattice strength $A = 0.15$. At low temperatures one finds that these are still dominated by the non-linear continuation of the same two-pole structure as we identified for small A , *i.e.*, the Drude and Umklapp charge diffusion poles identified in Umklapp hydrodynamics.

What is notable, is that the pole collision has already happened at a lower temperature than for perturbatively small A . Qualitatively this is easy to understand in terms of the RG wisdom that the lattice becomes irrelevant in the IR. If one starts with a stronger A in the UV, one is at a relatively stronger strength at a temperature T or vice versa one is at a comparable strength at a lower temperature T . This may seem like semantics, but crucially the DC conductivity linear-in- T scaling remains set by the local quantum critical IR fixed point, which is less affected by an increase in A . As a result we can again observe in the AC conductivity a transition in the dissipative mechanism as one increases T during which the resistivity stays essentially linear (Fig. 2.3 in the Introduction). The transition in this case is that from the mid-IR-peak regime to an incoherent metal. The latter means that the low frequency AC response is no longer well described by the “two-coupled-relaxational-current” formula. Other poles now also influence the AC response, especially the two Umklapped sound modes. They feature prominently in the AC response; see Fig. 2.9.

Though the AC conductivity really shows the emergence of the incoherent metal regime at larger T and the “two-coupled-relaxational-current” expressions fails, for most of the temperature range the DC limit $\omega \rightarrow 0$ is still well described by its asymptotic expression

$$\sigma_{DC} = \sigma_0 + \frac{Z}{\Gamma + \frac{\omega_0^2}{\Omega}} . \quad (2.33)$$

With careful fitting of the optical conductivity as well as the complex location of the four poles, one can fit the parameters $Z, \sigma_0, \Gamma, \Omega, \omega_0^2$ as well as the parameters of the two first Umklapped sound poles as a function of A and T . For the full 4-pole ansatz, see Section 2.C. In Fig. 2.10 we show how the three parameters in the denominator Ω, Γ and ω_0 evolve as function of temperature for intermediate $0.1 < A < 0.8$. One sees how these explain the observed DC conductivity quite well. Given that the DC conductivity is so well captured by Eq. (2.33), one concludes that for these potentials the DC conductivity is still limited by the momentum lifetime.

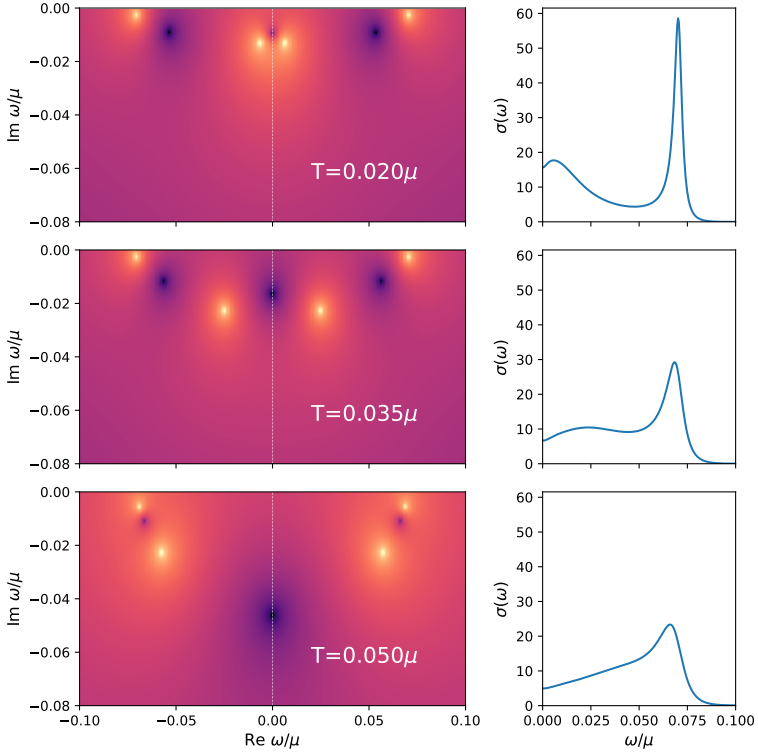


Figure 2.9: Optical conductivity (right) and the quasinormal mode spectra (left) for intermediate lattice strength GR lattices for $A = 1, G/\mu = 0.1$ at three different temperatures. Compared to small A the pole collision (see section 2.5.2) has already happened even at lowest $T/\mu = 0.02$. As one increases T the Umklapped sound poles which stay almost fixed at $\text{Re } \omega = \pm c_s G = \pm \frac{1}{\sqrt{2}} G$ (and others not shown) become more important and their dominance in the AC conductivity signals the transition to an incoherent metal regime.

2.5.4 On the applicability of Umklapp hydrodynamics

We end this section with a brief check on our earlier argument in Section 2.4 that Umklapp hydrodynamics is the relevant perspective to understand strange metal transport in a weak/intermediate lattice for $G \lesssim \mu$ rather than Hartnoll-Hofman scaling. The intuitive argument is that momentum dependent conductivities are strongly power-law suppressed as a function of T for $G \gtrsim \mu$ as the RG flow is not “halted”. Umklapping conductivities that have such marginal weight should have negligible observable effect. Fig. 2.11 shows that this insight is essentially correct. For a lattice with $G = 1.0\mu$, $T/\mu \lesssim 0.35$ and $A = 1.0$ the AC conductivity is Drude-like, and no transitions to a mid-IR-peak or incoherent metal are seen. An illustration that formally Umklapp hydrodynamics still applies is that one can still notice the now very highly suppressed

Umklapped sound peak. Even so, for $G \gtrsim \mu$ the better perspective is Hartnoll-Hofman scaling. Since G/μ is large here, the various exponents in the resistivity described in Section 2.4 are not close and the lowest exponent ν_G of Eq. (2.20) alone is enough to describe the DC conductivity at low temperatures.

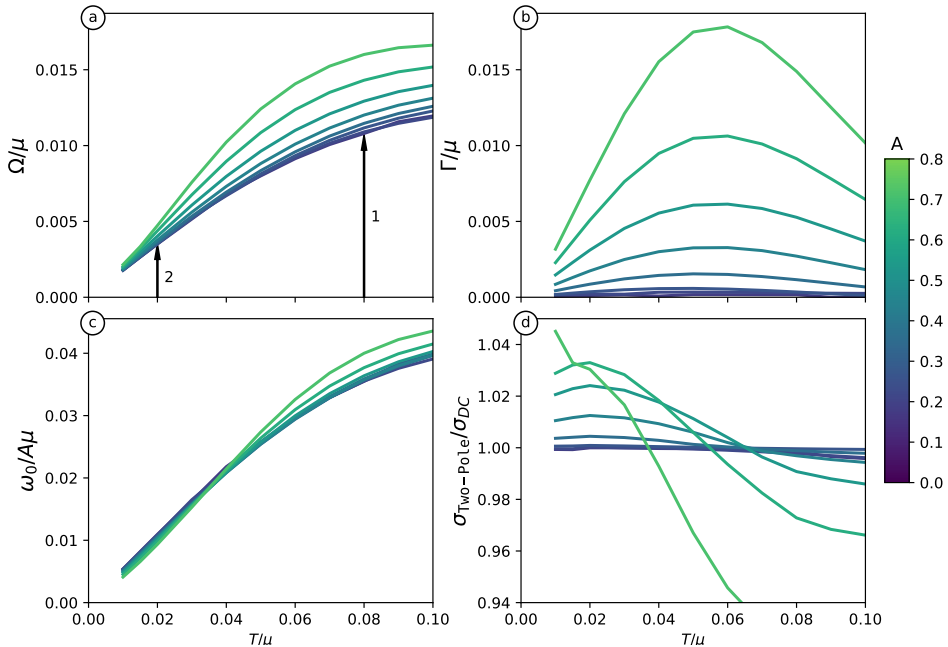


Figure 2.10: (a-c) The evolution of the phenomenological parameters $\Gamma/\mu, \Omega/\mu, \omega_0/A\mu$ as present in the “two-coupled-relaxational-current” expression Eq. 2.31 as a function of A and T/μ at $G/\mu = 0.12$ in the 1D Gubser-Rocha model. These parameters are extracted from a four-pole fit to the optical conductivity that includes the two lowest-order Umklapped sound peaks which reside at $\text{Re } \omega \approx \pm c_s G$. Both Ω/μ and $\omega_0/A\mu$ show little A -dependence, whereas Γ/μ depends strongly non-linearly on A . In (a), the arrows labelled 1 and 2 point to the temperatures at which the pole collision happens at $A = 0.1$ and $A = 0.2$, respectively. For the stronger lattices, the pole collision has already happened at lower temperatures than we have access to in our numerics. (d) Comparison of $\sigma_{\text{Two-Pole}}$, the conductivity reconstructed from only the “two-coupled-relaxational-current” part of the spectrum in figures to σ_{DC} , the observed DC conductivity. At larger values of A , it becomes clear that one must include more information, such as the Umklapped sound modes, in order to accurately reconstruct the DC conductivity at all temperatures.

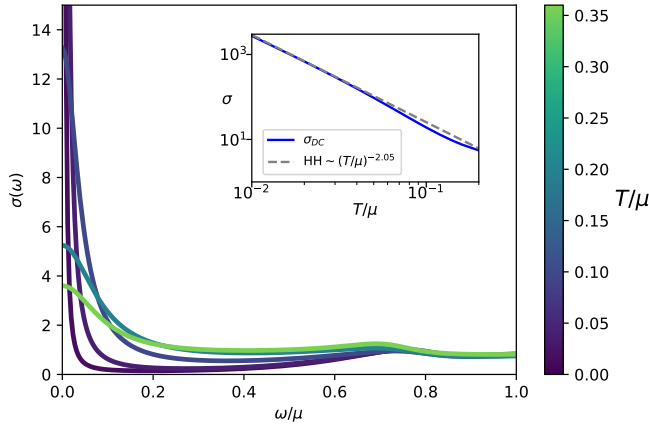


Figure 2.11: The AC conductivity of the GR model at $G = 1.0\mu$ and lattice strength $A = 1.0$ for a large temperature range. The low ω -response is of the Drude form for all values and no transition to a mid-IR-peak or an incoherent metal is seen in contrast to lattice momenta $G < \mu$. The small rise at $\omega/\mu = \frac{1}{\sqrt{2}} \frac{G}{\mu} = \frac{1}{\sqrt{2}}$ is the Umklapped sound mode which now has barely noticeable height at low temperatures. The inset shows that the DC conductivity obeys leading order Hartnoll-Hofman scaling at low temperature, which is expected to go as $(T/\mu)^{-2.05}$ at low temperatures.

2.6 Observations at strong lattice potentials: Planckian dissipation and incoherent metals

2.6.1 The remarkable ubiquity of Planckian dissipation

We now switch to analyzing our numerical results at large lattice potentials $A > 1$. As we reviewed in Section 2.2, for small lattice potentials $A < 1$, Planckian dissipation is unlikely to be universal as it will depend on the details of how translational symmetry is broken [73, 112]. At finite density one must be in a regime where translation is broken strongly and long time transport is controlled by another dissipative mechanism than translational symmetry breaking.

Performing this numerical experiment where we increase the lattice strength, one sees not only a beautiful sharper linear-in- T resistivity, but also a saturating behavior in that the resistivity appears to become independent of the lattice strength A , highlighted in the Introduction (Fig. 2.1). Though the thermo-electric and heat conductivity also appear to saturate, they do not. Replotting the results as a function of the inverse lattice strength $1/A$ rather than A , one sees that they asymptote to zero as $1/A$; see Fig. 2.12. One also notes that the electrical conductivity does not saturate but turns over when inspected this precisely. Treating the numerical results as a

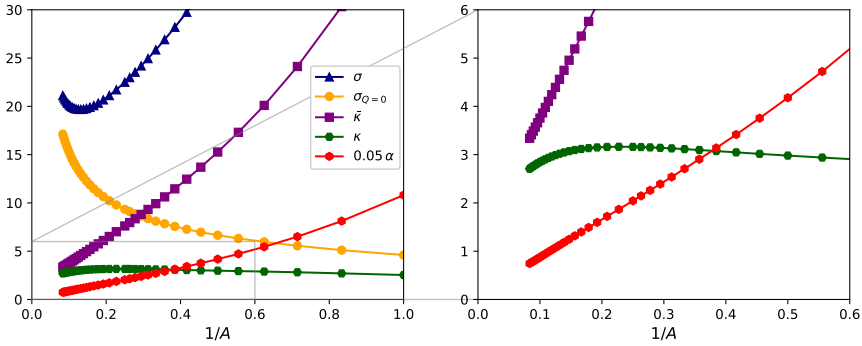


Figure 2.12: (Left panel) Absence of exact saturation of the conductivities as a function of lattice strength at fixed temperature in the 2D GR model is made quite clear when they are plotted as a function of $1/A$ instead of A . The electrical conductivity σ reaches a minimum and then starts to grow again at larger A , whereas the thermo-electric α and heat conductivity $\bar{\kappa}$ scale as $1/A$ rather than saturate. (Right panel) The open boundary heat conductivity κ at first instances does appear to be independent of the lattice strength A for most of the computed values. However, at the largest A it does show a downturn, asymptoting to $\bar{\kappa}$ which vanishes as $1/A \rightarrow 0$. In this large A regime, these asymptotes $\kappa \rightarrow \bar{\kappa}$ and $\sigma_{Q=0} \rightarrow \sigma$ indicate the increased dominance of the diffusive channel. These results are for the 2D GR lattice with $T = 0.06\mu$, $G = 0.1\sqrt{2}\mu$.

purely experimental finding, a naive Drude analysis does suggest that the dissipative process saturates — even though this does not apply for strong momentum relaxation. Increasing the lattice potential A has two effects, it changes the strength and possibly mechanism of dissipation, but it can also shift degrees of freedom from lower to higher energy and vice versa. In simple Drude language where one postulates $\sigma_{DC} = \omega_p^2/\Gamma$, increasing the lattice strength cannot only affect Γ , but also the Drude weight ω_p^2 . Again, the Drude formula doesn't necessarily apply at large A , of course. Nevertheless, to focus on the dissipation we must also account for possible shifts in the weight. Because the total weight of the optical conductivity is protected and conserved, a more appropriate measure of the dissipation is to normalize the measured DC conductivity by the total weight $\int_0^\Lambda d\omega \sigma(\omega)$ and study the resultant rate $\Gamma_{\text{corrected}}^{-1} = \sigma_{DC} / \int_0^\Lambda d\omega \sigma(\omega)$. Fig. 2.13 shows both the bare naive Drude rate $\Gamma_{\text{bare}}^{-1} = \sigma_{DC}/\omega_p^2$ and the corrected rate. Indeed in terms of the naive Drude rate even at the largest A the saturating behavior in the conductivity is not exact. However, when corrected for a possible spectral shift, the postulated relaxation rate does start to saturate. Not only does this relaxation rate appear to start to saturate, as Fig. 2.13 shows, it does so at a value that is numerically close to the Planckian dissipation rate $\Gamma_{\text{corrected}} \simeq 2\pi/\tau_{\hbar} = 2\pi T$. A naive Drude weak momentum relaxation analysis applied in the strong lattice regime may therefore inadvertently lead one to conclude to have detected Planckian dissipation. However, to understand whether Planckian dissipation is really occurring, we must resort to a different theoretical framework.

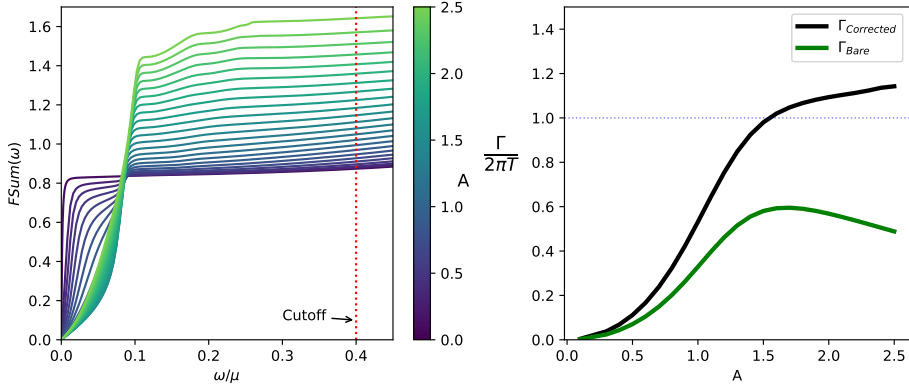


Figure 2.13: At large lattice potential one can construct a naively defined relaxation rate $\Gamma_{\text{bare}}^{-1} = \sigma_{\text{DC}}/\omega_p^2$. Strictly speaking this is only valid for weak lattices. Persisting in the analysis nevertheless, the change in Γ is not just given by the change in σ_{DC} . The integrated optical conductivity $F\text{Sum}(\Lambda) = \int_0^\Lambda \sigma(\omega)d\omega$ shows that the spectral weight ω_p^2 also increases with A . We can account for this effect by normalizing the Drude weight to this integrated spectral weight. The resulting corrected relaxation rate $\Gamma_{\text{corrected}}^{-1} \equiv \sigma_{\text{DC}}/F\text{Sum}(\Lambda)$ does appear to show a saturating behavior compared to the bare rate $\Gamma_{\text{bare}}^{-1} = \sigma_{\text{DC}}/\omega_p^2$. Furthermore, this rate is remarkably close to the Planckian value of $2\pi T/\mu$. From inspection a cut-off value $\Lambda/\mu = 0.4$ is sufficient to account for all the spectral weight in any Drude or Umklapped sound peaks. Tantalizing as these results may be, a correct analysis at large lattice strengths eschews the use of a momentum relaxation rate altogether as it is no longer the unique longest timescale. The results above are taken in the 1D GR model with $T = 0.06\mu, G = 0.12\mu$.

2.6.2 An incoherent metal explained with microscopic scrambling

How to understand transport in a system where translation invariance is badly broken was discussed in detail by Hartnoll [64], and its connection with Planckian dissipation was set out in a series of papers [72, 73, 134, 90, 74] in the context of systems with strong translational disorder. The essence is that in this regime only energy and charge are the conserved currents that survive at long distances. For this section we shall not just focus on the electrical conductivity but on the full thermo-electric transport matrix

$$\begin{pmatrix} \vec{J} \\ \vec{j}_Q \end{pmatrix} = \begin{pmatrix} \sigma & \alpha T \\ \alpha & \bar{\kappa} \end{pmatrix} \begin{pmatrix} \vec{E} \\ \frac{1}{T} \vec{\nabla} T \end{pmatrix} \quad (2.34)$$

with $j_Q^i = \frac{1}{T}(T^{0i} - \mu J^i)$. Here $\bar{\kappa} = \kappa + \frac{T\alpha^2}{\sigma}$ is the heat conductivity in the absence of electric field, and κ is the heat conductivity in the absence of electric current (open boundary heat conductivity). Fig. 2.1 shows the result for all conductivities for increasing lattice strength into the incoherent regime, both in the Gubser-Rocha ($s_{\text{GR}} \sim T + \dots$)

and in the Reissner-Nordström AdS₂ metal ($s_{\text{RN}} \sim c_0 + c_1 T + \dots$). The conductivities are rescaled such that their dominant power-law scaling with T is scaled out. In detail one observes also that the thermo-electric and the heat conductivity conform sharper to the conjectured appropriate temperature scaling as A increases, culminating again in a saturating behavior for large A .

It is tempting to view this scaling of the thermo-electric conductivities as validating that the system is dominated by a single common relaxation time that scales like the entropy at low temperatures, even though it does not apply here as A is large. Single relaxation time Drude theory would suggest that $\sigma = \omega_p^2/\Gamma$, $\alpha = \frac{s}{n}\sigma$, and $\frac{\kappa}{T} = \frac{s^2}{n^2}\sigma$. If $\Gamma \sim s(T)$ as naively guessed above, it is consistent with the above observations. As we will now explain, and confirmed with counterexamples in studies of strong translational disorder, this single relaxation time description is not correct.

To extract possible relaxation rates in an incoherent metal with strong translational symmetry breaking, one posits constitutive relations for the two remaining currents and does a hydrodynamic analysis. One finds that the DC conductivities are the zero frequency limit of the dynamics of two independent diffusive modes with diffusion constants D_+ and D_- . These are

$$\begin{aligned} D_+ + D_- &= \frac{\kappa}{c_n} + \frac{\sigma}{\chi} + \frac{T\sigma}{c_n} \left(\frac{\alpha}{\sigma} - \left(\frac{\partial s}{\partial n} \right)_T \right)^2, \\ D_+ D_- &= \frac{\kappa}{c_n} \frac{\sigma}{\chi}. \end{aligned} \quad (2.35)$$

Here $c_n = T \left(\frac{\partial s}{\partial T} \right)_n$ is the specific heat at fixed charge density, $\chi = \left(\frac{\partial n}{\partial \mu} \right)_T$ is the isothermal charge compressibility, and the conductivities σ, κ are both the transport coefficients as well as the DC values. One recognizes a charge diffusion and a heat/energy diffusion mode (the remnant of sound in absence of a nearly conserved momentum), cross coupled through the combination $g \equiv \frac{T\sigma}{c_n} \left(\frac{\alpha}{\sigma} - \left(\frac{\partial s}{\partial n} \right)_T \right)^2$. If we are to make the case that a single dissipative mechanism dominates, this cross-coupling is important, as in its absence, charge and energy diffusion are clearly independent. Fig. 2.14 shows what the strength of this coupling is numerically. As was shown in [74], this coupling behaves as $g/\sigma \sim T^{(z+d-\theta)/z}$ if the scaling of the homogeneous non-trivial IR fixed point remains valid in the presence of strong translational symmetry breaking. For the GR metal this means $g \sim T$. Compared to $\sigma/\chi \sim T^{-1}$ it is therefore small and can be treated perturbatively in the low temperature limit.

Solving for σ, κ in the limit where the terms in the cross coupling $\frac{T\sigma^2}{c_n\sigma} \sim T$,

$\frac{T\alpha}{c_n} \left(\frac{\partial s}{\partial n} \right)_T \sim T$ and $\frac{T\chi\sigma}{c_n} \left(\frac{\partial s}{\partial n} \right)_T^2 \sim T$ are small compared to $\sigma \sim T^{-1}$, one finds⁹

$$\begin{aligned} \frac{\sigma}{\chi} &= D_+ \left[1 + \frac{T}{c_n \chi} \frac{\left(\alpha - D_+ \chi \left(\frac{\partial s}{\partial n} \right)_T \right)^2}{D_+ (D_- - D_+)} \right], \\ \frac{\kappa}{c_n} &= D_- \left[1 - \frac{T}{c_n \chi} \frac{\left(\alpha - D_+ \chi \left(\frac{\partial s}{\partial n} \right)_T \right)^2}{D_+ (D_- - D_+)} \right]. \end{aligned} \quad (2.36)$$

To lowest order in the temperature the electrical and heat conductivity are therefore determined by independent diffusion constants; see Fig. 2.14. The electrical conductivity is determined by $D_+ \sim T^{-1}$ and the heat conductivity by $D_- \sim T$. There is therefore no simultaneous explanation for both conductivities in terms of universal Planckian dissipation. In holographic models with strong translational disorder there are systems where both conductivities are set by Planckian dissipation [72, 73]. This happens when the charge susceptibility is relevant. For irrelevant or marginal charge susceptibility, the electrical conductivity is set by a different dissipative mechanism. The Gubser-Rocha model with strong disorder belongs to this class [90], and so does our strong ionic lattice model with $\chi \sim T^0$.

Despite the existence of two independent dissipative mechanisms, the heat conductivity can be explained from Planckian dissipation. Very strongly coupled systems are similar to weakly coupled dilute classical gases in that their macroscopic transport can be understood from microscopic processes. For weakly coupled dilute gases this is through the Boltzmann equation summing microscopic scattering; for ultrastrongly coupled systems this is through parameters of microscopic scrambling as measured through the out-of-time-ordered correlation function $C(t, x) = \langle W(t, x) V(0) W(t, x) V(0) \rangle_T \sim e^{\lambda(t-x/v_B)}$.¹⁰ In holographic systems this connection manifests itself in that the OTOC is equivalent to computing the hydrodynamic response function (of longitudinal sound) at imaginary ω and k [135]. The Lyapunov exponent λ and the butterfly velocity v_B can then be read off from a skipped pole in the hydrodynamic dispersion relation [135]. One finds that in holographic systems λ saturates the Maldacena-Shenker-Stanford unitarity bound $\lambda \leq 2\pi/T$. The butterfly

⁹Note that the coupling term $\frac{T\chi}{c_n} \left(\frac{\partial s}{\partial n} \right)_T = \frac{nT}{(\epsilon+P)} - \frac{c_s^2 \mu}{\alpha_n s}$ contains the same thermodynamic factor as Γ_d . If the temperature scaling in the strong lattice is the same as in the homogeneous system, this coupling scales as $\frac{nT}{(\epsilon+P)} - \frac{c_s^2 \mu}{\alpha_n s} \sim T$ since $\alpha_n \sim T^{-2}$ as was shown in Appendix 2.E. Numerics confirm that this is the case.

¹⁰This “ballistic” OTOC expression applies to large N systems such as holographic and SYK systems. The more generic answer is “diffusive” $C(t, x) \sim e^{\lambda(t-x^2/v_B t)}$.

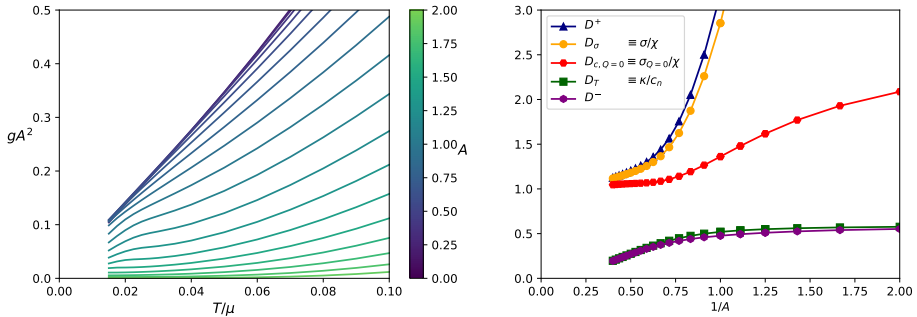


Figure 2.14: Left: The cross-coupling between the heat and electrical conductivity in the strongly coherent regime is governed by the combination $g = \frac{T\sigma}{c_n} \left(\frac{\alpha}{\sigma} - \left(\frac{\partial s}{\partial n} \right)^2 \right)$ respectively at low temperatures. Clearly g decreases linear in temperature at low T , but it also decreases with stronger lattice potential A . Right: As a consequence the diffusivities at low T in a strong lattice become independent. Shown are the empirical combinations $D_\sigma \equiv \frac{\sigma}{\chi}$, $D_T = \frac{\kappa}{c_n}$, $D_{\sigma_{Q=0}} = \frac{\sigma_{Q=0}}{\chi}$ as a function of $1/A$ for fixed $T/\mu = 0.05$.

velocity is more sensitive to the theory. On general grounds it scales near (translationally invariant) quantum critical IR fixed points as $v_B^2 \sim T^{2-2/z}$. The fact that both macroscopic transport and the scrambling parameters λ, v_B are encoded in the hydrodynamic response means that they are not unrelated. In particular the thermal diffusivity $D_T = \frac{\kappa}{c_n} = E \frac{v_B^2}{\lambda}$ with $E = \frac{1}{2}$ for AdS₂ $z \rightarrow \infty$ metals in strong disorder [73, 134, 74]. Since the natural units of diffusivity are $v^2\tau$, this is interpreted as Planckian dissipation with $\tau = \frac{1}{\lambda} = \frac{1}{2\pi T}$. The RN metal is a special case. As explained in [134], there the butterfly velocity is controlled by a dangerously irrelevant operator instead of universal scaling. A careful computation reveals that for the RN strange metal $v_B \sim \sqrt{T}$. Combined with Planckian dissipation $\tau = \frac{1}{\lambda} = \frac{1}{2\pi T}$, this explains the observed RN thermal diffusivity $D_- = \frac{\kappa}{c_n} = T^0 \sim v_B^2\tau$.

This result is established and confirmed in the many studies cited above on connecting scrambling to hydrodynamics for vanishing, weak momentum relaxation or “homogeneous” momentum relaxation both in holography [136, 137, 138, 139, 140, 141, 142, 143, 144] and in other strongly-correlated systems [145, 146, 147].¹¹ We postulate that the same applies in the explicit strong lattice systems studied here. This need not be, for computing the butterfly velocity v_B in a non-translationally invariant system is not straightforward (the Lyapunov exponent on the other hand is universally $\lambda = 2\pi/T$ [153]). At the same time the scaling we observe for strong lattice potentials is the same as that which is observed for strong translational disorder. This is strong evidence in favor of the argument that the same should apply here.

¹¹Presumably for all models with so-called maximal quantum chaos [148]. There are counterexamples [149, 150, 151, 152]; see [128] for a good discussion.

Within the framework of incoherent metals there is no universal explanation of the observed inverse-in-T scaling of the conductivity for the Gubser-Rocha metal. Its tantalizing behavior $\sigma \sim s(T)^{-1}$ or rather $\sigma \sim \frac{1}{\Gamma_h}$ on the other hand *does* suggest that some type of universality is at work. This is confirmed by the RN results. The obvious conjecture is that $D_- = (v^{\text{charged}})^2/\lambda$ where the velocity v^{charged} relevant for diffusion of charged objects *differs* from the butterfly velocity for neutral objects. Some evidence that this can be the case is presented in [91, 92, 93, 94]. If v^{charged} were independent of temperature, this would explain the observed incoherent metal phenomenology in the large lattice GR and RN metals in terms of a single Planckian relaxation time, but differing scrambling velocities. We leave this for future research.

2.6.3 Saturating behavior and Planckian dissipation

The diffusivities in the incoherent regime should be insensitive to the details of translational symmetry breaking. This is what allows them to expose universal dissipative physics. This resulting explanation of universality in terms of microscopic scrambling also makes physical sense: the onset of chaos is controlled by the short-range interactions and is not expected to be influenced significantly by a background lattice. The data we present is obviously dependent on the lattice strength A . For most values of A we are therefore not in the universal regime. However, as A increases to the largest value we can observe in our numerical data, there is a saturating behavior in the electrical conductivity that together with its sharper single power behavior argues strongly that we are close to this universal incoherent limit. Such saturating behavior in the incoherent electrical conductivity at large lattice strength was already noted in [154]. That study focused on the regime where the dimensionless combinations $\frac{\mu}{G} \rightarrow 0$, $\frac{A\mu}{G}$ fixed and large. Here we focus on the regime where both $\frac{\mu}{G}$ and $\frac{A\mu}{G}$ are fixed and large with the latter parametrically larger.

We can use our numerical results to directly check these assertions. Rather than observing the conductivities we do so for the diffusivities

$$D_\sigma = \frac{\sigma}{\chi}, D_T = \frac{\kappa}{c_n}, D_{\sigma_{Q=0}} = \frac{\sigma_{Q=0}}{\chi}. \quad (2.37)$$

We have introduced here a charge-without-heat diffusivity $D_{\sigma_{Q=0}} = \frac{\sigma_{Q=0}}{\chi}$ as this is the appropriate counterpart to the heat-without-charge open boundary thermal diffusivity $D_T \equiv \kappa/c_n$. Fig. 2.14 shows indeed how the charge diffusivities $D_\sigma, D_{\sigma_{Q=0}}$ not only both saturate, but also become approximately equal. The latter shows indeed that we have entered the incoherent regime. A more detailed depiction of the saturation is given in Fig. 2.15.

We have already shown in the Introduction that the crossover into the incoherent sector can also be seen in the conductivities directly (Fig. 2.2). The open boundary thermal conductivity κ starts to comprise more than 80% of the full heat conductivity. A stronger statement extrapolated from the incoherent metal considerations is that

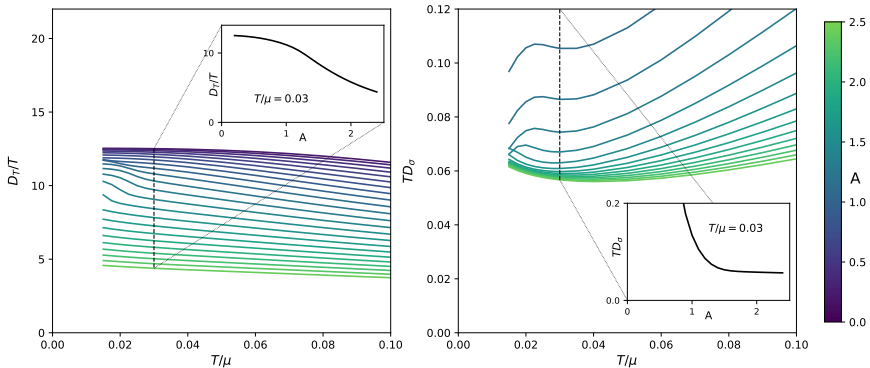


Figure 2.15: Electrical and thermal diffusivities as a function of T for various A . The T -dependence shows how they become more single-power like at larger A . The A -crosssection shows the saturation for large A for the charge diffusivity, but an increasing A dependence for the thermal diffusivity. These results are in the GR lattice at $G = 0.1\mu$.

the open boundary heat conductivity κ is rather insensitive to momentum relaxation for any translational symmetry breaking potential irrespective of its strength [74]. According to Fig. (2.12) this is indeed the case in the perturbative small A case. Upon pushing the potential to extremely large values we do observe that some changes in κ start to arise. This is fully in the incoherent regime, where we can equate $\kappa \equiv c_n D_T$ with one of the physical diffusion constants $\kappa = c_n D_-$. This diffusion constant also changes from A -independent to slight decaying behavior, explaining the change in behavior in κ . We conclude that at least for D_T our computations confirm the universal nature of the diffusion constants.

2.7 Discussion: is it relevant for condensed matter physics?

We started this paper with just presenting the data as these rolled out of the computer. As such these are highly suggestive. We focus in on a holographic strange metal that fulfills minimal conditions that appear to be imposed by experiment: local quantum criticality ($z \rightarrow \infty$) and a Fermi-liquid like thermodynamics in the form of a Sommerfeld entropy ($s \sim T$). We then invoke a lattice potential that may become very strong, again a minimal requirement suggested by experiment. For a wavevector of the potential that is not too large (smaller than the inverse local length) we find a resistivity that is to good approximation linear in temperature for a large range of potential strength. Ramping up the potential the slope of the linear resistivity saturates at a value that is consistent with a Planckian (τ_h) current lifetime. Although the dynamical range in temperature and potential strength is limited in our computations, we can track the temperature evolution of the optical conductivity in the regime

where the saturation is setting in. This temperature evolution is also suggestive with regard to experiment: at low temperature we find a simple Drude response that turns into an incoherent mid-IR peak, and this gross change does not imprint on the DC resistivity that stays linear. Taken together, this shines an unusual light on three problems of principle in strange metal transport: (a) Why is the resistivity linear in temperature down to the lowest temperatures? (b) Why is the empirically extracted current relaxation time so close to the Planckian rate τ_{\hbar} ? (c) Why does the cross-over from good metal (Drude optical conductivity) to bad metal (the mid-IR peak response) not affect the DC resistivity at all?

The question remains whether the resemblances between numerical observations from this holographic toy model and the complicated reality of the copper oxide electron systems are just a coincidence or whether they reveal a truly universal principle governing transport that supersedes all the differences between them. To get a better understanding, we focused in on both the small- and large lattice potential regimes. We showed that in the perturbative small potential regime the transport behavior can be completely reconstructed on basis of the thermodynamics and transport properties of the unbroken homogeneous system. This is based on hydrodynamical flow behavior in the presence of a weak periodic potential and we discovered a generic principle governing linear response: next to the usual shear drag, a mode coupling emerges with the Umklapped charge diffusion mode. As we increase temperature the coupling between two relaxation modes can account for a second new phenomenon: the two poles can collide and this explains the emerging mid-IR peak in the AC conductivity. Even though the temperature dependence of the DC-resistivity is formally set by the same thermodynamic quantities, the underlying non-trivial IR fixed point constrains these in such a way that the DC resistivity temperature scaling can be independent of the dynamical change in the AC conductivity.

The large lattice potential regime on the other hand is where the resistivity slope saturates. Our numerics indicate that this happens in the “incoherent metal” regime where momentum conservation does not play any role. Accordingly, the temperature dependence of the resistivity should be inversely proportional to the *charge* diffusivity. This charge diffusivity in the incoherent regime $D_- \sim T^{-1}$ should not be compared with the hydrodynamical charge diffusivity for weak or zero momentum relaxation which scales as $D_{\rho} \sim T$. The *thermal* diffusivity $D_T \sim T$ on the other hand is essentially insensitive to the strength of the lattice potential. It scales similarly for both small and large potential, though only at large potential can it be explained in terms of microscopic chaos anchored in a saturated Lyapunov bound $\Gamma = \lambda = 2\pi T$ having a Planckian magnitude. Although this is presently not well understood this is consistent with the analytical findings in a homogeneous holographic strange metal with momentum relaxation (Q-lattice).

Although this does shed light on various aspects we do not claim a complete understanding of our numerical results. The above suggests that there are quite different forms of physics at work pending the strength of the potential. Nevertheless,

we do find that the evolution of the transport quantities is of a strikingly smooth kind. Another striking aspect is the contrast between the GR and RN results in Fig. 2.1: the differences in temperature dependencies appear to be entirely linked to the different temperature dependence of the entropy. The above analysis, where we can expose the different origins in the weak and large lattice potential regime, does make clear that this connection with entropy is almost certainly a coincidence, though we cannot exclude that some yet to be identified greater universality may be at work linking the dissipative properties in the convective and diffusive regimes together where entropy may play a crucial role.

To use this to explain the experimental observations, the critical holographic input is in the form of the current being controlled by “generalized” hydrodynamics (including the incoherent metal) that in turn requires (a) an existence of hydrodynamics up to microscopic length scales shorter than the lattice spacing, (b) thermodynamical behavior that is anchored in a non-trivial IR fixed point, and (c) a saturation of the chaos bound (with a charge dependent butterfly velocity v_B^{charge}).

In fact, the most critical question is whether experimental strange metal transport is governed by hydrodynamics, and not by the usual quasiparticle transport. In this regard our finding that hydrodynamics provides a most natural explanation for the temperature evolution of the DC and AC charge response is encouraging: it is an elementary mechanism that offers a minimal and simple explanation for this otherwise mysterious affair.¹² However, to prove it one would like to mobilize the mesoscopic transport devices of the kind that have proven successful in this regard observing hydrodynamical flow behavior in graphene (e.g., [155]).

The next issue is, are the hydrodynamical modes surviving down to length scales of order of the microscopic lattice spacing $1/G$? We found this to be a special property of the local quantum critical holographic metals, but is this also at work in the cuprate strange metals? This is far from obvious. Besides the Umklapped charge diffusion mode, we also saw the sharp and prominent Umklapped sound peak in the optical conductivity when the potential becomes sizable. This relates directly to a first discrepancy between our results for the optical conductivity and the experimental results in the cuprates. We find that for the strongest potentials that our numerics can handle, the optical response rather abruptly switches off at frequencies above the Umklapped sound peak (Fig. 2.9). In experiment no sound peak is seen, and a power law (branch cut) tail is found instead, extending all the way up to $\mu \simeq 1$ eV [61, 156, 62]. Our holographic results do not shed any light on this matter, although one could imagine that perhaps an Umklapped *overdamped* sound channel could conspire to give rise to such a quasi-critical behavior. But the issue is whether the charge diffusion hydro-mode that is responsible for the mid-IR peak in holography may survive up to large momenta in the experimental systems. Different from sound, this mode is non-convective and perhaps

¹²Note that the focus here is only on the mysterious behavior of the longitudinal linear-in- T resistivity. We do not address other experimental cuprate strange metal conundrums, such as the concurrent T^2 -scaling in the Hall angle.

less sensitive to translational symmetry breaking. Presently we have no answer to this question. It could be interesting to study the optical conductivity of the cuprate metals experimentally at high temperatures. The data in so far available are sketchy and it would be interesting to find out what a systematical and high precision study would reveal regarding for instance the way in which the mid-IR peak depends on temperature. Alternatively the sound contribution to the density-density response can be measured directly by EELS [97, 157], with the caveat that sound is promoted to a plasmon in the presence of dynamical electromagnetism. This may be hard, because the plasmon is damped stronger in strange metallic states than ordinary Fermi liquids [158, 159, 160, 161]. The results are at this moment inconclusive, and need to still be found consistent with the AC optical conductivity.

Perhaps the most delicate issue relates to the connection with microscopic chaos. The connection with Planckian dissipation requires a saturation of the Maldacena-Shenker-Stanford bound on the Lyapunov exponent of the OTOC $\lambda \leq 2\pi T$. It appears that a necessary condition for this to happen is in the form of *dense many body entanglement*. One may argue that this is the secret of the experimental strange metals: these are born from strongly interacting *fermion* systems at a finite density and it may well be that the concomitant sign problem enforces dense entanglement in the non-Fermi-liquids [69]. But this may not be a sufficient condition. The chaos bound is known to saturate in matrix large N systems at strong coupling with a holographic dual as well as the disorder averaged SYK models. These systems are characterized by dense matrix interactions.

However, the Hubbard models that are the community standard as microscopic point of departure for the cuprate electrons are characterized by local interactions and the associated Hamiltonians correspond with rather sparse matrices. As with regard to the transport properties, the present benchmark is in the form of finite temperature quantum Monte Carlo computations for the resistivity [162]. The temperatures that can be reached are still quite high (≈ 1000 K) but arguably approaching the linear resistivity regime. However, the outcomes are quite different from what we find.

The Hubbard models are of course in their own way toy models, capturing the largest scales in the problem but ignoring a lot of other physics. Could it be that long range interactions arising e.g. from Coulomb interactions and/or phonon mediated interactions are crucial to support the rapid scrambling near the Lyapunov bound given their non-local nature [163]? Could there be a direct relation to SYK physics associated with the observation of spin glass physics [164, 165], with the obvious difficulty that this has only been observed in the spin striped 214 system?

At the least, holography inspires to ask quite unusual questions to experiment: it suggests a physics that is tantalizingly different from the usual Fermi-liquid quasiparticle physics. Eventually, it should be possible by targeted experimentation to reach a verdict. This is not easy: the cuprates have been subjected to unprecedented experimental scrutiny over the last 35 years but on basis of the available information it is still impossible to decide the issue.

An example of this law-of-Murphy that insightful results may be the hardest to obtain experimentally is the thermal transport. So much is clear that the thermal conductivity κ of the GR metal acquires a universal temperature dependence that is up to very high lattice potentials independent of the potential strength. Numerically we observe that $\kappa \sim T^2$. But this in gross contrast with the thermal conductivity in a Fermi liquid, where $D_T \sim \tau_c$ where $\tau_c \sim 1/T^2$ is the quasiparticle collision time such that $\kappa \sim 1/T$ [166]. There is a large difference of the order T^3 in the temperature dependence of the thermal conductivity between the holographic metal and a Fermi liquid!

This should be the smoking gun but why can this not be used? The reason is that at the high temperatures where the strange metal is realized (> 100 K) the thermal transport is rather completely dominated by the *phonons*. The phonon heat conduction short circuits the heat transport and it is virtually impossible to extract the electronic contributions. The same problem is there for a measurement a charge transport without heat $\sigma_{Q=0}$. Aside from the experimental hurdle of zeroing out heat transport cleanly, the definition of $\sigma_{Q=0} = \sigma - T\alpha^2/\bar{\kappa}$ implicitly refers to the *electronic* component of the heat transport only.

Finally, there is one thermo-electrical transport coefficient that is readily available experimentally: the Seebeck coefficient enumerating the thermopower. This is given by $s = \alpha/\sigma$. According to Fig. 2.1, $\alpha \sim T^0$ and $\sigma \sim 1/T$, and we predict $s \sim T$: although for different reason this is the same temperature dependence generic for a Fermi-liquid (the Mott formula), this is indeed the scaling that has been observed in cuprate strange metals, e.g. [167, 168].

Acknowledgments

We thank R. Davison, B. Goutéraux, S. Grozdanov, S. Hartnoll and A. Krikun for discussions. This research was supported in part by the Dutch Research Council (NWO) project 680-91-116 (*Planckian Dissipation and Quantum Thermalisation: From Black Hole Answers to Strange Metal Questions.*), the FOM/NWO program 167 (*Strange Metals*), and by the Dutch Research Council/Ministry of Education. K.G. acknowledges funding from the European Union's Horizon 2020 research and innovation programme under the Marie Skłodowska-Curie grant agreement No 101024967. The numerical computations were carried out on the Dutch national Cartesius and Snellius national supercomputing facilities with the support of the SURF Cooperative as well as on the ALICE-cluster of Leiden University. We are grateful for their help.

2.A AdS RN and GR black holes

We will be interested in perturbations of both Reissner-Nordström and Gubser-Rocha black holes.

2.A.1 Reissner-Nordström

The RN black holes start from the Einstein-Maxwell action

$$S = \int d^4x \sqrt{-g} \left[\frac{L^2}{2\kappa^2} (R - 2\Lambda) - \frac{L^2}{4e^2} F_{\mu\nu} F^{\mu\nu} \right], \quad (2.38)$$

with $2\kappa^2 = e^2 = L^2 = 1$ and $\Lambda = -3$. The equations of motion are

$$\begin{aligned} R_{\mu\nu} - \Lambda g_{\mu\nu} &= \frac{1}{2} \left[F_{\mu\rho} F_{\nu}^{\rho} - \frac{1}{4} g_{\mu\nu} F_{\rho\sigma} F^{\rho\sigma} \right], \\ \nabla_{\mu} F^{\mu\nu} &= 0. \end{aligned} \quad (2.39)$$

These equations admit an electrically charged black hole solution, the AdS-Reissner-Nordström (RN) solution in asymptotically AdS₄ space-time, for which the metric and gauge field are given by¹³

$$\begin{aligned} ds^2 &= g_{\mu\nu} dx^{\mu} dx^{\nu} = \frac{1}{z^2} \left[-f(z) dt^2 + \frac{dz^2}{f(z)} + dx^2 + dy^2 \right], \\ A &= A_t(z) dt, \end{aligned} \quad (2.40)$$

where

$$f(z) = (1-z) \left(1 + z + z^2 - \frac{\mu^2 z^3}{4} \right), \quad A_t(z) = \mu(1-z). \quad (2.41)$$

The radial coordinate z can be scaled such that the horizon is located at $z_h = 1$ and the boundary of the space-time is at $z = 0$. The temperature of the black hole can be computed by considering the surface gravity of the horizon, and is given by

$$T_{\text{RN}} = \left| \frac{f'(z_h)}{4\pi} \right| = \frac{12 - \mu^2}{16\pi} \quad (2.42)$$

2.A.2 Einstein-Maxwell-Dilaton

For the dilatonic black holes, we depart from the Einstein-Maxwell-Dilaton action[38, 118]

$$S = \frac{1}{2\kappa^2} \int d^4x \sqrt{-g} \left[R - \frac{Z(\phi)}{4} F_{\mu\nu} F^{\mu\nu} - \frac{1}{2} (\partial_{\mu}\phi)^2 + V(\phi) \right]. \quad (2.43)$$

The potentials Z, V are given by

$$Z(\phi) = \exp(\phi/\sqrt{3}), \quad V(\phi) = \frac{6}{L^2} \cosh(\phi/\sqrt{3}). \quad (2.44)$$

¹³Sometimes, it is more convenient to make a change of variable $z \rightarrow 1 - (1-r)^2$ [169].

The cosmological constant is given by $\Lambda = -V(0)/2 = -3$. Setting $2\kappa^2 = L^2 = 1$, the equations of motion for this system are given by

$$\begin{aligned} R_{\mu\nu} &= \frac{Z(\phi)}{2} \left[F_{\mu}{}^{\rho} F_{\nu\rho} - \frac{1}{4} g_{\mu\nu} F^2 \right] + \frac{1}{2} \partial_{\mu}\phi \partial_{\nu}\phi + \frac{1}{2} g_{\mu\nu} V(\phi), \\ \nabla_{\mu} [Z(\phi) F^{\mu\nu}] &= 0, \\ \square\phi &= V'(\phi) + \frac{Z'(\phi)}{4} F^2, \end{aligned} \quad (2.45)$$

where we used that on-shell $R = -2V(\phi) + \frac{1}{2}(\partial\phi)^2$. This setup also has an analytic solution which is given by a metric, gauge field and non-trivial scalar ϕ in the form of

$$\begin{aligned} ds^2 &= g_{\mu\nu} dx^{\mu} dx^{\nu} = \frac{1}{z^2} \left[-h(z) dt^2 + \frac{1}{h(z)} dz^2 + g(z)(dx^2 + dy^2) \right] \\ A &= \frac{\sqrt{3Qz_h(1+Qz_h)}(1-z/z_h)}{z_h(1+Qz)} dt \\ \phi &= \frac{\sqrt{3}}{2} \log(1+Qz) \end{aligned} \quad (2.46)$$

where

$$\begin{aligned} h(z) &= \frac{(1-z/z_h)}{g(z)} \left[1 + (1+3Qz_h) \frac{z}{z_h} + (1+3Qz_h(1+Qz_h)) \left(\frac{z}{z_h} \right)^2 \right], \\ g(z) &= (1+Qz)^{3/2}. \end{aligned} \quad (2.47)$$

The parameter Q encodes the charge of the black hole. The chemical potential is given by $\mu = \sqrt{3Qz_h(1+Qz_h)}/z_h$. The near-horizon form of the potentials in equation (2.43) corresponds to a scaling behavior of z , $-\theta \rightarrow \infty$, also identified by γ , $-\delta = 1/\sqrt{3}$ in [34]. The temperature here is given by

$$T_{\text{GR}} = \left| \frac{h'(1)}{4\pi} \right| = \frac{3\sqrt{1+Qz_h}}{4\pi z_h}. \quad (2.48)$$

2.A.3 Lattice Backgrounds

The translational symmetry of the black hole backgrounds is broken by applying a periodic ionic lattice in the boundary field theory through the modulation of the chemical potential [81]. In the gravitational theory, this corresponds to imposing a boundary condition on the gauge field

$$A_t(x, y, z = 0) = \bar{\mu} \left(1 + A_x \cos(G_x x) + A_y \cos(G_y y) \right). \quad (2.49)$$

$A_{x,y}$ parameterize the strength of the lattice, while $G_{x,y}$ are the reciprocal lattice dimensions, respectively. Our computational domain in (x, y) is chosen to always contain a whole number of lattice periods, *i.e.*, $x \sim x + 2\pi n_x/G_x$, $y \sim y + 2\pi n_y/G_y$ where $n_x, n_y \in \mathbb{Z}$. Throughout this work, we take $G_x = G_y \equiv G$ and $A_x = A_y \equiv A_0/2$ in a 2D lattice and $A_x \equiv A_0, A_y = 0$ for a 1D lattice.

This breaking of translational symmetry influences the solutions dramatically. The additional curvature generated by the periodic lattice means that in principle all the off-diagonal components of the metric as well as all components of the gauge field will become non-trivial.

For RN, the ansatz for the fields is adapted from reference [169]:

$$\begin{aligned}
 ds^2 &= \frac{1}{z^2} \left(-Q_{tt} f(z) \eta_t^2 + Q_{xx} \eta_x^2 + Q_{yy} \eta_y^2 + \frac{Q_{zz}}{f(z)} \eta_z^2 \right), \\
 \eta_t &= dt, \\
 \eta_x &= dx + Q_{xy} dy + Q_{xz} dz, \\
 \eta_y &= dy + Q_{yz} dz, \\
 \eta_z &= dz, \\
 A &= \mu(1-z) A_t dt
 \end{aligned} \tag{2.50}$$

Our EMD ansatz looks similar and is given by

$$\begin{aligned}
 ds^2 &= \frac{1}{z^2} \left(-Q_{tt} h(z) \eta_t^2 + g(z) (Q_{xx} \eta_x^2 + Q_{yy} \eta_y^2) + \frac{Q_{zz}}{h(z)} \eta_z^2 \right), \\
 \eta_t &= dt, \\
 \eta_x &= dx + Q_{xy} dy + Q_{xz} dz, \\
 \eta_y &= dy + Q_{yz} dz, \\
 \eta_z &= dz, \\
 A &= \frac{\mu(1-z)}{1+Qz} A_t dt, \quad \phi = \frac{3}{2} \log(1+\varphi Qz).
 \end{aligned} \tag{2.51}$$

For both types of solutions, we are interested in stationary solutions, and therefore all functions $F = \{Q_{ij}, A_i, \varphi\}$ are functions of (x, y, z) , each periodic in (x, y) with a periodicity of $L_{x,y} = 2\pi n_{x,y}/G_{x,y}$. The equations of motion in equation (2.39) and (2.45) form very complicated systems of non-linear partial differential equations in three dimensions, which in general cannot be solved analytically. For numerical convenience, the DeTurck trick and another gauge fixing term for the gauge field can be used to turn this set of equations into an elliptic boundary value problem [101, 102, 169]. The UV boundary conditions on the radial coordinate come from imposing an asymptotically AdS solution while imposing that the dilaton be a marginal operator with no source, as was highlighted in [170]. The horizon boundary conditions arise from requiring

regularity at the horizon, which means that in a series expansion in powers of $(z-1)$ we can relate each $\partial_z F_i$ to all functions and their tangential derivatives at the horizon,¹⁴ together with the condition that $Q_{tt}|_{z=1} = Q_{zz}|_{z=1}$.¹⁵

The boundary value problems are solved using a self-developed software package in C, using the PETSc library [171, 172]. A Newton line-search algorithm employing second- and third order finite difference schemes on rectangular grids is used to find solution to the non-linear problem. The computational grids are either uniformly spaced or have the radial coordinate run over the Chebyshev-Lobatto nodes for increased accuracy near the boundaries of the problem. Typical grid sizes for the simulations run between $N_x \times N_y \times N_z = 40 \times 40 \times 60$ to $80 \times 80 \times 120$. For convergence checks, the vanishing of the norm of the DeTurck vector provides a good measure [102]. Due to the large number of degrees of freedom involved ($O(10^7)$ for the largest lattices) most of the numerical work was done using the ALICE cluster at Leiden University and the Dutch national Cartesius and Snellius supercomputers with the support of SURF Cooperative. The code is publicly available [173, 174].

2.A.4 DC Conductivity

The DC conductivity is computed by solving a Stokes flow problem on the black hole horizon [103, 104, 105, 106]. Using a set of time-independent perturbations, one can show that the bulk linear response problem of computing (thermo)electric DC conductivities can be reduced to a linearized version of the Navier-Stokes equations for an auxiliary fluid that lives on a static black hole horizon background. The equations take a similar form for both EMD and RN black holes, and can be written as [105]

$$\begin{aligned} \eta^{(0)}(-2\nabla^j \nabla_{(i} v_{j)} + 3v^j \nabla_j \phi^{(0)} \nabla_i \phi^{(0)}) - d\chi_{ij}^{(0)} Q^j - F_{ij}^{(0)} J^j = \\ \rho^{(0)}(E_i + \nabla_j w) + T s^{(0)} \left(\zeta_i - \nabla_i \frac{P}{4\pi T} \right) \\ \partial_i Q^i = 0, \quad \partial_i J^i = 0. \end{aligned} \quad (2.52)$$

The superscript (0) indicates that these are background quantities evaluated at the horizon. These are the values we extract from the numerical solutions to the background lattices described above.¹⁶ The Stokes equations (2.52) is then a set of four equations for the four unknown functions v_x, v_y, w, p . The currents Q, J and transport coefficients $\rho^{(0)}, \eta^{(0)}, s^{(0)}, \chi^{(0)}$ can be written in terms of these four functions, the background horizon quantities and the induced metric on the horizon $h_{ij}^{(0)}$ [105]. E_i, ζ_i source the electric field and thermal gradient, and are taken to be constant over the unit cell.

¹⁴If the change of coordinates in footnote 13 is used, this simplifies to $\partial_r F_i = 0 \forall i$, as only even powers of r will appear in the near-horizon expansion. This comes at the cost of accuracy near the horizon.

¹⁵This ensures a constant temperature across the (corrugated) horizon.

¹⁶For the RN black holes, one should take $\phi = 0, Z(\phi) = 1, V(\phi) = 6$.

The thermo-electric DC conductivities are then extracted by evaluating

$$\begin{pmatrix} \vec{J} \\ \vec{Q} \end{pmatrix} = \begin{pmatrix} \sigma & \alpha T \\ \bar{\alpha} T & \bar{\kappa} T \end{pmatrix} \begin{pmatrix} \vec{E} \\ \vec{\zeta} \end{pmatrix}, \quad (2.53)$$

where \vec{J}, \vec{Q} are here the spatial averages of the solutions when evaluating equation (2.52). These averaged values do not renormalize when lifted to the boundary to be interpreted in the field theory. As a result, the thermo-electric conductivity matrix defined in equation (2.53) is that of the field theory.

In previous works, e.g. [106], these equations have been used to study simpler systems that do not fully break spatial translational symmetry or break it in a homogeneous way. That simplification allows for a largely analytic treatment of these equations. The systems we are interested in do not permit us such luxuries and therefore we have to solve this coupled linear PDE in two periodic dimensions numerically. For this, we developed a package in Python which can solve coupled (non-)linear partial differential equations for backgrounds as well as perturbations. This package is rather flexible, in that it can make use of both (pseudo)spectral and arbitrary-order finite difference methods to solve the equations. This package will be made available publicly at a later date.

2.B Semi-local criticality and an induced IR length scale

Semi-local quantum liquids can be defined by a “self-energy” that is either a power-law in frequency $\Sigma \sim \omega^{2\nu(k)}$ or exponential $\Sigma \sim \exp\left(-\frac{kz/(z-1)}{\omega^{z-1}}\right)$ with z the dynamical critical exponent. In the limit $z \rightarrow \infty$ the latter reduces to the former [99]. Both ω and k are dimensionless frequencies and momenta in units of the chemical potential μ . As emphasized in [33] the spatial structure of such semi-local quantum liquids is that the spread of local perturbations decays very rapidly and is bounded by an emergent length scale $\xi \propto \mu^{-1}$.

Though the emergence of this semi-local physics is poorly understood from a conventional point of view, its emergence bound is surprisingly clear from a dual holographic perspective. It is a direct consequence of the existence of a maximal distance, $x_{\max} \sim 1/\xi_\mu$ that two light-rays emitted from near the AdS black hole horizon can spread [33]. It implies that a local perturbation in the IR can only originate from/influence a finite spatial region (in the UV variables).

This supplementary section shows how this maximal distance arises. A light-ray parametrized by $X^\mu(\tau)$ follows a null geodesic, *i.e.*,

$$g_{\mu\nu} \dot{X}^\mu \dot{X}^\nu = 0. \quad (2.54)$$

Consider a generic $z = \infty$ metric

$$ds^2 = \left(\frac{r}{R}\right)^{-\frac{2\eta}{d}} \left[-\mu^2 R^2 r^2 dt^2 + \frac{R_2^2}{r^2} dr^2 + \mu^2 R^2 dx_i dx^i \right] \quad (2.55)$$

The parameter $\eta = -\frac{\theta}{z}$ is the remnant of the hyperscaling violation exponent θ in the limit $z \rightarrow \infty$ and $R_2 = R/\sqrt{6}$ is the emergent AdS₂ radius. For a geodesic emanating from the horizon we can use the radial r coordinate as the affine parameter τ , and the physical gauge $X^r = r$. Then solving the geodesic equation $D_\tau \dot{X}^\mu = 0$ subject to the null length constraint, one finds for the motion in the transverse directions

$$X_{i,\pm}(r) = x_i^{(0)} \pm \frac{v_i R_2}{\mu R v} \tan^{-1} \left(\frac{rv}{\sqrt{v_t^2 - r^2 v^2}} \right). \quad (2.56)$$

with $v^2 = \sum_i v_i^2$. Two light-rays starting from the same point $x_i^{(0)}$ one pointing to the left and one to the right therefore arrive at the boundary ($r = \infty$) a distance $2 \frac{v_i}{v} \frac{R_2}{\mu R} \frac{1}{\tan(i)}$ apart.

We are now interested in the intersection of two lightcones $x_{i,+}$ and $x_{i,-}$, which can be found from

$$x_{i,+}(r_0; x^{(0)} = 0) = x_{i,-}(r_0; x^{(0)}) \implies r_0 = \frac{v_t}{v} \sin \left(\frac{\mu R v x_i^{(0)}}{2v_i R_2} \right). \quad (2.57)$$

After combining (2.56) with (2.57), we find that the maximal allowed distance is

$$x_1^{(\max)} = \frac{R_2}{R\mu} \pi \cos \theta, \quad x_2^{(\max)} = \frac{R_2}{R\mu} \pi \sin \theta. \quad (2.58)$$

where we have chosen the parametrization for the initial velocity components along (x_1, x_2) as $v_1 = v \cos \theta$, $v_2 = v \sin \theta$, where $\theta \in [0, \pi/2]$ is the initial angle, measured with respect to the x_1 -axis.

The relative initial distance between the two geodesics Δs reads

$$\Delta s = \sqrt{x_1^{(\max)2} + x_2^{(\max)2}} = \frac{R_2}{R\mu} \pi, \quad (2.59)$$

which is universal and does not depend on the initial conditions. It coincides with the result presented in [33].

In figure 2.16, we plot the causal structure for two light-rays separated by a certain initial distance. For an initial separation larger than the critical distance, (2.58), both

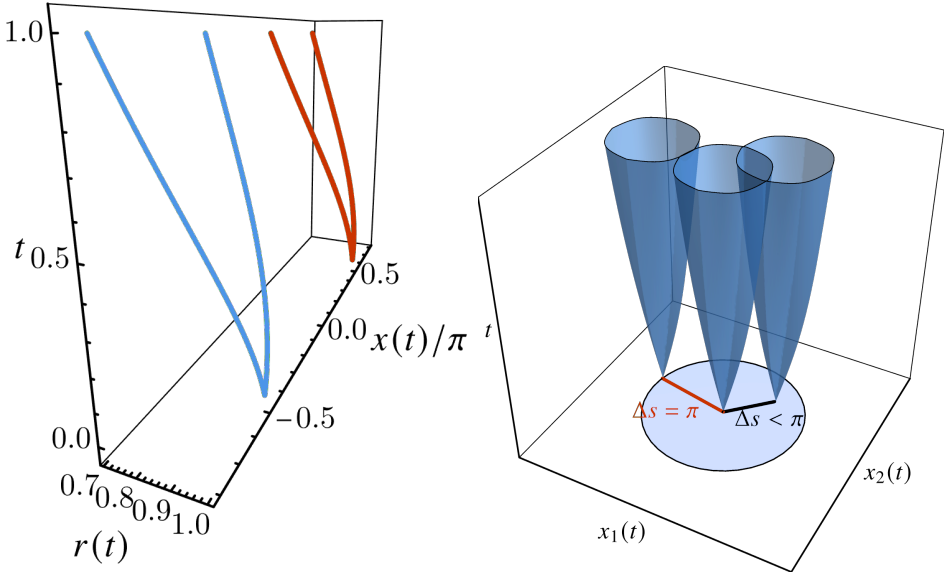


Figure 2.16: Left figure: Causal structure for two light-rays separated at a relative distance $x_0 = \pi$. The x -axis corresponds to the $x_1(t)$, while the y -axis to the $r(t)$ coordinate. The external time has been taken as the dialing parameter, along the z -axis in the figure. For the present purposes, we have considered no motion along the x_2 direction, and we have also set $R_2 = R = \mu = 1$. Right figure: Causal structures for three light-cones as functions of $(x_1(t), x_2(t))$. The z -axis corresponds to time, for which we have set $t = 1$ as the time that the geodesics reach the boundary. Those geodesics that start at any point within the disk of radius π will be causally connected, while disconnected if otherwise.

light-rays are not causally connected anymore. To illustrate this, we have chosen as a dialing parameter the external time t . After some computations, we get

$$t(x_i) = -\frac{R_2 v}{\mu R v_t} \cot \left[\frac{\mu R v}{v_i R_2} (x_i - x_i^{(0)}) \right]. \quad (2.60)$$

which is plotted in the second figure in 2.16. From here, we highlight that any geodesic that starts at an initial relative distance $\Delta s \leq \pi$, will be causally connected, whereas if $\Delta s > \pi$, it will be causally disconnected.

Based on (2.59) and on the fact that the 2-point correlation function $G \sim 1/\xi_m \sim \pi$, we conclude that the maximal correlation distance in Planckian dissipation is related to the existence of this maximal causality distance in geodesic.

2.C Four pole fitting formula

The full 4-pole fitting formula that can fit the four poles nearest to the origin in the complex frequency plane is given by the following nine-parameter formula

$$\sigma(\omega) = \sigma_0 + Z \frac{\Omega - i\omega}{(\Omega - i\omega)(\Gamma - i\omega) + \omega_0^2} + \left(\frac{Z_{s,1} + iZ_{s,2}}{\omega - (\omega_{s,1} + i\omega_{s,2})} + \text{time-reversed} \right). \quad (2.61)$$

The weights and positions of the sound poles is constrained by time reversal symmetry, which dictates that

$$\sigma^*(-\omega^*) = \sigma(\omega). \quad (2.62)$$

2.D Memory matrix formalism

The correlation functions of the homogeneous GR and RN fluids are well described by the standard hydrodynamics of relativistic conformal fluids with U(1) charge (see [119]). To compute (2.29), we simply need the correlator $G_{J^t J^t}$ which is given by

$$G_{J^t J^t}(\omega, k) = \frac{\sigma_Q k^2}{D_\rho k^2 - i\omega} - \frac{k^2 \omega_p^2}{\omega^2 + iD_\pi k^2 \omega - c_s^2 k^2}. \quad (2.63)$$

This form quite readily shows how this dynamical response has both a convective part (sound) and a dissipative part. At low frequencies, this correlator can be expanded as

$$G_{J^t J^t}(\omega, k) = \frac{\omega_p^2}{c_s^2} + \frac{\sigma_Q}{D_\rho} + i\omega \left[\frac{\sigma_Q}{D_\rho k^2} + \omega_p^2 \frac{D_\pi}{c_s^4} \right] + \mathcal{O}(\omega^2). \quad (2.64)$$

The leading term is entirely real and will not contribute to the imaginary part. Therefore, we can eventually obtain (2.29) as

$$\Gamma_{\text{mom.rel.}} = \frac{\bar{\mu}^2 A^2}{2(\bar{\epsilon} + \bar{p})D_\rho \alpha_n} + \frac{\bar{\mu}^2 A^2 D_\pi \bar{n}^2}{2c_s^4 (\bar{\epsilon} + \bar{p})^2} G^2 = \Gamma_d + \Gamma_\eta, \quad (2.65)$$

where we recognize the quantities Γ_d, Γ_η introduced in (2.16).

2.E Scaling of hydrodynamical relaxation rates

Consider an equation of state $P(T, \mu)/\mu^3 = a_0 + a_1(T/\mu)^{\hat{\eta}+1}$ where $\hat{\eta} = (d - \theta)/z$ is the generic effective dimension in the presence of a dynamical critical exponent z and hyperscaling violation exponent θ . This equation of state will be a valid approximation for the low-temperature regime of the holographic Einstein-Maxwell-Dilaton systems,

such as RN and GR. Then, the entropy and charge density one obtains from this pressure are $s/\mu^2 = (\hat{\eta} + 1)a_1(T/\mu)^{\hat{\eta}}$ and $n/\mu^2 = 3a_0 - (\hat{\eta} + 2)a_1(T/\mu)^{\hat{\eta}+1}$. We will now look at the momentum relaxation rate (2.29) for a relativistic charged fluid such that the viscosity saturates the minimal viscosity bound $\eta = s/(4\pi)$ and we will take the EMD T-scaling $\sigma_Q = \hat{\sigma}_Q(T/\mu)^{\hat{\eta}+2}$ [175]. From the integrated first law $\epsilon + P = sT + \mu n$, we find $\epsilon = 2P$ for this choice such that we still have a conformal system and therefore $\zeta = 0$.

The relaxation rate has two contributions, one G -dependent and one G -independent, reminiscent of our result (2.16), which we will by analogy name Γ_η and Γ_d . In the general non-conformal case we have now introduced, these therefore take the form

$$\begin{aligned}\Gamma_\eta/\mu &= A^2(G/\mu)^2 \frac{\pi a_1(\hat{\eta} + 1)}{6a_0} \left(\frac{T}{\mu}\right)^{\hat{\eta}} \frac{\left(1 - \frac{a_1(\hat{\eta}-2)}{3a_0}(T/\mu)^{\hat{\eta}+1}\right)^2}{\left(1 + \frac{a_1}{a_0}(T/\mu)^{\hat{\eta}+1}\right)^3}, \\ \Gamma_d/\mu &= A^2 \frac{a_1^2(\hat{\eta} + 1)^2}{6a_0 \hat{\sigma}_Q} \left(\frac{T}{\mu}\right)^{\hat{\eta}} \frac{\left(\hat{\eta} + \frac{a_1(\hat{\eta}-2)}{3a_0}(T/\mu)^{\hat{\eta}+1}\right)^2}{\left(1 + \frac{a_1}{a_0}(T/\mu)^{\hat{\eta}+1}\right)^3}.\end{aligned}\tag{2.66}$$

The leading order of Γ_η can therefore be obtained as

$$\Gamma_\eta/\mu \sim A^2(G/\mu)^2 \frac{\pi a_1(\hat{\eta} + 1)}{6a_0} \left(\frac{T}{\mu}\right)^{\hat{\eta}} \sim A^2(G/\mu)^2 \frac{\pi}{2} \frac{s}{n}.\tag{2.67}$$

This shear drag contribution is therefore entirely determined by the entropy at low temperature. The other contribution, Γ_d , is slightly less straightforward. When $\hat{\eta} > 0$, a similar behavior arises

$$\Gamma_d/\mu \sim A^2 \frac{a_1^2(\hat{\eta} + 1)^2 \hat{\eta}^2}{6a_0 \hat{\sigma}_Q} \left(\frac{T}{\mu}\right)^{\hat{\eta}} \sim \frac{A^2}{2n/\mu^2} \left(T \frac{\partial s}{\partial T}\right)^2 \sigma_Q^{-1} \left(\frac{T}{\mu}\right)^2.\tag{2.68}$$

Therefore in this general case, which encompasses the GR case $\hat{\eta} = 1$, Γ_d and Γ_η have the same temperature dependence although Γ_d is more sensible to the susceptibilities like the specific heat $T \frac{\partial s}{\partial T}$ and the hydrodynamic transport coefficient σ_Q . A counterexample of this general rule however arises when $\hat{\eta} = 0$, as it is for the RN black hole for instance, where the leading order of Γ_d vanishes and instead one must expand to second order to have

$$\Gamma_d/\mu \stackrel{\hat{\eta}=0}{\sim} A^2 \frac{a_1^4}{3a_0^3 \hat{\sigma}_Q} \left(\frac{T}{\mu}\right)^2.\tag{2.69}$$

Finally, we can explain how this $(T/\mu)^2$ factor in (2.68) arises naturally from the α_n factor introduced in (2.9). To do so, consider the quantity $D_\rho \Gamma_d = A^2 \frac{\bar{\mu}^2}{2(\bar{\epsilon} + \bar{p})\alpha_n}$. We will relax here our assumptions about the equation of state and only assume some

Sommerfeld entropy $s = \gamma(\bar{\mu})\bar{T}$ and $n = n_0(\bar{\mu})$ at low temperature. The scaling of $D_\rho\Gamma_d$ is therefore entirely determined by that of α_n^{-1} which can be determined using

$$\begin{aligned}
 \left(\frac{\partial \bar{n}}{\partial \bar{T}}\right)_{\bar{\mu}} &= \left(\frac{\partial \bar{s}}{\partial \bar{\mu}}\right)_{\bar{T}} \sim \gamma'(\bar{\mu})\bar{T}, \\
 \left(\frac{\partial \bar{n}}{\partial \bar{\mu}}\right)_{\bar{T}} &\sim n'_0(\bar{\mu}), \\
 \left(\frac{\partial \bar{\epsilon}}{\partial \bar{T}}\right)_{\bar{\mu}} &= \bar{T} \left(\frac{\partial \bar{s}}{\partial \bar{T}}\right)_{\bar{\mu}} + \bar{\mu} \left(\frac{\partial \bar{n}}{\partial \bar{T}}\right)_{\bar{\mu}} \sim (\gamma(\bar{\mu}) + \bar{\mu}\gamma'(\bar{\mu}))\bar{T}, \\
 \left(\frac{\partial \bar{\epsilon}}{\partial \bar{\mu}}\right)_{\bar{T}} &= \bar{T} \left(\frac{\partial \bar{s}}{\partial \bar{\mu}}\right)_{\bar{T}} + \bar{\mu} \left(\frac{\partial \bar{n}}{\partial \bar{\mu}}\right)_{\bar{T}} \sim \bar{\mu}n'_0(\bar{\mu}) + \gamma'(\bar{\mu})\bar{T}^2.
 \end{aligned} \tag{2.70}$$

Then, we can plug these relations into Eqs. (2.9) and obtain

$$\alpha_n \sim \frac{\bar{T}^2 (\gamma(\bar{\mu}) + 2\bar{\mu}\gamma'(\bar{\mu})) + \bar{\mu}n'_0(\bar{\mu})}{\bar{T} \left[n'_0(\bar{\mu}) (\gamma(\bar{\mu}) + \bar{\mu}\gamma'(\bar{\mu})) \bar{T} - \gamma'(\bar{\mu})\bar{T} (\bar{\mu}n'_0(\bar{\mu}) + \gamma'(\bar{\mu})\bar{T}^2) \right]} \sim \frac{\bar{\mu}}{\bar{T}^2 \gamma(\bar{\mu})}. \tag{2.71}$$

Therefore, given Sommerfeld entropy, we naturally get that $D_\rho\Gamma_d \sim T^2$. Provided then that $D_\rho \sim T$, which is the case for the GR holographic metal, you recover the scaling $\Gamma_d \sim T$.

2.F Lorentz oscillator decoupling

Consider a system of modes coupled to one another in the following way

$$\begin{aligned}
 \partial_t J_1 + \Gamma_1 J_1 + \gamma_1 J_2 &= E_1, \\
 \partial_t J_2 + \Gamma_2 J_2 - \gamma_2 J_1 &= E_2,
 \end{aligned} \tag{2.72}$$

where $\Gamma_{1,2}$ are relaxation rates for the currents $J_{1,2}$, $E_{1,2}$ are explicit sourcing and $\gamma_{1,2}$ couple the two modes to one another. In matrix notation $\partial_t J_a + M_{ab} J_b = E_a$, this leads to the following evolution matrix

$$M_{\text{LO}} = \begin{pmatrix} \Gamma_1 & \gamma_1 \\ -\gamma_2 & \Gamma_2 \end{pmatrix}. \tag{2.73}$$

We can then solve this dynamic system and obtain, in frequency space,

$$\begin{aligned}
 J_1(\omega) &= \frac{(\Gamma_2 - i\omega) E_1}{(\Gamma_1 - i\omega)(\Gamma_2 - i\omega) + \gamma_1 \gamma_2}, \\
 J_2(\omega) &= \frac{\gamma_2 E_1}{(\Gamma_1 - i\omega)(\Gamma_2 - i\omega) + \gamma_1 \gamma_2},
 \end{aligned} \tag{2.74}$$

where we have set $E_2 = 0$ as we are only interested in externally sourcing one of the currents. Critically, we will be interested in a total current J which overlaps with both J_1 and J_2 through

$$J = \sigma_0 E_1 + aJ_1 + bJ_2 \quad (2.75)$$

where σ_0 is some explicit contribution by the external sourcing. Therefore, the conductivity associated to this current is

$$\sigma = J/E_1 = \sigma_0 + \frac{a(\Gamma_2 - i\omega) + b\gamma_2}{(\Gamma_1 - i\omega)(\Gamma_2 - i\omega) + \gamma_1\gamma_2}. \quad (2.76)$$

This form is very reminiscent of (2.18) with

$$\begin{aligned} Z_{\text{eff}} &= a, \quad \Omega = \Gamma_2 + \frac{b}{a}\gamma_2 \\ \Gamma &= \Gamma_1 - \frac{b}{a}\gamma_2, \quad \omega_0^2 = \gamma_1\gamma_2 - \frac{b}{a}\gamma_2 \left[\Gamma_1 - \Gamma_2 - \frac{b}{a}\gamma_2 \right]. \end{aligned} \quad (2.77)$$

Let us now compare to the matrix M (2.11) describing the dynamical hydrodynamic system in the small lattice expansion. From this system of 4 coupled fields, it is possible to decouple two by taking the large speed of sound limit $c_s \rightarrow \infty$ ¹⁷ which formally just encodes the assumption that the sound poles live far from the two poles close to origin. While this is a relatively simple limit to illustrate the qualitative behavior of the isolated two pole sector, we must emphasize that this limit will not reproduce quantitatively the mapping (2.19) exactly, and that is because there are higher order effects of the coupling to the sound sector which should be more carefully disentangled. It will be however a helpful illustration of the dynamics of the low frequency sector. The two currents remaining $J_{1,2}$ are then the momentum current density $\delta\pi_x^{(0)}$ and the parity-odd charge density $\delta n^{(S)}$.

The decoupled system then takes the form

$$M = \begin{pmatrix} 0 & AG\bar{\mu}/2 \\ -\frac{AG\bar{\mu}}{(\bar{\epsilon} + \bar{\rho})\alpha_n} & D_\rho G^2 \end{pmatrix} = \begin{pmatrix} 0 & AG\bar{\mu}/2 \\ -\frac{2D_\rho G\Gamma_d}{A\bar{\mu}} & D_\rho G^2 \end{pmatrix}, \quad (2.78)$$

while the total current of interest is $J = \sigma_Q E_x + \omega_p^2 \delta\pi_x^{(0)} - \frac{\bar{\mu}A}{2} \omega_p^2 D_\rho G \delta n^{(S)}$. Thus, we deduce from this that $Z_{\text{eff}} = \omega_p^2$ while the effective momentum relaxation rates and effective couplings are

$$\begin{aligned} \Omega &= D_\rho G^2 \left[1 - D_\rho \Gamma_d \right], \\ \Gamma &= (D_\rho G)^2 \Gamma_d, \\ \omega_0^2 &= D_\rho G^2 \Gamma_d \left[1 - (D_\rho G)^2 + D_\rho^3 G^2 \Gamma_d \right]. \end{aligned} \quad (2.79)$$

¹⁷To take this limit carefully, one needs to rescale the momentum modes $\delta e^{(C)}, \delta\pi_x^{(C)}$ by a factor of c_s^2 beforehand.

As expected, there is a discrepancy between Eqs. (2.19) and Eqs. (2.79) which just highlights that the limit $c_s \rightarrow \infty$ should be refined. However, this correctly predicts the leading order in A of every coefficient and gives a very close, qualitative estimate of the corrections at the next order.

Chapter 3

Relativistic hydrodynamics in a periodic potential

Attribution

This chapter was published as a journal article under the title “Hydrodynamics of a relativistic charged fluid in the presence of a periodically modulated chemical potential” in the journal *Scipost Physics*, volume 16, issue 1 (2024), together with Koenraad Schalm.

3.1 Introduction

In considering the quantum mechanical wave function of a single electron in a lattice of atoms Bloch had the insight that one should expand the wavefunction in a manner consistent with the discrete periodicity¹

$$\begin{aligned}\Psi(x) &= \int_{-\frac{\pi}{L}}^{\frac{\pi}{L}} dk e^{ikx} u_k(x) = \sum_n \int_{-\frac{\pi}{L}}^{\frac{\pi}{L}} dk e^{i(k + \frac{2n\pi}{L})x} u_n(k), \\ u_k(x+L) &= u_k(x).\end{aligned}\tag{3.1}$$

The novel part of Bloch was its application to quantum wavefunctions rather than waves in general. How waves propagate in periodic structures was already considered by Newton, and that waves in periodic structures exhibit peculiar interference phenomena

¹The Fourier transform here is chosen with a different convention than the traditional physics convention $f(x) = \int \frac{dk}{2\pi} \hat{f}(k) e^{ikx}$. This prevents a proliferation of 2π -factors in non-linear terms in dynamical fluctuation equations.

that we now know as level repulsion/Umklaup/gap opening at Brillouin zone boundaries or Bragg reflection from point-like lattices was already recognized by Kelvin in the 1880s [176]. In electrical engineering the propagation of electromagnetic waves in periodic structures was [177], and is an important topic, see *e.g.*, [178].² Also sound waves in lattices were considered from the earliest days up to today, see *e.g.*, [179].

Sound waves, however, are hydrodynamic fluctuations – a long-time long-wavelength perturbation around thermodynamic equilibrium of a conserved charge associated to a global symmetry – and in that sense differ from electromagnetic waves or single particle wavefunctions in that the fundamental equations of motion, *i.e.*, the hydrodynamic conservation laws, are non-linear. The wave-like fluctuations propagate on a background that is itself a full (equilibrium) solution to the non-linear set of equations, and through the non-linearity the properties of the fluctuating waves depend on this background solution. Though gradients are energetically disfavored, through external forcing the equilibrium background can be imprinted with a spatially varying temperature $T(x)$, pressure $P(x)$, or chemical potential $\mu(x)$. Due to the non-linear coupling between fluctuations and the background in hydrodynamics, the wave propagation properties can be self-consistently determined from the (spatially varying) background. This was elucidated particularly clearly in recent years in the context of electron hydrodynamics in systems with random charge impurities [180, 115]. Such charge disorder is encoded in a spatially varying chemical potential with average $\mathbb{E}[\mu(x)] = \mu_0$ and variance $\mathbb{E}[\mu(x)\mu(y)] - \mathbb{E}[\mu(x)]\mathbb{E}[\mu(y)] = \sigma_\mu^2 \delta(x - y)$. Quantum mechanical single particle electron motion in the presence of random impurities is a classic condensed matter problem. As Anderson showed, the random wavefunction interference is essentially uniformly destructive; at low temperatures all motion is inhibited and the system becomes an insulator. In the hydrodynamic regime, however, *i.e.*, in a situation where many electrons collectivize to a classical fluid rather than a quantum mechanical wave, the conductivity rather strikingly remains finite indicating the existence of an “incoherent metal” state [115]. Observing this electron hydrodynamics in sufficiently pure 2D systems is currently actively pursued, see *e.g.*, [181] or [182], references therein and the recent review [183].

Here we study not hydrodynamics with random spatial disorder but with strictly periodic modulations of the background, *i.e.*, a lattice. Moreover, we also consider hydrodynamics of a charged rather than a neutral fluid with an eye towards condensed matter systems. Compared to the many existing studies on sound waves in periodic structures, the presence of electromagnetic charge as an additional conserved quantum number changes the fluctuating wave response fundamentally. This is again due to the non-linear nature of the hydrodynamic equations. At finite chemical potential sound mixes with charge diffusion. In a companion article we focus on the significant consequences of this cross-coupling of Bloch modes in a lattice for the measurable

²In the latter context Bloch’s theorem is known as Floquet’s theorem. This is not to be confused with periodically driven Floquet systems, though the underlying mathematics of periodic structures is the same after switching “space” and “time”.

DC and AC conductivities in condensed matter systems where this hydrodynamics approach may apply [184]. In this article we provide the deeper hydrodynamic analysis of the full fluctuation spectrum of charged hydrodynamics in a periodic background.

3.2 Hydrodynamics: Set-up and brief review of homogeneous fluctuations

The principal reason that linearized hydrodynamic fluctuations in a lattice background should also be expanded in Bloch modes has already been emphasized: the essence is wave propagation in a periodic structure. Waves are described by coupled first order differential equations of the form ³

$$(\partial_t + M(x))\phi(x) = 0 . \quad (3.3)$$

If $M(x)$ is periodic $M(x + \frac{2\pi}{G}) = M(x)$, then $\phi(x)$ can be decomposed in Bloch waves⁴ $\phi(x) = \sum_n \int_{-G/2}^{G/2} dk \phi_n(k) e^{i(k+nG)x}$. Taking $M(x) = -M_0 \partial_x^2 + A \cos(Gx)$ as canonical example, one can solve Eq. (3.3) perturbatively in A . Diagonalizing M in terms of $\phi_n(k) = \sum_p A^p \phi_n^{(p)}(k)/p!$, the lowest eigenvector to first order in A is

$$\phi_n(k) = \phi_n^{(0)}(k) - \frac{A}{2G(G-2k)M_0} \phi_{n-1}^{(0)}(k) - \frac{A}{2G(G+2k)M_0} \phi_{n+1}^{(0)}(k) + \dots \quad (3.5)$$

in terms of the unperturbed eigenmodes. This mixing between the different Bloch waves is Umklapp. In this article we shall only focus on these perturbative solutions for small lattice amplitudes.

We also already noted that what is special about hydrodynamics is that the fluctuation equations are themselves a linearization expansion of the fundamental non-linear equations. The principle behind the theory of hydrodynamics is local equilibrium and encoded in the local conservation laws of macroscopic charges, *i.e.*, , of a slowly spatially varying energy-momentum tensor $T_{\mu\nu}(x)$ and in the presence of a $U(1)$ charge,

³The standard wave equation $(\partial_t^2 - M_{12}M_{21})\phi_1 = 0$ follows from

$$\begin{pmatrix} \partial_t & M_{12} \\ M_{21} & \partial_t \end{pmatrix} \begin{pmatrix} \phi_1 \\ \phi_2 \end{pmatrix} = 0 . \quad (3.2)$$

⁴The Bloch theorem essentially states that the plane wave decomposition $\phi(x) = \int_{-\infty}^{\infty} dq \phi(q) e^{iqx}$ can be segmented into unit cells $q_n \in [(n-1/2)G, (n+1/2)G]$ where $n \in \mathbb{Z}$ labels each cell – or Brillouin zone – as $\phi(x) = \sum_n \int_{(n-\frac{1}{2})G}^{(n+\frac{1}{2})G} dq_n \phi(q_n) e^{iq_n x}$. The wavevector in each Brillouin zone can be shifted $q_n = k + nG$ with $k \in [-G/2, G/2]$ such that

$$\phi(x) = \sum_n \int_{-G/2}^{G/2} dk \phi(k + nG) e^{i(k+nG)x} \equiv \sum_n \int_{-G/2}^{G/2} dk \phi_n(k) e^{i(k+nG)x} . \quad (3.4)$$

The advantage of this decomposition is that discrete periodic shifts $x \rightarrow x + 2m\pi/G$ relate modes in different Brillouin zones at the same Bloch momentum $k \in \{-G/2, G/2\}$.

a current $J^\mu(x)$. In turn this implies that one can also describe fluid behavior in the presence of a slowly spatially varying external potential whether temperature $T(x)$, pressure $P(x)$, or chemical potential $\mu(x)$.

For simplicity — as well as for the experimental supposition that strongly correlated condensed matter systems can have an emergent Lorentz symmetry at low energies — we shall use $d = 2$ relativistic charged hydrodynamics in this article. In principle all we state also applies to arbitrary d non-relativistic charged hydrodynamics, even if the precise expressions may be subtly different. In relativistic charged hydrodynamics the dynamical equations are simply the conservation equation of the energy-momentum tensor and the charge-current

$$\partial_\mu T^{\mu\nu} = F_{\text{ext}}^{\nu\rho} J_\rho, \quad \partial_\mu J^\mu = 0. \quad (3.6)$$

Here we have allowed for an external electromagnetic field strength $F_{\text{ext}}^{\mu\nu} = \partial^\mu A_{\text{ext}}^\nu - \partial^\nu A_{\text{ext}}^\mu$ in terms of a local external vector potential. In this paper, we will be interested in taking $A_{\mu,\text{ext}} = (\mu_{\text{ext}}(x), 0, 0)$ with $\mu_{\text{ext}}(x)$ a periodic function. Though again, in principle our results also hold for a spatially varying (external) pressure (see *e.g.*, [185]), or a spatially varying (external) temperature.⁵

The dynamical variables of the fluid are the temperature T , the unit timelike velocity vector $u^\mu = (1, v^i)/\sqrt{1 - v^2}$, and the chemical potential μ . Away from equilibrium, the conserved currents in our theory — which we assumed to be parity-invariant, see [186] for more general cases — are given by the constitutive relations at first order in gradients in Landau frame

$$T^{\mu\nu} = \epsilon u^\mu u^\nu + P \Delta^{\mu\nu} - \eta \Delta^{\mu\rho} \Delta^{\nu\sigma} (\partial_\rho u_\sigma + \partial_\sigma u_\rho) - \Delta^{\mu\nu} (\zeta - 2\eta/d) \partial_\rho u^\rho, \quad (3.7a)$$

$$J^\mu = n u^\mu - \sigma_Q \Delta^{\mu\nu} [T \partial_\nu (\mu/T) - F_{\nu\rho,\text{ext}} u^\rho]. \quad (3.7b)$$

Here $d = 2$ is the number of spatial dimensions and the shear viscosity η , the bulk viscosity ζ , and the microscopic conductivity σ_Q are hydrodynamic transport coefficients — in principle set by the microscopic details of a given theory, see *e.g.*, [187, 188], in practice phenomenologically determined. $\Delta^{\mu\nu} = \eta^{\mu\nu} + u^\mu u^\nu$ is a projector orthogonal to the fluid velocity. The Landau frame choice is such that at any order in gradients, we have $J^t = n$ and $T^{tt} = \epsilon$.

The above constitutive relations also hold in a static equilibrium background. In a system with Galilean or relativistic Lorentz boost invariance — which we use in this paper — it is convenient to choose the reference frame for which the equilibrium fluid is at rest. In absence of contact to a spatially varying heat bath, the temperature must then also be constant and independent of position. In the presence of a spatially varying

⁵A spatially varying temperature without forcing by contact with a spatially varying heat bath is difficult to have in a static equilibrium configuration, however.

external chemical potential $\mu_{\text{ext}}(x)$, the equilibrium solution to the hydrodynamic equations Eqs. (3.6) is then parametrized as

$$\begin{aligned} v^i &= 0, \quad T(t, x) = \bar{T} = T_0, \quad \mu(t, x) = \bar{\mu}(x) = \mu_{\text{ext}}(x), \\ n(t, x) &= \bar{n}(x), \quad c(t, x) = \bar{c}(x), \quad P(t, x) = \bar{P}(x). \end{aligned} \quad (3.8)$$

In the grand canonical ensemble, the hydrostatic equilibrium yields moreover

$$\nabla_x \bar{P} = \bar{n} \nabla_x \bar{\mu}. \quad (3.9)$$

Throughout this paper we will use the bar notation \bar{X} to denote such static background quantities. For a homogeneous background, they will be spatially constant and we will use a subscript 0 as X_0 to denote them. For spatially varying quantities, we will use superscripts $Y^{(n)}$ to describe higher order (Bloch wave) moments

$$Y(x) = \sum_n \int_{-G/2}^{G/2} dk Y^{(n)}(k) e^{i(k+nG)x}. \quad (3.10)$$

The hydrodynamic equations need to be supplemented by an equilibrium equation of state relating the energy density ϵ , the pressure P and the charge density n to solve in terms of the equilibrium values of T and μ . In this paper, we will be considering a general fluid whose equation of state $P(T, \mu)$ determines the thermodynamic equilibrium of the theory. In Sec. 3.4, we will specialize to conformal systems.

On top of this background, we now consider perturbations $X(t, x) = \bar{X}(x) + \delta X(t, x)$. The conservation equations (3.6) then take the form

$$\partial_t \delta \epsilon + \sigma_Q (\nabla_x \bar{\mu})^2 \delta \lambda_\epsilon = -\sigma_Q (\nabla_x \bar{\mu}) [\nabla_x \delta \lambda_n + \delta E_x] - \nabla_x (\bar{\chi}_{\pi\pi} \delta v_x) + (\nabla_x \bar{P}) \delta v_x, \quad (3.11a)$$

$$\partial_t \delta n - \sigma_Q \nabla_x^2 \delta \lambda_n = \sigma_Q \nabla_x [\delta \lambda_\epsilon \nabla_x \bar{\mu} + \delta E_x] - \nabla_x (\bar{n} \delta v_x), \quad (3.11b)$$

$$\partial_t \delta \pi_x - \hat{\eta} \nabla_x^2 \delta v_x = (\nabla_x \bar{\mu}) \delta n - \nabla_x (\bar{n} \delta \lambda_n) - \nabla_x (\bar{\chi}_{\pi\pi} \delta \lambda_\epsilon) - \bar{n} \delta E_x, \quad (3.11c)$$

$$\partial_t \delta \pi_y - \eta \nabla_x^2 \delta v_y = 0, \quad (3.11d)$$

which can further be simplified into

$$\partial_t \delta \epsilon + \sigma_Q (\nabla_x \bar{\mu})^2 \delta \lambda_\epsilon = -\sigma_Q (\nabla_x \bar{\mu}) \delta E_x^{\text{tot}} - \bar{\chi}_{\pi\pi} \nabla_x \delta v_x - (\nabla_x \bar{\epsilon}) \delta v_x, \quad (3.12a)$$

$$\partial_t \delta n - \sigma_Q \nabla_x \delta E_x^{\text{tot}} = \sigma_Q \nabla_x (\delta \lambda_\epsilon \nabla_x \bar{\mu}) - \nabla_x (\bar{n} \delta v_x), \quad (3.12b)$$

$$\partial_t \delta \pi_x - \hat{\eta} \nabla_x^2 \delta v_x = -\bar{n} \delta E_x^{\text{tot}} - \nabla_x (\bar{\chi}_{\pi\pi} \delta \lambda_\epsilon) + (\nabla_x \bar{\epsilon}) \delta \lambda_\epsilon, \quad (3.12c)$$

$$\partial_t \delta \pi_y - \eta \nabla_x^2 \delta v_y = 0. \quad (3.12d)$$

In the previous expression, we have defined a renormalized viscosity $\hat{\eta} \equiv \zeta + \frac{2(d-1)}{d} \eta$. We also introduced the ‘‘potential’’-variations $\delta \lambda_\epsilon \equiv \frac{\delta T}{T_0}$ and $\delta \lambda_n \equiv \delta \mu - \frac{\bar{\mu}}{T_0} \delta T$ conjugate to the energy and charge densities. The velocity perturbations δv_i are conjugate to the momenta $\delta \pi_i$. These are not independent due to the hydrodynamic local equilibrium

condition. The momenta $\delta\pi_i$ are related to the velocity perturbations δv_i through the constitutive relations $\delta\pi_i = \delta T^{ii} = \bar{\chi}_{\pi\pi}\delta v_i$ at this order.⁶ Similarly, the charge and energy densities $\delta n, \delta\epsilon$ are related to the sources $\delta\lambda_n, \delta\lambda_\epsilon$ through the thermodynamic susceptibilities derived in Appendix 3.A. Using that $\bar{\chi}_{\pi\pi} = \bar{\epsilon} + \bar{P}$, we can use the fundamental thermodynamic relation $\bar{\epsilon} + \bar{P} = T_0\bar{s} + \bar{\mu}\bar{n}$ and the first law of thermodynamics to relate

$$\delta P = \frac{\bar{\chi}_{\pi\pi} - \bar{\mu}\bar{n}}{T_0}\delta T + \bar{n}\delta\mu = \bar{\chi}_{\pi\pi}\delta\lambda_\epsilon + \bar{n}\delta\lambda_n. \quad (3.13)$$

Finally, we introduced an external electric field $\delta E_x \equiv \partial_t \delta A_{x,\text{ext}}$ and in (3.12) we introduced the total electric field $\delta E_x^{\text{tot}} \equiv \delta E_x + \nabla_x \delta\lambda_n$. In what follows, we will be interested in the hydrodynamics response of the modes $\{\delta\epsilon, \delta n, \delta\pi_x, \delta\pi_y\}$ obeying the equations (3.12). In the following sections, we will use the static susceptibilities relating the potentials $\{\delta\lambda_\epsilon, \delta\lambda_n, \delta v_x, \delta v_y\}$ to the densities $\{\delta\epsilon, \delta n, \delta\pi_x, \delta\pi_y\}$ to express the equations in terms of the latter only, *i.e.*, we work in the microcanonical ensemble.

3.2.1 Hydrodynamic fluctuations in a homogeneous background

In this section, we first review the hydrodynamics of a long wavelength perturbation above a homogeneous conformal charged fluid. Further details can be found in [189, 119]. Since the background is homogeneous, this means every barred quantity will be a constant $\bar{X} = X_0$. The equations (3.12) decouple into the longitudinal and transverse sectors. We will start by looking at the latter whose equation of motion is simpler. Choosing the wavenumber k_x along the x direction without loss of generality, the transverse fluctuations $\delta\pi_y$ obey

$$\partial_t \delta\pi_y(t, k) + D_\perp k^2 \delta\pi_y(t, k) = 0, \quad D_\perp \equiv \eta/\chi_{\pi\pi,0}. \quad (3.14)$$

This is a simple diffusion equation with the shear diffusion constant D_\perp . We can now use the (Fourier-)Laplace transform⁷ such that the transverse equation of motion becomes

$$\left(-i\omega + D_\perp k^2\right) \delta\hat{\pi}_y(\omega, k) = \delta\pi_y(t=0, k) = \chi_{\pi\pi,0} \delta v_y(t=0, k). \quad (3.15)$$

⁶ Formally the susceptibility $\bar{\chi}_{\pi\pi}(x_1, t_2; x_2, t_2) = \frac{\partial}{\partial v_i(x_1, t_1)} \frac{\partial}{\partial v_i(x_2, t_2)} Z(v_i)$ denotes how a local charge density $\pi^i(x_1, t_1)$ is influenced by a (chemical) potential $v_i(x_2, t_2)$ at a different space-time point. Here $Z(v_i)$ is the partition function in the presence of a chemical potential (velocity) v_i for the charge density (momentum) π^i . In the hydrodynamic limit, however, one assumes that all equilibrium ($t_1 + t_2 = 0$) static ($t_1 - t_2 \rightarrow \infty$) charges depend only *locally* on the potentials $\pi^i(v_i(x))$. In a homogeneous equilibrium background where $\bar{\chi}_{\pi\pi}^{\text{static}} = \chi^{\text{static}}(x_1 - x_2)$ this is equivalent to approximating the static susceptibility with its constant part $\bar{\chi}_{\pi\pi}^{\text{static}}(x_1 - x_2) = \chi_{\pi\pi,0} + (x_1 - x_2)\partial_x \bar{\chi}_{\pi\pi}(0) = \chi_{\pi\pi,0} + \dots$. We discuss this in more detail below and in Appendix 3.A.

⁷The Laplace transform is required to have a well-defined right-hand side to our linearized equations. One could also just use a Fourier transform while setting external sources. More details can be found in [189, 119].

The solution is formally given in terms of the retarded correlator for the transverse momentum which is defined as

$$\delta\pi_y(t, k) = \int_{-\infty}^{\infty} dt' G_{\pi_y\pi_y}^R(t-t', k) \delta v_y(t', k). \quad (3.16)$$

Using that $\hat{G}_{\pi_y\pi_y}^R(\omega=0, k) = \chi_{\pi\pi,0}$ in the hydrodynamic long wavelength limit (*i.e.*, , we only keep the leading term in an expansion in k ; see footnote 6.), we have

$$\hat{G}_{\pi_y\pi_y}^R(\omega, k) = \chi_{\pi\pi,0} \frac{D_{\perp} k^2}{D_{\perp} k^2 - i\omega}. \quad (3.17)$$

The correlator exhibits a pole on the imaginary axis at $\omega = -iD_{\perp} k^2$ indicative of a purely diffusive mode.

We can now carry the same analysis in the longitudinal sector where the dynamical equations are coupled. Denoting $\delta\phi_a(t, k) = (\delta\epsilon(t, k), \delta n(t, k), \delta\pi_x(t, k))$, the dynamical equations can be written succinctly as

$$\partial_t \delta\phi_a(t, k) + M_{ab}(k) \delta\phi_b(t, k) = 0. \quad (3.18)$$

We can once again use a (Fourier)-Laplace transform to rewrite this system of equations as

$$\hat{K}(\omega, k) \cdot \delta\phi(\omega, k) = \delta\phi(t=0, k) \quad (3.19)$$

with the dynamical matrix

$$\hat{K}(\omega, k) \equiv -i\omega \mathbb{1}_3 + M(k) = \begin{pmatrix} -i\omega & 0 & ik \\ -\frac{\chi_{n\epsilon,0}}{d_{\chi}} \sigma_Q k^2 & \frac{\chi_{\epsilon\epsilon,0}}{d_{\chi}} \sigma_Q k^2 - i\omega & ik \frac{n_0}{\chi_{\pi\pi,0}} \\ ik \frac{\chi_{nn,0} \chi_{\pi\pi,0} - n_0 \chi_{n\epsilon,0}}{d_{\chi}} & ik \frac{n_0 \chi_{\epsilon\epsilon,0} - \chi_{n\epsilon,0} \chi_{\pi\pi,0}}{d_{\chi}} & \frac{\hat{\eta}}{\chi_{\pi\pi,0}} k^2 - i\omega \end{pmatrix}, \quad (3.20)$$

where we defined $d_{\chi} = \chi_{\epsilon\epsilon,0} \chi_{nn,0} - (\chi_{n\epsilon,0})^2$ the determinant of the susceptibility matrix in the ϵ, n sector. The poles of the Green's functions associated to this system are the frequencies for which $\det \hat{K} = 0$. The roots of this polynomial in the long wavelength limit are a diffusion mode (originating in charge diffusion) and two propagating sound modes

$$\omega_D = -iD_{\rho}^0 k^2 + \mathcal{O}(k^3), \quad \omega_{\pm} = \pm c_s^0 k - \frac{i}{2} D_s^0 k^2 + \mathcal{O}(k^3), \quad (3.21)$$

where the speed of sound and the two diffusion constants are defined as

$$D_{\pi}^0 \equiv \frac{\hat{\eta}}{\chi_{\pi\pi,0}}, \quad (c_s^0)^2 \equiv \frac{n_0^2 \chi_{\epsilon\epsilon,0} + (\chi_{\pi\pi,0})^2 \chi_{nn,0} - 2n_0 \chi_{\pi\pi,0} \chi_{n\epsilon,0}}{\chi_{\pi\pi,0} d_{\chi}}, \quad (3.22a)$$

$$D_{\rho}^0 \equiv \frac{\sigma_Q (\chi_{\pi\pi,0})^2}{n_0^2 \chi_{\epsilon\epsilon,0} + (\chi_{\pi\pi,0})^2 \chi_{nn,0} - 2n_0 \chi_{\pi\pi,0} \chi_{n\epsilon,0}}, \quad D_s^0 \equiv D_{\pi}^0 - D_{\rho}^0 + \sigma_Q \frac{\chi_{\epsilon\epsilon,0}}{d_{\chi}}. \quad (3.22b)$$

Note that for $n_0 = 0$ the speed of sound reduces to the familiar expression $c_s^2 = \delta P / \delta \epsilon$ (using Eq. (3.13) and the inverse susceptibility matrix). Similarly to what we did in the transverse sector, we can compute the retarded Green's functions by inverting the dynamical system [119]

$$\hat{G}_L^R(\omega, k) = \hat{K}^{-1} \cdot \hat{K}(\omega = 0) \cdot \chi_{L,0} = (\mathbb{1}_3 + i\omega \hat{K}^{-1}) \cdot \chi_{L,0}, \quad (3.23)$$

where the middle equation enforces the condition that the static $\omega = 0$ part reduces to the longitudinal part of the thermodynamic susceptibility matrix $\chi_{L,0}$. The various correlators can then be obtained

$$\hat{G}_{\epsilon\epsilon}^R(\omega, k) = \frac{k^2 \chi_{\pi\pi,0}}{d(\omega, k)} \left[\frac{(c_s^0)^2 \chi_{\epsilon\epsilon,0}}{\chi_{\pi\pi,0}} D_\rho^0 k^2 - i\omega \right], \quad (3.24a)$$

$$\hat{G}_{nn}^R(\omega, k) = \frac{\chi_{\pi\pi,0}}{k^2 d(\omega, k)} \left[(c_s^0)^2 D_\rho^0 \left(\chi_{\pi\pi,0} \chi_{nn,0} k^2 - d_\chi i\omega D_\pi^0 k^2 - d_\chi \omega^2 \right) - i\omega n_0^2 \right], \quad (3.24b)$$

$$\hat{G}_{\pi_x \pi_x}^R(\omega, k) = \frac{k^2}{d(\omega, k)} \left[(c_s^0)^2 \left(\chi_{\pi\pi,0} D_\rho^0 k^2 - i\omega (\chi_{\pi\pi,0} + D_\rho^0 \chi_{\epsilon\epsilon,0} D_\pi^0 k^2) \right) - \chi_{\pi\pi,0} D_\pi^0 \omega^2 \right], \quad (3.24c)$$

$$\hat{G}_{\epsilon n}^R(\omega, k) = \frac{k^2}{d(\omega, k)} \left[(c_s^0)^2 \chi_{n\epsilon,0} D_\rho^0 k^2 - i\omega n_0 \right], \quad (3.24d)$$

with the normalized determinant of the dynamical matrix $d(\omega, k) = i(\omega - \omega_D)(\omega - \omega_+)(\omega - \omega_-)$. The other correlators can be obtained via the Ward identities

$$\hat{G}_{\pi_x \epsilon}^R = \frac{\omega}{k} \hat{G}_{\epsilon\epsilon}^R, \quad \hat{G}_{\pi_x n}^R = \frac{\omega}{k} \hat{G}_{\epsilon n}^R, \quad \hat{G}_{\epsilon \pi_x}^R = \frac{k}{\omega} \hat{G}_{\pi_x \pi_x}^R, \quad (3.25)$$

as well as the Onsager reciprocal relations

$$G_{\pi_x n}^R(\omega, k) = -G_{n \pi_x}^R(\omega, -k), \quad G_{\pi_x \epsilon}^R(\omega, k) = -G_{\epsilon \pi_x}^R(\omega, -k), \quad G_{\epsilon n}^R(\omega, k) = G_{n \epsilon}^R(\omega, -k). \quad (3.26)$$

3.3 Hydrodynamic fluctuations in a lattice background

We shall now redo the fluctuation analysis in a lattice background. This lattice will be sourced by a periodically modulated external chemical potential

$$\mu_{\text{ext}}(x) = \mu_0 \left(1 + A \cos(Gx) \right), \quad (3.27)$$

such that the fluid is still at rest and in local equilibrium, but all its constituents will now slowly vary in space. In particular, this last assumption of local equilibrium means

that the scale of spatial fluctuations of μ_{ext} and other local quantities must be larger than the local equilibration scale. Therefore, we must have $G \lesssim \mu, T$.⁸

This lattice background manifestly breaks translation invariance. Momentum is therefore no longer a strictly conserved quantity. However, as the breaking is sourced through a hydrodynamic variable and as we assume it is weakly broken, we can still use hydrodynamic analysis [115, 180, 88, 125]. The spectral function of the associated operator to this deformation — the charge density $J^t = n$ —, evaluated in the homogeneous background, can be used to compute the momentum relaxation rate. This is known as the memory matrix formalism and was thoroughly detailed in *e.g.*, [133, 180]. The momentum relaxation rate induced by an operator \mathcal{O} sourced at wavenumber G with strength g takes the form [87]

$$\Gamma_{\text{mem.}}(g, G) \equiv \frac{g^2 G^2}{\bar{\chi}_{\pi\pi}} \lim_{\omega \rightarrow 0} \frac{\text{Im} \hat{G}_{\mathcal{O}\mathcal{O}}^R(\omega, k = G)}{\omega}. \quad (3.28)$$

For a cosine ionic lattice Eq. (3.27), $g = \mu_0 A/2$, and we have two deformation sources, one copy each at $\pm G$ — noting that the expression (3.28) is parity invariant in G . Therefore, the memory matrix relaxation rate for an ionic lattice is

$$\Gamma_{\text{ionic, mem.}} = \frac{\mu_0^2 A^2}{2} \left[\frac{(\chi_{nn,0} - n_0 \chi_{n\epsilon,0} / \chi_{\pi\pi,0})^2}{\sigma_Q \chi_{\pi\pi,0}} + D_\pi^0 G^2 \left(\frac{\chi_{n\epsilon,0}}{\chi_{\pi\pi,0}} \right)^2 \right]. \quad (3.29)$$

It will prove useful to separate the terms according to their scaling with G in this expression as $\Gamma_{\text{ionic, mem.}} = \Gamma_\eta + \Gamma_d$ with

$$\Gamma_\eta = \frac{\mu_0^2 A^2}{2} \left(\frac{\chi_{n\epsilon,0}}{\chi_{\pi\pi,0}} \right)^2 D_\pi^0 G^2, \quad \Gamma_d = \frac{\mu_0^2 A^2}{2} \frac{(\chi_{nn,0} - n_0 \chi_{n\epsilon,0} / \chi_{\pi\pi,0})^2}{\sigma_Q \chi_{\pi\pi,0}}. \quad (3.30)$$

Using the Einstein relations Eq. (3.22a), together with $\chi_{\pi\pi,0} = \epsilon_0 + P_0$, $\chi_{\pi n,0} = n_0$ these are a convective shear drag term Γ_η and an intrinsic diffusive term [87, 86, 115]

$$\Gamma_\eta = \frac{\mu_0^2 A^2}{2} \frac{\hat{\eta} G^2}{\epsilon_0 + P_0} \left(\frac{\chi_{n\epsilon,0}}{\epsilon_0 + P_0} \right)^2, \quad \Gamma_d = \frac{\mu_0^2 A^2}{2} \frac{1}{\sigma_Q} \frac{((\epsilon_0 + P_0) \chi_{nn,0} - n_0 \chi_{n\epsilon,0})^2}{(\epsilon_0 + P_0)^3}. \quad (3.31)$$

We will recover this same expression for the momentum relaxation time from our Bloch wave analysis. This analysis improves on the memory matrix technique by understanding how all the hydrodynamic fluctuations behave.

In a periodically modulated background, every background quantity in local thermal equilibrium $\bar{X}(x) = \bar{X}(\bar{\mu}(x), T_0)$ now admits Fourier series expansions

$$\bar{X}(x) = \sum_n e^{inGx} \bar{X}^{(n)}. \quad (3.32)$$

⁸For this reason our analysis does not immediately apply to graphene or other sufficiently pure semimetals as there, the scale where hydrodynamics applies is much larger than the atomic lattice scale. One would need to have a periodically undulating graphene sheet or otherwise externally imposed periodicity for this analysis to apply.

In order to apply the same method as in the previous section, we must first know how to relate perturbations of sources and responses in this new background. Because the background is static, the susceptibilities will also be static. However, because the thermodynamic quantities are position dependent and have non-vanishing Bloch modes, the susceptibilities will now also be position/momentum dependent. In principle, they depend on *two* Bloch momenta. However, in the slowly varying hydrodynamic background we may approximate them as local functions $\chi(x)$ (see also footnote 6) that follow the expansion (3.32).⁹ The relation between perturbations in the sources and responses is then

$$\delta\phi_A(t, x) = \bar{\chi}_{AB}(x)\delta\lambda_B(t, x). \quad (3.33)$$

The breaking of isometry by the lattice means there is no longer a decoupling between a longitudinal and transverse sector, *i.e.*, ϕ_A, λ_A collectively denote the responses $\{\delta\epsilon, \delta n, \delta\pi_x, \delta\pi_y\}$ and the sources $\{\delta\lambda_\epsilon, \delta\lambda_n, \delta v_x, \delta v_y\}$. Both perturbations are likewise expanded on Bloch modes matching the discrete lattice symmetry

$$\delta X_A(t, x) = \sum_n \int_{-\frac{G}{2}}^{\frac{G}{2}} dk e^{i(k+nG)x} \delta X_A^{(n)}(t, k), \quad (3.34)$$

for $X \in \{\delta\phi_A, \delta\lambda_A\}$. As a result of the spatial dependence in the background different Bloch modes of the perturbations cross couple

$$\delta\phi_A^{(n)}(t, k) = \sum_m \bar{\chi}_{AB}^{(m)} \delta\lambda_B^{(n-m)}(t, k). \quad (3.35)$$

The dynamical equation can then be written, after Laplace transform, as

$$\hat{K}^{(n,m)}(\omega, k) \cdot \delta\hat{\phi}^{(m)}(\omega, k) = \delta\phi^{(n)}(t=0, k). \quad (3.36)$$

The indices n, m indicate the Brillouin zones while each block $\hat{K}^{(n,m)}$ is a 4×4 matrix. The diagonal blocks $\hat{K}^{(n,n)}$ correspond to the couplings between the responses in the same Brillouin zone while the off-diagonal blocks will account for coupling between different zones. These are due to the presence of the lattice and will vanish in the limit where the lattice amplitude goes to zero $A \rightarrow 0$. We will be interested in a weak lattice where the lattice amplitude A is very small, and keep only terms up to order A^2 .¹⁰ The coupling between two modes with momenta $k + nG$ and $k + mG$ for $m > n$ will be of order A^{m-n} . Moreover, within perturbation theory, terms of order A in the off-diagonal

⁹ One can analyze the general behavior of two-point functions under lattice symmetries of the background [117]. Given a two-point function $G(x, y)$, one can pick a center of mass point $x = r + \delta$, $y = r - \delta$. Under the lattice symmetry, $r \rightarrow r + L$, but δ is unchanged. Then $G(x, y) = G(r = \frac{x+y}{2}, \delta) = G(r + L, \delta)$ can be expanded in Bloch modes $G(r, \delta) = \sum_n \int dk G^{(n)}(k, \delta) e^{i(k+2n\pi/L)r}$. For hydrodynamic susceptibilities $\chi = G_{Jt Jt}$ we assume that they are local, *i.e.*, we can restrict to $\delta = 0$ to leading order. In a strictly periodic background there is no structure beyond the lattice scale and hence only the $\chi^{(n)}(k=0, \delta=0)$ modes are non-vanishing.

¹⁰ For a strong lattice or strong isotropy breaking the transport coefficients become tensors and this requires an independent analysis.

blocks will contribute to the same order as terms of order A^2 in the diagonal blocks; we can therefore drop terms of order A^2 and higher in the off-diagonal blocks. This also means we can consider “nearest-neighbor” interactions only – by which we mean off-diagonal terms with $m = n \pm 1$. In the long wavelength approximation we therefore can narrow our study to the three momenta $k + nG$ with $n \in \{-1, 0, 1\}$, *i.e.*, the first three Brillouin zones. It is important to note that the diagonal terms even in the $n = 0$ Brillouin zone can still have non-trivial higher order corrections in A . A similar setup was already considered in [190].

We will discuss this momentarily. We shall, however, first make one more simplification. It will prove more useful to use the equations in terms of the sources $\delta\lambda_A$ with

$$\hat{\mathcal{K}}^{(n,m)}(\omega, k) \cdot \delta\hat{\lambda}^{(m)}(\omega, k) = \delta\lambda^{(n)}(t=0, k), \quad (3.37)$$

where we can relate the two matrices using the susceptibility matrix χ by $\hat{\mathcal{K}} = \hat{K} \cdot \chi$. In this language, the $A = 0$ dynamical matrix (3.20) takes the form

$$\hat{\mathcal{K}} = \begin{pmatrix} -i\omega\chi_{\epsilon\epsilon,0} & -i\omega\chi_{\epsilon n,0} & ik\chi_{\pi\pi,0} & 0 \\ -i\omega\chi_{n\epsilon,0} & \sigma_Q k^2 - i\omega\chi_{nn,0} & ikn_0 & 0 \\ ik\chi_{\pi\pi,0} & ikn_0 & \hat{\eta}k^2 - i\omega\chi_{\pi\pi,0} & 0 \\ 0 & 0 & 0 & \eta k^2 - i\omega \end{pmatrix}. \quad (3.38)$$

This choice seems to a priori obfuscate the relationship between modes more than (3.20) due to the off-diagonal frequency dependency. However, because χ is a static matrix, the determinants of $\hat{\mathcal{K}}$ and \hat{K} have the same poles in the complex frequency plane, and in the lattice case where the inverse susceptibilities present in (3.20) are more complicated, this form will prove clearer.

In the next few sections, we will determine this matrix $\hat{\mathcal{K}}$ in a lattice background with lattice vector G for both finite k momentum fluctuations and $k = 0$ momentum fluctuations to order A^2 in the lattice amplitude. As standard, the zeroes of its determinants will indicate the position of the dynamical modes of this system. We will then compute the conductivity as an example of how the various correlators are modified by the presence of the lattice.

3.3.1 Finite momentum aligned fluctuation spectrum

For a generic fluctuation with momentum k , even in the long wavelength limit, the fluctuation matrix truncated to nearest neighbor cross-coupling sufficient for the leading order in A correction will be a 12×12 matrix. This is because there is no decoupling into transverse and longitudinal sectors for a generic momentum. However, if one chooses the fluctuation momentum k to align with the lattice wavevector, a decoupling does occur. Choosing k along a lattice vector defined to be in the x -direction,

a parity symmetry in the y -direction remains. The even and odd sectors decouple into the longitudinal and transverse parts:

$$\delta Y_L = \left\{ \delta \lambda_\epsilon^{(-1)}, \delta \lambda_n^{(-1)}, \delta v_x^{(-1)}, \delta \lambda_\epsilon^{(0)}, \delta \lambda_n^{(0)}, \delta v_x^{(0)}, \delta \lambda_\epsilon^{(1)}, \delta \lambda_n^{(1)}, \delta v_x^{(1)} \right\}, \quad (3.39a)$$

$$\delta Y_T = \left\{ \delta v_y^{(-1)}, \delta v_y^{(0)}, \delta v_y^{(1)} \right\}. \quad (3.39b)$$

The dynamical matrix is then diagonal in a 9×9 and a 3×3 block.

Transverse sector

Starting with the transverse sector, the associated dynamical matrix $\hat{\mathcal{K}}_T$ is

$$\hat{\mathcal{K}}_T = \begin{pmatrix} \eta(k-G)^2 - i\omega\chi_{\pi\pi}^{(0)} & -i\omega\chi_{\pi\pi}^{(-1)} & 0 \\ -i\omega\chi_{\pi\pi}^{(1)} & \eta k^2 - i\omega\chi_{\pi\pi}^{(0)} & -i\omega\chi_{\pi\pi}^{(-1)} \\ 0 & -i\omega\chi_{\pi\pi}^{(1)} & \eta(k+G)^2 - i\omega\chi_{\pi\pi}^{(0)} \end{pmatrix}. \quad (3.40)$$

In the hydrodynamic approximation the local static susceptibility $\bar{\chi}_{\pi\pi}(x) = \frac{\partial \pi^x}{\partial v^x}(\mu(x))$ (see footnote 6 & 9) now also depends on the lattice amplitude as can be seen from its Bloch components

$$\chi_{\pi\pi}^{(0)} = \frac{G}{2\pi} \int_{-\frac{\pi}{G}}^{\frac{\pi}{G}} dx \bar{\chi}_{\pi\pi}(\bar{\mu}(x)) \quad (3.41a)$$

$$= \frac{G}{2\pi} \int_{-\frac{\pi}{G}}^{\frac{\pi}{G}} dx \left[\chi_{\pi\pi,0} + \mu_0 A \cos(Gx) \frac{\partial \chi_{\pi\pi,0}}{\partial \mu_0} + \frac{\mu_0^2 A^2}{2} (\cos(Gx))^2 \frac{\partial^2 \chi_{\pi\pi,0}}{\partial \mu_0^2} + \dots \right] \quad (3.41b)$$

$$= \chi_{\pi\pi,0} + \frac{\mu_0^2 A^2}{4} \frac{\partial^2 \chi_{\pi\pi,0}}{\partial \mu_0^2} \quad (3.41c)$$

$$\equiv \chi_{\pi\pi,0} + A^2 \chi_{\pi\pi,2}^{(0)}, \quad (3.41d)$$

$$\chi_{\pi\pi}^{(1)} = \frac{G}{2\pi} \int_{-\frac{\pi}{G}}^{\frac{\pi}{G}} dx e^{-iGx} \bar{\chi}_{\pi\pi}(\bar{\mu}(x)) = \frac{\mu_0 A}{2} \frac{\partial \chi_{\pi\pi,0}}{\partial \mu_0} \equiv A \chi_{\pi\pi,1}^{(1)} = A \chi_{\pi\pi,1}^{(-1)}, \quad (3.41e)$$

$$\chi_{\pi\pi}^{(2)} = \frac{\mu_0^2 A^2}{8} \frac{\partial^2 \chi_{\pi\pi,0}}{\partial \mu_0^2} \equiv A^2 \chi_{\pi\pi,2}^{(2)} = A^2 \chi_{\pi\pi,2}^{(-2)} = \frac{1}{2} A^2 \chi_{\pi\pi,2}^{(0)}. \quad (3.41f)$$

In the previous expression, we have introduced the expansion for a given Bloch mode $X^{(n)} = \sum_m X_m^{(n)} A^m$. Note that by definition, $X_0^{(0)} = X_0$ which we will keep this way.

The poles of the transverse fluctuation matrix can now be found easily, and we

have

$$\omega_{T,-1} = -iD_{\perp}(k-G)^2 \left[1 - A^2 \left(\frac{\chi_{\pi\pi,2}^{(0)}}{\chi_{\pi\pi,0}} - \chi_{\pi\pi,1}^{(1)} \chi_{\pi\pi,1}^{(-1)} \frac{(k-G)^2}{G(G-2k)} \right) \right], \quad (3.42a)$$

$$\omega_{T,0} = -iD_{\perp}k^2 \left[1 - A^2 \left(\frac{\chi_{\pi\pi,2}^{(0)}}{\chi_{\pi\pi,0}} - \chi_{\pi\pi,1}^{(1)} \chi_{\pi\pi,1}^{(-1)} \frac{2k^2}{(G-2k)(G+2k)} \right) \right], \quad (3.42b)$$

$$\omega_{T,1} = -iD_{\perp}(k+G)^2 \left[1 - A^2 \left(\frac{\chi_{\pi\pi,2}^{(0)}}{\chi_{\pi\pi,0}} - \chi_{\pi\pi,1}^{(1)} \chi_{\pi\pi,1}^{(-1)} \frac{(k+G)^2}{G(G+2k)} \right) \right]. \quad (3.42c)$$

The poles remain purely diffusive, and we see that the only effect of the lattice on the transverse sector is to renormalize the shear diffusion constants D_{\perp} at order $\mathcal{O}(A^2)$. We do see an Umklapp-like pole in the dispersion relation at the edges of the Brillouin zones $k = \pm \frac{G}{2}$. Formally, this value of k is outside of the regime of validity of the expansion in small A . One has to resum the perturbative expansion and then one finds level repulsion, as is well known; see also the discussion at the beginning of Sec. 3.3.2 and footnote 11. It is distinct from conventional Umklapp, however, in that it is not level-repulsion in the dispersion (the real part of the pole in the complex frequency plane), but in the width of the fluctuation. At the edge of the Brillouin zone the width narrows and vanishes at exactly $k = \pm \frac{G}{2}$.

Longitudinal sector

The longitudinal sector is characterized by a 9×9 dynamical matrix $\hat{\mathcal{K}}_L$ of the form of 3×3 blocks

$$\hat{\mathcal{K}}_L = \begin{pmatrix} \hat{\mathcal{K}}_L^{(D)}(\omega, k-G) & \hat{\mathcal{K}}_L^{(OD)}(\omega, k-G, k) & 0 \\ \hat{\mathcal{K}}_L^{(OD)}(\omega, k, k-G) & \hat{\mathcal{K}}_L^{(D)}(\omega, k) & \hat{\mathcal{K}}_L^{(OD)}(\omega, k, k+G) \\ 0 & \hat{\mathcal{K}}_L^{(OD)}(\omega, k+G, k) & \hat{\mathcal{K}}_L^{(D)}(\omega, k+G) \end{pmatrix}. \quad (3.43)$$

The $\mathcal{K}_L^{(OD)}(\omega, k, p)$ block with $k < p$ belongs to the Bloch sector $n = -1$, and the one with $k > p$ to the Bloch sector $n = 1$. In a cosine lattice, however, all background quantities are parity-invariant $X^{(-n)} = X^{(n)}$, and so from here on out, we will only use the $n > 0$

expressions. The 3×3 blocks $\mathcal{K}_L^{(D)}$ and $\mathcal{K}_L^{(OD)}$ are then given by

$$\hat{\mathcal{K}}_L^{(D)}(\omega, k) = \begin{pmatrix} \frac{\mu_0^2 A^2}{2} \sigma_Q G^2 - i\omega \chi_{\epsilon\epsilon}^{(0)} & -i\omega \chi_{ne}^{(0)} & ik \chi_{\pi\pi}^{(0)} \\ -i\omega \chi_{ne}^{(0)} & \sigma_Q k^2 - i\omega \chi_{nn}^{(0)} & ikn^{(0)} \\ ik \chi_{\pi\pi}^{(0)} & ikn^{(0)} & \hat{\eta} k^2 - i\omega \chi_{\pi\pi}^{(0)} \end{pmatrix}, \quad (3.44)$$

$$\hat{\mathcal{K}}_L^{(OD)}(\omega, k, p) = A \begin{pmatrix} -i\omega \chi_{\epsilon\epsilon,1}^{(1)} & \frac{\mu_0 \sigma_Q}{2} p(p-k) - i\omega \chi_{ne,1}^{(1)} & \frac{\mu_0}{2} (ipn_0 + ik \chi_{ne,0}) \\ \frac{\mu_0 \sigma_Q}{2} k(k-p) - i\omega \chi_{ne,1}^{(1)} & -i\omega \chi_{nn,A}^{(1)} & \frac{\mu_0}{2} ik \chi_{nn,0} \\ \frac{\mu_0}{2} (ikn_0 + ip \chi_{ne,0}) & \frac{\mu_0}{2} ip \chi_{nn,0} & -i\omega \chi_{\pi\pi,1}^{(1)} \end{pmatrix}.$$

To leading order in A^2 , the $n=0$ Bloch momenta $X^{(0)}$ still have a dependency in A just as in the previous section.

While difficult, it is possible to find the poles associated to this 9×9 matrix generically. For very small momentum $k = \mathcal{O}(\varepsilon^2)$ and $G = \mathcal{O}(\varepsilon)$, they take the form

$$\omega_{D,n} = -iD_\rho^0 (nG)^2 + \frac{i}{2} \Gamma_d + \dots, \quad (3.45a)$$

$$\omega_{D,0} = -iD_\rho^0 k^2 + \dots, \quad (3.45b)$$

$$\omega_{S,\pm,n} = \pm c_s^0 (k + nG) - \frac{i}{2} D_s^0 G^2 + \dots, \quad (3.45c)$$

$$\omega_{S,\pm,0} = -\frac{i}{2} \Gamma_{\text{ionic,mem.}} \pm c_s^0 k - \frac{i}{2} D_s^0 k^2 + \dots, \quad (3.45d)$$

with $n \in \{-1, 1\}$ and “...” indicate corrections of order $\mathcal{O}(A^2 k)$ and higher. The relaxation rates $\Gamma_d, \Gamma_{\text{ionic,mem.}}$ are of order A^2 and equal to the memory matrix expressions given in Eqs. (3.31).

For large k the expressions are not easy to express. However, we can use the mixing with Umklapped Bloch waves analysis to understand numerical simulations. In the longitudinal sound sector we do observe genuine level repulsion in the modified dispersion relation at the edges of the Brillouin zone. For a visualization in an explicit example later, see Fig. 3.8. There is thus a true sound “band gap”. Sound modes with frequencies $\omega = \pm c_s G/2$ do not exist in this latticized medium. Or more precisely put, sound with wavelengths $\lambda = 2\pi k \ll G$ propagate normally with essentially unaltered speed of sound $c_s = \frac{d\omega}{dk} = c_s^0$. As the wavelength approaches the edges of the Brillouin zone, sound slows down, and right at the edge of Brillouin zone for $\lambda = (2\pi)\frac{G}{2}$, they cease to propagate as the group velocity $c_s = \frac{d\omega}{dk}|_{k=G/2} = 0$. The medium is opaque to sound at these wavelengths. Considering possible applications to condensed matter physics, we note for completeness that all these results are of course derived assuming a fixed infinitely stiff external lattice. Lattice vibrations/phonons are not taken into account. Were one to include these in the analysis, this will likely make the level repulsion and opaqueness to sound less sharp.

3.3.2 The $k = 0$ zero momentum perturbation

The $k = 0$ zero momentum is special and asks for a separate discussion. This is for three reasons. Again in the context of condensed matter physics, the $k = 0$ fluctuation describes the homogeneous responses of the system to outside probes. These are the observed macroscopic thermal and electrical conductivities, and warrant being singled out. Secondly, we shall see that in the limit of $k \rightarrow 0$ several modes becomes degenerate. One must always be careful with accidental degeneracies. This is also the case here. The degeneracy is lifted in the presence of the lattice deformation. However, since we only consider the lattice perturbatively, this implicitly means we consider $AV_{\text{int}} \ll k$ where V_{int} is a characteristic scale denoting the strength of the interactions between the Bloch modes. The degeneracy limit and the small lattice amplitude limit do not commute. We shall illustrate this in more detail below. We can still do a perturbation analysis in A , but this must be done from the $k = 0$ starting point separately.¹¹ Finally, mathematically, the $k = 0$ fluctuation is special in that at vanishing momentum, parity in the x -direction ($G \leftrightarrow -G$) is restored. In the 1D lattice we consider — with lattice vector in the x -direction — the longitudinal and transverse fluctuations at $k = 0$ therefore break up into odd and even superselection sectors under $G \leftrightarrow -G$

$$\delta Y_{L-} = \left\{ \frac{\delta \lambda_\epsilon^{(1)} - \delta \lambda_\epsilon^{(-1)}}{2i}, \frac{\delta \lambda_n^{(1)} - \delta \lambda_n^{(-1)}}{2i}, \frac{\delta v_x^{(1)} + \delta v_x^{(-1)}}{2}, \delta v_x^{(0)} \right\}, \quad (3.47a)$$

$$\delta Y_{L+} = \left\{ \delta \lambda_n^{(0)}, \delta \lambda_\epsilon^{(0)}, \frac{\delta \lambda_\epsilon^{(1)} + \delta \lambda_\epsilon^{(-1)}}{2}, \frac{\delta \lambda_n^{(1)} + \delta \lambda_n^{(-1)}}{2}, \frac{\delta v_x^{(1)} - \delta v_x^{(-1)}}{2i} \right\}, \quad (3.47b)$$

$$\delta Y_{T-} = \left\{ \frac{\delta v_y^{(1)} - \delta v_y^{(-1)}}{2i} \right\}, \quad (3.47c)$$

$$\delta Y_{T+} = \left\{ \delta v_y^{(0)}, \frac{\delta v_y^{(1)} + \delta v_y^{(-1)}}{2} \right\}. \quad (3.47d)$$

For the sake of brevity, as $k = 0$ we have suppressed all k arguments in the dynamical expressions $\delta \hat{X}^{(n)}(\omega, k = 0) = \delta \hat{X}^{(n)}(\omega)$. In this basis, the overall dynamical matrix $\hat{\mathcal{K}}' = U \hat{\mathcal{K}} U^{-1}$ is diagonal by block and the dynamical equations take the form

$$\begin{pmatrix} \hat{\mathcal{K}}_{L-}(\omega) & 0 & 0 & 0 \\ 0 & \hat{\mathcal{K}}_{L+}(\omega) & 0 & 0 \\ 0 & 0 & \hat{\mathcal{K}}_{T-}(\omega) & 0 \\ 0 & 0 & 0 & \hat{\mathcal{K}}_{T+}(\omega) \end{pmatrix} \cdot \begin{pmatrix} \delta \hat{Y}_{L-}(\omega) \\ \delta \hat{Y}_{L+}(\omega) \\ \delta \hat{Y}_{T-}(\omega) \\ \delta \hat{Y}_{T+}(\omega) \end{pmatrix} = \begin{pmatrix} \delta Y_{L-}(t=0) \\ \delta Y_{L+}(t=0) \\ \delta Y_{T-}(t=0) \\ \delta Y_{T+}(t=0) \end{pmatrix}, \quad (3.48)$$

¹¹ A simple example that illustrates the point is the toy model fluctuation matrix

$$\hat{\mathcal{K}}_{\text{toy}} = \begin{pmatrix} E - k & AV_{\text{int}} \\ AV_{\text{int}} & E + k \end{pmatrix} \quad (3.46)$$

This has poles at $E = \pm \sqrt{k^2 + A^2 V_{\text{int}}^2}$ signaling level repulsion at $k = 0$. Expanding these poles in A gives

$$E = \pm k \left(1 + \frac{1}{2} \frac{A^2 V_{\text{int}}^2}{k^2} \right), \text{ whereas expanding in } k \text{ gives } E = \pm AV_{\text{int}} \left(1 + \frac{1}{2} \frac{k^2}{A^2 V_{\text{int}}^2} \right).$$

where $U = \begin{pmatrix} U_L & 0 \\ 0 & U_T \end{pmatrix}$ is the matrix that reorders the fields from the basis in Eq. (3.39) to Eq. (3.47)

$$U_L = \left(\begin{array}{ccc|ccc|ccc} \frac{i}{2} & 0 & 0 & 0 & 0 & 0 & -\frac{i}{2} & 0 & 0 \\ 0 & \frac{i}{2} & 0 & 0 & 0 & 0 & 0 & -\frac{i}{2} & 0 \\ 0 & 0 & \frac{1}{2} & 0 & 0 & 0 & 0 & 0 & \frac{1}{2} \\ \hline 0 & 0 & 0 & 0 & 0 & 1 & 0 & 0 & 0 \\ 0 & 0 & 0 & 0 & 1 & 0 & 0 & 0 & 0 \\ 0 & 0 & 0 & 1 & 0 & 0 & 0 & 0 & 0 \\ \hline \frac{1}{2} & 0 & 0 & 0 & 0 & 0 & \frac{1}{2} & 0 & 0 \\ 0 & \frac{1}{2} & 0 & 0 & 0 & 0 & 0 & \frac{1}{2} & 0 \\ 0 & 0 & \frac{i}{2} & 0 & 0 & 0 & 0 & 0 & -\frac{i}{2} \end{array} \right), \quad U_T = \begin{pmatrix} \frac{i}{2} & 0 & -\frac{i}{2} \\ 0 & 1 & 0 \\ \frac{1}{2} & 0 & \frac{1}{2} \end{pmatrix}. \quad (3.49)$$

Transverse sector

Let us again consider the transverse sector first. The dynamical matrices $\hat{\mathcal{K}}_{T-}$ and $\hat{\mathcal{K}}_{T+}$ are

$$\hat{\mathcal{K}}_{T-} = \left(\eta G^2 - i\omega \chi_{\pi\pi}^{(0)} \right), \quad \hat{\mathcal{K}}_{T+} = \begin{pmatrix} -i\omega \chi_{\pi\pi}^{(0)} & -2i\omega A \chi_{\pi\pi,1}^{(1)} \\ -i\omega A \chi_{\pi\pi,1}^{(1)} & \eta G^2 - i\omega \chi_{\pi\pi}^{(0)} \end{pmatrix}, \quad (3.50)$$

These have the following diffusive poles

$$\omega^{(T-)} = -iD_{\perp} G^2 \left[1 - A^2 \frac{\chi_{\pi\pi,2}^{(0)}}{\chi_{\pi\pi,0}} \right], \quad (3.51a)$$

$$\omega_0^{(T+)} = 0, \quad (3.51b)$$

$$\omega_1^{(T+)} = -iD_{\perp} G^2 \left[1 - A^2 \frac{\chi_{\pi\pi,2}^{(0)}}{\chi_{\pi\pi,0}} + 2A^2 \left(\frac{\chi_{\pi\pi,1}^{(1)}}{\chi_{\pi\pi,0}} \right)^2 \right]. \quad (3.51c)$$

There are several aspects to note: firstly, as mentioned above these poles do not correspond to the $k \rightarrow 0$ limit of the finite k fluctuations in Eq. (3.42). The indicated emergent degeneracy at $k \rightarrow 0$ between $\omega_{T,-1}$ and $\omega_{T,1}$ is obvious in Eq. (3.42). The lattice perturbation A lifts this degeneracy and therefore the limits $k \rightarrow 0$ and $A \rightarrow 0$ do not commute. Secondly, there is a zero mode in the $T+$ -sector. This is the standard transverse $k = 0$ excitation, that corresponds to a change of the static homogeneous transverse pressure background and as a zero mode should not be considered in the fluctuation spectrum.

Longitudinal sector

Consider the G -parity odd longitudinal sector first. Its dynamical matrix $\hat{\mathcal{K}}_{L-}$ is given by

$$\hat{\mathcal{K}}_{L-} = \left(\begin{array}{ccc|c} & & & \frac{\mu_0 A G}{2} \chi_{\epsilon n,0} \\ & \mathcal{L}_- & & \frac{\mu_0 A G}{2} \chi_{nn,0} \\ & & & -i\omega A \chi_{\pi\pi,1}^{(1)} \\ \hline -\mu_0 A \chi_{nc,0} G & \mu_0 A \chi_{nn,0} G & -2i\omega A \chi_{\pi\pi,1}^{(1)} & -i\omega \chi_{\pi\pi}^{(0)} \end{array} \right), \quad (3.52)$$

with

$$\mathcal{L}_- = \left(\begin{array}{ccc} -i\omega \chi_{\epsilon\epsilon}^{(0)} + \frac{\mu_0^2 A^2}{2} \sigma_Q G^2 & -i\omega \chi_{\epsilon n}^{(0)} & \chi_{\pi\pi}^{(0)} G \\ -i\omega \chi_{nc}^{(0)} & \sigma_Q G^2 - i\omega \chi_{nn}^{(0)} & n^{(0)} G \\ -\chi_{\pi\pi}^{(0)} G & -n^{(0)} G & \hat{\eta} G^2 - i\omega \chi_{\pi\pi}^{(0)} \end{array} \right). \quad (3.53)$$

The lines are there to highlight the coupling between two sub-sectors. The top-left block is equivalent to the coupling matrix (3.20) in the homogeneous system at momentum G encoding the G -parity odd part of two sound modes and a charge diffusion mode (see Eq. (3.21)), while the lower-right block reflects the conservation of momentum in the homogeneous case. In the presence of the lattice deformation the momentum conservation mode now couples with the Umklapped finite G sound-, and charge diffusion modes through the off-diagonal terms. We can find the modes of this dynamical matrix in the same way we did before, and we find

$$\omega_{\text{Drude}}^{(L-)} = -i(\Gamma_d + \Gamma_\eta), \quad (3.54a)$$

$$\omega_D^{(L-)} = -i \left(D_\rho^0 + A^2 D_\rho^{(L-),2} \right) G^2 + i\Gamma_d, \quad (3.54b)$$

$$\omega_\pm^{(L-)} = \pm \left(c_s^0 + A^2 c_s^{(L-),2} \right) G - \frac{i}{2} \left(D_s^0 + A^2 D_s^{(L-),2} \right) G^2. \quad (3.54c)$$

We therefore see that the poles in (3.54) are those of the homogeneous system (3.21) at momentum G with corrected diffusion constants due to the effects of the lattice. The procedure to compute the explicit form of the corrections $D_\rho^{(L-),2}$, $c_s^{(L-),2}$, $D_s^{(L-),2}$ is detailed in Appendix 3.C. For a generic relativistic fluid these are quite involved; in the explicit case of a fluid with conformal invariance they simplify greatly and we give the expressions below in Eq. (3.61).

The most noteworthy part is the Drude pole ω_{Drude} . As previewed at the beginning of this Sec. 3.3 the lattice breaks translational symmetry and this induces a momentum decay rate. The more detailed Bloch wave analysis which gives us all fluctuations at finite k, ω in the hydrodynamic regime beautifully recovers the finite ω memory matrix

result (3.29), as it should. In the condensed matter context, it is this sector specifically that governs the $k = 0$ thermoelectric conductivities, where the presence of the second diffusive mode ω_D (originating in Umklapped charge diffusion) in addition to the Drude mode has significant observable consequences as expounded in [184].

For the G -parity even sector the dynamical matrix is given by

$$\hat{\mathcal{K}}_{L^+} = \begin{pmatrix} -i\omega\chi_{nn}^{(0)} & -i\omega\chi_{n\epsilon}^{(0)} & -2i\omega A\chi_{n\epsilon,1}^{(1)} & -2i\omega A\chi_{nn,1}^{(1)} & 0 \\ -i\omega\chi_{n\epsilon}^{(0)} & -i\omega\chi_{\epsilon\epsilon}^{(0)} + \frac{\mu_0^2 A^2}{2}\sigma_Q G^2 & -2i\omega A\chi_{\epsilon\epsilon,1}^{(1)} & A(\mu_0\sigma_Q G^2 - 2i\omega\chi_{n\epsilon,1}^{(1)}) & -\mu_0 A G n_0 \\ -i\omega A\chi_{n\epsilon,1}^{(1)} & -i\omega A\chi_{\epsilon\epsilon,1}^{(1)} & & & \\ -i\omega A\chi_{nn,1}^{(1)} & A\left(\frac{\mu_0\sigma_Q}{2}G^2 - i\omega\chi_{n\epsilon,1}^{(1)}\right) & & \mathcal{L}_+ & \\ 0 & \frac{\mu_0 A}{2}G n_0 & & & \end{pmatrix}, \quad (3.55)$$

with

$$\mathcal{L}_+ = \begin{pmatrix} \frac{\mu_0^2 A^2}{2}\sigma_Q G^2 - i\omega\chi_{\epsilon\epsilon}^{(0)} & -i\omega\chi_{n\epsilon}^{(0)} & -\chi_{\pi\pi}^{(0)}G \\ -i\omega\chi_{n\epsilon}^{(0)} & \sigma_Q G^2 - i\omega\chi_{nn}^{(0)} & -n^{(0)}G \\ \chi_{\pi\pi}^{(0)}G & n^{(0)}G & \hat{\eta}G^2 - i\omega\chi_{\pi\pi}^{(0)} \end{pmatrix} \quad (3.56)$$

Once again, the lines show how the various sub-sectors couple through the off-diagonal A -dependent terms. The \mathcal{L}_+ sector is again a pair of sound modes and a charge diffusion mode, but now the part that is even under G -parity. The $n = 0$ charge and energy conservation modes are reflected in the upper-left blocks. The modes of this system are

$$\omega_c^{(L^+)} = 0, \quad (3.57a)$$

$$\omega_d^{(L^+)} = 0, \quad (3.57b)$$

$$\omega_D^{(L^+)} = -i\left(D_\rho^0 + A^2 D_\rho^{(L^+,2)}\right)G^2, \quad (3.57c)$$

$$\omega_\pm^{(L^+)} = \pm\left(c_s^0 + A^2 c_s^{(L^+,2)}\right)G - \frac{i}{2}\left(D_s^0 + A^2 D_s^{(L^+,2)}\right)G^2, \quad (3.57d)$$

We see again that the latter three poles in (3.57) are those of the homogeneous system (3.21) at momentum G with corrected diffusion constants due to the effects of the lattice. The shifts differ, however, from the L^- sector. The explicit form of the corrections $D_\rho^{(L^+,2)}$, $c_s^{(L^+,2)}$, $D_s^{(L^+,2)}$ can again be derived through the method detailed in Appendix 3.C, and tractable expressions for the special case of a conformal fluid are given in Eq. (3.61). The first two poles are the ones encoding charge conservation and energy conservation; they remain unshifted at this order in perturbation theory. As we explain in Appendix 3.C, one of these modes is an exact conservation mode and by rotating the system back to $\hat{\mathcal{K}}$ instead of $\hat{\mathcal{K}}$, it is easy to see that this mode corresponds

to overall charge conservation — associated here to $\delta\lambda_n^{(0)}$. The other mode is merely unshifted at this order in perturbation theory.

Having computed the corrections to the $k = 0$ modes, one clearly sees that these are not equal to the limit $k \rightarrow 0$ of (3.45). In that limit, at leading order, $\omega_{D,\pm 1} = -iD_\rho^0 G^2 + \frac{i}{2}\Gamma_d$ and $\omega_{S,\pm,0} = -\frac{i}{2}\Gamma_{\text{ionic,mem.}}$, whereas the explicit $k = 0$ computation has $\omega_{\text{Drude}}^{(L^-)} = -\Gamma_{\text{ionic,mem.}}$, and an additional (to leading order in A^2) zero mode. This difference is due to the non-commutativity of the $k \rightarrow 0$ and $A \rightarrow 0$ limits. In the next section, where we illustrate the emergence of these hydrodynamic modes in an explicitly computed example, we will show precisely how these poles are related in the $k \rightarrow 0$ limit.

3.4 Bloch wave hydrodynamics emerging from holographic models: a comparison

We will now validate the understanding of charged (relativistic) hydrodynamics in a periodic potential by comparing it with the low energy physics of holographic models. Holographic models describe the strong coupling regime of quantum field theories in a manifestly real time formalism. Uniquely so, this includes the emergence of hydrodynamics at low frequencies and long wavelengths $\omega, k \ll T, \mu$ [77, 191, 19, 1]. This last part is also known as fluid-gravity duality [113]. By considering a strongly coupled quantum field theory in a spatially periodic chemical potential background, *i.e.*, an ionic lattice,¹² described holographically in terms of its dual gravitational description, we will see that the Bloch wave hydrodynamics described above emerges. There is one simplifying feature in the two holographic models we choose here. Both describe a conformally invariant system for which the equation of state takes the scaling form

$$P(T, \mu) = T^{d+1} f(T/\mu), \quad (3.58)$$

which directly implies $P = \epsilon/d$. Furthermore, due to the conformal symmetry such a system must also have a vanishing bulk viscosity, *i.e.*, $\zeta = 0$.

The two specific models we consider are the strongly coupled theories holographically dual to the RN black hole [192, 193, 194, 195, 132] as well as the GR black hole [38]. We will solve the fluctuations in these systems modulated by a finite chemical potential numerically and compare to the predictions from Bloch wave hydrodynamics as presented in the previous sections. These two systems are chosen as their ground states are possible candidates to explain the mysterious strange metal physics underlying high T_c superconductors. There is reason to believe that this physics is indeed that of strongly coupled electrons in an ionic lattice. The possible relevance of Bloch wave

¹²This mimics the charge distribution of a frozen atomic lattice, or more appropriately an ionic lattice with valence electrons.

hydrodynamics in the context of strange metal physics is described in a companion article [184].

A brief description of the numerical holographic set-up is provided in appendix 3.D.2; more details can be found in [184]. The crucial aspect of relevance here to the comparison of the numerics with our Bloch hydrodynamic analysis is the equation of state of the two models. The 2 + 1-dimensional (finite temperature) field theories dual to AdS₄ RN and GR black holes are conformal charged fluids¹³ with equation of state

$$\frac{P_{\text{RN}}(\hat{T})}{\mu^3} = \hat{T}^3 \left(\frac{-1 - 8\pi^2 \hat{T}^2 + 2\pi \hat{T} \sqrt{3 + 16\pi^2 \hat{T}^2}}{2\hat{T}^3 (4\pi \hat{T} - \sqrt{3 + 16\pi^2 \hat{T}^2})^3} \right), \quad (3.59)$$

$$\frac{P_{\text{GR}}(\hat{T})}{\mu^3} = \hat{T}^3 \left(\frac{(3 + 16\pi^2 \hat{T}^2)^{3/2}}{27\hat{T}^3} \right), \quad (3.60)$$

where we have defined $\hat{T} \equiv T/\mu$.

A direct consequence of this conformal equation of state is that $\chi_{\text{cc},0} = d \chi_{\pi\pi,0}$ and $\chi_{nc,0} = d n_0$. As a consequence many previous expressions simplify. Specifically the order A^2 corrections to the poles for $k = 0$ are now given by the tractable expressions:

$$D_{\rho}^{(L-),2} = -\frac{\sigma_Q}{\chi_{\pi\pi,0}} \frac{\chi_{nn,2}^{(0)} (\chi_{\pi\pi,0})^3 - 2\chi_{nn,1}^{(1)} (\chi_{\pi\pi,0})^2 \mu_0 n_0 + \chi_{nn,0} \chi_{\pi\pi,0} \mu_0^2 n_0^2 + \mu_0^2 n_0^4}{(d\chi)^2}, \quad (3.61a)$$

$$D_{\rho}^{(L+),2} = \frac{\sigma_Q}{4\chi_{\pi\pi,0}} \frac{(\chi_{\pi\pi,0})^2 ((\chi_{nn,0})^2 \mu_0^2 - 4\chi_{nn,2}^{(0)} \chi_{\pi\pi,0}) + 8\chi_{nn,1}^{(1)} (\chi_{\pi\pi,0})^2 \mu_0 n_0 - 12\chi_{nn,0} \chi_{\pi\pi,0} \mu_0^2 n_0^2 + 12\mu_0^2 n_0^4}{(d\chi)^2}, \quad (3.61b)$$

$$c_s^{(L-),2} = \frac{\mu_0^2 n_0^2}{4\sqrt{2}(\chi_{\pi\pi,0})^2}, \quad D_s^{(L-),2} = \frac{\mu_0^2}{4\chi_{\pi\pi,0}} \left[\sigma_Q + \frac{10n_0^2 - 3\chi_{nn,0} \chi_{\pi\pi,0}}{(\chi_{\pi\pi,0})^2} \hat{\eta} \right], \quad (3.61c)$$

$$c_s^{(L+),2} = \frac{\mu_0^2 n_0^2}{\sqrt{2}(\chi_{\pi\pi,0})^2}, \quad D_s^{(L+),2} = \frac{\mu_0^2}{4\chi_{\pi\pi,0}} \left[\sigma_Q - \frac{3\chi_{nn,0}}{(\chi_{\pi\pi,0})^2} \hat{\eta} \right]. \quad (3.61d)$$

The explicit expressions for the thermodynamic quantities in the grand canonical ensemble for the RN and GR black holes can be found in Appendix 3.D.1.

We will use the longitudinal optical conductivity $\sigma_{xx}(\omega, k_x = k) = \frac{1}{i\omega} \langle J^x(-\omega, -k_x) J^x(\omega, k_x) \rangle$ as a probe. Generically this current will receive contributions from all hydrodynamic fluctuations; these essentially determine the low frequency long-wavelength response. At finite k , this means we should see all 9 modes described in (3.45). At $k = 0$, however,

¹³While this result is well-known for the RN black hole, it only applies in the GR black hole for a suitable choice of quantization of the boundary scalar operator — the dilaton must be a marginal deformation. One must therefore use mixed boundary conditions for the dilaton at the boundary [170].

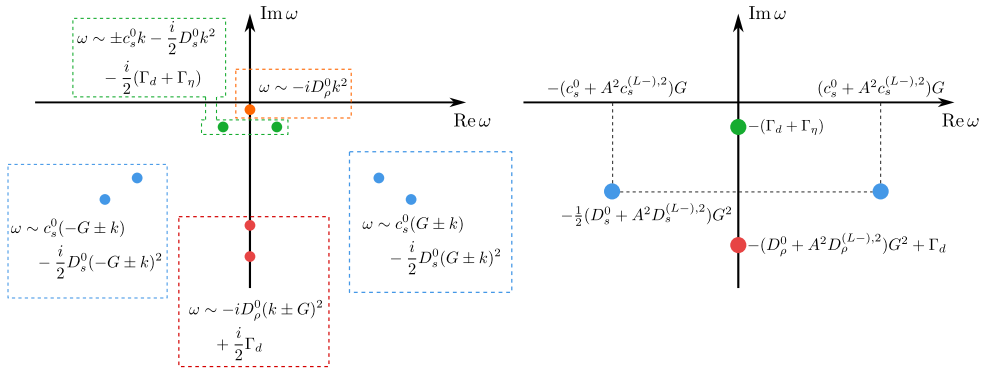


Figure 3.1: Drawing of the expected position of the poles in the current-current correlator at finite k (left) and at $k = 0$ (right) based on the hydrodynamical predictions in terms of Bloch waves in Sec. 3.3. Generically there are 9 poles: the standard two sound modes plus a (charge) diffusive mode of charged hydrodynamics cross coupled with the $n = 1$ and $n = -1$ Umklapp copies of each. At $k = 0$, there is an emergent symmetry due to which the longitudinal current-current correlator only probes the first sector $\hat{\mathcal{K}}_{L-}$ that contains the 4 modes that are odd under inverting the lattice momentum $G \leftrightarrow -G$.

the current is part of the $L-$ sector and we will only see the first sector with its 4 modes. Fig. 3.1 gives a schematic sketch of what the spectrum of the current-current correlator — and therefore the optical conductivity — should look like in the complex frequency plane based on our hydrodynamic predictions.

Precisely this expectation is reproduced by the numerical results in holographic duals to RN and GR black holes where hydrodynamics is emergent. Fig. 3.2 plots the density of the absolute value and argument of the optical conductivity for small values of the real part of the frequencies, *i.e.*, zoomed in near the imaginary frequency axis. Each picture is at a different value of $k/\mu \in \{0, 0.001, 0.005\}$. We see that for $k = 0$ there are only two purely diffusive poles, as predicted, that split into two propagating and two diffusive poles at finite k . For finite k , there should also be a third diffusive pole very close to the real axis. Its weight is very low, however, but it can be unveiled by zooming in carefully. This was plotted in Fig. 3.3 for $k/\mu \in \{0.006, 0.008, 0.01\}$ (this choice of momenta proved more convenient to display). In all cases the location of these poles can be compared with the predictions from our hydrodynamical analysis after substituting in the relevant equation of state. The match is perfect for both $k = 0$ and k finite as denoted by the white circles in Fig. 3.2 and the triangles in Fig. 3.3. Similarly, we plotted in Fig. 3.4 the argument of the optical conductivity near the sound poles at momenta $G \pm k$. The weight of these poles is very small and they are therefore difficult to identify in $|\sigma|$. The argument of σ , on the other hand, displays a jump at the poles. A similar analysis holds for the conjugate pair of poles at $-G \pm k$. These sound poles give rise to a characteristic peak in the real conductivity, first noted in [82, 118, 84].

To illustrate in more detail the hydrodynamical origin of all these poles and their

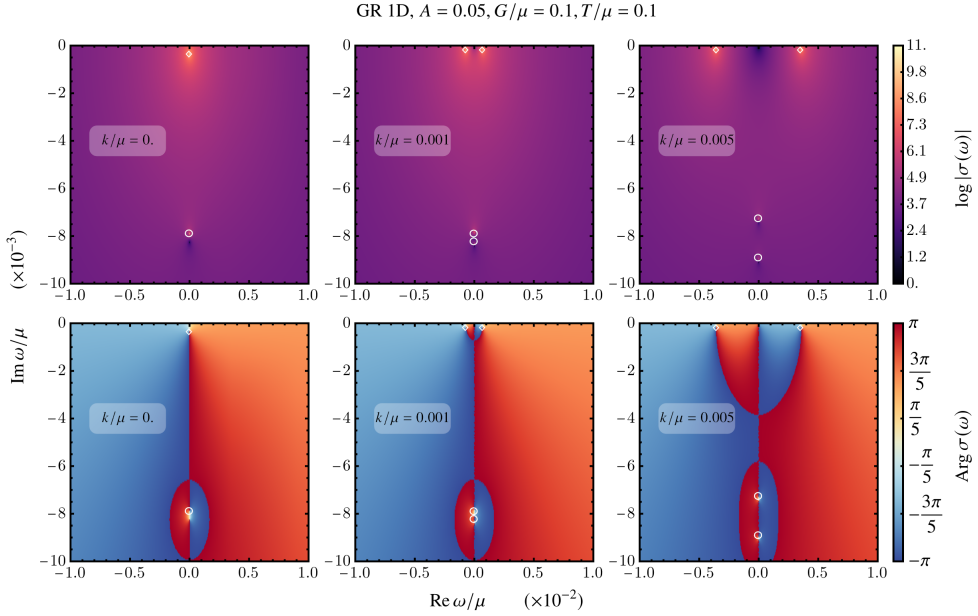


Figure 3.2: Density plot of (the logarithm of) the GR longitudinal conductivity $\log|\sigma(\omega)|$ (top) and its argument $\text{Arg}\sigma(\omega)$ (bottom) in the complex frequency plane close to the imaginary axis for $T/\mu = 0.1$, $A = 0.05$ and $G/\mu = 0.1$, for four values $k/\mu \in \{0, 0.001, 0.005, 0.01\}$. At $k = 0$, we see the poles $\omega_{\text{Drude}}^{(L-)}$ and $\omega_D^{(L-)}$ while at $k > 0$, the Drude pole splits into the two sound modes $\omega_{S,\pm,0}$ (denoted by a white \diamond) and the diffusion pole splits into $\omega_{D,\pm,1}$ (denoted by a white \circ). The markers indicate the analytical position of these poles prescribed by our hydrodynamical derivation. A priori, a fifth pole $\omega_{D,0}$ at $k > 0$ also couples to the electrical current, but it is not visible on the range plotted. A more refined computation, does reveal it (Fig. 3.3).

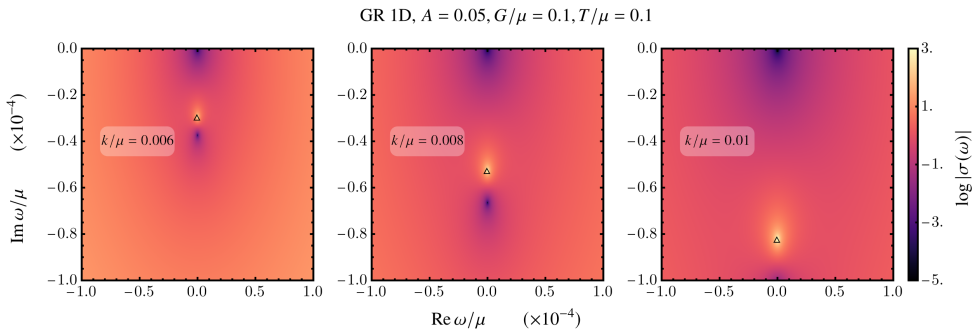


Figure 3.3: GR conductivity $\log|\sigma(\omega)|$ in the complex plane close to the imaginary axis for $T/\mu = 0.1$, $A = 0.05$ and $G/\mu = 0.1$, varying $k/\mu \in \{0.006, 0.008, 0.01\}$. We see a purely diffusive pole on the imaginary axis which matches the hydrodynamic diffusion pole $\omega_{D,0}$ (denoted by Δ). The area plotted is zoomed on the origin compared to Fig. 3.2. There the diffusive pole was too small to be visible.

full explanation in terms of thermodynamic quantities, one can track the location of the poles as a function of temperature. Focusing only on the purely diffusive poles (two for $k = 0$, and three for $k \neq 0$), as they are more easily extracted numerically by scanning carefully over the negative imaginary frequency axis, we also find here a perfect match between numerics and hydrodynamic prediction, Eqs. (3.54) and (3.45) respectively, but now as function of T/μ ; see Fig. 3.5 and Fig. 3.6.

With our computational RN and GR examples we can also illustrate the subtle nature of the $k \rightarrow 0$ limit. As we saw in the previous section, the naive extrapolation to $k \rightarrow 0$ of the two $n = 0$ sound modes $\omega_{S,0,\pm} = -\frac{i}{2}\Gamma_{\text{ionic,mem.}} + \mathcal{O}(k)$ does not correspond with the physical $k = 0$ Drude pole $\omega_{\text{Drude}}^{(L-)} = -i\Gamma_{\text{ionic,mem.}}$ and its $(L+)$ equivalent $\omega_d^{(L+)} = 0$. To emphasize this once more, the origin of this difference comes from the non-commutativity of the $k \rightarrow 0$ and $A \rightarrow 0$ limits. In Fig. 3.7, we have carefully analyzed the low k regime of the GR black hole. For $k/\mu = 10^{-4}$, the two diffusive poles are close to their $k = 0$ values (3.54) and (3.57). As we increase k , they get closer and collide, leading to the two sound modes of (3.45). This diffusion-to-sound crossover happens when $\frac{k}{G} \sim A^2$ illustrating the non-commuting limits $k \rightarrow 0$, $A \rightarrow 0$ which means we can estimate the characteristic length scale of the interactions to be $V_{\text{int}} \sim AG$ (see footnote 11).

Finally, to re-emphasize the underlying Bloch wave Umklapp physics, Fig. 3.8 shows the real part of the momentum-dependent optical conductivity $\sigma(\omega, k)$ in the ω, k plane. The right-hand plot is a zoomed-in version of the left-hand plot near the edge of the Brillouin zone $k = \frac{G}{2}$. The gray dots are numerically obtained solutions of $\det \hat{\mathcal{K}}_L = 0$ for the same parameters, showing that the hydrodynamic description of the matrix (3.43) at order $\mathcal{O}(A^2)$ matches the data over the entire Brillouin zone. At low frequency, we see the expected sound mode $\omega \sim c_s k$ dominating the low frequency regime, but we also can see its interaction with the sound mode $\omega \sim c_s(G - k)$. They meet at the edge of the Brillouin zone $k = \frac{G}{2}$ and in the right-hand plot, we see the traditional level repulsion of Umklapp and the opening of a gap in the sound mode spectrum.

3.5 Conclusion

The crucial message of this paper is that hydrodynamic fluctuations in a periodically modulated background should be understood based on a Bloch wave analysis instead of simple plane waves. If the typical length scale of this modulation is sufficiently large and the amplitude sufficiently small, we can still use hydrodynamics to study the long-time response of the conserved charges. This is an old observation in neutral hydrodynamics, but deserves restudy for charged hydrodynamics given the novel experimental progress of observed hydrodynamic flow in electronic condensed matter systems [181, 182, 183]. This is particularly so in the presence of a charged fluid, which introduces an additional intrinsic diffusive mode. The presence of a spatial periodic modulation introduces Brillouin zone copies, also for this additional mode, and

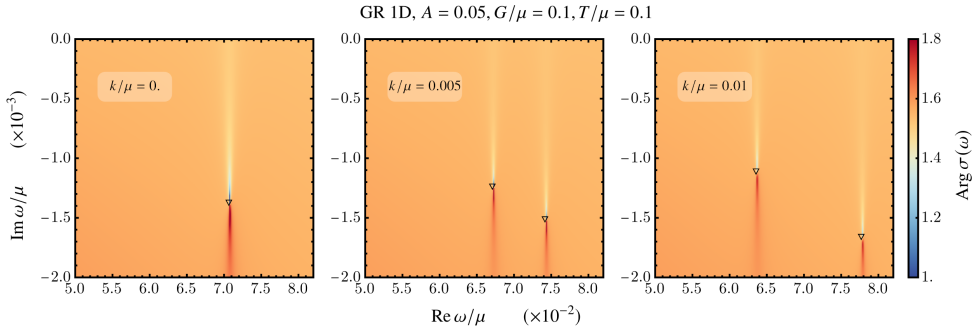


Figure 3.4: Argument of the GR conductivity $\arg \sigma(\omega)$ in the complex plane for $T/\mu = 0.1$, $A = 0.05$ and $G/\mu = 0.1$, varying $k/\mu \in \{0, 0.001, 0.005, 0.01\}$. At $k = 0$, we see the sound pole $\omega_+^{(L-)}$. Its real part is precisely at $c_s G$ with $c_s = 1/\sqrt{2}$ in a $d = 2$ conformal fluid. At $k > 0$, it splits into the two sound modes $\omega_{S,\pm,1}$ (denoted by ∇). The markers indicate the analytical position of these poles prescribed by our hydrodynamical derivation. These poles are more difficult to observe in $|\sigma|$ than those on the imaginary axis and are easier to see as jumps in the argument of the complex function.

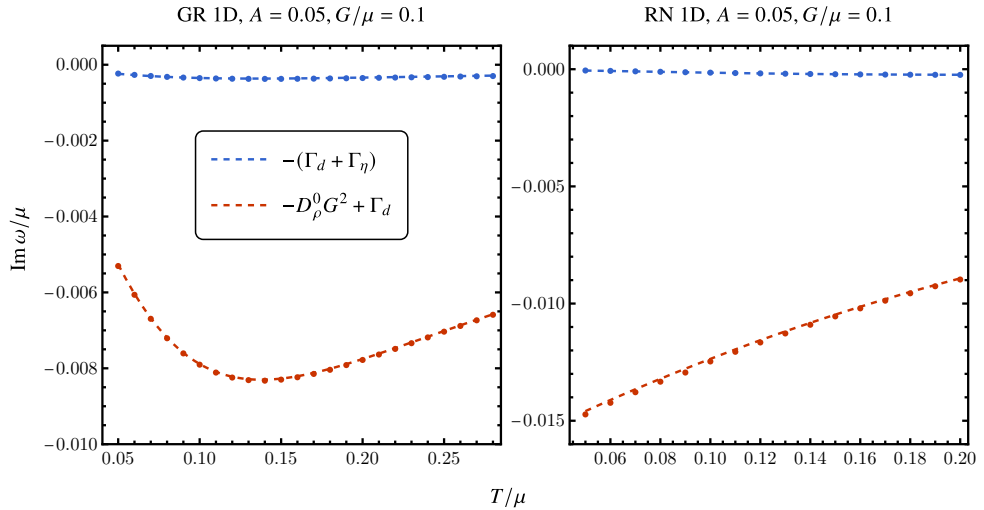


Figure 3.5: Comparison between the position of the poles on the imaginary axis (points) and the analytical hydrodynamical formula (3.54) at $k = 0$, as a function of T/μ , and for $A = 0.05$ and $G/\mu = 0.1$. This is done for GR on the left and RN on the right. The blue data is the Drude pole $\omega_{\text{Drude}}^{(L-)}$ and the red data corresponds to the Umklapped diffusion pole $\omega_D^{(L-)}$ (Eqs. (3.54)). The corrections to the diffusion constants are smaller than our numerical accuracy for our choice of parameters, so we can simply ignore them here.

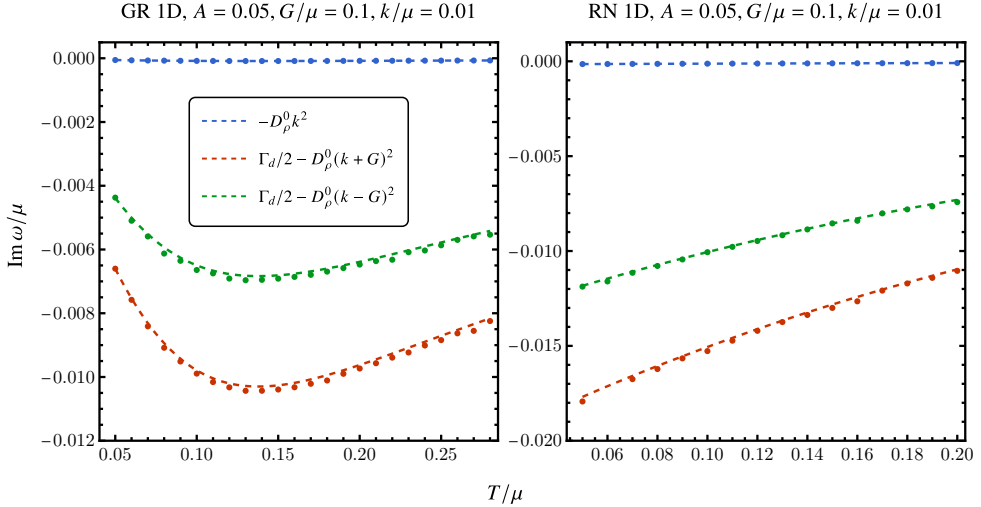


Figure 3.6: Comparison between the position of the poles $\omega_{D,0}$ and $\omega_{D,\pm 1}$ on the imaginary axis (points) and the analytical hydrodynamical expressions (3.45) at $k/\mu = 0.01$, as a function of T/μ , and for $A = 0.05$ and $G/\mu = 0.1$. This is done for GR on the left and RN on the right. The corrections to the diffusion constants are smaller than our numerical accuracy for our choice of parameters, so we can simply ignore them here.

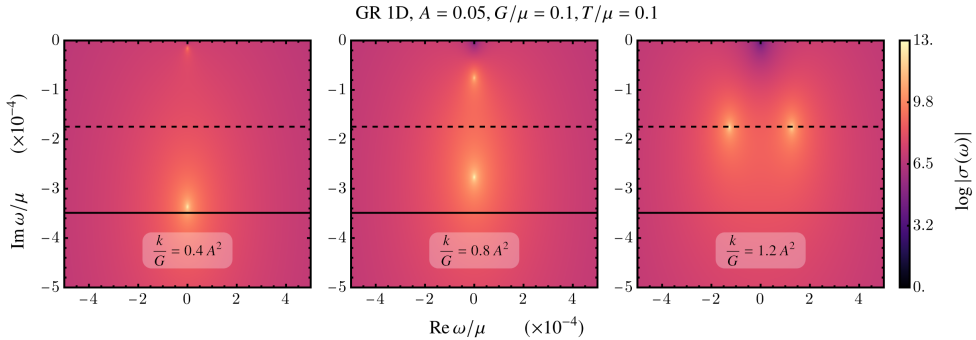


Figure 3.7: (Logarithm of the) GR conductivity $\log |\sigma(\omega)|$ in the complex plane close to the imaginary axis for $T/\mu = 0.1$, $A = 0.05$ and $G/\mu = 0.1$, varying $k/\mu \in \{10^{-4}, 2 \times 10^{-4}, 3 \times 10^{-4}, 4 \times 10^{-4}\}$. For $k = 10^{-4}$, we see the poles $\omega_{\text{Drude}}^{(L-)}$ and $\omega_{\text{d}}^{(L+)}$ with small corrections. For $k > 3 \times 10^{-4}$, the poles are now the two sound modes $\omega_{S,\pm 0}$ close to their $k \rightarrow 0$ limit. The lines indicate the positions $\omega_{\text{Drude}}^{(L-)} = -i\Gamma_{\text{ionic,mem.}}$ (solid) and $\omega_{S,0,\pm}(k \rightarrow 0) = -\frac{i}{2}\Gamma_{\text{ionic,mem.}}$ (dashed). When expressed in terms of $\frac{k}{G}$, the transition appears to happen at $\frac{k}{G} \sim A^2$.

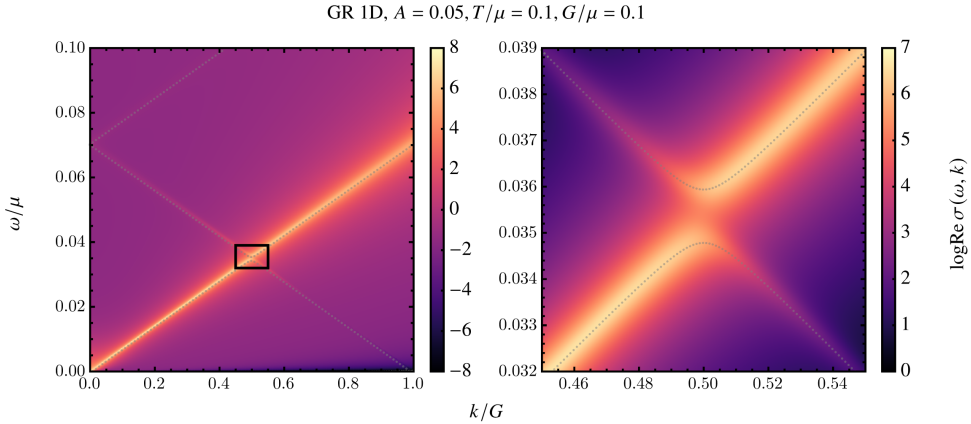


Figure 3.8: (Left) $\text{Re } \sigma(\omega, k)$ plotted in the $(k/G, \omega/\mu)$ plane for $A = 0.05$, $T/\mu = 0.1$ and $G/\mu = 0.1$. (Right) Zoom on the Brillouin zone boundary at $k = G/2$ (region indicated by a black frame from on the left-hand plot) showing the level repulsion and the gapped sound mode at the edge of the zone. The gray dots are the hydrodynamic prediction given by numerically finding the roots of the determinant of Eq. (3.43).

due to Umklapp at the Brillouin zone boundary this higher Bloch mode mixes with the long distance late time $k = 0$ sound modes.

We showed how one can compute the explicit pattern and strengths of these mixings from the underlying hydrodynamics. As is standard but ever so useful in hydrodynamics is that the behavior of both the patterns and the strengths can be expressed in underlying thermodynamic quantities, notably the susceptibilities, combined with the transport coefficients.

An important feature of a periodic modulation — well known in the condensed matter physics context — is that it breaks translational symmetry. For a perturbatively small lattice the correction to the momentum pole can be interpreted as the momentum relaxation rate and our result agrees with the relaxation rate obtained through the memory matrix formalism, as it should. It is important to emphasize once more that even though there is one relaxation rate, this relaxation rate has two contributions Γ_d and Γ_η corresponding to the two longitudinal diffusive processes. A priori these can have different scaling in temperature.¹⁴ They also exhibit different scaling in the lattice wavevector G . Due to this, in systems with charge disorder parametrized as an averaging over many independent lattices, one of these terms will dominate. It is rather the other aspect of the periodic modulation — the presence of Bloch modes in higher Brillouin zones that we wish to emphasize here. At finite density this includes an Umklapped charge diffusion mode. As we analyzed in a companion paper, this mode

¹⁴This is the case in RN where $\Gamma_\eta \sim T^0$ and $\Gamma_d \sim T^2$ while in GR, they both scale with temperature with $\Gamma_\eta \sim \Gamma_d \sim T$.

may be of relevance in condensed matter physics [184]. The strange metal phase of high T_c superconductors shows the development of a mysterious mid-IR peak in the optical conductivity at temperatures $T \simeq 300K$; see *e.g.*, [196, 67]. The phenomenology of this peak is almost exactly reproduced by a collision between the Drude pole and the Umklapped charge diffusion pole in a holographic model of the strange metal dual to the Gubser-Rocha black hole [184]. If it can be experimentally verified that charge transport in the strange metal is in fact hydrodynamical, this will be the explanation of that phenomenon.

Finally, we verified our results by numerically computing response functions in strongly coupled systems holographically dual to Reissner-Nordström and Gubser-Rocha black holes. The important feature is that hydrodynamics emerges naturally in holographic systems and is not an input. In the computed optical conductivities, we found precisely the poles matching those predicted by our hydrodynamics computation. As a function of varying parameters such as momentum and lattice strength, these poles show complicated behavior including pole collisions and level repulsion denoting various regime changes.

We conclude with emphasizing that the hydrodynamics description of those holographic systems remains valid throughout these collisions and level repulsions. This contrasts with recent studies on the validity of hydrodynamics postulated as a pole collision/level repulsion with a first UV (gapped) pole [126, 197, 198]. Our result here shows that this identification has to be done with care. The Umklapped modes are also a priori gapped modes in the zero momentum limit $k \rightarrow 0$. However, they remain modes of the conserved charges, can be fully captured in a hydrodynamic description and play a different role from non-hydrodynamic UV modes.

The analysis carried in this paper crucially relied on a static background charge distribution to mimic the effects of a frozen ionic lattice. This ignores the effect of lattice vibrations. Including phonon modes would require a different setup. Moreover, the assumption of local thermal equilibrium rather strongly constrains the hierarchy of scales as $\omega, k \ll G \ll T$. While the results we have achieved are rather general and only rely on the presence of global symmetries and periodicity – which would seem to imply this is valid for a wide range of metallic systems – one must remain cautious as to whether such hierarchy of scales is realized within physical systems.

Acknowledgements

We are very grateful to F. Balm and J. Zaanen for collaboration in the early stages of this project. We also thank D. Brattan, B. Goutéraux, K. Grosvenor, V. Ziogas and especially A. Krikun for discussions during the Nordita scientific program "Recent developments in strongly correlated quantum matter". This research was supported in part by the FOM program 167 (*Strange Metals*), by the Dutch Research Council (NWO) project 680-91-116 (*Planckian Dissipation and Quantum Thermalisation: From Black Hole Answers to Strange Metal Questions.*), and by the Dutch Research Council/Ministry

of Education. The numerical computations were carried out on the Dutch national Cartesius and Snellius national supercomputing facilities with the support of the SURF Cooperative as well as on the ALICE-cluster of Leiden University. We are grateful for their help.

3.A Thermodynamics and susceptibilities

In this section of the supplementary material, we will briefly review some key thermodynamic identities related to the static susceptibilities. We will be interested in the conserved charges $\{\delta\epsilon, \delta n\}$ and their associated sources $\{\delta\lambda_\epsilon, \delta\lambda_n\} = \{\delta T/T, \delta\mu - \frac{\mu}{T}\delta T\}$. Since we will be focusing on thermodynamics, we will only be interested in the equilibrium solution and therefore we will drop the \bar{X} notation for background thermodynamics quantities. As a reminder, the susceptibility matrix in the (ϵ, n) sector is defined as

$$\begin{pmatrix} \delta\epsilon \\ \delta n \end{pmatrix} = \chi \cdot \begin{pmatrix} \delta\lambda_\epsilon \\ \delta\lambda_n \end{pmatrix}, \quad \chi = \begin{pmatrix} \chi_{\epsilon\epsilon} & \chi_{\epsilon n} \\ \chi_{n\epsilon} & \chi_{nn} \end{pmatrix} = \begin{pmatrix} T \left(\frac{\partial\epsilon}{\partial T} \right)_{\mu/T} & \frac{1}{T} \left(\frac{\partial\epsilon}{\partial\mu/T} \right)_T \\ T \left(\frac{\partial n}{\partial T} \right)_{\mu/T} & \frac{1}{T} \left(\frac{\partial n}{\partial\mu/T} \right)_T \end{pmatrix}, \quad (3.62)$$

while the momentum susceptibility is $\chi_{\pi\pi} = \epsilon + P$. Furthermore, we have the thermodynamic identity

$$T dX = T \left(\frac{\partial X}{\partial T} \right)_{\mu/T} dT + T \left(\frac{\partial X}{\partial\mu/T} \right)_T d(\mu/T), \quad (3.63a)$$

$$= \left[T \left(\frac{\partial X}{\partial T} \right)_{\mu/T} - \mu \left(\frac{\partial X}{\partial\mu} \right)_T \right] dT + T \left(\frac{\partial X}{\partial\mu} \right)_T d\mu, \quad (3.63b)$$

$$= T \left(\frac{\partial X}{\partial T} \right)_\mu dT + T \left(\frac{\partial X}{\partial\mu} \right)_T d\mu, \quad (3.63c)$$

such that $T \left(\frac{\partial X}{\partial T} \right)_{\mu/T} = T \left(\frac{\partial X}{\partial T} \right)_\mu + \mu \left(\frac{\partial X}{\partial\mu} \right)_T$. Using this relation and the first law $d\epsilon = T ds + \mu dn$, we have

$$\chi_{\epsilon n} = \left(\frac{\partial\epsilon}{\partial\mu} \right)_T = T \left(\frac{\partial s}{\partial\mu} \right)_T + \mu \left(\frac{\partial n}{\partial\mu} \right)_T \quad (3.64a)$$

$$= T \frac{d^2 P}{d\mu dT} + \mu \left(\frac{\partial n}{\partial\mu} \right)_T = T \left(\frac{\partial n}{\partial T} \right)_\mu + \mu \left(\frac{\partial n}{\partial\mu} \right)_T = T \left(\frac{\partial n}{\partial T} \right)_{\mu/T}. \quad (3.64b)$$

Looking back at (3.62), this means that $\chi_{n\epsilon} = \chi_{\epsilon n}$.

When considering conformal matter in Sec. 3.4, we used that $P = \epsilon/d$ which is directly implied by the equation of state (3.58). In that particular case,

$$\chi_{n\epsilon} = \chi_{\epsilon n} = \left(\frac{\partial \epsilon}{\partial \mu} \right)_T = \left(\frac{\partial P}{\partial \mu} \right)_T d = nd , \quad (3.65)$$

$$\chi_{\epsilon\epsilon} = T \left(\frac{\partial \epsilon}{\partial T} \right)_{\mu/T} = d \left(T \left(\frac{\partial P}{\partial T} \right)_{\mu} + \mu \left(\frac{\partial P}{\partial \mu} \right)_T \right) = d(sT + \mu n) = (\epsilon + P)d . \quad (3.66)$$

3.B Onsager relations

One of the important checks we must make that our dynamical system is well-defined is that it respects Onsager's relations. These can be derived by considering how the system behaves under time-reversal invariance. Given the anti-unitary operator T such that $[H, T] = 0$, we can classify each of the operators associated to our hydrodynamical variables by their representation under this operator. For a given operator δX_a , we will have $T\delta X_a(t, x)T^{-1} = \eta_a \delta X_a(-t, x)$ with $\eta_a = \pm 1$. Denoting the retarded Green's function associated to a dynamical matrix K_{ab} by G_{ab}^R , we have

$$G_{ab}^R(t - t', x, x') = -i\Theta(\tau) \text{tr}(\rho[\delta X_a(\tau, x), \delta X_b(0, x')]) , \quad \text{with } \rho = e^{-\beta H}/Z . \quad (3.67)$$

We can then see that, due to the anti-unitarity of T ,

$$G_{ab}^R(\tau, x, x') = \eta_a \eta_b G_{ba}^R(\tau, x', x) . \quad (3.68)$$

In Fourier space, this means $\hat{G}_{ab}^R(\omega, p, p') = \eta_a \hat{G}_{ba}^R(\omega, -p', -p)\eta_b$ and specifically for our periodic background, we can write the Green's function as [117]

$$\hat{G}_{ab}^R(\omega, p, p') = \hat{G}_{ab}^{R(n,m)}(\omega, k) , \quad p = k + nG , \quad p' = -k + mG , \quad (3.69)$$

where we have used that the discrete lattice symmetry $G_{ab}^R(\tau, x, x') = G_{ab}^R(\tau, x + \frac{2\pi}{G}, x' + \frac{2\pi}{G})$ implies that $p + p' \in \mathbb{Z}G$. For this decomposition, the Onsager relation becomes

$$\hat{G}_{ab}^{R(n,m)}(\omega, k) = \eta_a \hat{G}_{ba}^{R(-m,-n)}(\omega, -k)\eta_b \quad (3.70a)$$

$$= \eta_a (\hat{G}^\top)_{ab}^{R(-n,-m)}(\omega, -k)\eta_b \quad (3.70b)$$

$$= S \cdot (\hat{G}^\top)^{R(-n,-m)}(\omega, -k) \cdot S , \quad (3.70c)$$

$$\hat{G}^R(\omega, k) = S \cdot \overline{(\hat{G}^\top)^R(\omega, k)} \cdot S . \quad (3.70d)$$

In the previous expression, we have introduced S the diagonal matrix of eigenvalues η and the notation $\hat{G}^{R(n,m)}(\omega, k) \equiv \hat{G}^{R(-n,-m)}(\omega, -k)$. It is easy to check that for our background, $\bar{\chi} = \chi$ and therefore since $\chi = \hat{G}^R(\omega = 0)$, we also have $\chi = S \cdot \chi^\top \cdot S^{-1}$. We can write this relation in terms of the matrix of couplings

$$N(k) \equiv M(k) \cdot \chi = (i\omega + \hat{K}(\omega, k)) \cdot \chi = i\omega\chi + \hat{K}(\omega, k) , \quad (3.71)$$

The elements of N are simply the coefficients of the equations (3.6) written in terms of the sources and expanded in the basis (3.34). By using that $\hat{G}^R = (1 + i\omega K^{-1}) \cdot \chi$, the relation (3.70) can then be written as

$$N = S \cdot \overline{N^\top} \cdot S^{-1}. \quad (3.72)$$

Let us apply this to the conservation equations (3.12) for an in-going momentum p and an outgoing momentum p'

$$N_{en}(p, p') = \sigma_Q \int dq (-pq \bar{\mu}(q)) \delta(p + q - p'), \quad (3.73a)$$

$$N_{ne}(p, p') = \sigma_Q \int dq (pq \bar{\mu}(q) + q^2 \bar{\mu}(q)) \delta(p + q - p'), \quad (3.73b)$$

$$N_{e\pi}(p, p') = - \int dq (p \chi_{\pi\pi,0}(q) + q \bar{\epsilon}(q)) \delta(p + q - p'), \quad (3.73c)$$

$$N_{\pi e}(p, p') = \int dq (-p' \chi_{\pi\pi,0}(q) + q \bar{\epsilon}(q)) \delta(p + q - p'), \quad (3.73d)$$

$$N_{n\pi}(p, p') = \int dq (-p' \bar{n}(q)) \delta(p + q - p'), \quad (3.73e)$$

$$N_{\pi n}(p, p') = \int dq (-p \bar{n}(q)) \delta(p + q - p'). \quad (3.73f)$$

We now want to check the Onsager condition for N using that $\eta_e = \eta_n = -\eta_\pi = 1$. This can be done as follows for the (e, n) sub-sector

$$N_{ne}(p', p) = \sigma_Q \int dq (p'q \bar{\mu}(q) + q^2 \bar{\mu}(q)) \delta(p' + q - p), \quad (3.74a)$$

$$= \sigma_Q \int dq ((p - q)q \bar{\mu}(q) + q^2 \bar{\mu}(q)) \delta(p' + q - p), \quad (3.74b)$$

$$= \sigma_Q \int dq (pq \bar{\mu}(q)) \delta(p' + q - p), \quad (3.74c)$$

$$\eta_e \eta_n \overline{N_{ne}(p', p)} = -\sigma_Q \int dq (pq \bar{\mu}(q)) \delta(-p' + q + p) = N_{en}(p, p'), \quad (3.74d)$$

while for the momentum-charge sector, we have

$$N_{n\pi}(p', p) = \int dq (-p \bar{n}(q)) \delta(p' + q - p), \quad (3.75a)$$

$$\eta_n \eta_\pi \overline{N_{n\pi}(p', p)} = - \int dq (p \bar{n}(q)) \delta(-p' + q + p) = N_{\pi n}(p, p'). \quad (3.75b)$$

Finally, we only have to check the energy-momentum sector

$$N_{e\pi}(p', p) = - \int dq (p' \chi_{\pi\pi,0}(q) + q \bar{\epsilon}(q)) \delta(p' + q - p), \quad (3.76a)$$

$$\eta_e \eta_\pi \overline{N_{e\pi}(p', p)} = \int dq (-p' \chi_{\pi\pi,0}(q) + q \bar{\epsilon}(q)) \delta(-p' + q + p) = N_{\pi e}(p, p'). \quad (3.76b)$$

We see therefore that the Onsager reciprocal relations are obeyed by our equations (3.12).

3.C Second order corrections in lattice strength

Let us consider here a dynamical matrix $\hat{\mathcal{K}}$ of size $N \times N$. The modes of this matrix are given by the solutions to the polynomial equation $\mathcal{P}(\omega) \equiv \det \hat{\mathcal{K}} = 0$, where we can write

$$\mathcal{P}(\omega) = \sum_{n=0}^N a_n \omega^n . \quad (3.77)$$

Suppose the coefficients $a_n = \sum_p a_{n,p} A^p$ have a power series expansion in a parameter A . We are now interested in perturbative solutions $\omega = \bar{\omega} + A^2 \omega_2$, around a given $A = 0$ solution $\mathcal{P}(\bar{\omega})|_{A=0} = 0$. To do so we can define auxiliary polynomials $\mathcal{P}_p(\omega) = \sum_{n=0}^N a_{n,p} \omega^n$ such that

$$\mathcal{P}(\omega) = \sum_p A^p \mathcal{P}_p(\omega) . \quad (3.78)$$

We can now expand the equation $\mathcal{P}(\omega) = 0$ in A at leading and subleading orders, and we find the following two conditions

$$\mathcal{P}_0(\bar{\omega}) = 0 , \quad \omega_2 = -\frac{\mathcal{P}_2(\bar{\omega})}{\mathcal{P}'_0(\bar{\omega})} . \quad (3.79)$$

The first equation is simply the leading order of the mode when there is no lattice while the second equation gives us the subleading correction. Finally, all the coefficients $a_{n,p}$ are themselves polynomials in G, k which can be further expanded in order to get the corrections at higher order in momentum.¹⁵

So far, it was implicitly assumed that the modes have no degeneracy when $A \rightarrow 0$ as that would imply that $\mathcal{P}'_0(\bar{\omega}) = 0$. When that happens, the correction is given by higher order terms with

$$\mathcal{P}_0(\bar{\omega}) = 0 , \quad \mathcal{P}_2(\bar{\omega}) = 0 , \quad \omega_2 = \frac{-\mathcal{P}'_2(\bar{\omega}) \pm \sqrt{\left(\mathcal{P}'_2(\bar{\omega})\right)^2 - 4\mathcal{P}_4(\bar{\omega})\mathcal{P}''_0(\bar{\omega})}}{2\mathcal{P}''_0(\bar{\omega})} . \quad (3.80)$$

This is the case for $\hat{\mathcal{K}}_{L+}$ with $\bar{\omega} = 0$. However, it turns out that for this matrix, $\mathcal{P}_4(\bar{\omega}) = 0$ and $\mathcal{P}'_2(\omega) = 0$, so the two degenerate poles remain degenerate at this order in perturbation theory, with $\omega_2 = 0$. A simpler way to see this is also to notice that the first line of $\hat{\mathcal{K}}_{L+}$ is proportional to $i\omega$ and therefore so will be $\det \hat{\mathcal{K}}_{L+}$. Consequently, this sector admits an exact conservation mode and we can use our non-degenerate method on the 4×4 lower-right sub-block of this matrix where there is no degeneracy left. We would then see that the other $\bar{\omega} = 0$ pole also remains unshifted $\omega_2 = 0$.

¹⁵Note that in this method, the order of limits is chosen such that at finite k , we would be getting the $k > AV_{\text{int}}$ branch of solutions.

All that is therefore needed to compute the corrections in (3.54) and (3.57) is to know the coefficients $a_{n,p}$ for a given matrix $\hat{\mathcal{K}}$. In the case of $\hat{\mathcal{K}}_{L-}$, we have

$$a_{0,0} = 0, \quad a_{1,0} = -i(\chi_{\pi\pi,0})^3 \sigma_Q G^4, \quad a_{4,0} = (\chi_{\pi\pi,0})^2 d_\chi, \quad (3.81a)$$

$$a_{2,0} = -\chi_{\pi\pi,0} \left[\chi_{\epsilon\epsilon,0} n_0^2 - 2\chi_{n\epsilon,0} \chi_{\pi\pi,0} n_0 + \chi_{nn,0} (\chi_{\pi\pi,0})^2 \right] G^2 - \chi_{\epsilon\epsilon,0} \chi_{\pi\pi,0} \hat{\eta} \sigma_Q G^4, \quad (3.81b)$$

$$a_{3,0} = i\chi_{\pi\pi,0} \left(d_\chi \hat{\eta} + \chi_{\epsilon\epsilon,0} \chi_{\pi\pi,0} \sigma_Q \right) G^2, \quad (3.81c)$$

$$a_{0,2} = \frac{\mu_0^2}{2} (\chi_{n\epsilon,0} n_0 - \chi_{nn,0} \chi_{\pi\pi,0})^2 G^4 + \frac{\mu_0^2}{2} (\chi_{n\epsilon,0})^2 \hat{\eta} \sigma_Q G^6, \quad (3.81d)$$

$$a_{1,2} = -i \frac{1}{2} G^4 \left[\chi_{nn,0} \hat{\eta} \mu_0^2 d_\chi + \chi_{\pi\pi,0} \sigma_Q \left(2\mu_0 (\chi_{n\epsilon,1}^{(1)} \chi_{\pi\pi,0} - 2\chi_{n\epsilon,0} \chi_{\pi\pi,1}^{(1)}) + \mu_0^2 (\chi_{n\epsilon,0}^2 + \chi_{nn,0} \chi_{\pi\pi,0}) \right) \right. \\ \left. + 2\chi_{\pi\pi,2}^{(0)} \chi_{\pi\pi,0} + \mu_0^2 n_0^2 \right] - i \frac{\mu_0^2}{2} \chi_{\pi\pi,0} \hat{\eta} \sigma_Q^2 G^6, \quad (3.81e)$$

$$+ 2\chi_{\pi\pi,2}^{(0)} \chi_{\pi\pi,0} + \mu_0^2 n_0^2 \left] - i \frac{\mu_0^2}{2} \chi_{\pi\pi,0} \hat{\eta} \sigma_Q^2 G^6, \quad (3.81f)$$

$$a_{2,2} = \frac{1}{2} G^2 \left[-2n_0^2 (\chi_{\epsilon\epsilon,2}^{(0)} \chi_{\pi\pi,0} + \chi_{\epsilon\epsilon,0} \chi_{\pi\pi,2}^{(0)}) + \chi_{\pi\pi,0} n_0 (\mu_0 (-2\chi_{\epsilon\epsilon,0} \chi_{nn,1}^{(1)} + 2\chi_{n\epsilon,1}^{(1)} \chi_{n\epsilon,0} + \chi_{n\epsilon,0} \chi_{nn,0} \mu_0)) \right. \\ \left. + 4\chi_{n\epsilon,2}^{(0)} \chi_{\pi\pi,0} + 4\chi_{n\epsilon,0} \chi_{\pi\pi,2}^{(0)} - \chi_{\pi\pi,0} \left(\chi_{nn,0} \mu_0^2 (\chi_{nn,0} \chi_{\pi\pi,0} + d_\chi) \right) \right. \\ \left. + 2\chi_{\pi\pi,0} \mu_0 (\chi_{n\epsilon,1}^{(1)} \chi_{nn,0} - \chi_{n\epsilon,0} \chi_{nn,1}^{(1)}) + 2\chi_{\pi\pi,0} (\chi_{nn,2}^{(0)} \chi_{\pi\pi,0} + \chi_{nn,0} \chi_{\pi\pi,2}^{(0)}) + 4\chi_{\pi\pi,1}^{(1)} \mu_0 n_0 d_\chi \right] \\ (3.81g)$$

$$+ 4\chi_{n\epsilon,2}^{(0)} \chi_{\pi\pi,0} + 4\chi_{n\epsilon,0} \chi_{\pi\pi,2}^{(0)} - \chi_{\pi\pi,0} \left(\chi_{nn,0} \mu_0^2 (\chi_{nn,0} \chi_{\pi\pi,0} + d_\chi) \right) \quad (3.81h)$$

$$+ 2\chi_{\pi\pi,0} \mu_0 (\chi_{n\epsilon,1}^{(1)} \chi_{nn,0} - \chi_{n\epsilon,0} \chi_{nn,1}^{(1)}) + 2\chi_{\pi\pi,0} (\chi_{nn,2}^{(0)} \chi_{\pi\pi,0} + \chi_{nn,0} \chi_{\pi\pi,2}^{(0)}) + 4\chi_{\pi\pi,1}^{(1)} \mu_0 n_0 d_\chi \left] \\ (3.81i)$$

$$- \frac{\sigma_Q}{2} G^4 \left[\chi_{\pi\pi,0} \left(2\chi_{\epsilon\epsilon,2}^{(0)} \hat{\eta} + \chi_{nn,0} \hat{\eta} \mu_0^2 + \chi_{\pi\pi,0} \mu_0^2 \sigma_Q \right) + 2\chi_{\epsilon\epsilon,0} \chi_{\pi\pi,2}^{(0)} \hat{\eta} \right], \quad (3.81j)$$

$$a_{3,2} = \frac{1}{2} i G^2 \left[2\hat{\eta} \left(\chi_{\epsilon\epsilon,2}^{(0)} \chi_{nn,0} \chi_{\pi\pi,0} + \chi_{\epsilon\epsilon,0} \chi_{nn,2}^{(0)} \chi_{\pi\pi,0} + d_\chi \chi_{\pi\pi,2}^{(0)} - 2\chi_{n\epsilon,2}^{(0)} \chi_{n\epsilon,0} \chi_{\pi\pi,0} \right) \right. \\ \left. + \chi_{\pi\pi,0} \sigma_Q \left(2\chi_{\epsilon\epsilon,2}^{(0)} \chi_{\pi\pi,0} + 4\chi_{\epsilon\epsilon,0} \chi_{\pi\pi,2}^{(0)} + \chi_{nn,0} \chi_{\pi\pi,0} \mu_0^2 \right) - 4\chi_{\epsilon\epsilon,0} (\chi_{\pi\pi,1}^{(1)})^2 \sigma_Q \right], \quad (3.81k)$$

$$+ \chi_{\pi\pi,0} \sigma_Q \left(2\chi_{\epsilon\epsilon,2}^{(0)} \chi_{\pi\pi,0} + 4\chi_{\epsilon\epsilon,0} \chi_{\pi\pi,2}^{(0)} + \chi_{nn,0} \chi_{\pi\pi,0} \mu_0^2 \right) - 4\chi_{\epsilon\epsilon,0} (\chi_{\pi\pi,1}^{(1)})^2 \sigma_Q \left] , \quad (3.81l)$$

$$a_{4,2} = \chi_{\pi\pi,0} \left[\chi_{\epsilon\epsilon,2}^{(0)} \chi_{nn,0} \chi_{\pi\pi,0} + \chi_{\epsilon\epsilon,0} \chi_{nn,2}^{(0)} \chi_{\pi\pi,0} + 2d_\chi \chi_{\pi\pi,2}^{(0)} - 2\chi_{n\epsilon,2}^{(0)} \chi_{n\epsilon,0} \chi_{\pi\pi,0} \right] - 2d_\chi (\chi_{\pi\pi,1}^{(1)})^2. \\ (3.81m)$$

On the other hand, for the 4×4 lower-right sub-block of the matrix $\hat{\mathcal{K}}_{L+}$, we find the following coefficients for the determinant

$$a_{0,0} = 0, \quad a_{1,0} = -i\chi_{\epsilon\epsilon,0} (\chi_{\pi\pi,0})^2 \sigma_Q G^4, \quad a_{4,0} = \chi_{\pi\pi,0} \chi_{\epsilon\epsilon,0} d_\chi, \quad (3.82a)$$

$$a_{2,0} = -\chi_{\epsilon\epsilon,0} \left[\chi_{\epsilon\epsilon,0} n_0^2 - 2\chi_{n\epsilon,0} \chi_{\pi\pi,0} n_0 + \chi_{nn,0} (\chi_{\pi\pi,0})^2 \right] G^2 - (\chi_{\epsilon\epsilon,0})^2 \hat{\eta} \sigma_Q G^4, \quad (3.82b)$$

$$a_{3,0} = i\chi_{\epsilon\epsilon,0} G^2 \left(d_\chi \hat{\eta} + \chi_{\epsilon\epsilon,0} \chi_{\pi\pi,0} \sigma_Q \right), \quad (3.82c)$$

$$a_{0,2} = 0, \quad (3.82d)$$

$$\alpha_{1,2} = -\frac{1}{2}iG^4\sigma_Q \left[\chi_{\pi\pi,0} \left(2\chi_{\epsilon\epsilon,2}^{(0)}\chi_{\pi\pi,0} + 2\chi_{n\epsilon,1}^{(1)}\mu_0(\chi_{\epsilon\epsilon,0} - 2\chi_{\pi\pi,0}) + \chi_{nn,0}\mu_0^2(\chi_{\epsilon\epsilon,0} + \chi_{\pi\pi,0}) \right) \right] \quad (3.82e)$$

$$+ \chi_{\epsilon\epsilon,0}\mu_0^2n_0^2 \left] - \frac{1}{2}i\chi_{\epsilon\epsilon,0}\hat{\eta}G^6\mu_0^2\sigma_Q^2, \quad (3.82f)$$

$$\alpha_{2,2} = \frac{1}{2}G^2 \left[n_0^2 \left(-4\chi_{\epsilon\epsilon,2}^{(0)}\chi_{\epsilon\epsilon,0} + 4(\chi_{\epsilon\epsilon,1}^{(1)})^2 + 4\mu_0(\chi_{\epsilon\epsilon,0}\chi_{n\epsilon,1}^{(1)} - \chi_{\epsilon\epsilon,1}^{(1)}\chi_{n\epsilon,0}) - d_\chi\mu_0^2 \right) \right] \quad (3.82g)$$

$$+ 4\chi_{\pi\pi,0}n_0(\chi_{\epsilon\epsilon,2}\chi_{n\epsilon,0} - 2\chi_{\epsilon\epsilon,1}^{(1)}\chi_{n\epsilon,1}^{(1)} + \chi_{\epsilon\epsilon,1}^{(1)}\chi_{nn,0}\mu_0 + \chi_{\epsilon\epsilon,0}\chi_{n\epsilon,2}^{(0)} - \chi_{n\epsilon,1}^{(1)}\chi_{n\epsilon,0}\mu_0) \quad (3.82h)$$

$$- \chi_{\pi\pi,0} \left(2\chi_{\pi\pi,0} \left(\chi_{\epsilon\epsilon,2}^{(0)}\chi_{nn,0} + \chi_{\epsilon\epsilon,0}\chi_{nn,2}^{(0)} - 2(\chi_{n\epsilon,1}^{(1)})^2 \right) + 2\chi_{\epsilon\epsilon,0}\mu_0(\chi_{n\epsilon,1}^{(1)}\chi_{nn,0} - \chi_{n\epsilon,0}\chi_{nn,1}^{(1)}) \right) \quad (3.82i)$$

$$+ \chi_{\epsilon\epsilon,0}(\chi_{nn,0})^2\mu_0^2 + \chi_{\epsilon\epsilon,0}\mu_0n_0(-2\chi_{\epsilon\epsilon,0}\chi_{nn,1}^{(1)} + 2\chi_{n\epsilon,1}^{(1)}\chi_{n\epsilon,0} + \chi_{n\epsilon,0}\chi_{nn,0}\mu_0) \left] \quad (3.82j)$$

$$+ \frac{1}{2}G^4\sigma_Q \left[\hat{\eta} \left(-4\chi_{\epsilon\epsilon,2}^{(0)}\chi_{\epsilon\epsilon,0} + 4(\chi_{\epsilon\epsilon,1}^{(1)})^2 + 4\mu_0(\chi_{\epsilon\epsilon,0}\chi_{n\epsilon,1}^{(1)} - \chi_{\epsilon\epsilon,1}^{(1)}\chi_{n\epsilon,0}) \right) \right] \quad (3.82k)$$

$$+ \mu_0^2 \left((\chi_{n\epsilon,0})^2 - 2\chi_{\epsilon\epsilon,0}\chi_{nn,0} \right) - \chi_{\epsilon\epsilon,0}\chi_{\pi\pi,0}\mu_0^2\sigma_Q \left] , \quad (3.82l)$$

$$\alpha_{3,2} = \frac{1}{2}iG^2 \left[-2\hat{\eta} \left(-\chi_{\epsilon\epsilon,0} \left(2\chi_{\epsilon\epsilon,2}^{(0)}\chi_{nn,0} + \chi_{\epsilon\epsilon,0}\chi_{nn,2}^{(0)} - 2(\chi_{n\epsilon,1}^{(1)})^2 \right) + \chi_{\epsilon\epsilon,2}^{(0)}(\chi_{n\epsilon,0})^2 \right) \right] \quad (3.82m)$$

$$+ 2(\chi_{\epsilon\epsilon,1}^{(1)})^2\chi_{nn,0} + 2\chi_{n\epsilon,0}(\chi_{\epsilon\epsilon,0}\chi_{n\epsilon,2}^{(0)} - 2\chi_{\epsilon\epsilon,1}^{(1)}\chi_{n\epsilon,1}^{(1)}) \quad (3.82n)$$

$$+ \chi_{\pi\pi,0}\sigma_Q \left(4\chi_{\epsilon\epsilon,2}^{(0)}\chi_{\epsilon\epsilon,0} - 4(\chi_{\epsilon\epsilon,1}^{(1)})^2 + \mu_0(4\chi_{\epsilon\epsilon,1}^{(1)}\chi_{n\epsilon,0} - 4\chi_{\epsilon\epsilon,0}\chi_{n\epsilon,1}^{(1)}) \right) \quad (3.82o)$$

$$- \mu_0^2 \left(\chi_{n\epsilon,0}^2 - 2\chi_{\epsilon\epsilon,0}\chi_{nn,0} \right) + 2(\chi_{\epsilon\epsilon,0})^2\chi_{\pi\pi,2}^{(0)}\sigma_Q \left] , \quad (3.82p)$$

$$\alpha_{4,2} = \chi_{\pi\pi,0} \left[2\chi_{\epsilon\epsilon,2}^{(0)}\chi_{\epsilon\epsilon,0}\chi_{nn,0} - \chi_{\epsilon\epsilon,2}^{(0)}(\chi_{n\epsilon,0})^2 - 2(\chi_{\epsilon\epsilon,1}^{(1)})^2\chi_{nn,0} + 4\chi_{\epsilon\epsilon,1}^{(1)}\chi_{n\epsilon,1}^{(1)}\chi_{n\epsilon,0} \right] \quad (3.82q)$$

$$+ (\chi_{\epsilon\epsilon,0})^2\chi_{nn,2}^{(0)} - 2\chi_{\epsilon\epsilon,0}\chi_{n\epsilon,2}^{(0)}\chi_{n\epsilon,0} - 2\chi_{\epsilon\epsilon,0}(\chi_{n\epsilon,1}^{(1)})^2 + \chi_{\epsilon\epsilon,0}\chi_{\pi\pi,2}^{(0)}d_\chi \quad (3.82r)$$

The coefficients for the determinant of the full longitudinal matrix (3.45) are too involved to be written down here but can be obtained in the exact same way. All these corrections were derived using Mathematica.

3.D Numerical computations in strongly coupled field theories dual to Reissner-Nordström and Gubser-Rocha AdS black holes: set-up

3.D.1 Thermodynamics

In Sec. 3.4, we focused on the specific conformal hydrodynamics that emerges at long wavelength and low frequencies from the holographic dynamics of the RN and GR black holes. In equilibrium the thermodynamic equation of state of each is given by (3.59) and (3.60) respectively. From these, we can determine the charge density $n_0 = \left(\frac{\partial P}{\partial \mu}\right)_T$ as well as the entropy density $s_0 = \left(\frac{\partial P}{\partial T}\right)_\mu$ while the energy density just follows from conformal invariance and is given by $\epsilon_0 = 2P_0$. One can further compute the various susceptibilities $\chi_{ab,m}^{(n)}$ appearing in the hydrodynamics expressions of Sec. 3.3. As a reminder from Appendix 3.A, the conformal equation of state also imposes $\chi_{\epsilon\epsilon,0} = 2\chi_{\pi\pi,0}$ and $\chi_{n\epsilon,0} = \chi_{\epsilon n,0} = 2n_0$. For the RN black hole, the various susceptibilities and thermodynamic quantities are

$$n_0 = \frac{\mu_0}{6} \sqrt{3\mu_0^2 + 16\pi^2 T_0^2} + \frac{2\pi\mu_0 T_0}{3} = \frac{\chi_{n\epsilon,0}}{2} = \frac{\chi_{\epsilon n,0}}{2}, \quad (3.83a)$$

$$s_0 = \frac{8\pi^2}{9} T_0 \sqrt{3\mu_0^2 + 16\pi^2 T_0^2} + \frac{\pi}{9} (3\mu_0^2 + 32\pi^2 T_0^2), \quad (3.83b)$$

$$\chi_{nn,0} = \frac{1}{6} \left(\frac{2(3\mu_0^2 + 8\pi^2 T_0^2)}{\sqrt{3\mu_0^2 + 16\pi^2 T_0^2}} + 4\pi T_0 \right), \quad (3.83c)$$

$$\chi_{\pi\pi,0} = \frac{3\mu_0^4 \left(2\pi T_0 \left(4\pi T_0 - \sqrt{3\mu_0^2 + 16\pi^2 T_0^2} \right) + \mu_0^2 \right)}{2 \left(\sqrt{3\mu_0^2 + 16\pi^2 T_0^2} - 4\pi T_0 \right)^3} = \frac{\chi_{\epsilon\epsilon,0}}{2}, \quad (3.83d)$$

$$\chi_{nn,1}^{(1)} = \frac{3\mu_0^2 (\mu_0^2 + 8\pi^2 T_0^2)}{2 (3\mu_0^2 + 16\pi^2 T_0^2)^{3/2}}, \quad \chi_{n\epsilon,1}^{(1)} = \frac{\mu_0}{6} \left(\frac{2(3\mu_0^2 + 8\pi^2 T_0^2)}{\sqrt{3\mu_0^2 + 16\pi^2 T_0^2}} + 4\pi T_0 \right), \quad (3.83e)$$

$$\chi_{\pi\pi,1}^{(1)} = \frac{\mu_0^2}{4} \sqrt{3\mu_0^2 + 16\pi^2 T_0^2} + \pi\mu_0^2 T_0 = \frac{\chi_{\epsilon\epsilon,1}^{(1)}}{2}, \quad (3.83f)$$

$$\chi_{nn,2}^{(0)} = \frac{96\pi^4 \mu_0^2 T_0^4}{(3\mu_0^2 + 16\pi^2 T_0^2)^{5/2}}, \quad \chi_{n\epsilon,2}^{(0)} = \frac{3\mu_0^3 (\mu_0^2 + 8\pi^2 T_0^2)}{2 (3\mu_0^2 + 16\pi^2 T_0^2)^{3/2}}, \quad (3.83g)$$

$$\chi_{\pi\pi,2}^{(0)} = \frac{3\mu_0^4 + 2\pi\mu_0^2 T_0 \left(\sqrt{3\mu_0^2 + 16\pi^2 T_0^2} + 4\pi T_0 \right)}{4\sqrt{3\mu_0^2 + 16\pi^2 T_0^2}} = \frac{\chi_{\epsilon\epsilon,2}^{(0)}}{2}, \quad (3.83h)$$

while for the GR black hole we have

$$n_0 = \frac{\mu_0}{3} \sqrt{3\mu_0^2 + 16\pi^2 T_0^2} = \frac{\chi_{\epsilon n,0}}{2}, \quad s_0 = \frac{16\pi^2}{9} T_0 \sqrt{3\mu_0^2 + 16\pi^2 T_0^2}, \quad (3.84a)$$

$$\chi_{nn,0} = \frac{2(3\mu_0^2 + 8\pi^2 T_0^2)}{3\sqrt{3\mu_0^2 + 16\pi^2 T_0^2}}, \quad \chi_{\pi\pi,0} = \frac{1}{9} (3\mu_0^2 + 16\pi^2 T_0^2)^{3/2} = \frac{\chi_{\epsilon\epsilon,0}}{2}, \quad (3.84b)$$

$$\chi_{nn,1}^{(1)} = \frac{3\mu_0^2 (\mu_0^2 + 8\pi^2 T_0^2)}{(3\mu_0^2 + 16\pi^2 T_0^2)^{3/2}}, \quad \chi_{nc,1}^{(1)} = \frac{2\mu_0 (3\mu_0^2 + 8\pi^2 T_0^2)}{3\sqrt{3\mu_0^2 + 16\pi^2 T_0^2}}, \quad (3.84c)$$

$$\chi_{\pi\pi,1}^{(1)} = \frac{\mu_0^2}{2} \sqrt{3\mu_0^2 + 16\pi^2 T_0^2} = \frac{\chi_{\epsilon\epsilon,1}^{(1)}}{2}, \quad \chi_{nn,2}^{(0)} = \frac{192\pi^4 \mu_0^2 T_0^4}{(3\mu_0^2 + 16\pi^2 T_0^2)^{5/2}}, \quad (3.84d)$$

$$\chi_{nc,2}^{(0)} = \frac{3\mu_0^3 (\mu_0^2 + 8\pi^2 T_0^2)}{(3\mu_0^2 + 16\pi^2 T_0^2)^{3/2}}, \quad \chi_{\pi\pi,2}^{(0)} = \frac{\mu_0^2 (3\mu_0^2 + 8\pi^2 T_0^2)}{2\sqrt{3\mu_0^2 + 16\pi^2 T_0^2}} = \frac{\chi_{\epsilon\epsilon,2}^{(0)}}{2}. \quad (3.84e)$$

Lastly, we need to know some information on the transport coefficients η and σ_Q to compute the hydrodynamic response. These can be determined in the momentum-dependent homogeneous systems through $\eta = \lim_{\omega \rightarrow 0} \frac{1}{\omega} \text{Im} G_{T_{xy}T_{xy}}(\omega, k=0)$ and $\sigma_Q = \lim_{\omega \rightarrow 0} \frac{1}{\omega} \text{Im} G_{J_x J_x}(\omega, k=0)$. In the case of conformal-to-AdS₂ solutions like the RN and GR black holes, these expressions can be solved analytically for the two transport coefficients. The shear viscosity η saturates the minimal viscosity bound $\eta = \frac{s_0}{4\pi}$ [199] while σ_Q was computed for a wide class of scaling black hole solutions [175] and here is given by

$$\sigma_Q = \frac{4\pi^2 T_0^2}{9} \left(\frac{\sqrt{3\mu_0^2 + 16\pi^2 T_0^2} - 4\pi T_0}{\mu_0^2 - 2\pi T_0 \sqrt{3\mu_0^2 + 16\pi^2 T_0^2} + 8\pi^2 T_0^2} \right)^2 \quad \text{for RN}, \quad (3.85a)$$

$$\sigma_Q = \left(1 + \frac{3\mu_0^2}{16\pi^2 T_0^2} \right)^{-3/2} \quad \text{for GR}. \quad (3.85b)$$

3.D.2 Numerics

We briefly review here how we compute the optical conductivity in the 2+1 dimensional strongly coupled conformal field theory holographically dual to the RN and

GR black holes in the presence of a lattice. More details about the numerical methods used to compute these backgrounds and fluctuations can be found in the companion article [184]. The homogeneous RN black hole is a saddle point of the Einstein-Maxwell action

$$S = \int d^4x \sqrt{-g} \left[(R - 2\Lambda) - \frac{1}{4} F_{\mu\nu} F^{\mu\nu} \right], \quad (3.86)$$

with metric

$$ds^2 = g_{\mu\nu} dx^\mu dx^\nu = \frac{1}{z^2} \left[-f(z) dt^2 + \frac{dz^2}{f(z)} + dx^2 + dy^2 \right], \quad A = A_t(z) dt, \quad (3.87)$$

where $f(z) = (1-z) \left(1+z+z^2 - \frac{\mu^2 z^3}{4} \right)$ is the emblackening factor and $A_t(z) = \mu(1-z)$ a $U(1)$ gauge field. In the above expressions, z is the radial coordinate ranging from the AdS boundary at $z=0$ to the horizon of the black hole at $z=1$. The temperature of this black hole is $T = \frac{12-\mu^2}{16\pi}$.¹⁶

The GR black hole is similarly obtained by extremizing the Einstein-Maxwell-Dilaton action

$$S = \frac{1}{2\kappa^2} \int d^4x \sqrt{-g} \left[R - \frac{Z(\phi)}{4} F_{\mu\nu} F^{\mu\nu} - \frac{1}{2} (\partial_\mu \phi)^2 + V(\phi) \right], \quad (3.88)$$

with the potentials $Z(\phi) = e^{\phi/\sqrt{3}}$ and $V(\phi) = 6 \cosh(\phi/\sqrt{3})$. Its metric is

$$ds^2 = g_{\mu\nu} dx^\mu dx^\nu = \frac{1}{z^2} \left[-h(z) dt^2 + \frac{1}{h(z)} dz^2 + g(z) (dx^2 + dy^2) \right], \quad (3.89a)$$

$$A = \sqrt{3Q(1+Q)} \frac{(1-z)}{1+Qz} dt, \quad \phi = \frac{\sqrt{3}}{2} \log(1+Qz). \quad (3.89b)$$

The functions $h(z)$ and $g(z)$ are given by

$$h(z) = \frac{(1-z)}{g(z)} \left[1 + (1+3Q)z + (1+3Q(1+Q))z^2 \right], \quad g(z) = (1+Qz)^{3/2}. \quad (3.90)$$

This model is similar to the Einstein-Maxwell model with the addition of a neutral scalar field ϕ which controls the strength of the $U(1)$ charge through the potential $Z(\phi)$. A consequence of this is the ability to discharge some of the black hole charge near the horizon such that the extremal $T=0$ solution of this GR black hole will have a vanishing horizon and therefore vanishing entropy $S_{T=0} = 0$. The distance from extremality is controlled by the parameter Q : it is related to the chemical potential

¹⁶A priori, if we allowed the black hole horizon to be arbitrarily located at $z = z_h$, the temperature and chemical potential would be two independent parameters. However, when using the freedom to rescale the radial coordinate such that $z_h = 1$, we have implicitly fixed the temperature as a function of the chemical potential such that the only thermodynamic degree of freedom here is T/μ .

through $\mu = \sqrt{3Q(1+Q)}$ and the temperature of the non-extremal black hole is given by $T = \frac{3\sqrt{1+Q}}{4\pi}$.

To obtain backgrounds with an explicit lattice, we will allow for a more general ansatz

$$ds^2 = \frac{1}{z^2} \left(-Q_{tt} f(z) \eta_t^2 + Q_{xx} \eta_x^2 + Q_{yy} \eta_y^2 + \frac{Q_{zz}}{f(z)} \eta_z^2 \right), \quad (3.91a)$$

$$\eta_t = dt, \quad \eta_y = dy, \quad \eta_z = dz, \quad \eta_x = dx + Q_{xz} dz, \quad (3.91b)$$

$$A = \mu(1-z) a_t dt, \quad (3.91c)$$

for RN with $f(z)$ unchanged from (3.87) and

$$ds^2 = \frac{1}{z^2} \left(-Q_{tt} h(z) \eta_t^2 + g(z) (Q_{xx} \eta_x^2 + Q_{yy} \eta_y^2) + \frac{Q_{zz}}{h(z)} \eta_z^2 \right), \quad (3.92a)$$

$$\eta_t = dt, \quad \eta_y = dy, \quad \eta_z = dz, \quad \eta_x = dx + Q_{xz} dz, \quad (3.92b)$$

$$A = \frac{\mu(1-z)}{1+Qz} a_t dt, \quad \phi = \frac{3}{2} \log(1 + \varphi(z) Qz). \quad (3.92c)$$

for GR with $h(z)$ and $g(z)$ unchanged from (3.89), but every field Q_{ij}, a_t, φ is now a priori a function of x and z . We require these fields to be regular near the horizon¹⁷ and that their UV behavior at $z = 0$ recovers AdS asymptotics.¹⁸ Moreover, to encode the modulation of the chemical potential, we must impose the following boundary condition on the gauge field

$$a_t(z=0) = 1 + A \cos(Gx). \quad (3.93)$$

The system is then solved numerically for the unknown functions Q_{ij}, a_t, φ .

To compute the optical conductivity in the holographically dual field theory, we must consider small fluctuations on top of this spatially modulated background. We linearize the Einstein equations around our lattice background

$$g_{\mu\nu} = \bar{g}_{\mu\nu} + \delta h_{\mu\nu} e^{-i\omega t + ikx}, \quad (3.94a)$$

$$A_\mu = \bar{A}_\mu + \delta b_\mu e^{-i\omega t + ikx}, \quad (3.94b)$$

$$\varphi = \bar{\varphi} + \delta \psi e^{-i\omega t + ikx}, \quad (3.94c)$$

and solve for these fluctuations with infalling boundary conditions, corresponding to choosing the response sourced through the retarded Green's function. The response

¹⁷One of the regularity conditions near the horizon is that $Q_{tt}(z=1) = Q_{zz}(z=1)$. This choice has the direct consequence that the temperature of the black hole remains constant and given by the homogeneous value for each model.

¹⁸In the case of the dilaton ϕ , the UV boundary condition chosen is a multi-trace deformation chosen such that the deformation is marginal and the boundary remains conformal. For more details, see [170].

in the radial electric field F_{zx} in answer to an oscillating source in the potential $\delta\partial_t A_x(\omega) \equiv \delta b_x$ keeping the other components sourceless¹⁹ evaluated in the limit $z \rightarrow 0$ then translates through the holographic AdS/CFT correspondence into the longitudinal optical conductivity $\sigma = \lim_{z \rightarrow 0} \frac{F_{zx}}{\partial_t A_x} = \frac{\delta J_x}{\delta E_x}$. In the language of our hydrodynamic setup in Sec. 3.2, this is akin to simply turning on an external electric field δE_x with momentum k and frequency ω . This response is also solved for numerically.

The numerical solutions to these equations were obtained using a publicly available custom package [173] and computed on the Dutch national Cartesius and Snellius supercomputers with the support of SURF Cooperative.

¹⁹Note that the condition for the dilaton to be sourceless is non-trivial and inherited from the mixed boundary condition of the background dilaton (see footnote 18).

Chapter 4

Quantization and thermodynamics of the Gubser-Rocha black hole solution

Attribution

This chapter was published as a journal article under the title “Quantization and variational problem of the Gubser-Rocha Einstein-Maxwell-Dilaton model, conformal and non-conformal deformations, and its proper thermodynamics” in the *Journal of High Energy Physics (JHEP)*, volume 2023, article number 81 (2023), together with Floris Balm and Koenraad Schalm.

4.1 Introduction

One of the main insights holography has provided into the physics of strongly correlated systems is the existence of previously unknown (large N) non-trivial IR fixed points. These fixed points are characterized by an emergent scaling symmetry of the Lifshitz form categorized by a dynamical critical exponent z , a hyperscaling exponent θ , and a charge anomalous dimension ζ .

$$x \rightarrow \lambda^{1/z} x, \quad t \rightarrow \lambda t, \quad F \rightarrow \lambda^{\frac{d-\theta}{z}} F, \quad \rho \rightarrow \lambda^{\frac{d-\theta+\zeta}{z}} \rho. \quad (4.1)$$

Here F is the free energy density and ρ the charge density [32, 34, 35, 36]. Within these Lifshitz fixed points those with $z = \infty$ are special. Such theories have energy/temperature scaling with no corresponding spatial rescaling. These are there-

fore systems with exact *local quantum criticality*. Phenomenologically this energy/temperature scaling without a corresponding spatial part is observed in high T_c cuprates, heavy fermions and other strange metals, where this nomenclature originates (see *e.g.*, [200]). In holography $z = \infty$ IR fixed points correspond to an emergent AdS_2 symmetry near the horizon of the extremal black hole. The two most well-known such solutions are the plain extremal Reissner-Nordström (RN) black hole and the extremal Gubser-Rocha (GR) black hole [38]. The RN solution of AdS-Einstein-Maxwell theory has been studied extensively primarily because it is the simplest such model. Its simplicity also means it is too constrained to be realistic as a model of observed locally quantum critical metals. Notably the RN has a non-vanishing ground-state entropy and emerges from a $d > 2$ -dimensional conformal field theory. The more realistic GR model arises from a non-conformal strongly correlated theory, where one isolates the leading irrelevant deformation from the IR fixed point. This “universal” subsector gives it a chance to be applicable to observed local quantum critical systems. Moreover the groundstate now has vanishing entropy (to leading order). In the gravitational description this leading (scalar) (IR)-irrelevant operator is encoded in a dilaton field that couples non-minimally to both the Einstein-Hilbert action and the Maxwell action. Even with its more realistic appeal, the more complex nature of the GR dynamics means it has been studied less; some examples are [201, 118, 86, 202, 203].

In the course of these studies of non-minimally coupled Einstein-Maxwell-Dilaton (EMD) theories, it was noted in particular that the proper holographic interpretation of the analytical Gubser-Rocha (aGR) black hole solution depends sensitively on the particular quantization [202, 203]. Within holography, relevant and marginally relevant scalars allow for different quantization schemes. A relevant operator of dimension $\frac{d}{2} < \Delta < d$ always has a conjugate operator of dimension¹ $\frac{d}{2} - 1 < \Delta_{\text{conj}} = d - \Delta < \frac{d}{2}$, and one can choose whether one considers the original operator as the dynamical variable (standard quantization) or the conjugate operator (alternate quantization) or any intermediate linear combination through a double-trace deformation [204, 205].

An additional complication results from the fact that the (static and isotropic) aGR solution is a two-parameter solution depending on T and μ , whereas one expects a third independent parameter encoding the asymptotic source value of the dilaton field. A low-energy scalar can have a sourced (or unsourced) vacuum-expectation value; this changes the energy of the ground-state and hence should contribute to the thermodynamics. For minimally coupled scalars this was recently elucidated in [206].

In this paper we will show that the correct way to interpret the aGR solution is as a two-parameter subset of solutions within the three-parameter thermodynamic phase diagram. For essentially all quantization schemes this constrains the source of the dilaton field in terms of the temperature and chemical potential of the solution. Crucially this implies that derivatives of thermodynamic potentials mix the canonical

¹The upper bound of Δ would suggest $\Delta_{\text{conj}} > 0$ but requiring unitarity of the conjugate theory leads to a higher bound.

contribution with an additional contribution from the scalar response. We will show this explicitly in Section 4.3.2. A proper understanding of the solution requires one to carefully separate out this contribution.

It also turns out, however, that there is a specific quantization scheme where the dilaton corresponds to an exactly marginal operator in the theory. This was previously noted for another set of the EMD actions [203].² In this special quantization choice the aGR solution corresponds to a solution with no explicit source for the dilaton field. Within this special quantization scheme one can deform the analytical solution to a nearby solution with a finite scalar source. We do so in Section 4.4. We conclude with a brief discussion on the meaning of this newly discovered exactly marginal deformation.

4.2 Setup

The GR black hole is a solution to the EMD action

$$S_{\text{bulk}} = \frac{1}{2\kappa^2} \int d^4x \sqrt{-g} \left[R - \frac{Z(\phi)}{4} F^2 - \frac{1}{2} (\partial\phi)^2 - V(\phi) \right], \quad (4.2)$$

where the potentials are given by $Z(\phi) = e^{\phi/\sqrt{3}}$ and $V(\phi) = -6 \cosh(\phi/\sqrt{3})$.³ This action is a consistent truncation of $d = 11$ supergravity compactified on $AdS_4 \times S_7$ [38]. The equations of motion for this system are

$$\begin{aligned} R_{\mu\nu} &= \frac{Z(\phi)}{2} \left[F_{\mu}{}^{\rho} F_{\nu\rho} - \frac{1}{4} g_{\mu\nu} F^2 \right] + \frac{1}{2} \partial_{\mu}\phi \partial_{\nu}\phi + \frac{1}{2} g_{\mu\nu} V(\phi), \\ \nabla_{\mu} [Z(\phi) F^{\mu\nu}] &= 0, \\ \square\phi &= V'(\phi) + \frac{Z'(\phi)}{4} F^2, \end{aligned} \quad (4.3)$$

where we used that, on-shell, $R = 2V(\phi) + \frac{1}{2}(\partial\phi)^2$. The static and isotropic metric ansatz that is asymptotically AdS is

$$ds^2 = g_{\mu\nu} dx^{\mu} dx^{\nu} = \frac{1}{z^2} \left[-f(z) dt^2 + g(z) (dx^2 + dy^2) + \frac{dz^2}{f(z)} \right], \quad (4.4)$$

²We thank Blaise Goutéraux for bringing this paper to our attention.

³Note that the dilaton has dimension zero.

where the coordinate z is the radial direction with $z = 0$ the AdS boundary (UV). The aGR solution [38] is then given by

$$\begin{aligned}
 g(z) &= (1 + Qz)^{3/2}, \\
 f(z) &= \frac{1 - z/z_h}{g(z)} \left[1 + (1 + 3Qz_h) \frac{z}{z_h} + \left(1 + 3Qz_h + 3Q^2 z_h^2 \right) \left(\frac{z}{z_h} \right)^2 \right], \\
 A_t(z) = \mu j(z) &= \frac{\sqrt{3Qz_h(1 + Qz_h)}}{z_h} \frac{1 - z/z_h}{1 + Qz}, \\
 \phi(z) &= \frac{\sqrt{3}}{2} \log[1 + Qz],
 \end{aligned} \tag{4.5}$$

where z_h is the horizon of this non-extremal black hole. From hereon we choose units where $2\kappa^2 = 16\pi G = 1$, such that the temperature, chemical potential and entropy-density of the GR-black hole are

$$\begin{aligned}
 T = - \left. \frac{f'(z)}{4\pi} \right|_{z=z_h} &= \frac{3\sqrt{1 + Qz_h}}{4\pi z_h}, \quad s = 4\pi a_h = 4\pi \frac{(1 + Qz_h)^{3/2}}{z_h^2}, \\
 \mu = A_t(z = 0) &= \sqrt{3Qz_h(1 + Qz_h)}/z_h,
 \end{aligned} \tag{4.6}$$

where $a_h = \sqrt{g_{xx}(z_h)g_{yy}(z_h)}$ is the area density of the horizon. Expressed in terms of the temperature, it is easy to see that the entropy vanishes linearly $s = \frac{16\pi^2}{3\sqrt{3}} \mu T + \dots$ at low temperatures with no remnant ground state entropy. Important in the remainder is (1) to recall that both the temperature and the entropy can be read off from the near-horizon behavior of the metric alone. As local properties of the black hole they do not depend on the boundary conditions. (2) The analytic solution depends on two parameters Q and z_h . And (3) note that the metric gauge choice is not of the Fefferman-Graham (FG) type in that the change in metric functions starts at order z and not z^3 .

4.3 Regularization, boundary terms and choice of quantization

4.3.1 Boundary action

We must add to the gravitational action (4.2) a boundary action. This is to regularize its on-shell value as well as to make the variational principle well-defined. In the case of the scalar it also prescribes the quantization of the scalar field. We will be using in this work a standard multi-trace deformation of the Neumann boundary theory, which were generally described in [204, 205, 207] and more specifically in EMD

theories [203], with a boundary action of the form

$$S_{\text{bdy}} = - \int_{z=\epsilon} d^3x \sqrt{-\gamma} \left[2K + 4 + {}^{(3)}R_\gamma \right] + S_{\text{bdy},\phi}, \quad (4.7)$$

Here $N^\mu = -\sqrt{g^{zz}}(0, 0, 0, 1)$ is an outward pointing spacelike unit normal vector defining the hypersurface $z = \epsilon \ll z_h$ and $\gamma_{\mu\nu} = g_{\mu\nu} - N_\mu N_\nu$ is the induced metric on the surface. Furthermore $K \equiv \gamma^{ij} K_{ij}$ is the trace of the extrinsic curvature $K_{ij} \equiv -\gamma_i^\mu \gamma_j^\nu \nabla_{(\mu} N_{\nu)}$ and ${}^{(3)}R_\gamma$ the Ricci scalar curvature of the hypersurface (Latin symbols correspond to coordinates on the hypersurface while the Greek symbols are those of the original manifold). The first three terms correspond to the usual Gibbons-Hawking-York counterterms necessary to make the variational principle for the metric well-defined and also to regularize the Einstein-Hilbert-Cosmological Constant part of the action on shell. In our coordinatization Eq. (4.4) the induced metric is flat on-shell. The scalar part of the boundary term $S_{\text{bdy},\phi}$ can take two forms depending on whether we consider the standard quantization boundary theory where only the ϕ^2 regularization term appears

$$S_{\text{bdy},\phi}^{(\text{SQ})} = \int_{z=\epsilon} d^3x \sqrt{-\gamma} \frac{\Lambda_\phi}{2} \phi^2, \quad \Lambda_\phi = -1, \quad (4.8)$$

— here the value of Λ_ϕ is set to regularize the boundary term arising from varying the bulk action — or whether we consider a multi-trace deformation of the alternate quantization boundary theory

$$S_{\text{bdy},\phi}^{(\text{MT})} = \int_{z=\epsilon} d^3x \sqrt{-\gamma} \left[\frac{\Lambda_\phi}{2} \phi^2 + \phi N^\mu \partial_\mu \phi \right] + S_F, \quad \Lambda_\phi = 1. \quad (4.9)$$

The $\phi N^\mu \partial_\mu \phi$ is a Legendre transform from Dirichlet to Neumann boundary conditions, which also diverges at leading order and is the reason for the shift in Λ_ϕ as we will see.⁴ The multi-trace deformation S_F is a finite contribution to the boundary action and will be described when the asymptotics of the solution are analyzed. We will continue the derivation with the choice $S_{\text{bdy},\phi} = S_{\text{bdy},\phi}^{(\text{MT})}$ while keeping in mind that a similar derivation can easily be done using instead $S_{\text{bdy},\phi} = S_{\text{bdy},\phi}^{(\text{SQ})}$, and we will invoke those results when necessary.

Varying the total action $S = S_{\text{bulk}} + S_{\text{bdy}}$ to first order, a proper holographic interpretation demands that one obtains a variation of the form [208]

$$\delta S = \int_{z=\epsilon} d^3x \sqrt{-\gamma} \left[\frac{1}{2} T_{\mu\nu} \delta \gamma^{\mu\nu} + J^\mu \delta A_\mu + \mathcal{O}_\phi \delta \phi \right], \quad (4.10)$$

where the terms multiplying the EMD fields are interpreted as the operators in the boundary CFT where $T_{\mu\nu}$ is the boundary stress tensor, J_μ the boundary current

⁴Strictly speaking $\phi N^\mu \partial_\mu \phi$ is a combination of a true Legendre transform $\mathcal{J}\mathcal{O} = z^{\lambda-} z^{-\lambda+} \phi \partial_n z^{-\lambda-} \phi$ (see Eq. (4.13)) and counterterms.

associated with the U(1) charge, and \mathcal{O}_φ the operator dual to a scalar which may be a non-linear function of the dilaton field. The important point is that the action evaluated on the black hole solution is equated with (minus) its Gibbs free energy density. The variation of the action (restricted to preserve isotropy) thus includes thermodynamic variations. The expression above makes clear that in addition to the temperature and the chemical potential there ought to be a dependence of the Gibbs free energy on an external (source) variation of (the boundary value of) the scalar field [206].

Performing this variation on Eqs (4.2) plus (4.7), we can write it as a bulk integral of an integrand proportional to the equations of motion (4.3), that vanishes on-shell, and a remaining boundary part. In the boundary part the normal derivatives of $\delta\gamma_{\mu\nu}$ cancel due to the Gibbons-Hawking-York term; there are no normal derivatives in A_μ . Restricting to boundary indices we have⁵

$$\begin{aligned} T_{ij} &= 2K_{ij} - 2({}^d R_{\gamma,ij}) - 2(K+2)\gamma_{ij} + \gamma_{ij} \left[\phi N^z \partial_z \phi + \Lambda_\phi \phi^2/2 \right] + T_{ij}^F, \\ J_i &= -Z(\phi) N^z F_{zi}, \end{aligned} \quad (4.11)$$

where T_{ij}^F is the contribution from S_F . The expression for \mathcal{O}_φ requires a more detailed discussion. Focusing on the variation in the dilaton ϕ in (4.10), we have

$$\delta S_\phi = \int_{z=\epsilon} d^3x \sqrt{-\gamma} \left[\Lambda_\phi \phi \delta\phi + \phi N^z \partial_z \delta\phi \right] + \delta S_F. \quad (4.12)$$

From its linearized equation of motion the dilaton has the following expansion in the near-boundary region

$$\phi(z) = \alpha z^{\lambda_-} + \beta z^{\lambda_+} + \mathcal{O}(z^3), \quad (4.13)$$

where $\lambda_\pm = \frac{3}{2} \pm \frac{1}{2} \sqrt{9+4m^2}$ and m is the effective mass. In the GR model the effective mass equals

$$m^2 = \frac{\partial}{\partial \phi^2} \left[V(\phi) + \frac{Z(\phi)}{4} F^2 \right] \Big|_{\phi=0, z \rightarrow 0} = -2. \quad (4.14)$$

This value of the mass $-\frac{9}{4} < m^2 < 1 - \frac{9}{4} = -\frac{5}{4}$ is in the regime where two different quantizations are allowed, *i.e.*, for this value of m both $\lambda_\pm > 0$ and either α (standard) or β (alternate) can be chosen as the source for the dual CFT operator with the other the response. One can also choose a mixture of the two, corresponding to a multi trace deformation, as we shall elucidate below.

The proper holographic normalization is most conveniently performed in a FG ansatz for the metric

$$ds^2 = \frac{1}{z^2} \left[-H_{tt}(z) dt^2 + H_{xx}(z) dx^2 + H_{yy}(z) dy^2 + dz^2 \right], \quad (4.15)$$

⁵The radial components of $T_{\mu\nu}$ and J_μ vanish due to the projection on the hypersurface.

where we require Anti-deSitter (AdS) asymptotics $H_{\mu\nu}(z=0) = 1$ and use the equations of motion (4.3) to constrain the near-boundary expansion of $H_{\mu\nu}$ in terms of a small subset of degrees of freedom. We will use this ansatz for the remainder of this section. Using that $N^z(z) = -z$, and substituting (4.13) into (4.12), we can expand the variation w.r.t. the dilaton as

$$\delta S_\phi = \int_{z=\epsilon} d^3x \left[\frac{\Lambda_\phi - 1}{\epsilon} \alpha \delta\alpha + \alpha \delta\beta (\Lambda_\phi - 2) + \beta \delta\alpha (\Lambda_\phi - 1) + \mathcal{O}(\epsilon) \right] + \delta S_F . \quad (4.16)$$

As we claimed in (4.9), we must remove the leading divergence by imposing $\Lambda_\phi = 1$, leaving a finite contribution

$$\delta S_\phi = \int_{z=\epsilon} d^3x [-\alpha \delta\beta + \mathcal{O}(\epsilon)] + \delta S_F . \quad (4.17)$$

For the standard quantization term (4.8), it is easy to see that a similar derivation leads to $\Lambda_\phi = -1$.

One can modify the quantization by the addition of a multitrace deformation. This can in general be encoded in the boundary action S_F . Following [207, 209, 203], we choose $S_F = \int d^3x \sqrt{-\bar{\gamma}} \epsilon^d \mathcal{F}(\alpha)$ such that, ignoring the metric variation, $\delta S_F = \int d^3x \sqrt{-\bar{\gamma}} \epsilon^d \mathcal{F}'(\alpha) \delta\alpha$. Without loss of generality we choose \mathcal{F} of the form $\mathcal{F}(\alpha) = \frac{a}{2} \alpha^2 + \frac{b}{3} \alpha^3$ from here on. The variation of the boundary action then becomes

$$\delta S_\phi = \int_{z=\epsilon} d^3x \alpha [-\delta\beta + (a + b\alpha) \delta\alpha] . \quad (4.18)$$

We can therefore identify the VEV of the boundary scalar operator as $\mathcal{O}_\phi = \alpha$ while the source of the operator is

$$J_{\text{MT}} = -\beta + a\alpha + \frac{b}{2} \alpha^2 . \quad (4.19)$$

Once again, had we chosen the standard quantization boundary term, then we would have $\delta S_\phi = \int d^3x \beta \delta\alpha$ such that $\mathcal{O}_\phi = \beta$ and $\varphi = \alpha$ leading to the boundary condition $J_{\text{SQ}} = \alpha$.

We have now almost all the ingredients to compute the scalar contribution to the stress tensor, but we still need to derive the variation of S_F w.r.t. the leading order of the boundary metric in order to compute the term T_{ij}^F , as was done before in [203]. Doing so, one simply finds $T_{ij}^F = \gamma_{ij} \epsilon^d \mathcal{F}(\alpha)$. It is interesting to note that the contribution S_F can also be absorbed into corrections to the ϕ^2 term as well as a ϕ^3 term as

$$S_{\text{bdy}} = \int_{z=\epsilon} d^3x \sqrt{-\bar{\gamma}} \left[-(2K + 4 + {}^{(3)}R_\gamma) + \frac{\Lambda_\phi + \epsilon a}{2} \phi^2 + \phi N^\mu \partial_\mu \phi + \frac{b}{3} \phi^3 \right] , \quad (4.20)$$

where $\Lambda_\phi + \epsilon a$ is a renormalized ϕ^2 coupling which will reproduce the α^2 contribution of \mathcal{F} , as was done in *e.g.*, [204, 210]. The ϕ^3 coupling on the other end will reproduce

the α^3 contribution of \mathcal{F} . This way of writing the boundary action highlights why we concentrated on \mathcal{F} of the form $\mathcal{F}(\alpha) = \frac{a}{2}\alpha^2 + \frac{b}{3}\alpha^3$. Lower order in α terms are constant shifts variationally and can be absorbed in a field redefinition – they are tadpoles. Any term α^n for $n > d$ would lead to vanishing contributions ϵ^{n-d} in the action – they are irrelevant deformations. The equality $\Lambda_\phi = 1$ remains true in order to regularize δS .

In the presence of such a boundary action, the contribution T_{ij}^F in the expression (4.11) simply includes the ϕ^2, ϕ^3 contributions and leads to

$$T_{ij} = 2K_{ij} - 2({}^d R_{\gamma,ij}) - 2(K+2)\gamma_{ij} + \gamma_{ij} \left[\phi N^z \partial_z \phi + \frac{\Lambda_\phi + \epsilon a}{2} \phi^2 + \frac{b}{3} \phi^3 \right]. \quad (4.21)$$

We recognize the \mathcal{F} -dependent part of the stress tensor which agrees with the direct method. It is then immediate to compute the trace of the stress tensor

$$T_i^i = \frac{\alpha}{2} (3a\alpha + 2b\alpha^2 - 4\beta) = -\frac{\alpha}{2} (a\alpha - 4J_{\text{MT}}), \quad (4.22)$$

where in the last equality we used the boundary condition (4.19). This result points to the existence of a line of critical points with $\alpha = 0$ where the sourceless ($J_{\text{MT}} = 0$ equivalent to the boundary condition $-\beta + a\alpha + \frac{b}{2}\alpha^2 = 0$) deformation \mathcal{F} is just marginal. This is equivalent to only deforming the boundary theory through a ϕ^3 term which indeed has dimension d and should therefore be marginal.

For completeness we mention that in the case of the standard quantization the trace of the stress tensor is simply $T_i^i = \alpha\beta = \beta J_{\text{SQ}}$.

4.3.2 Choice of quantization and thermodynamics

In this subsection, we will derive the thermodynamics of a black hole solution in a general compatible quantization choice. This goes beyond the analyses in [202, 203] where only the thermodynamics of a marginal scalar were considered, *i.e.*, the case of alternate quantization with a multitrace deformation such that the stress tensor remains traceless. In view of extending the choice of possible theories to non-marginal ones, we will show that the thermodynamics space is extended from a 2-parameter to a 3-parameter space, as also emphasized for Einstein-Scalar theory in [206].

Let us start with the constraint that a choice of solution imposes on the possible quantization schemes. Indeed, while the choice of boundary terms in the action and therefore of the boundary deformation is a priori agnostic of a given solution to the bulk equations of motion, we have seen that the multi-trace deformation leads to a specific choice of boundary condition on the scalar (4.19). Not every solution to the bulk equations of motion (4.3) are compatible with every possible boundary condition, as was noted in [203, 211]. In the case of the metric corresponding to the aGR solution (4.5), the scalar ϕ has the following falloffs

$$\phi \sim \alpha z + (\beta - f'(0)\alpha/2)z^2 = \alpha z + (\beta - 3Q\alpha/4)z^2, \quad (4.23)$$

where we have related the values of $\phi'(0), \phi''(0)$ to the falloffs α, β in the FG ansatz (4.15). This matching is made explicit in Section 4.B. Comparing with the full solution (4.5), we can therefore equate $\alpha = \sqrt{3}Q/2$ and $\beta = \sqrt{3}Q^2/8$. Consider then alternate quantization deformed by an arbitrary (relevant and marginal) multitrace deformation. In that case the source equals

$$J_{\text{MT}}(Q) = \frac{\sqrt{3}Q}{8} \left(4\alpha + (\sqrt{3}b - 1)Q \right). \quad (4.24)$$

From this equation, we see there are a few distinct cases to consider

- (i) $\alpha = 0, b = b_{\text{aGR}} \equiv 1/\sqrt{3}$: every instance of the 2-parameter aGR solution (4.5) is compatible with this choice and is sourceless $J = 0$. This is the sourceless marginal deformation we previously mentioned and which was studied in [202, 203, 211]. From Eq. (4.22), we see that this boundary theory has $T_i^i = 0$.
- (ii) $\alpha = 0, b = 0$: the quantization procedure is conventional alternate quantization. In this case, since the solution (4.5) is not sourceless, we must impose a Neumann boundary condition $\beta = -J$ with fine-tuned source $J(Q) = -\sqrt{3}Q^2/8$. The explicit source leads to an explicitly broken conformal symmetry in the boundary. (A similar argument holds for standard quantization with a Dirichlet boundary condition $\alpha = J$. One would then need to consider the boundary term $S_{\text{bdy},\phi} = S_{\text{bdy},\phi}^{(\text{SQ})}$ instead, and a fine-tuned source $J(Q) = \sqrt{3}Q/2$. Also here the explicit source leads to an explicitly broken conformal symmetry in the boundary.)
- (iii) For all the other cases, one can look for explicitly sourced solutions $J = J(Q, \alpha, b)$ defined in Eq. (4.24).⁶ This case is fundamentally similar to the case (ii), with the explicit sourcing leading to a non-zero trace of the boundary stress-tensor.

In the end, we see that the only natural sourceless description we have of the solutions (4.5) corresponds to the marginal multi-trace deformation, case (i). The other cases, (ii) and (iii), are better understood as explicitly sourced deformations where the source is fine-tuned to select a certain subset of solutions at a fixed Q .

An important aspect is that even though a bulk solution may have different interpretations depending on the quantization choices set out above, the thermodynamics does know about the quantization choice. Let us consider the free energy of the solutions (4.5). Substituting the solution into the action, the free energy density Ω of the aGR black hole solution with compatible boundary condition is given by

$$S_{\text{on-shell}}^{\text{regularized}} = - \int d^3x \Omega, \quad \text{so} \quad \Omega = - \left(\frac{1}{z_h} + Q \right)^3 + \frac{Q^2}{8} \left(Q(1 - \sqrt{3}b) - 3\alpha \right). \quad (4.25)$$

⁶If we insist on looking for solutions with $J = 0$, one of the couplings a or b must be fine-tuned *e.g.*, $b(Q) = \frac{1}{\sqrt{3}}(1 - 4a/Q)$. As it was noted in [211], this means that fixing a, b to some constant will restrict the space of solutions to those for which $Q = \frac{4a}{1 - \sqrt{3}b}$. Allowing for a finite, albeit fine-tuned, source $J = J(Q)$ leads to the same result and we will choose this more natural point of view.

Furthermore, the holographic dictionary tells us that the chemical potential and the temperature of the boundary theory are given by (4.6). One might be inclined to use this to deduce a variation of Ω in the 2-parameter grand canonical ensemble $d\Omega = -s_1 dT - \rho_1 d\mu$ and derive from it the thermodynamic entropy and charge density of the theory

$$s_1 = -\left(\frac{\partial\Omega}{\partial T}\right)_\mu, \quad \rho_1 = -\left(\frac{\partial\Omega}{\partial\mu}\right)_T. \quad (4.26)$$

However, we have seen from Eq. (4.10) that the free energy variation in the presence of an explicit source should be corrected by a scalar contribution of the form (see also [206])

$$d\Omega = -s_2 dT - \rho_2 d\mu - \mathcal{O}_\varphi dJ. \quad (4.27)$$

This is the full 3-parameter thermodynamics of the system. The fact that the free energy (4.25) of the aGR solution only depends on T and μ , and not on the value of the scalar source means that the aGR solution should be seen as a 2-parameter constrained solution within this 3-parameter space. This family of solutions is only a subset of all the possible ones for *any* given compatible quantization scheme. A direct corollary is that to explore only this analytical set of solutions, variations of J, T, μ are not independent. Denoting J as the dependent variable, *i.e.*, it is not independent but is a function of both T and μ , then the grand canonical potential varies as

$$d\Omega = -\left(s_2 + \mathcal{O}_\varphi \frac{\partial J(T, \mu)}{\partial T}\right) dT - \left(\rho_2 + \mathcal{O}_\varphi \frac{\partial J(T, \mu)}{\partial \mu}\right) d\mu \quad (4.28)$$

if one constrains one's considerations to aGR solutions only.

The precise relation of the VEV \mathcal{O}_φ and the source J to the fall-off of the dilaton depends on the quantization scheme as we have just reviewed. A choice of quantization is not a canonical transformation, as shown by [206] in the standard quantization case for Einstein-Scalar theories. Therefore the value of the free energy will depend on this choice. This is evident in the dependence on a, b in Eq. (4.25). In the full 3-parameter space of solutions this quantization choice dependence would only appear in the dilaton contribution part. In the constrained 2-parameter space of solutions, it would appear to imply that now also the thermodynamic entropy s_1 and charge density ρ_1 deduced from Eq. (4.26) depend on the quantization, as

$$s_1 = 4\pi \frac{(1 + Qz_h)^{3/2}}{z_h^2} \left[1 + \frac{Q^2 z_h^3}{8(1 + Qz_h)^3} (Q(1 - \sqrt{3}b) - 2a) \right], \quad (4.29)$$

$$\rho_1 = \mu \frac{1 + Qz_h}{z_h} \left[1 - \frac{Qz_h^2(2 + Qz_h)}{8(1 + Qz_h)^3} (Q(1 - \sqrt{3}b) - 2a) \right].$$

This is strange, as the Bekenstein-Hawking entropy and the charge density – the VEV of the sourced gauged field – are properties of the black hole solution and do not depend

on the boundary action which sets the quantization. Indeed they can be read off directly from the geometry as

$$s_2 = 4\pi \sqrt{g_{xx}(z_h)g_{yy}(z_h)} = \frac{4\pi(1+Qz_h)^{3/2}}{z_h^2} \quad \text{the area of the horizon of the black hole,}$$

$$\rho_2 = -\partial_z A_t(z \rightarrow 0) = \mu \frac{(1+Qz_h)}{z_h} \quad \text{the global U(1) charge.}$$

(4.30)

The solution is of course that in the constrained system s_1 and ρ_1 are not the true entropy and charge density, as they include the artificial contribution from varying $J(T, \mu)$ following from the constraint to stay within the 2-parameter aGR solution space. It is then a rather straightforward computation to connect Eqs. (4.29) and (4.30) through the variation of J expressed in Eq. (4.27). To that end, we can remember that the source J is constrained by the boundary condition (4.24) and that in our choice of quantization, we always have $\mathcal{O}_\varphi = \alpha$. In summary, the geometric expressions for the entropy and charge of the aGR solution are always the correct ones. The difference from the quantities computed from the Gibbs potential can be attributed to the fact that one considers a constrained system: the expression $s_1 = -\left(\frac{\partial\Omega}{\partial T}\right)_\mu = -\left(\frac{\partial\Omega}{\partial T}\right)_\mu - \mathcal{O}_\varphi \left(\frac{\partial J}{\partial T}\right)_\mu$ contains a term that is absent in the correct definition of the entropy $s_2 = -\left(\frac{\partial\Omega}{\partial T}\right)_{\mu, J}$, and similarly for ρ .

There is, however, the special case (i). When the deformation is purely marginal and sourceless – $a = 0$ and $b = \frac{1}{\sqrt{3}}$ – we can immediately infer that the variations of $J = 0$ will be trivial. In that case, we will have $s_1 = s_2$ and $\rho_1 = \rho_2$. The way to understand this is that within the 3-parameter space of possible solutions quantified by (T, μ, J) the 2-parameter aGR solution spans a different subspace depending on the quantization choice for the dual boundary theory. Figure 4.1, illustrates how this difference of boundary interpretation between the alternate quantization with sourceless marginal deformation of case (i) and the standard quantization of case (ii) changes the shape of the aGR solution manifold inside the thermodynamic space of sources $\{T, \mu, J\}$. This visualization allows us to see at a glance how the sourceless marginal deformation reduces to a 2-charge thermodynamic space where 2-parameters of the solution naturally coincide with T, μ while the standard quantization interpretation of the aGR solution induces some non-trivial projection when varying the Gibbs free energy w.r.t. T, μ . For the sourceless marginal deformation the thermodynamics of the boundary thus simplifies greatly and will behave in a similar fashion to the conformal fluid dual to the RN black hole solution.

To complete the argument above we shall construct numerical solutions to the equations of motion (4.3) in the next section that differ from the aGR solution in that they explore the third direction orthogonal to T, μ and analyse their various boundary interpretations.

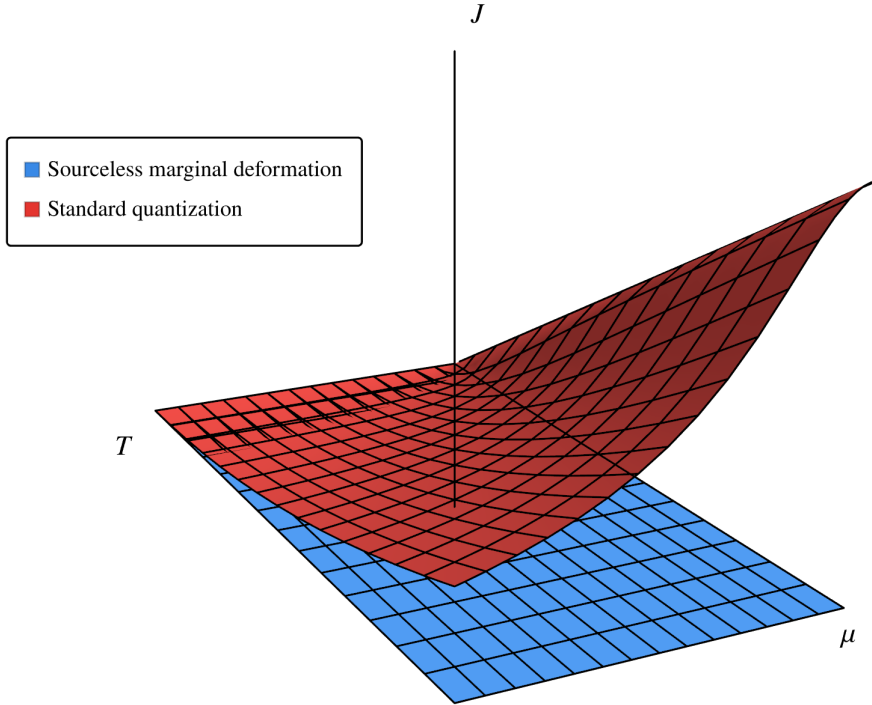


Figure 4.1: aGR solution manifold in the thermodynamic parameter space of source $\{T, \mu, J\}$ for two specific choices of boundary interpretations (cases (i) and (ii)). The sourceless marginal case has trivial source and is by itself a 2-charge submanifold while the standard quantization case has a constrained source which leads to the non-trivial corrections in s_1, ρ_1 .

4.4 Deformed Gubser-Rocha black holes

4.4.1 Numerically constructed solutions

The solutions that generically differ from (4.5) correspond to setting different boundary conditions for the dilaton field. However, for each such new solution, its interpretation depends on the quantization one considers, *i.e.*, what the on-shell value of the action including boundary terms reads.

We will solve the GR equations of motion (4.3) numerically using the following parametrization

$$\phi = \frac{\sqrt{3}}{2} z \psi(z), \quad A_t(z) = \mu j(z) a_t(z), \quad (4.31)$$

and with metric ansatz

$$ds^2 = \frac{1}{z^2} \left[-f(z)G_{tt}(z)dt^2 + \frac{dz^2}{f(z)}G_{zz}(z) + g(z)G(z) \left(dx^2 + dy^2 \right) \right], \quad (4.32)$$

where $f(z), g(z), j(z)$ are held fixed to their expressions in the aGR solution (4.5) and $\psi, a_t, G_{tt}, G_{zz}, G$ are the dynamical fields. The radial coordinate z spans the range from the boundary at $z = 0$ to the outer horizon at $z = z_h$. The IR boundary conditions are chosen to have a single zero horizon corresponding to a non-extremal black hole and to impose regularity at the horizon for other fields (see *e.g.*, [81]).⁷ The UV boundary conditions are chosen to impose AdS asymptotics for the metric components and $A_t(0) = \mu$. Parametrizing $\mu = \sqrt{3Qz_h(1+Qz_h)}/z_h$ as in the aGR solution, the scalar boundary condition (4.19) can be rewritten in terms of the falloffs of ψ as

$$\psi'(0) = -\frac{2J}{\sqrt{3}} + \left(a - \frac{3Q}{4} \right) \psi(0) + \frac{\sqrt{3}b}{4} \psi(0)^2. \quad (4.33)$$

For simplicity, we will choose $z_h = 1$ and the temperature of the solutions will therefore be encoded by $Q = \frac{3\mu^2}{16\pi^2 T^2}$. In holography, we would usually first fix the boundary theory of interest by choosing a, b . Then every solution to the equations of motion would be labeled by (T, μ, J) imposed through the boundary conditions. However in this section, we will be interested in how a given set of solutions, labeled by $(T, \mu, \psi(0))$, behaves in the various compatible boundary theories. This is possible because the boundary condition we impose on the scalar is simply a way to parametrize how we choose a bulk solution constrained to have a black hole in the interior. Every boundary theory determined by a, b and the value of sourcing J compatible with the condition (4.33) will provide a valid boundary description. We will focus on the boundary interpretations in the next subsection. In many holographic studies $\psi(0)$ is often used interchangeably with the source J , but this is of course only true in standard quantization. We shall, however, be careful to distinguish between the boundary value $\psi(0)$ of the AdS scalar field and the source J of the operator in the quantization choice dependent dual field theory.

Let us now briefly describe the effect of changing $\psi(0)$ without referring to any specific boundary theory. By looking at the aGR solution (4.5), we see that $\psi(0) = Q \sim (T/\mu)^{-2}$ for this family. Therefore, increasing $\psi(0)$ is akin to lowering the temperature and vice versa. To confirm our intuition, we can compare solutions at fixed $Q_0 \sim (T_0/\mu)^{-2}$, and varying $\psi(0)$, to aGR solutions with $\psi(0) = Q \neq Q_0$ *i.e.*, at different $T/\mu \neq T_0/\mu$. We will choose to focus on the gauge field $A_t(z)$ and more specifically the component $a_t(z)$ defined in (4.31). Formally, $a_t(z) = A_t(z)/(\mu j(z, T_0/\mu))$ for a fixed T_0/μ . Since the aGR solution at a different temperature T/μ will have a gauge field $A_t(z) = \mu j(z, T/\mu)$, the correct field to compare with will be $a_t^{\psi(0)=Q}(z, T/\mu \neq T_0/\mu) = j(z, T/\mu)/j(z, T_0/\mu)$. We plot

⁷The boundary conditions from regularity imply in particular that $G_{tt}(z_h) = G_{zz}(z_h)$. This conveniently allows us to set the temperature with the parameters Q and z_h just like in the aGR solution in Eq. (4.6), as the temperature of this generalized model is given by $T = T_{\text{GR}} \sqrt{G_{tt}(z_h)/G_{zz}(z_h)} = 3\sqrt{1+Qz_h}/4\pi z_h$.

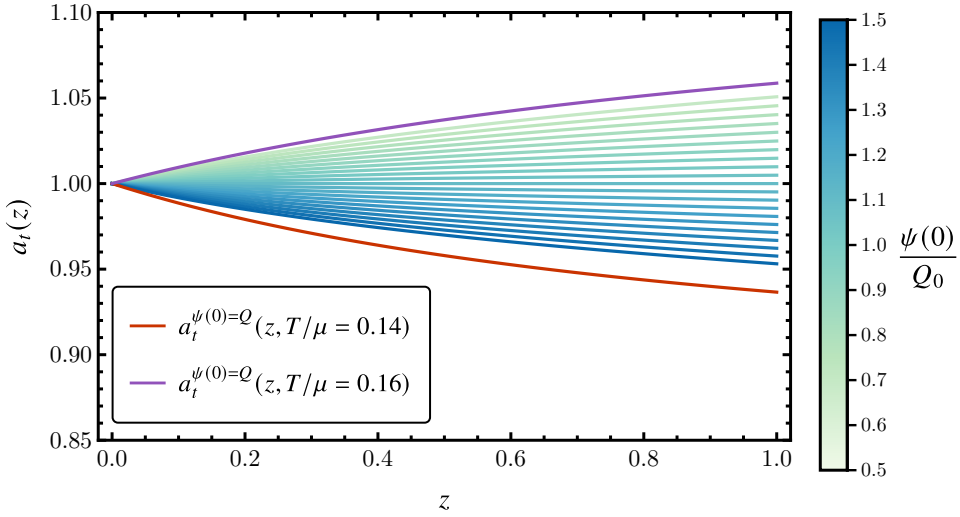


Figure 4.2: Gauge field component $a_t(z)$ as defined in (4.31) at $T_0/\mu = 0.15$ and for various values of $\psi(0)$. We compare with the equivalent function $a_t^{\psi(0)=Q}$ of the aGR solution at different temperatures $T/\mu = 0.16$ (purple) and $T/\mu = 0.14$ (red). This illustrates that qualitatively the effect of changing the dilaton boundary value has similarities to changing the ratio T/μ .

the profiles $a_t^{\psi(0)\neq Q_0}(z, T_0/\mu)$ in Figure 4.2 and compare these to $a_t^{\psi(0)=Q}(z, T/\mu > T_0/\mu)$ (purple) and $a_t^{\psi(0)=Q}(z, T/\mu < T_0/\mu)$ (red). We see that indeed, starting from $\psi(0) = Q_0$, as we increase (decrease) $\psi(0)$ with Q_0 fixed, the solution becomes similar to the aGR solution at lower (higher) T/μ .

4.4.2 The holographic dual of the one-parameter family of solutions in different quantization choices

Having numerically constructed instances of this one-parameter deformation of fixed T/μ GR black holes, *each* instance in turn has multiple holographic dual interpretations depending on the quantization scheme. These are constrained by the compatibility condition (4.33). We will focus on three specific choices:

1. the conformal symmetry preserving quantization $a, J = 0$ boundary theory for which we can then label our solutions by $b(\psi(0)) = \frac{4}{\sqrt{3}\psi(0)^2} \left(\psi'(0) + \frac{3Q}{4} \psi(0) \right)$,
2. the standard quantization boundary theory with the label $J = \alpha = \frac{3}{2} \psi(0)$,
3. the alternate quantization boundary theory with $a, b = 0$ for which the label is now $J = -\beta = -\frac{3}{2} \psi'(0) - \frac{3\sqrt{3}Q}{8} \psi(0)$.

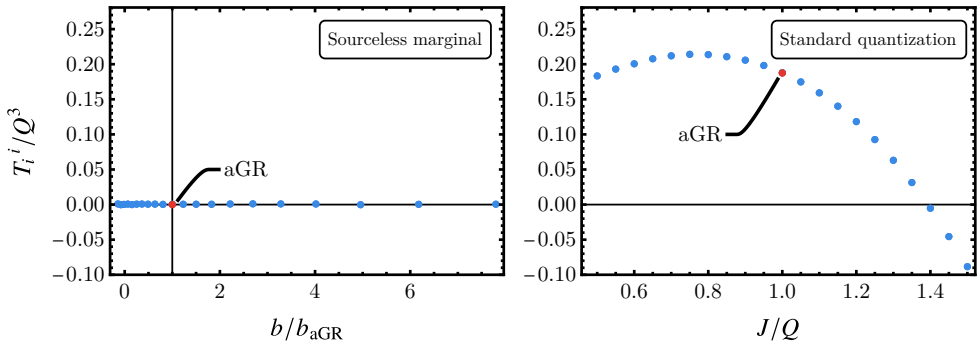


Figure 4.3: Trace of the boundary stress tensor when varying the Dirichlet boundary condition $\psi(0)$. This can be interpreted as exploring boundaries with $\alpha = 0, J = 0$ and varying marginal coupling b (left) or as changing the source $J = \alpha$ in standard quantization (right). aGR denotes the analytically known Gubser-Rocha solution. (Left) We see that in this case, T_{ij} remains traceless regardless of b which is consistent with a marginal deformation and the result (4.22). (Right) In standard quantization, the trace is generically not zero, but this can happen for specific boundary theories: sourceless $J = 0$ – not visible on the graph – and when $\mathcal{O}_\varphi = 0$ – which happens at $J/Q \approx 1.4$.

Using Eq. (4.11) we can compute the energy and the pressure of a solution in a specific quantization scheme and construct the trace of the stress tensor $T_i^i = -\epsilon + 2P$ for each of these solutions. For the choice 1, as we can see in Figure 4.3, the stress tensor remains traceless for any value of $b(\psi(0))$, confirming the analytic result Eq. (4.22). This is what we expect from a CFT deformed by a marginal operator. On the other hand, for the choice 2, we see that generically conformality is broken and the stress tensor acquires a non-zero trace. In this quantization scheme, this is also true for the aGR solution, as we described in the case (ii). There are two exceptions: the first one is when $J = 0$ (but $\mathcal{O}_\varphi \neq 0$) – which is reminiscent of a \mathbb{Z}_2 spontaneously symmetry breaking solution but here, the finite charge of the black hole actually always leads to an explicitly symmetry broken (ESB) solution $\phi(z) \neq 0$. This case is outside the range of the plot Figure 4.3. The second solution would happen around $J/Q \approx 1.4$ such that $\mathcal{O}_\varphi = 0$. These are consistent with what we would have expected from $T_i^i = \alpha\beta$.

Each one of these new black hole solutions has a different thermodynamics compared to the aGR solution. A clean way to exhibit this is to show the boundary charge density ρ_2 , which for the choice 1 is the same as the variation of the Gibbs free energy w.r.t. the chemical potential, *i.e.*, in that case $\rho_2 = \rho_1$. In Figure 4.4, we plot the charge density as a function of temperature for various values of the marginal coupling b . It is clear from this figure that the charge density as a function of T/μ is dependent on the choice of boundary theory and the deformed solution describes a different state, even if the change is small.

To reiterate this last point, let us remember that a priori, the true charge density of the theory ρ_2 , as well as the true entropy of the theory s_2 , only depend on the bulk

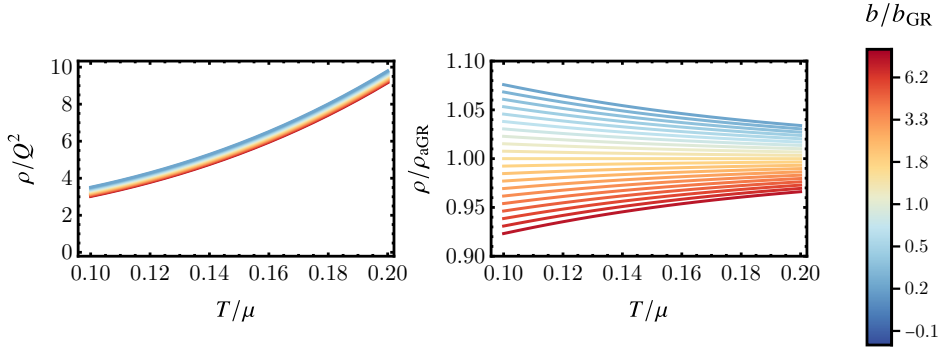


Figure 4.4: Boundary charge density as a function of the temperature T/μ when imposing Dirichlet boundary conditions, which we interpret as varying the boundary theory through b . The charge density is normalized by Q^2 in the left-hand plot and by its aGR value defined in (4.30) in the right-hand plot. The qualitative behavior of all these theories is extremely similar to the aGR solution (left) but quantitatively differs as a function of T/μ (right), showing the theories described are different.

solution – they are geometric quantities. Yet we now argue that different boundary theories have different thermodynamics. The resolution of this apparent contradiction is that while the entropy and charge density of a black hole solution only really depend on the bulk solution, how we explore the space of solutions is dependent on the choice of quantization. As we mentioned in Section 4.4, the holographic interpretation of black hole thermodynamics shows that we should label solutions by their sources $\{T, \mu, J\}$ – and in the case of the sourceless solutions of the choice 1, b plays the role of the label J . But different boundary theories have different notion of source J such that varying T and μ at fixed J will mean different path in the space of bulk solutions labeled by $\{T, \mu, \psi(0)\}$. In Figure 4.5, we illustrate this point by looking at the Bekenstein-Hawking entropy s_2 as a function of T/μ – all solutions are normalized by the aGR entropy defined in (4.30). Both choices 1 and 3 are used to label the solutions when varying the temperature, which can be done by imposing the boundary condition (4.33) for each of the choices. The values of $b(\psi(0))$ and $J = -\beta$ are chosen such that solutions meet in pair at $T/\mu = 0.2$. Upon lowering the temperature, we see that these pairs split indicating that the bulk solutions they belong to are not the same anymore. A path at fixed $J = -\beta$ is therefore generically different than a path at fixed $J = \alpha$ or fixed $b(\psi(0))$.

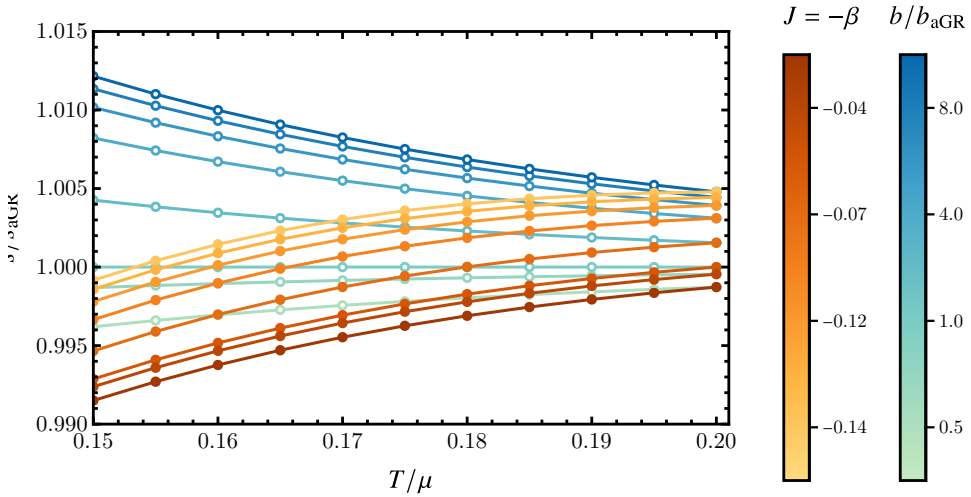


Figure 4.5: Black hole entropy as a function of T/μ when keeping either the alternate quantization source $J = -\beta$ fixed (choice 3, orange gradient curves) or when keeping the label $b(\psi(0))$ fixed (choice 1, blue gradient curves). The curves meet in pairs at T/μ – indicating identical bulk solutions – and separate for other temperatures – indicating different black hole solutions.

4.5 Conclusion

In this paper, we have clarified how the GR black hole thermodynamics works in the context of holography and the appropriate quantization thereof. The well-known analytical solution (4.5) of [38] covers only a 2-parameter subspace of the full 3-parameter thermodynamics of black hole solutions to the action (4.2). The 2-parameter aGR black hole solution has been used widely as a physically sound version of the $z = \infty$ AdS₂ IR critical point that preserves the quantum critical properties but does so with a vanishing zero temperature entropy. It was already pointed out [202] that an unusual quantization choice could preserve conformal thermodynamics and hence stay within the analytically known 2-parameter family. This indicates the existence of a marginal operator in this specific quantization scheme [203] and we have recovered this in our analysis. For other quantization choices, the analytic solution has a fine-tuned value for the source. To prove this point we have numerically computed the solutions corresponding to different boundary values of the dilaton. This fills out the full 3-parameter thermodynamic phase space. The filled out phase-space therefore elucidates that other quantization choices are just as valid as the one we chose to focus on. This had to be so, but the trade-off that one must make is to properly account for various scalar contributions to the general thermodynamics of the theory in line with the findings in [206].

Because the GR action is a consistent truncation of $d = 11$ supergravity compactified on $\text{AdS}_4 \times S_7$ and has ABJM theory as its known holographically dual CFT, in principle one should be able to identify this marginal operator in the CFT. The fact that marginality is associated with a multitrace deformation makes this not as straightforward as may seem. In particular as it originates naturally in alternate quantization, it is likely that it is an operator which is only marginal in the large N limit where the classical gravity description applies. We leave this for future research.

Our focus and interest is the use of the GR and other EMD models as phenomenological descriptions of AdS_2 fixed points, especially due to its resemblance to the experimental phenomenology of strange metals. In this comparison, thermodynamic susceptibilities and (hydrodynamic) transport play an important role. Our result here shows that in EMD models one must be precise in the choice of boundary conditions and scalar quantization as they will directly affect the long-wavelength regime of the dual boundary theory as well as correct the thermodynamics of any extension of the GR model. This is especially true for any boundary interpretation differing from the pure marginal case of [202, 203], as was shown by [206] for Einstein-Scalar models and we have shown here for the GR model. A proper understanding of the boundary conditions is necessary both for the thermodynamics of the background and the hydrodynamic fluctuations on top of that background.

Acknowledgements

We thank J. Aretz, R. Davison, K. Grosvenor, J. Zaanen and especially A. Krikun for discussions during the Nordita scientific program *Recent Developments in Strongly Correlated Quantum Matter*. This research was supported in part by the Dutch Research Council (NWO) project 680-91-116 (*Planckian Dissipation and Quantum Thermalisation: From Black Hole Answers to Strange Metal Questions.*), the FOM/NWO program 167 (*Strange Metals*), and by the Dutch Research Council/Ministry of Education.

4.A Validity of the boundary action

In a previous version of this paper, we considered the boundary term introduced by [202] which is of the form

$$S_{\text{bdy},\phi}^{(c_\phi)} = \int_{z=\epsilon} d^3x \sqrt{-\gamma} \left[\frac{\Lambda_\phi}{2} \phi^2 + c_\phi \phi N^z \partial_z \phi \right], \quad \Lambda_\phi = 2c_\phi - 1, \quad (4.34)$$

which matches our boundary terms for specific values $S_{\text{bdy},\phi}^{(c_\phi=0)} = S_{\text{bdy},\phi}^{(\text{SQ})}$ and $S_{\text{bdy},\phi}^{(c_\phi=1)} = S_{\text{bdy},\phi}^{(\text{MT})}$ for $a = 0, b = 0$. The claim of [202] is that more general values of c_ϕ are also possible, which from a renormalization point of view is an acceptable assumption. The only prescription one has for boundary terms is to choose relevant and marginal ones (the irrelevant boundary terms contribute as corrections in the cutoff ϵ and can be

truncated) which respect the symmetries of the action. However, choosing the boundary term (4.34) leads to

$$\begin{aligned} \delta \left(S_{\text{bulk}} + S_{\text{bdy},\phi}^{(c_\phi)} \right) &= \int_{z=c} d^3x \sqrt{-\gamma} \left[(1 - c_\phi) \beta \delta \alpha - c_\phi \alpha \delta \beta \right] \\ &= \int_{z=c} d^3x \sqrt{-\gamma} \left(-c_\phi \alpha^{1/c_\phi} \right) \delta \left(\beta \alpha^{1-1/c_\phi} \right) \end{aligned} \quad (4.35)$$

which generically differs from our result for the standard quantization or multi-trace deformation where $\mathcal{O}_\phi = \alpha$ or β .

The question of the validity of such variational problem as Eq. (4.35) was raised before in *e.g.*, [212] for the simple case of a non-relativistic particle. Consider a particle with action $S_1 = \int_{t_1}^{t_2} dt (-\dot{q}^2/2)$ to which one adds the total derivative term $S_2 = \left[\frac{1}{2} q \dot{q} \right]_{t_1}^{t_2}$. The variation of the total action on-shell $\delta(S_1 + S_2) = \left[\frac{1}{2} q \delta \dot{q} - \frac{1}{2} \dot{q} \delta q \right]_{t_1}^{t_2}$ is of a similar form as the variation (4.35) for $c_\phi = 1/2$. The boundary condition required to make the boundary variation well-defined is then to fix $\dot{q}/q = C$ at $t = t_1$ and $t = t_2$. However, in the case of S_1 , this is not a correct boundary condition to impose. Since the bulk equation of motion is $\ddot{q} = 0$ with solutions $q(t) = At + B$ and $\dot{q}(t) = A$, the quantity to fix is $\frac{\dot{q}}{q} = \frac{A}{At+B} = \frac{1}{t+B/A}$ which only depends on the ratio B/A . Therefore, fixing it at t_1 leaves no freedom to also fix it at t_2 . At the same time the two boundary conditions at t_1 and t_2 do not select a unique solution. A direct check one can do is whether for other values of the analogous c_ϕ , this problem remains. Taking for example $S_2 = \left[\frac{1}{3} q \dot{q} \right]_{t_1}^{t_2}$, the boundary condition to impose is now to fix $\dot{q}/q^2 = \frac{A}{(At+B)^2}$. Solving this condition at the boundaries for values $C_{1,2}$ now does lead to fully determined solutions, unlike the previous case. However, the solutions are not unique, because the boundary conditions itself have arbitrary constants $C_{1,2}$. There are therefore multiple branches to the system of equations $AC_{1,2} = (At_{1,2} + B)^2$.

In holography only the UV boundary conditions are imposed in the exact same manner. The IR boundary condition in a black hole spacetime is different. We simply require regularity of the scalar at the event horizon. For $c_\phi = 1/n$, $n \in \mathbb{N}^*$, the question of whether the variational problem is well-defined is then whether the UV boundary condition of fixing $\frac{\beta}{\alpha^{n-1}} = C$ is sufficient to pick a unique solution once the IR boundary conditions are taken into account. It is quite straightforward to show that these are the same boundary conditions as the usual multi-trace deformation boundary condition (4.24), for $J = 0$ and specific choices of monomial $\mathcal{F}_n = \frac{\alpha_n}{n} \alpha^n$. From (4.19), we see that for $n > 1$, the sourceless boundary condition for the deformation associated with \mathcal{F}_n is $\frac{\beta}{\alpha^{n-1}} = \frac{\alpha_n}{n-1}$ so the matching between boundary theories occurs for $C = \frac{\alpha_n}{n-1}$. Interestingly, choosing the boundary value C is equivalent to choosing a deformation coupling constant with (single-trace) scalar source $J = 0$. This is because the coupling constant α_n is really the same as a source for the multi-trace operator \mathcal{O}^n .

In Table 4.1 we look at $n = 1, 2, 3, \infty$ and what type of multi-trace deformation they match. For $n \geq 4$ the higher order terms in \mathcal{F} represent irrelevant operators and we shall not consider them. The special cases $n = 1$ and $n = \infty$ *i.e.*, $c_\phi = 1$ and $c_\phi = 0$ are the alternate and standard quantization case of fixing $\alpha = J$ and $\beta = -J$. In the previous version of this article we argued that the aGR solution quantized with boundary term (4.34) and $c_\phi = 1/3$ could be viewed as a marginal deformation with $n = 3$ and $\beta/\alpha^2 = \frac{1}{2\sqrt{3}}$ which according to our mapping is equivalent to the case (i), as expected.

n	Boundary condition	Analog multi-trace choice
$n = 1$	$\beta = C$	$a = 0, \quad b = 0, \quad J = -C$
$n = 2$	$\frac{\beta}{\alpha} = C$	$a = C, \quad b = 0, \quad J = 0$
$n = 3$	$\frac{\beta}{\alpha^2} = C$	$a = 0, \quad b = 2C, \quad J = 0$
$n = \infty$	$\alpha = C$	$a = 0, \quad b = 0, \quad J = C$

Table 4.1: Matching between the boundary conditions obtained from the multi-trace deformation boundary action (4.9) and those obtained from the boundary term (4.34).

Moreover, and importantly, the on-shell values of the boundary actions (4.9) with monomial multitrace deformations $\mathcal{F} = \mathcal{F}_n$ and (4.34) are also equivalent through the mapping described in Table 4.1. Indeed, we see that the difference between the boundary terms is

$$S_{\text{bdy},\phi}^{(\text{MT})}(\mathcal{F} = \mathcal{F}_n) - S_{\text{bdy},\phi}^{(c_\phi)} = \int_{z=\epsilon} \left[\frac{a_n}{n} \alpha^n - (1 - c_\phi) \alpha \beta \right] = \int_{z=\epsilon} [a_n - C(n-1)] \frac{\alpha^n}{n}, \quad (4.36)$$

where we injected the expansion $\phi \sim \alpha z + \beta z^2$ and in the second equality, we used the boundary condition $\beta = C \alpha^{n-1}$ with $c_\phi = 1/n$. We see that the difference (4.36) vanishes for the choice $C = \frac{a_n}{n-1}$ and thus the actions are the same through the mapping described in Table 4.1. We can conclude that as far the two roles of the boundary terms go – setting the boundary conditions of the variational problem and specifying an on-shell value for the action – these boundary terms yield the same answer for specific choices of the boundary theory. This explains how our previous derivation based on (4.34) yielded the same results as the derivation based on (4.9) for sourceless solutions. The on-shell action equivalence does not hold in generality, however. The boundary term (4.34) fails to account for polynomial deformations \mathcal{F} and therefore would miss out on the most general theories of case (iii).

4.B Matching of metric gauge choices

In Eq. (4.13) we have expressed our scalar field UV expansion in the FG gauge choice for the metric (4.15). In this section we will use r to denote this choice of radial coordinate. However, the aGR solution (4.5) uses a different metric gauge choice (4.4). This means that the expansion of the scalar field $\phi = \hat{\alpha}z + \hat{\beta}z^2 + \dots$ in the (4.4) coordinates is not directly identical to that given in Eq. (4.13). They are related by solving $\frac{dr^2}{r^2} = \frac{dz^2}{z^2 f(z)}$. This relation is formally given by

$$\log r(z) - \log \epsilon = \int_{\epsilon}^z \frac{dx}{x \sqrt{f(x)}}, \quad \text{with } \epsilon \rightarrow 0. \quad (4.37)$$

In the near-boundary regime, we will only be interested in the leading and subleading orders of this relation – since we only want to see how the leading and subleading orders in the scalar expansion mix – and we therefore expand $f(z) = 1 + f'(0)z + \dots$, where the analytical value of f is given in Eq. (4.5). Doing so, we find

$$r(z) \sim z - \frac{3Qz^2}{4} + \mathcal{O}(z^3). \quad (4.38)$$

It is then straightforward to input this in the FG UV expansion

$$\phi \sim \alpha r + \beta r^2 \sim \alpha z + \left(\beta - \frac{3Q}{4} \alpha \right) z^2, \quad (4.39)$$

as was claimed in Eq. (4.23).

Chapter 5

Emerging Fermi liquids from regulated quantum electron stars

Attribution

This chapter was published as a journal article under the title “Emerging Fermi liquids from regulated quantum electron stars” in the Journal of High Energy Physics (JHEP), volume 2022, article number 222, together with Vladan Djukić, Mihailo Čubrović and Koenraad Schalm.

5.1 Introduction

Strongly correlated electrons at finite density remain a deep and interesting puzzle, encountered in various quantum-many body systems, from condensed matter to heavy ion physics to astrophysics. Apart from some special cases, Fermi liquids are the only interacting fermionic systems at finite density where we have good control. A breakthrough was provided by the application of AdS/CFT to finite density large N -matrix fermionic systems. This allowed new strongly coupled IR fixed points characterized by an emergent Lifshitz scaling with dynamical critical exponent z to be discovered.¹ Though many of such results were found in bottom-up holographic models where only bosonic operators are tracked, there is reason to believe that any holographic finite density systems must also have microscopic fermionic degrees of freedom. Indeed a number of these holographically discovered fixed points have now been independently confirmed as Sachdev-Ye-Kitaev-like large N quantum spin-liquid fermionic ground

¹At finite N these fixed points may be not be true IR fixed points but intermediate scale attractors in the RG flow.

states, where the additional microscopic description allows valuable extra insights into the workings of these novel states of matter.

In holography these new ground states are qualitatively understood to arise as a deconfined phase of an underlying microscopic theory with the confined phase corresponding to a conventional Fermi liquid; see [213]. A dozen years ago this was a hotly debated topic and it was found that the prototypical deconfined state, characterized by the AdS_2 , $z = \infty$ near horizon dynamics of AdS Reissner-Nordstrom (RN) black holes and an associated multitude N of non-Fermi-liquid Fermi surfaces [214, 215, 32] in the Thomas-Fermi limit of $N \rightarrow \infty$ indeed transitions at low temperatures to a charged Tolman-Oppenheimer-Volkov electron star [42, 216, 43, 44, 48]. These states are partially confined - partially deconfined in that they still have a finite z Lifshitz horizon; for a review and the transport responses of these states, see [19, 1].

However, away from the Thomas-Fermi limit a holographic description of a direct single Fermi-surface deconfined non-Fermi-liquid-to-confined Fermi-liquid $T = 0$ quantum phase transition has so far not yet been found. In the bulk, this problem corresponds to solving an Einstein-Maxwell-Dirac system in a self-consistent way, accounting for the backreaction of fermions on geometry, but keeping the number of Fermi surfaces finite or specifically keeping only one. The distinct puzzle here is that the signal of the putative instability towards confinement at low temperature — a log-oscillatory response in the single fermion spectral function [32] — occurs at a distinct point in parameter space from the one where the first stable Fermi surface is located (Fig. 5.1). In [46] an electron star model is introduced where N is finite but still very large; this hinted at a first order rather than a continuous transition. Approaching the question from the other side, a holographic description of confined single Fermi surface Fermi-liquid was constructed in [47] by enforcing confinement through a hard wall IR cut-off [47]. This confirmed that confinement-deconfinement is the correct viewpoint of the quantum phase transition, but did not yet include the gravitational backreaction. The most comprehensive study to date is the attempt at quantum electron star model of [49, 50] which regulates the system by putting it on a sphere and then tries to carefully remove this regularization procedure for a self-consistent solution of the Einstein-Maxwell-Dirac equations in the asymptotic AdS background.

The simple hard-wall solution of [47] already illustrates the fundamental problem. In the presence of an occupied Fermi surface the gravitational backreaction is uncontrolled, see [49, 50]. These subsequent papers then address this by a second cut-off for the backreaction, and then attempt to remove both cut-offs in a precarious balancing act. In the present paper we address this in a different way. We construct a fully gravitationally backreacted single-Fermi surface solution confined through a soft rather than a hard wall. From the gravitational point of view this soft wall determines the deep interior boundary conditions of the fermionic wave functions instead of the horizon geometry. As illustrated in detail in [49, 50] at the technical level the puzzle is that with the vanishing of the horizon (signalling deconfinement) at the quantum

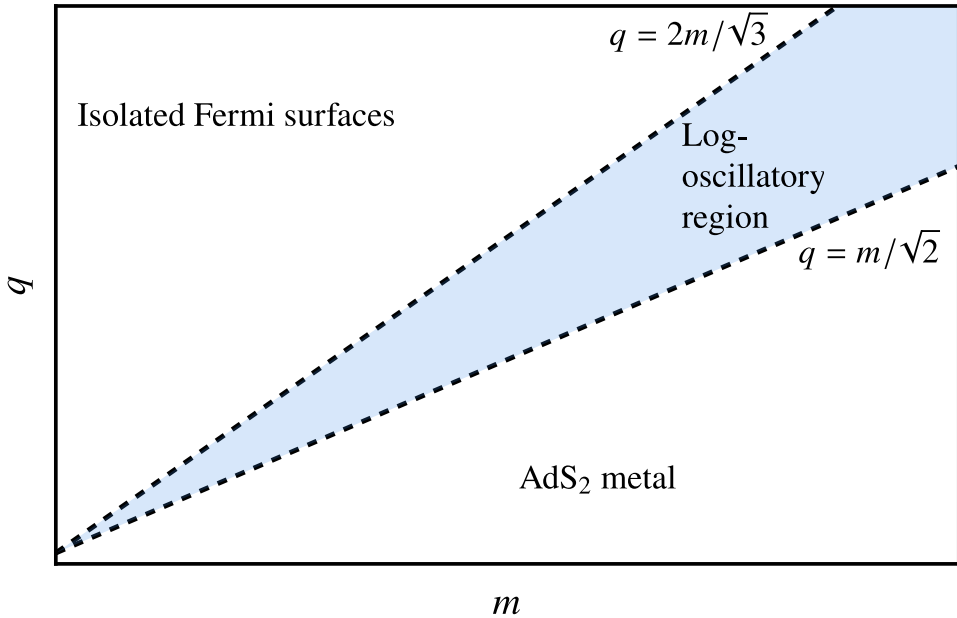


Figure 5.1: A schematic representation of the phase diagram of holographic fermions, where q and m are the charge and the mass (related to the scaling dimension in field theory $\Delta = 3/2 + m$) of the bulk fermion respectively. Along the line $q = m/\sqrt{2}$, determined by the Schwinger pair production threshold, the quantum phase transition ought to happen between the Reissner-Nordström black hole describing the strange metal phase and the quantum electron star solution (no black hole) corresponding to a metallic phase. However, this line is not identical to boundary of the regime where the Reissner-Nordström system supports stable Fermi surfaces as probed through the Reissner-Nordström spectral functions. The electron star (fluid) model requires taking the limit $q, m \rightarrow 0$ where both critical lines become indistinguishable. To understand the transition at finite q, m is the motivation for our approach. Adapted from [32].

phase transition, not only must one find a new self-consistent (confining) IR geometry, but also an associated set of self-consistent boundary conditions for the fermion wave-function.

Because the confining boundary conditions suppress the fermion wave function in the IR, there is also no associated backreaction in the deep IR, which remains AdS. This confined regulated quantum electron star (rQES) is therefore the fermionic analogue of the Horowitz-Roberts-Gubser-Rocha AdS₄-to-AdS₄ groundstate/domain wall for holographic superconductors [217, 218]. This solution (just like our soft wall confining electron star solution) describes a system that flows from a conformal pure AdS UV to an intermediate ordered holographic superconductor (Fermi liquid) state with a gap in the sense that below that gap it returns to the renormalized conformal

theory and low energy excitations cannot disturb the ordered state. As is well-known the generic holographic superconductor ground state is not AdS₄-to-AdS₄ but of the Lifshitz type [41]. It is the technical difficulties described above that guided us to first construct this Horowitz-Roberts-Gubser-Rocha type solution. We leave the full Lifshitz quantum electron star for future work. One natural way to construct the latter is that, rather than trying to remove the soft-wall regulator, one can also make it dynamical, similar to the electron star study in [45].

We do confirm that within the class of non-dynamical soft-wall solutions this gapped confined holographic Fermi liquid is the thermodynamically preferred state over the deconfined Reissner-Nordström metallic state for appropriate charge and mass of the fermion. Because we are not yet able to remove the regulator we do not yet solve the puzzle of Fig. 5.1 directly.

The outline of the paper is the following. In Sec. 5.2 we present the gravity setup and the regulated quantum electron star (rQES) solution. In Sec. 5.3, we present the properties of our rQES solution, *i.e.*, the gapped confined Fermi liquid: we show it is the thermodynamically preferred solution in a certain range of parameters, and demonstrate the existence of the infinitely long-lived quasiparticle peaks in the spectrum of the boundary theory. In Sec. 5.4, we present some considerations about removing the confining soft wall. Sec. 5.5 sums up the conclusions together with some musings on further directions of work and the physical meaning of our results.

5.2 A confined Quantum Electron Star: set-up

The minimal bottom-up gravity dual of a strongly correlated electron system is the Einstein-Maxwell-Dirac system [214, 215, 32]. The new element of our setup is the phenomenological soft-wall-like regulator inspired by bottom-up AdS/QCD [219]. The regulator is a fixed non-dynamic scalar field, which neither backreacts on the metric itself nor does it feel the backreaction by the fermions. This is again in line with AdS/QCD models. Therefore, the geometry starts as pure AdS in the UV, in the interior it is influenced by the gauge and matter fields and deviates from AdS, and in far IR all matter fields are exponentially damped by the confining potential. However, in contrast to most hard/soft-wall models we will let the potential only damp the matter sector and not the gravitational sector. The action of the system is:

$$S = \int d^4x \sqrt{-g} \left[\frac{L^2}{2\kappa^2} (R + 6) - \frac{L^2}{4} F_{\mu\nu} F^{\mu\nu} + L^3 \mathcal{L}_f[\Psi, \Phi] \right] \quad (5.1)$$

where κ is the gravitational coupling constant; and L is set to $L = 1$ in the remainder. The Dirac Lagrangian is:

$$\mathcal{L}_f = \bar{\Psi} \left[e_A^\mu \Gamma^A \left(\partial_\mu + \frac{1}{4} \omega_\mu^{BC} \Gamma_{BC} - iq A_\mu \right) - (m + \hat{M}\Phi) \right] \Psi \quad (5.2)$$

where $\bar{\Psi} = i\Psi^\dagger\Gamma^0$, e_A^μ is the vierbein, Γ^A are the gamma matrices in four dimensions, and ω_μ^{AB} is the spin connection. The regulator is fully encoded in an effective mass contribution $\hat{M}(z)\Phi(z)$ for the Dirac field, with $\Phi(z)$ a non-dynamical scalar field whose profile we shall choose later. Inspired by [220], we will consider two types of the confining potential:

$$\hat{M} = \begin{cases} -e_3^z\Gamma^3, & \text{the potential preserves chirality,} \\ z\mathbb{1}_4, & \text{the potential breaks chirality.} \end{cases} \quad (5.3)$$

Here z , both as index and a variable, refers to the radial coordinate of the AdS space. We will assume a radially symmetric metric which is asymptotically AdS_{d+1} with $d = 3$, parametrized as:

$$ds^2 = -\frac{f(z)h(z)}{z^2}dt^2 + \frac{dx_i dx^i}{z^2} + \frac{dz^2}{z^2 f(z)}. \quad (5.4)$$

The radial coordinate is defined for $z \geq 0$, where $z = 0$ is the location of AdS boundary (UV). Development of a horizon at finite z is in principle signified by the appearance of a zero of the function f : $f(z_H) = 0$. At zero temperature (the only case we consider), the space extends to infinity, $0 \leq z \leq \infty$.

Our choice to let the wall only confine the fermion-matter sector (together with the absence of backreaction by the confining scalar) implies that at finite chemical potential but zero bulk fermion density, the thermodynamically preferred solution is the regular charged (RN) black hole, though pure AdS with a constant electrostatic potential is also a solution.

For a certain value of the charge q of the fermion, it will be thermodynamically preferred to store all charge in an occupied bulk fermionic state, *i.e.*, nonzero bulk density $n_c \equiv \langle \Psi^\dagger \Psi \rangle$, rather than a Reissner-Nordström black hole. Now the precise radial profile of the scalar $\Phi(z)$ becomes important. The original AdS/QCD papers used a quadratic scalar, behaving in the IR as $\Phi \sim z^2$ [221], which ensures confinement while still being smooth. Another form found in the literature is a profile which flattens out to a constant in the IR [222]. At the same time the UV completion of the scalar field has to ensure that its contribution to the Dirac equation decays quickly enough for small z to reproduce the equation of motion in pure AdS in the limit $z \rightarrow 0$. The forms that satisfy all the requirements and which we find numerically convenient are

$$\begin{aligned} \Phi(z) &= \lambda z^2, & \text{quadratic scalar} \\ \Phi(z) &= \lambda \frac{z^\alpha}{z_0^\alpha + z^\alpha}, & \text{flat scalar.} \end{aligned} \quad (5.5)$$

The amplitude of the scalar (*i.e.*, the measure of the "hardness" of the wall) is parametrized by λ , and z_0 is the scale at which the scalar begins to flatten (in the second, flat scalar model). The choice of α is merely that of computational convenience and we choose $\alpha = 4$. Similarly, we will consistently choose $z_0 = 2$ throughout the rest of this paper.

5.2.1 Einstein-Maxwell-Dirac equations

From the action we obtain the Maxwell equation and two convenient linear combinations of the tt and zz components of the Einstein equations. With the ansatz that only $A_t \neq 0$, and that all functions only depend on z , compatible with homogeneity and isotropy, they reduce to

$$\begin{aligned} A_t''(z) - \frac{h'(z)}{2h(z)} A_t'(z) &= \sqrt{h(z)} n(z), \\ 1 + \frac{z}{3} f'(z) - f(z) &= \frac{z^2}{3f(z)h(z)} \rho(z) + \frac{z^4}{12h(z)} A_t'(z)^2, \\ h'(z) &= -zh(z)p(z) - \frac{z}{f(z)^2} \rho(z). \end{aligned} \quad (5.6)$$

Compatible with the symmetries the current vanishes $J^i = 0$, the charge density J^0 is denoted as $J^0 = n(z)/\sqrt{-g} = z^4 n(z)/\sqrt{h(z)}$, and the stress tensor is parametrized as

$$(T_f)_{\mu\nu} = \text{diag}(\rho(z), p_\perp(z), p_\perp(z), p(z)), \quad (5.7)$$

where $p_\perp(z)$ is the pressure in the transverse x, y directions.

The ii components of the Einstein equations are both equal to

$$\begin{aligned} &z h(z) \left[-z^3 A_t'(z)^2 + (3z f'(z) - 4f(z)) h'(z) + 2z f(z) h''(z) \right] + \\ &+ 2h(z)^2 \left[z (z f''(z) - 4f'(z) - 2\beta z p_\perp(z)) + 6f(z) - 6 \right] - z^2 f(z) h'(z)^2 = 0. \end{aligned}$$

They are not independent, however. Denoting the Einstein field equations as $E_{\mu\nu} \equiv G_{\mu\nu} - T_{\mu\nu}$ and the Maxwell equation as $E_M \equiv \nabla_\mu F^{\mu\nu} - J^\nu$, one can show that²

$$E_{xx} = \hat{L} \cdot E - \frac{1}{2z} \nabla_\mu T^{\mu\nu}, \quad (5.8)$$

where $\hat{L} \cdot E \equiv A_1 \partial_z E_{tt} + A_2 \partial_z E_{zz} + A_3 E_M + A_4 f'(z) E_{tt} + E_{zz} (A_5 f'(z) + A_6 h'(z) + A_7)$ is a linear combination of both $\{E_{tt}, E_{zz}, E_M\}$ and their derivatives and $T^{\mu\nu}$ is the total stress-energy tensor associated with the matter content of the theory. The stress-tensor is covariantly conserved if the matter sector is on-shell, *i.e.*, obeys its equations of motion. Thus

$$E_{xx}^{\text{on-shell}} = \nabla_\mu T^{\mu\nu} = 0 \quad (5.9)$$

It is therefore sufficient to solve the three equations (5.6) together with the matter sector.

The charge, energy and pressure densities $n(z), \rho(z), p(z)$ are determined by the occupied fermionic states in the AdS bulk space. Importantly, we will compute them

²This is essentially $\nabla_\mu G^{\mu\nu} = \nabla_\mu T^{\mu\nu}$.

solely from microscopic considerations: we do not assume anything like a fluid limit or a specific form of the equation of state. We compute them from the Dirac Lagrangian, within the one-loop Hartree correction to the background. This is discussed in detail in the next subsection.

We will now proceed to derive the equation of motion for the Dirac field. From (5.2), the equation reads:

$$e_A^\mu \Gamma^A \left(\partial_\mu + \frac{1}{4} \omega_\mu^{BC} \Gamma_{BC} - iqA_\mu \right) \Psi = \left(m + \hat{M}(z)\Phi \right) \Psi. \quad (5.10)$$

It is known that the spin connection in this type of metric can be eliminated by rescaling the fermion [214, 223]:

$$\Psi = \left(-g^{zz} \det g_{\mu\nu} \right)^{-\frac{1}{4}} \tilde{\psi} = \left(\frac{f(z)h(z)}{z^{2d}} \right)^{-\frac{1}{4}} \tilde{\psi} \equiv \alpha(z)\tilde{\psi}. \quad (5.11)$$

In addition, it is convenient to eliminate any singular terms from the fermionic wavefunction. Since our solutions are smooth in the interior as we shall see, the only singularity is the branch cut in the UV behaving as z^m . We thus rescale one more time

$$\tilde{\psi} = z^m \psi \equiv b(z)\psi. \quad (5.12)$$

In most cases we will use the rescaled form and write the equations for ψ . So far this is all independent of the gamma matrix representation. In order to simplify the equations of motion, we now employ the representation

$$\Gamma^\mu = \begin{pmatrix} 0 & \gamma^\mu \\ \gamma^\mu & 0 \end{pmatrix}, \quad \Gamma^3 = \begin{pmatrix} 1 & 0 \\ 0 & -1 \end{pmatrix}, \quad (5.13)$$

with $\mu \in \{0, 1, 2\}$, $\gamma^0 = i\sigma^2$, $\gamma^1 = \sigma^1$, $\gamma^2 = \sigma^3$ and $\sigma^{1,2,3}$ are the usual Pauli matrices. Homogeneity and isotropy along the t, x, y directions allow us to take the energy ω and momentum $k \equiv k_x$ as good quantum numbers, so the Dirac bispinor is expressed as

$$\psi = e^{-i\omega t + ikx} (\psi_1(z), \chi_1(z), -i\chi_2(z), i\psi_2(z))^T. \quad (5.14)$$

As in [47, 223], this yields two (equivalent) decoupled systems for the two independent components, for $\psi_{1,2}$ and $\chi_{1,2}$, corresponding to the spin degeneracy of our system. We will focus on the ψ_i components for which the Dirac equation reads

$$\begin{aligned} \left[\partial_z + \varepsilon_+ \Phi + \frac{m}{z} \left(1 - \frac{1}{\sqrt{f(z)}} \right) \right] \psi_1(z) - \left[\frac{k}{\sqrt{f(z)}} + \frac{\omega + qA_t}{f(z)\sqrt{h(z)}} \right] \psi_2(z) &= 0 \\ \left[\partial_z + \varepsilon_- \Phi + \frac{m}{z} \left(1 + \frac{1}{\sqrt{f(z)}} \right) \right] \psi_2(z) + \left[\frac{\omega + qA_t}{f(z)\sqrt{h(z)}} - \frac{k}{\sqrt{f(z)}} \right] \psi_1(z) &= 0. \end{aligned} \quad (5.15)$$

where $\varepsilon_+ = \varepsilon_- = 1$ corresponds to the chiral-preserving potential and $\varepsilon_+ = -\varepsilon_- = -1/\sqrt{f(z)}$ corresponds to the chiral-breaking potentials.

5.2.2 Fermion densities and backreaction

The fermionic densities and pressures are obtained microscopically, from the Dirac Lagrangian (5.2):

$$\begin{aligned}\rho &= \langle \Psi^\dagger e_0^t \Gamma^0 (-i\omega - iqA_t) \Psi \rangle, \\ n &= -\langle \Psi^\dagger \Psi \rangle.\end{aligned}\tag{5.16}$$

The components of the pressure p_\perp, p are likewise formally equal to

$$\begin{aligned}p_\perp &= \langle \bar{\Psi} i e_1^x k_x \Gamma^1 \Psi \rangle, \\ p &= \langle \bar{\Psi} e_3^z \Gamma^3 \partial_z \Psi \rangle.\end{aligned}\tag{5.17}$$

The expectation value $\langle \dots \rangle$ in (5.16-5.17) is the quantum-mechanical expectation value, *i.e.*, one solves the Dirac equation with appropriate boundary conditions (see below) and sums over the quantum numbers in the appropriate range. The quantum numbers are the radial modes ℓ , and momenta k_x, k_y in the x, y -directions which determine the on-shell energy in terms of a dispersion relation $\omega = E_\ell(k)$. The role of the confining potential is essential here: it quantizes the radial number ℓ . Each discrete radial mode corresponds to a separate Fermi surface [214, 215, 32, 44, 48, 47]. As emphasized in the Introduction, we seek a state where only a single Fermi surface is occupied. This must be the lowest radial mode. Note that despite occupying a single mode, this mode still contains a thermodynamically large number of states counted by the x, y -momenta. Each radial mode is thus a fluid of fermions.

We will ignore the subtleties of the zero-point energy and the Dirac sea; in principle these are absorbed in a renormalization of the cosmological constant and the AdS radius; see however [49, 50] for a more detailed treatment. Then, in terms of the solutions to the Dirac equation, formally the expressions for the density are

$$\begin{aligned}n(z) &= \frac{2q}{z^3 \sqrt{f(z)}} a(z)^2 b(z)^2 \sum_{k, \ell} \Theta(-E_\ell(k)) \left(\psi_{1; \ell, k}^\dagger(z) \psi_{1; \ell, k}(z) + \psi_{2; \ell, k}^\dagger(z) \psi_{2; \ell, k}(z) \right) \\ \rho(z) &= a(z)^2 b(z)^2 e_0^t(z) (-i\omega - iqA_t(z)) \sum_{k, \ell} \Theta(-E_\ell(k)) \left(\psi_{1; \ell, k}^\dagger(z) \psi_{1; \ell, k}(z) + \psi_{2; \ell, k}^\dagger(z) \psi_{2; \ell, k}(z) \right) \\ p(z) &= a(z)^2 b(z)^2 e_3^z(z) \sum_{k, \ell} \Theta(-E_\ell(k)) \left(\psi_{1; \ell, k}^\dagger \partial_z \psi_{2; \ell, k} - \psi_{2; \ell, k}^\dagger \partial_z \psi_{1; \ell, k} \right)\end{aligned}\tag{5.18}$$

where the step-function $\Theta(x)$ selects the positive energy states. Note that due to the antisymmetry of the two spin components, the derivatives of the scaling factors $a(z), b(z)$ cancel out in the expression for p .

The self-consistent Hartree calculation

We solve the system (5.6, 5.15) in the one-loop Hartree approximation. As a reminder, the Hartree correction is the local single-particle diagram (vacuum bubble),

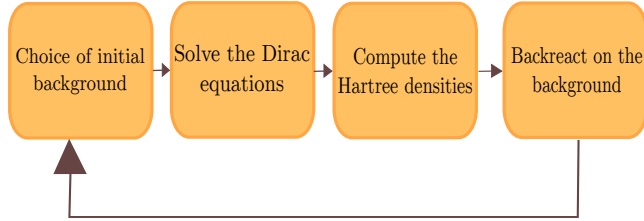


Figure 5.2: Iteration algorithm used to compute the rQES solution.

ignoring anti-particles, *i.e.*, ignoring the contribution from the Dirac sea. We do not take into account the Fock correction. In flat space, the Hartree correction is trivial [224]: in terms of the causal fermionic propagator G_R it equals $\lim_{t \rightarrow 0^-} \int d\omega d^2k G_R(\omega, k) e^{-i\omega t} = \delta\mu$,³ merely renormalizing the chemical potential. In curved space however, the local chemical potential is $\mu_{\text{loc}}(z) = A_t(z) \sqrt{-g^{tt}(z)}$, with a nontrivial radial profile, thus the correction $\delta\mu(z)$ is also variable along z and therefore it can have nontrivial physical effects.

The Hartree approximation then proceeds by computing this one-loop Hartree correction self-consistently. One starts with an ansatz for the background, solves the Dirac equation in this background, computes the one-loop Hartree densities in the assumption that they are small, updates the background and iterates to convergence as in Fig. 5.2.

5.2.3 Boundary conditions on the Einstein-Maxwell sector

The Einstein-Maxwell equations (5.6) require four boundary conditions in total (two for $A_t(z)$ and one for each of the metric functions $f(z), h(z)$). The UV boundary conditions are

$$\begin{aligned} A_t(z_{\text{UV}}) &= \mu, & \text{the chemical potential.} \\ f(z_{\text{UV}}) &= h(z_{\text{UV}}) = 1, & \text{AdS}_4 \text{ asymptotics.} \end{aligned} \quad (5.19)$$

³The infinitesimal time separation $t \rightarrow 0^-$ is really the point-splitting regularization, as the integral of G_R at coincident points in spacetime generally diverges; the sign of t is dictated by the contour choice for the retarded propagator [224].

The fourth boundary condition we impose is given by our demand that we seek a state where *all* the charge is contained in occupied fermionic states.⁴ The confining potential ensures that the fermionic wavefunctions are localized at a finite value in the radial direction. Thus by construction the charge density will vanish in the deep AdS interior. From this follows that the fourth boundary condition is $\partial_z A_t(z_{\text{IR}}) = 0$. Formally $z_{\text{IR}} = \infty$; in our numerical computation it will be finite but large, and we have checked that our results do not depend on its value.

In practice, we solve the boundary value problem by shooting from the IR. We impose directly the condition $\partial_z A_t(z_{\text{IR}}) = 0$ as well as the condition $\partial_z f(z_{\text{IR}}) = 0$. The latter indirectly encodes our demand that we seek a $T = 0$ solution; recall that for a black hole solution $\partial_z f(z_{\text{horizon}}) \sim T$. Then we use the free value $A_t(z_{\text{IR}})$ and $h(z_{\text{IR}})$ to shoot for $A_t(z_{\text{UV}}) = \mu$, $h(z_{\text{UV}}) = 1$ at the boundary. From the equation of motion for $f(z)$ one obtains automatically that $f(z_{\text{IR}}) = 1$ once we fall on the right branch; for the same reason one can also use $f(z_{\text{IR}}) = 1$ as an IR boundary condition if one demands in addition that there is no energy density or electric field in the deep interior.

5.2.4 Boundary conditions for the fermions

The UV boundary conditions for the appropriate solutions to the Dirac equation are straightforward. Near the AdS boundary the rescaled field behaves as

$$\begin{aligned}\psi_1(z \rightarrow 0) &\sim A_\ell(\omega, k) \frac{\omega - k - \mu q}{2m - 1} z^{1-2m} + B_\ell(\omega, k) + \dots, \\ \psi_2(z \rightarrow 0) &\sim A_\ell(\omega, k) z^{-2m} + B_\ell(\omega, k) \frac{\omega + k - \mu q}{2m + 1} z + \dots\end{aligned}\tag{5.20}$$

On-shell solutions are normalizable, *i.e.*, $A_\ell(\omega, k) = 0$. This agrees with the AdS/CFT dictionary, where a finite $A_\ell(\omega, k)$ would imply an external source for the fermions for a specific band ℓ and energy ω, k . Demanding normalizability $A_\ell(\omega, k) = 0$ instead, implicitly translates in a dispersion relation $\omega(k) = E_\ell(k)$.

The IR boundary conditions for the fermions require a more detailed discussion. Firstly, for the fermionic wavefunctions, the amplitude is set by normalization of each wavefunction to unity. For each radial mode ℓ this implies

$$\int dz \sqrt{-g} |\psi_{i;\ell,k}(z)|^2 < \infty.\tag{5.21}$$

For finite temperature backgrounds this is usually not an issue as the horizon is parametrically at finite distance and finite IR boundary conditions, together with the UV-condition that the un-normalizable fall-off vanish, guarantees a finite integral. For the $T = 0$ background we consider here, the interior is parametrically at infinite

⁴There could be interpolating solutions with both a charged horizon and a charge in occupied fermionic states. We will not seek for those here as the presence of the charged Reissner-Nordstrom like horizons should imply the continued presence of log-oscillatory instabilities.

distance and finiteness of the integral can only follow from bounded behavior of the wavefunction. Since the spin components are not independent, it is sufficient to demand $\psi_{1;\ell}(z \rightarrow \infty) \rightarrow 0$, *i.e.*, the leading component should vanish in the interior.

It is well known in AdS/CFT that it is then the simultaneous requirement of a UV and an IR boundary condition that determines the spectrum of the small excitations. This spectrum can still be continuous or discrete; we address this directly below. Formally, however, the normalization together with two boundary conditions make the system overconstrained and one must search for accidental solutions. We again do so by shooting from the interior to search for parameters where the UV conditions are also satisfied.

The shooting condition we use is the ratio ψ_2/ψ_1 , which still leaves the freedom to normalize the norm (5.21) to unity, and which we do after the solution is found.

Effective potentials and confinement

Pure $T = 0$ AdS — representing a deconfined phase of the strongly coupled boundary theory — has a continuum spectrum of normal modes computed in the way described above. The system must be considered in a different phase or have its IR dynamics modified by a confining potential to discretize the spectrum; this spectrum may still be ungapped or gapped. We will now demonstrate that the chiral-breaking soft-confining potential supports a discrete Fermi surface, *i.e.*, a tower of bound states at discrete energies, for momenta up to some k_F , the Fermi momentum. The spectrum is also gapped. A convenient way to see the effect of this potential is to transform the Dirac equation to the Schrödinger form [32, 48, 19]:

$$\begin{aligned} \chi_{\text{Sch}}(z) &= e^{\frac{1}{2} \int_0^z du \mathcal{P}(u)} , \\ \left[\partial_z^2 - V(z) \right] \chi_{\text{Sch}}(z) &= 0 , \\ V(z) &= \frac{1}{2} \mathcal{P}'(z) + \frac{1}{4} \mathcal{P}(z)^2 - \mathcal{Q}(z) , \end{aligned} \tag{5.22}$$

where the coupled equations (5.15) were decoupled into two second order equations, each taking the form

$$\psi''(z) + \mathcal{P}(z)\psi'(z) + \mathcal{Q}(z)\psi(z) = 0 , \tag{5.23}$$

with the indices 1,2 on $\psi, \chi_{\text{Sch}}(z), V$ omitted.

In principle, the Schrödinger potential is itself a function of the background spacetime and electrostatic potential $f(z), h(z), A_t(z)$ and can be fully determined only by calculating numerically the full solution. However, we can give a qualitative estimate whether it is confining or not by studying its asymptotics. Since the bulk remains asymptotically AdS₄, we have $V(z \rightarrow 0) \sim \frac{1}{z^2}$. In pure AdS₄ the IR behavior

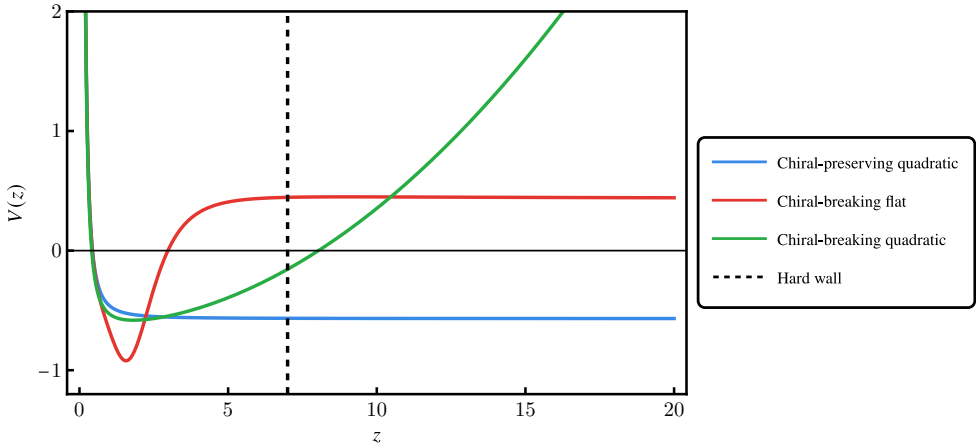


Figure 5.3: Comparison of the Schrödinger potentials for $\psi_1(z)$ for the two types of confining potential: chiral-breaking quadratic (green), chiral-breaking flat (red) and chiral-preserving quadratic (blue). The dashed black line indicates the truncation of spacetime which happens in the hard wall model of [47] at $z = 7$. Only the chiral-breaking potential and the hard wall allow for bound states. Parameters are $\{m, \mu q, k, \omega\} = \{0.1, 1.05, 0, -0.027\}$. The scalar parameters are $\lambda = 0.1$ for the two quadratic scalars and $\lambda = 1$ for the flat scalar.

would be $V_{\text{AdS-IR}}(z \rightarrow \infty) = -(\omega + \mu q)^2 + k^2 + m(m+1)/z^2 + \mathcal{O}(1/z^3)$ (Fig. 5.3).⁵ This now gets modified by the confining potential due to the scalar $\Phi(z)$. Making the ansatz that the confining potential in the deep IR for $z \rightarrow \infty$ suppresses exponentially all sources in the Einstein and Maxwell equations for large z , *i.e.*, the geometry in the deep IR is again an (emergent) AdS_4 geometry, the leading order IR behavior of the potential is then schematically

$$V_{\text{AdS-IR}} = V(z \rightarrow \infty) + (\varepsilon_- - \varepsilon_+) \left[-\frac{\phi'(z)}{2z} + \frac{\phi(z)(4m+2) + (\varepsilon_- - \varepsilon_+)\phi(z)^2}{4z^2} + \right] + \mathcal{O}(1/z^3), \quad (5.24)$$

Note that the chiral-preserving solution $\varepsilon_+ = \varepsilon_- = 1$ leads to a vanishing contribution and therefore does not lead to fermionic bound states. In contrast the chiral-breaking solution $\varepsilon_+ = -\varepsilon_- = -1/\sqrt{f(z)} = -1 + \mathcal{O}(1/z)$ in an AdS_4 IR does lead to a potentially bounding potential depending on the choice of $\Phi(z)$. For this reason, we will work solely with the chiral-breaking scalar field.

Fig. 5.3 shows the behavior of the Schrödinger potential for the various profiles of the scalar field and regulation schemes. With a chiral-breaking regulator, we indeed see that the infrared behavior of the potential is dominated by the large z behavior of

⁵We are interested in $k^2 < (\omega + \mu q)^2$ since the potential is otherwise confining even in AdS_4 with no regulator, as discussed in [225]. We will discuss this later.

each profile. The final choice of which scalar field profile to use is determined by the convergence of the iteration scheme. We numerically found the quadratic profile to be unstable while the flat profile leads to an emergent AdS₄ in the infrared. Specifically for the chiral-breaking confining potential with flat asymptotics the Schrödinger potential in the deep IR becomes

$$V(z \rightarrow z_{\text{IR}}) = -\omega_{\text{IR}}^2 + \lambda_{\text{IR}}^2 + k_{\text{IR}}^2 + \mathcal{O}(1/z) \equiv V_{\text{IR}} + \mathcal{O}(1/z), \quad (5.25)$$

where we have used that $f(z), h(z), A_t(z)$ become constant in the emergent AdS₄ IR and we have defined $\omega_{\text{IR}} \equiv \frac{\omega + qA_t(z_{\text{IR}})}{f(z_{\text{IR}})\sqrt{h(z_{\text{IR}})}}$, $\lambda_{\text{IR}} \equiv \frac{\lambda}{\sqrt{f(z_{\text{IR}})}}$ and $k_{\text{IR}} \equiv \frac{k}{\sqrt{f(z_{\text{IR}})}}$.

In the IR limit, Schrödinger equation becomes

$$\left[\partial_z^2 - V_{\text{IR}} \right] \chi_{\text{Sch}}(z) = 0, \quad (5.26)$$

which is solved by

$$\chi_{\text{Sch}}(z) = \chi_{\text{Sch}+}(z)e^{\sqrt{V_{\text{IR}}}z} + \chi_{\text{Sch}-}(z)e^{-\sqrt{V_{\text{IR}}}z}. \quad (5.27)$$

We see from (5.27) that, for frequencies such that $V_{\text{IR}} > 0$, the solutions have a growing and a decaying branch. The decaying branch clearly confines the wavefunction. This is the one we shall choose. This leads to the following IR form for our original Dirac fermion components

$$\psi_{1,2}^{\text{IR}}(z) = c_{1,2}^{\text{IR}}(z)e^{-\sqrt{V_{\text{IR}}}z}, \quad (5.28)$$

where the ratio of the coefficients is fixed by the Dirac equation (5.15):

$$\frac{\psi_2^{\text{IR}}(z)}{\psi_1^{\text{IR}}(z)} = \frac{c_2^{\text{IR}}(z)}{c_1^{\text{IR}}(z)} = \frac{1}{\omega_{\text{IR}} + k_{\text{IR}}} \left[\frac{m}{z} \left(\frac{1}{\sqrt{f_{\text{IR}}}} - 1 \right) + \sqrt{V_{\text{IR}}} + \lambda_{\text{IR}} \right] \quad (5.29)$$

and the normalization of the wavefunction to unity sets the remaining overall scale. With these IR boundary conditions the equations (5.15) are solved by shooting from z_{IR} to z_{UV} .

The confinement imposed by both IR and UV boundary conditions leads to a discrete and gapped spectrum which defines a band structure (see Fig. 5.6 later). The fall-off of the wavefunction both at the AdS boundary and the interior also implies an absence of any backreaction in those regions. Once backreaction is included the resulting solutions will therefore be AdS₄-to-AdS₄ domain wall solutions, as we will show in the next section.

As a last remark, equation (5.25) gives us a simple way to view the effect of the chiral-breaking flat potential. As has been pointed out in [32, 225], in AdS₄ with constant electrostatic potential where $\lambda = 0$, the potential is deconfining for modes with $|\omega_{\text{IR}}| > |k_{\text{IR}}|$ and confining for modes such that $|\omega_{\text{IR}}| < |k_{\text{IR}}|$. The addition of a

flat profile means that now modes with $|k_{\text{IR}}| \leq |\omega_{\text{IR}}| < \sqrt{k_{\text{IR}}^2 + \lambda_{\text{IR}}^2}$, which previously were not bound states, also become confined. This allows the existence of a window $\omega_{-}(k) < \omega < \omega_{+}(k)$, with $\omega_{\pm}(k) \equiv qA_t(z_{\text{IR}}) \pm \sqrt{k_{\text{IR}}^2 + \lambda_{\text{IR}}^2}$ where a discrete set of (gapped) modes can be populated.

5.3 Regulated Quantum Electron Star: thermodynamics and spectrum

Now that the problem is well-posed, we can follow the algorithm in Fig. 5.2 and construct a fully backreacted regulator-confined $T = 0$ quantum electron star. Choosing the chirality-breaking flat regulator the resulting solution is shown in Fig. 5.4. This is by construction an AdS₄-to-AdS₄ domain wall solution. Just like the analogous domain wall solutions for the holographic superconductor [218, 41, 217], it has a UV AdS₄ and an IR AdS₄ with the *same* radius but different effective speed of light. This can be checked by considering the diffeomorphism-invariant ratios $v_{\text{IR}}/v_{\text{UV}}$ and $L_{\text{IR}}/L_{\text{UV}}$ which are equal to

$$\frac{L_{\text{IR}}}{L_{\text{UV}}} = \sqrt{\frac{R(z \rightarrow z_{\text{UV}})}{R(z \rightarrow z_{\text{IR}})}} = 1, \quad \frac{v_{\text{IR}}}{v_{\text{UV}}} \equiv \frac{v(z \rightarrow z_{\text{IR}})}{v(z \rightarrow z_{\text{UV}})} = \sqrt{\frac{h(z \rightarrow z_{\text{IR}})}{h(z \rightarrow z_{\text{UV}})}} < 1 \text{ in our solution.} \quad (5.30)$$

Here $R(z)$ is the Ricci scalar and $v(z) = \sqrt{h(z)}$ is deduced from the null vector $\frac{d}{dt}X^\mu(z)$ where $X^\mu(z) \equiv \{t, 0, v(z)t, 0\}$ is a x -directed trajectory. Therefore, our solution obeys the c -theorem since the effective speed of light in the dual field theory is lower in the IR than in the UV, as discussed in detail in [218].

In accordance with our discussion in the Introduction, the chemical potential is chosen such that only the lowest radial mode of the fermionic wavefunction is occupied. The associated matter content shows that a localized distribution of fermions in the mid-infrared region is characterized by a stable finite density of fermions with total charge $Q = -A'_t(z \rightarrow 0)$.

With the chirality-breaking flat potential the convergence is in fact quite fast at low density. The Hartree algorithm provides a discrete sequence of fields $(f^{(n)}, h^{(n)}, A_t^{(n)})$ as we iterate from $n = 1, 2, \dots$. We can introduce a criterion for the convergence of the solution using the IR parameters used for shooting

$$\epsilon_n = \sqrt{f^{(n)}(z_{\text{IR}})^2 + A_t^{(n)}(z_{\text{IR}})^2 + h^{(n)}(z_{\text{IR}})^2}, \quad (5.31)$$

Convergence is obtained if $(\Delta\epsilon)_n \equiv \epsilon_n - \epsilon_{n-1} \xrightarrow{n \rightarrow \infty} 0$. For a small occupation number/charge Fig. 5.5 shows that the solution already stabilizes after three iterations; for large occupation numbers the convergence rapidly becomes much slower. We have checked that the solution is not sensitive to the choice of the numerical cut-offs $\{z_{\text{UV}}, z_{\text{IR}}\}$.

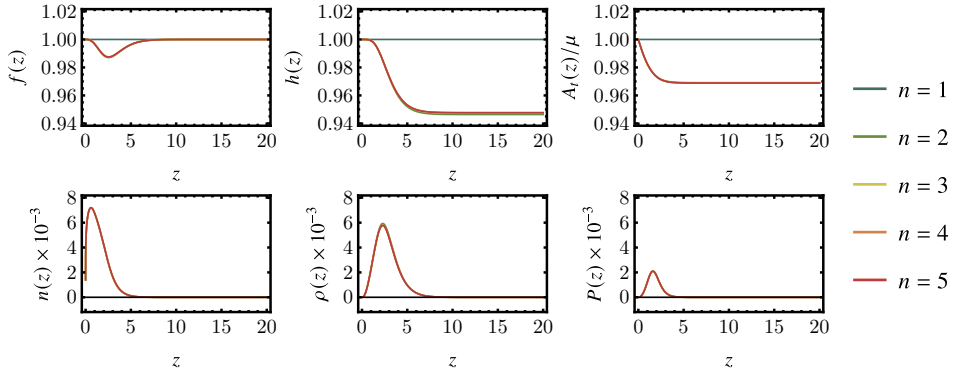


Figure 5.4: Iterative backreactions on the background fields ($f(z)$, $h(z)$, $A_t(z)$) and their associated currents ($n(z)$, $\rho(z)$, $P(z)$) with the same parameters as in Fig. 5.5. In total 5 iterations are performed, denoted by the color scale from violet (first iteration) to red (last iteration). For these values $\{m, \mu q, \lambda\} = \{0.1, 0.9, 1\}$ only the first iteration differs significantly from the final solution, and the other curves are visually barely distinguishable from each other; for higher q convergence rapidly becomes slower.

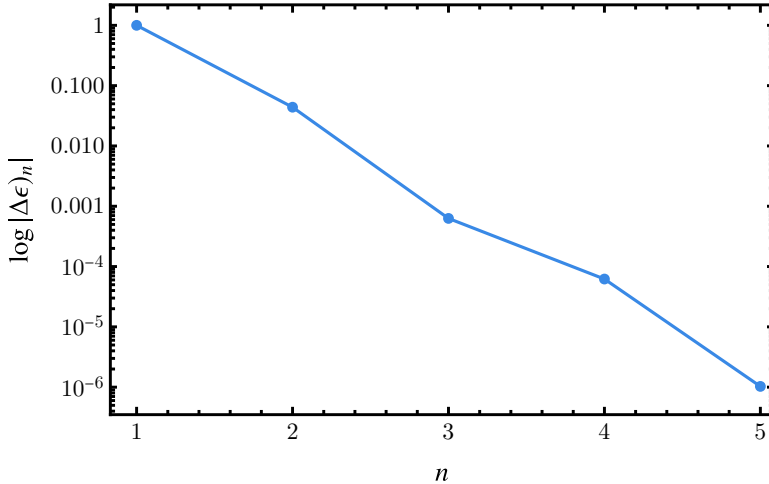


Figure 5.5: Convergence in terms of the logarithm of the difference in the IR between the n -th and $n + 1$ -st iteration $(\Delta\epsilon)_n$ for a rQES with $\{m, \mu q, \lambda\} = \{0.1, 0.9, 1\}$. The convergence is exponentially fast and the agreement is very good already around the 3rd iteration. The convergence is very good already around the 3rd iteration.

5.3.1 Thermodynamics

For a large q/m ratio we expect that the quantum electron star at a given chemical potential μ is the thermodynamically preferred solution over the extremal Reissner-

Nordström solution. In order to study the thermodynamics of the regulated quantum electron star, we need to compute its free energy. It consists of two parts. There is a direct saddle point contribution from the regularized Euclidean action:

$$S_E = \int d^4x \sqrt{g_E} \left[\frac{1}{2\kappa^2} (R + 6) - \frac{1}{4} F^2 \right] + \oint_{J_z=c} d^3x \sqrt{h} (-2K + 2\gamma), \quad (5.32)$$

where g_E is the Euclidean metric, h is the induced metric on a hypersurface normal to a radial (z) slice, pointing outwards, K is the trace of the extrinsic curvature and $\gamma = 2$ is required to make the AdS free energy vanish. The imaginary time at temperature T is compactified with the radius $\beta = 1/T$, the integral in the x - y plane produces the (infinite) volume Vol_2 , and the radial integration is performed to some UV cutoff ϵ , yielding

$$S_E = \beta \text{Vol}_2 \int dz \sqrt{g_E} \left[\frac{1}{2\kappa^2} (R + 6) - \frac{1}{4} F^2 \right] + \beta \text{Vol}_2 \sqrt{h(\epsilon)} (-2K(\epsilon) + 2\gamma). \quad (5.33)$$

This accounts for the contribution of the bosonic fields. The Dirac action vanishes on-shell and therefore does not contribute to this part. It does have a one-loop contribution to the free energy density

$$f \equiv \frac{S_E}{\beta \text{Vol}_2} + f_{\text{Dirac}}. \quad (5.34)$$

Here f_{Dirac} represents the fermionic contribution. Following [47, 226, 223, 227], at $T = 0$ we can simply sum the energies along the filled band of fermions (above the Dirac sea). This is the internal energy shifted by the chemical potential. For our normal modes, this leads to the expression

$$f_{\text{Dirac}} = \sum_{\ell} \int \frac{k dk}{2\pi} \Theta(-E_{\ell}(k)) \Theta(E_{\ell}(k) - \mu q) E_{\ell}(k) = \int \frac{k dk}{2\pi} \Theta(-E_1(k)) E_1(k)$$

where in the last line we have made explicit that we choose our chemical potential such that only states of the lowest electronic radial mode $E_{\ell=1}$ will be occupied. One must first choose the potential strength λ such that the Schrödinger potential supports at least one normalizable mode. At the same time, it is only these normalizable modes that can be populated. If there is only one band in the window of existence of normalizable modes $[\omega_-(k), \omega_+(k)]$, *i.e.*, $E_{\ell=1}(k) < \omega_+(k) < E_{\ell=2}(k)$, then increasing the chemical potential beyond that upper limit will not populate further normalizable modes. Our rQES is in this sense not plagued by the usual large- N Fermi surfaces artifact.

It is furthermore quite easy to show that both before and after accounting for backreaction the band structure follows a similar form as in pure AdS₄ [47]

$$E_{\ell}(k) = -E_0 + \sqrt{k^2 + k_0^2}, \quad (5.35)$$

where $k_F \equiv \sqrt{E_0^2 - k_0^2}$ and the parameters E_0, k_0 are most easily found by fitting from the numerical dispersion curves, as in Fig. 5.6.

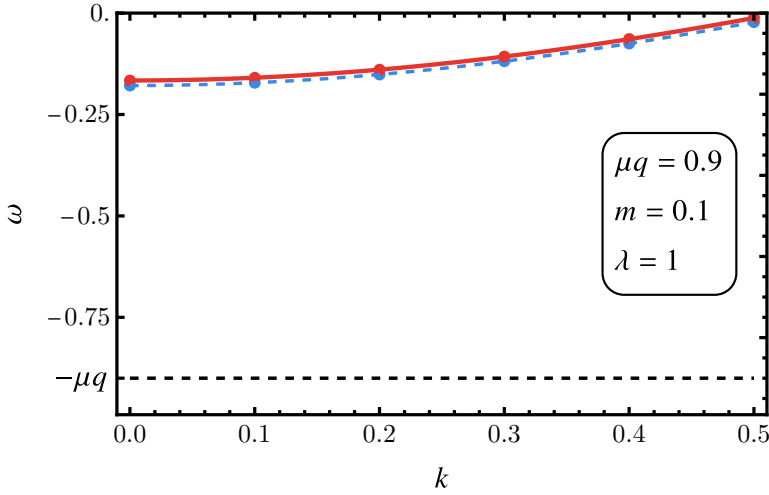


Figure 5.6: First electronic band for $\{m, \mu q, \lambda\} = \{0.1, 0.9, 1\}$, for the AdS_4 background with constant electrostatic potential (blue) and the backreacted solution (red). The lines are a fit to the form (5.35).

Note that f_{Dirac} is negative semi-definite. This does not mean, however, that the occupied state is automatically thermodynamically preferred. The backreaction also changes the bosonic saddle point contribution compared to its original AdS_4 value $f(\text{AdS}_4) = 0$. Adding both contributions we compare to the RN free energy

$$f(\text{RN}) = -\frac{4 + z_h^2 \mu^2}{4z_h^3} = -\frac{\mu^3}{6\sqrt{3}} \text{ at } T = 0. \quad (5.36)$$

Because the regulator does not act on the background sector, the Reissner-Nordström free energy is unaffected by it.

Fig. 5.7 shows the free energy of the rQES as a function of the charge μq for a fixed mass m and confining potential strength λ . As q increases, the rQES grows, so we need to compute more and more modes. This becomes more and more time consuming. By constructing an interpolating curve based on low q rQES solutions (using the points until $\mu q \simeq 1.2$), we can estimate where the solution becomes thermodynamically preferred and verify this with a fewer number of large q datapoints ($\mu q = 1.4$ and $\mu q = 1.58$). We see that at $\mu q = \mu q_c \simeq 1.56$, the rQES becomes thermodynamically preferable over the RN background.

In Fig. 5.8a, we show that this transition point evolves linearly with the fermion mass m for fixed q and λ . Based on this finding, we can sketch a thermodynamic phase diagram for our model in Fig. 5.8b. The critical charge satisfies an approximate relation $q_c(m; \lambda) \simeq c_0(\lambda) + c_1(\lambda) \frac{m}{\mu}$ with c_0 and c_1 dependent on λ . It is tempting to compare this to the confounding phase diagram based on RN holography alone. For pure RN

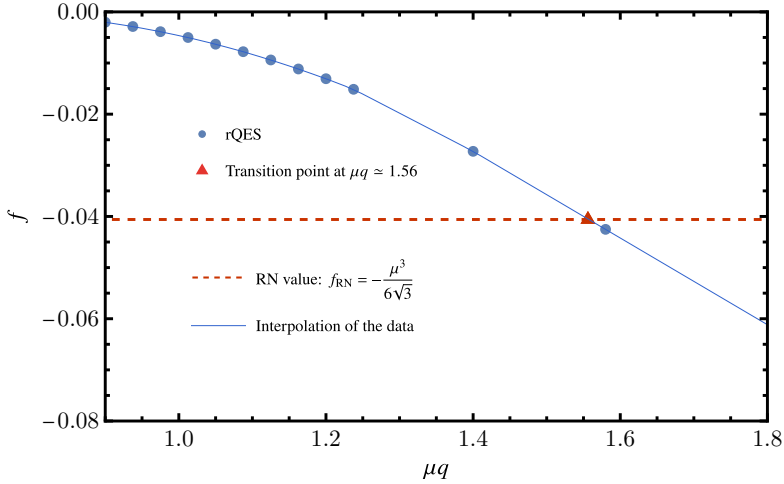


Figure 5.7: Plot of the free energy density for rQES at $\{\mu, m, \lambda\} = \{0.75, 0.1, 1\}$ as a function of the fermionic charge μq (blue dots) and the reference RN black hole free energy (red dashed line); the thin blue line and the red triangle are to guide the eye to the transition point. Since RN has no fermions its free energy curve is flat, *i.e.*, does not depend on the fermion charge. The first-order phase transition from RN to rQES happens at the intersection of the two lines. Since the calculations for larger μq values are costly, we only compute two points for $\mu q > 1.5$ and interpolate.

holography it is surmised [33] that the superradiant instability of the RN black hole toward an electron star (seen in the spectrum as log-periodic oscillations) sets in at $q = \sqrt{3}m$. This should correspond to the limit $\lambda \rightarrow 0$. As λ decreases we therefore expect the phase-boundary to pivot anti-clockwise. This comparison should be done with care, because the smaller λ becomes, the harder it is to observe bands that can be occupied — see the section on removing the regulator below. Another way to see this is that the effective Schrödinger potential in the extremal RN black hole for $\omega = k = 0$ (the onset of instability) has no linear term in m : $V_{RN} \sim -4q^2 + 2m^2$. Hence we cannot extrapolate freely to $\lambda = 0$.

5.3.2 Spectrum of the rQES

To confirm our results, we consider the fermionic spectral function on rQES backgrounds. As a reminder, the spectral function is defined as the trace of the imaginary part of the retarded propagator: $A(\omega, k) = \text{Im Tr } G_R(\omega, k)$. In holography the type of propagator is defined by the boundary conditions in the interior. Therefore the only difference with computing the normalizable Dirac solutions is the choice of appropriate boundary conditions.

Considering that we have an emergent AdS_4 geometry in the IR, we can use the known prescription for infalling boundary conditions in pure AdS, *i.e.*, the presence of

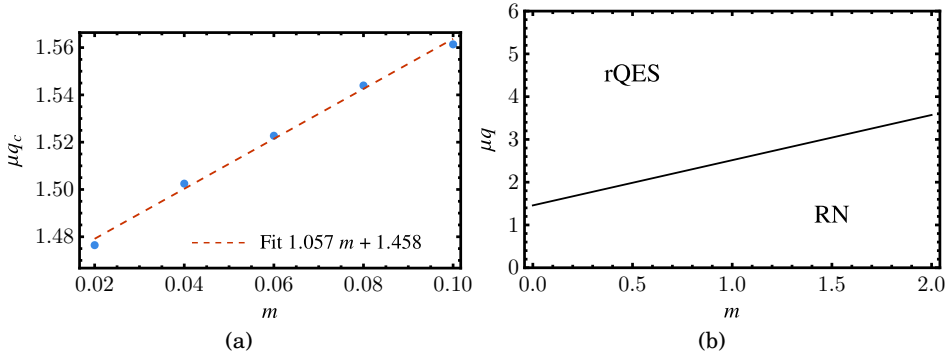


Figure 5.8: (a) Transition point μq_c as a function of m and its linear fit, for $\lambda = 1$. (b) Sketch of the phase diagram of the rQES. The black line indicates a first order transition between the regulated Reissner-Nordström and the rQES, occurring when their free energies cross.

a Poincaré horizon [228]. Accounting for the confining potential, these are

$$\psi_1(z \rightarrow \infty) = \begin{cases} e^{-z\sqrt{k_{\text{IR}}^2}}, & \text{if } \omega_{\text{IR}}^2 < k_{\text{IR}}^2 + \lambda_{\text{IR}}^2, \\ e^{iz\sqrt{-k_{\text{IR}}^2}}, & \text{if } \text{Re}[\omega_{\text{IR}}] > \sqrt{k_{\text{IR}}^2 + \lambda_{\text{IR}}^2}, \\ e^{-iz\sqrt{-k_{\text{IR}}^2}}, & \text{if } \text{Re}[\omega_{\text{IR}}] < -\sqrt{k_{\text{IR}}^2 + \lambda_{\text{IR}}^2}, \end{cases} \quad (5.37)$$

where $\omega_{\text{IR}}, k_{\text{IR}}, \lambda_{\text{IR}}$ were defined by (5.25), $k_{\text{IR}} = (\omega_{\text{IR}}, \sqrt{k_{\text{IR}}^2 + \lambda_{\text{IR}}^2}, 0)$ and $k_{\text{IR}}^2 = -\omega_{\text{IR}}^2 + k_{\text{IR}}^2 + \lambda_{\text{IR}}^2 = V_{\text{IR}}$. As we saw with the normal modes, the IR boundary condition for ψ_2 can be obtained using the Dirac equation and the boundary condition for ψ_1 . After imposing these boundary conditions, the retarded propagator is then computed as

$$G_R(\omega, k) = B/A = \lim_{z \rightarrow 0} z^{-2m} \frac{\psi_1(z)}{\psi_2(z)}, \quad (5.38)$$

where A and B are the coefficients in the UV expansion of the spinor (5.20).

Inside the gap ($\omega_{\text{IR}}^2 < k_{\text{IR}}^2 + \lambda_{\text{IR}}^2$) the IR boundary conditions are the same for the probe fermions as for the bulk normalizable modes – the wavefunction should fall off for $z \rightarrow \infty$, which yields $A = 0$ for the normal mode frequencies $\omega = E_\ell(k)$. Therefore, the propagator will present a pole along the bands of the background. Moreover, since the fermionic wavefunctions and thus also the Green's functions are real inside the domain where bound states exist, the spectral function will vanish there. Thus, we expect to see $\text{Im} G_R(\omega, k) = 0$ for $\omega \in [\omega_-(k), \omega_+(k)]$, except when $\omega = E_\ell(k)$ where a pole should appear.

This general structure of the spectral function including the gap for $\omega_- \leq \omega \leq \omega_+$ can be seen in Fig. 5.9. The data here and in the remainder of this section is computed

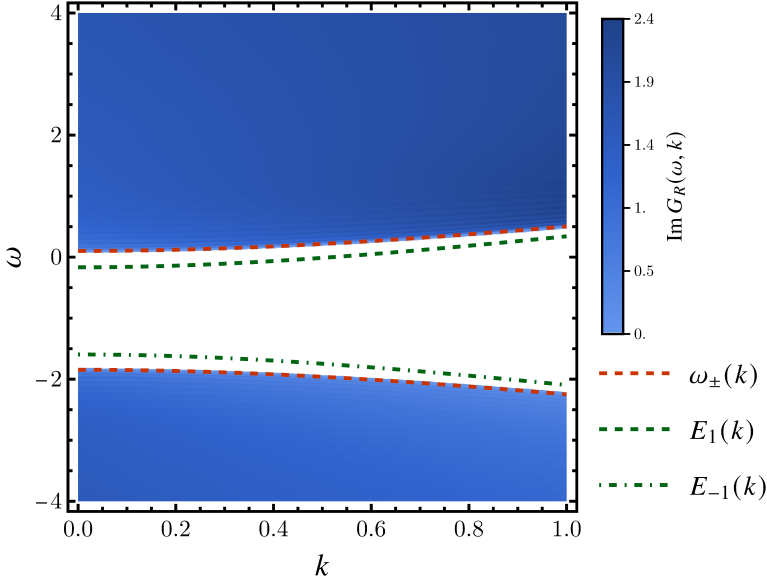


Figure 5.9: Spectral function $\text{Im}G_R(\omega, k)$ for $\{m, \mu q, \lambda\} = \{0.1, 0.9, 1\}$. The gap appears in white and is well delimited by $\omega_{\pm}(k)$ (red dashed lines). The normal mode bands have been superimposed to show the infinitely long-lived modes, see Fig. 5.10. Outside the gap, there is no particle (normal mode) but a continuum shaped by the remnant of the UV conformal branch cuts. Since the regulator and the chemical potential explicitly break conformality, we do not reproduce the pure AdS Lorentz-invariant spectrum for any finite value of ω and k .

for $\{\mu, q, m, \lambda\} = \{3/4, 1.2, 1/10, 1\}$. Inside the gap (white area), the spectral weight of excitations is indeed zero to numerical accuracy except at the positions of the normal modes of the background fermions. The latter are computed directly from the solution of the background Dirac equation (green lines in Fig. 5.9), as they cannot be seen numerically in the spectral function because they are infinitely long-living modes which show in the spectrum as Dirac delta peaks. Being infinitely narrow on the real axis, they can only be detected in the complex- ω plane. Representing schematically the normal mode located at ω_{\star} by $\text{Im}G(\omega = \text{Re}(\omega)) = Z\delta(\omega - \omega_{\star})$ where Z is the peak weight (wavefunction renormalization), we have, for complex ω :

$$\text{Im}G_R(\omega, k) = -Z \frac{\text{Im}\omega - \text{Im}\omega_{\star}}{(\text{Re}\omega - \text{Re}\omega_{\star})^2 + (\text{Im}\omega - \text{Im}\omega_{\star})^2}. \quad (5.39)$$

When $\text{Re}\omega = \text{Re}\omega_{\star}$, this simplifies to

$$\text{Im}G_R(\omega, k) = -\frac{Z}{\text{Im}\omega - \text{Im}\omega_{\star}}. \quad (5.40)$$

We check this picture against the numerics first in Fig. 5.10 (A), where the absolute value of the spectral function in complex frequency plane shows the typical structure

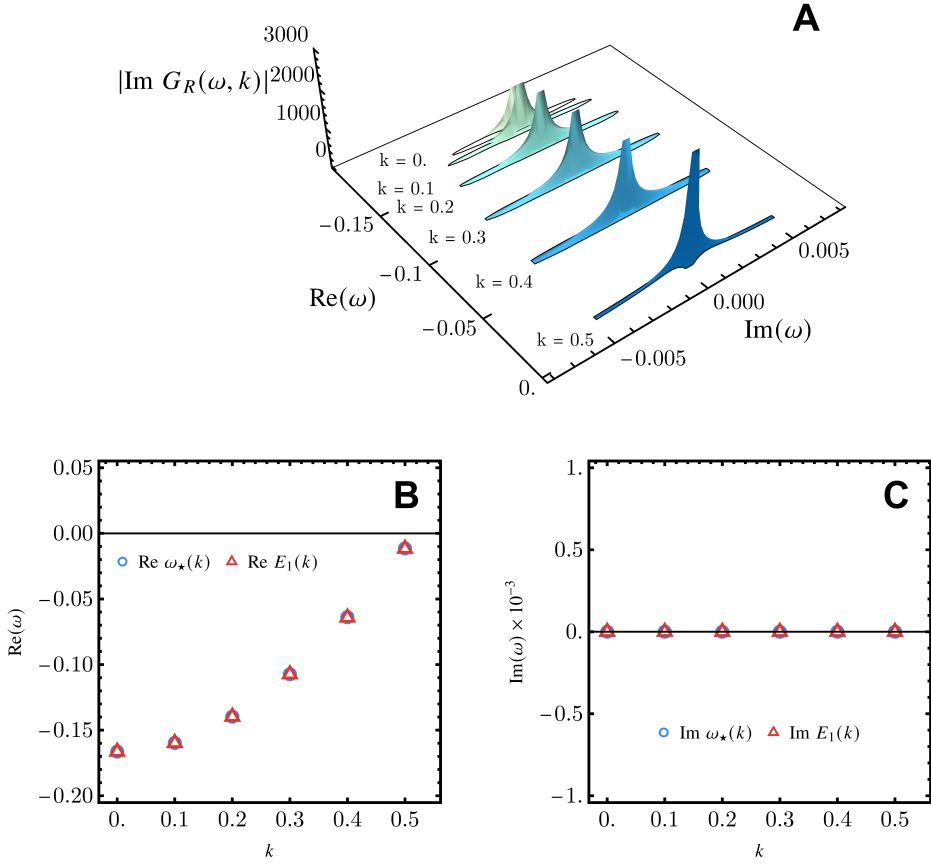


Figure 5.10: (A) Absolute value of the fermionic spectral function for different values of momentum. The plot is cropped for values below 100 to highlight the quasiparticle peaks. (B and C) Comparison of the poles in the spectrum (blue circles), identified in (A), to the first electron band of the background (red triangles). The real parts (B) of both sets agree perfectly; the imaginary parts (C) are both zero to high accuracy. All this data is computed for $\{m, \mu q, \lambda\} = \{0.1, 0.9, 1\}$.

of a string of poles (for various momentum values) lying on the real axis. The relation (5.40) is then used to identify the dispersion relation of the pole $\omega_*(k)$ by fitting $\text{Im}G_R(\omega, k)$. We find, with no big surprise, a perfect agreement with the normal mode excitations $E_1(k)$ corresponding to the first electron band, as seen in Fig. 5.10 (C) and (D). A similar picture is found for the first hole band $E_{-1}(k)$ and this yields the spectrum inside the gap, plotted in Fig. 5.9.

In Fig. 5.11 we compare the spectral function at finite μ for our regulated quantum electron star (blue data points) to the fermionic spectral function in a pure AdS_4 background with finite chemical potential, either with (green line) and without (red line) regulation by the confining scalar. The comparison is given at $k = 0$ (left) and $k = 1$ (right). The Dirac spectrum in AdS_4 is well-known [228]:

$$G_R(\omega, k) = \begin{cases} \frac{2}{\omega^2 - k^2} \frac{\Gamma(1/2 - m)}{\Gamma(1/2 + m)} \left[-\frac{i}{2} (\omega^2 - k^2) \right]^{2m+1} [\omega\gamma^0 - k\gamma^1] & \text{if } \omega > k, \\ \frac{2}{\omega^2 - k^2} \frac{\Gamma(1/2 - m)}{\Gamma(1/2 + m)} \left[\frac{i}{2} (\omega^2 - k^2) \right]^{2m+1} [\omega\gamma^0 - k\gamma^1] & \text{if } \omega < -k. \end{cases} \quad (5.41)$$

It has a conformal branch-cut at $\omega = k$ and a gap for $\omega^2 < k^2$. For AdS_4 with finite electrostatic potential, one merely needs to replace $\omega \rightarrow \omega + \mu q$ in the previous expression. Adding confining potential by turning on the chirality-breaking flat scalar widens the gap to $(\omega + \mu q)^2 < k^2 + \lambda^2$; in particular the gap is open also at $k = 0$. The rQES solution outside the gap exhibits qualitatively the same spectral function as that of the confined Dirac spectrum in pure AdS_4 but for renormalized IR values $\omega_{\text{IR}}, k_{\text{IR}}, \lambda_{\text{IR}}$ given in (5.25). It is important to emphasize that none of the modes in this continuum are normalizable and thus do not contribute when building the bulk rQES, even when μq is large enough that $\omega_+(k) < 0$. This is guaranteed by our choice of UV boundary conditions.

5.4 Towards a self-confining quantum electron star

5.4.1 Comparison to the holographic superconductor

By construction the confinement in our setup gives an AdS_4 -to- AdS_4 solution. With the fully backreacted solution in hand we can also understand what the field theory dual describes. The confining regulator scale λ gaps the field theory fermion spectral function. Considering then the RG flow from the IR emergent conformal field theory towards the UV, this means that as one increases the energy scale it takes a finite distance for occupiable fermion states to be encountered. This can also be seen in the band structure of Fig. 5.6. At this scale the theory deforms away from the strict conformal theory up to the scale μ beyond which it is no longer energetically favorable to occupy more states. The flow up the RG then continues towards the UV AdS_4 fixed point.

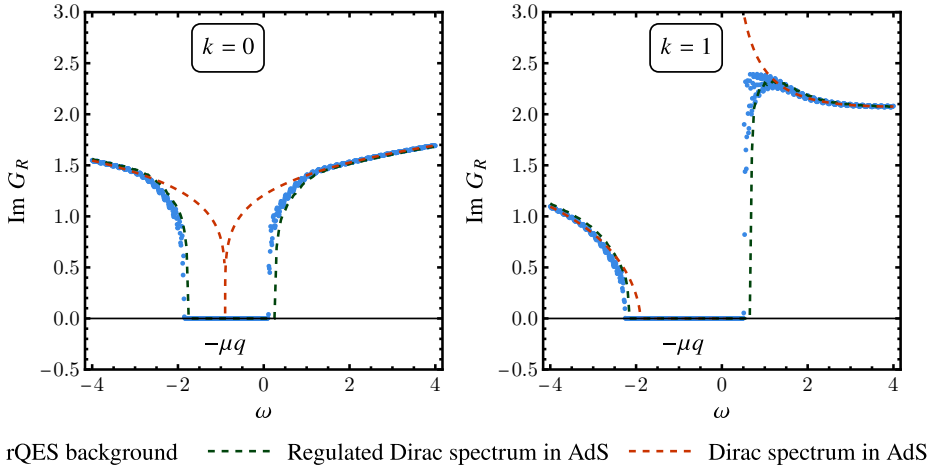


Figure 5.11: (Confined) Dirac spectral function (blue points) in the rQES background for $k = 0$ (left) and $k = 1$ (right), compared with the standard/unconfined (red dashed line) and regulated/confined (green dashed line) Dirac spectral function in AdS with finite electrostatic potential.

In the more usual flow from the UV to the IR this is not a natural RG trajectory. The generic IR will not be a non-trivial conformal field theory. Nevertheless, within holography such AdS_4 -to- AdS_4 domain walls are well-known. Especially in the search for the holographic dual of the holographic superconductor ground state, Horowitz and Roberts and independently Gubser and Rocha have found AdS_4 -to- AdS_4 domain walls (in some cases with logarithmic corrections) in a finite parameter range [217, 218]; the other solution found is the Lifshitz geometry. It was later understood that Lifshitz rather than an AdS_4 IR is the generic holographic superconductor ground state [218, 41], but this is only seen with the inclusion of a stabilizing quartic potential.

In detail of course the solutions are different. The Horowitz-Roberts-Gubser-Rocha holographic superconductor ground states do not need an additional confining scalar. They can also be obtained classically without the need for a one-loop Hartree mean field. This is due to the fact that the bosonic field already couples quadratically to the electrostatic potential A_t . A fermion only couples linearly, but its one-loop contribution can couple at all orders. This is why for fermionic systems one needs to go to one-loop.

5.4.2 Confinement in the rQES solution

Given that the Horowitz-Roberts-Gubser-Rocha AdS_4 -to- AdS_4 solutions do not need a confining potential, and that the more generic holographic superconductor Lifshitz solutions are known, it is a natural question why we do not try to remove the soft-confining regulator altogether. There was in fact a concerted effort to do so several years ago [42, 48, 46], culminating in the QES model of [49, 50]. The latter two articles

show in detail how the presence of the gap and the discretized spectrum are crucial to construct any type of quantum fermionic backreacted solution, *i.e.*, where one or a small finite number of radial modes are occupied. Any attempt to remove the confining potential results in a uncontrolled continuum spectrum.

It is precisely this insight that was the starting point for our confining potential. What we have furthermore shown, is that even then there are several severe technical hurdles to overcome to construct a converging fully backreacted confined quantum electron star solution. At the same time the general insight still holds. Our infrared boundary conditions crucially depend on the coupling to the scalar $\Phi(z)$ to extend the domain of existence of normalizable modes of AdS_4 all the way to $k = 0$. The parameter λ , as we previously noted, acts as a momentum shift in this domain such that a mode at $k = 0$ will behave as a mode at $k_{\text{eff}} = \lambda$ and therefore normalizable modes with $|\omega + \mu q| < \lambda$ will be found. These can be populated and will condense in the bulk. Turning off the potential, even slowly, will invariably lead to a lack of normalizable modes at the lowest momenta and will bring us back to a situation similar to that of AdS_4 .

One sliver of hope would be that the domain wall solution itself, after convergence, can support a well in the Schrödinger potential such that a regulator is no longer necessary. We have therefore looked at this (Fig. 5.12) by comparing the Schrödinger potential for a $k = 0$, $\omega = E_1(0)$ mode in the confined quantum electron star AdS_4 -to- AdS_4 background with and without the confining potential. Without a potential, however, the AdS_4 -to- AdS_4 quantum electron star domain wall solution is not confining. We do see that $V_{\text{domain wall}}(z \rightarrow \infty) > V_{\text{AdS}}$ which means the wedge of existence of normalizable modes is indeed wider in the domain wall solution than in the AdS_4 solution. Yet, the modes with sufficiently small momenta (including $k = 0$) are always outside the wedge.

This therefore leads us to believe a true QES would not *remove* the regulator but must *incorporate* it into the model, *i.e.*, make the scalar field a dynamical dilaton which couples to the Dirac fermion and drives the geometry from one fixed point to another.

5.5 Discussion and conclusions

In this paper we have constructed a self-consistent model of a single band confined holographic Fermi liquid. The crucial technical problem, the infrared divergence brought about by the fermionic wavefunctions, is solved by controlling it by hand. We control the far infrared by the means of a scalar regulator, equivalent to a soft-confining potential. The confinement is drastic and 100%: our regulated quantum electron star is dual to a gas of infinitely-long living particles with zero self-energy. In the limit where we compute, it is a single-band Fermi-gas rather than a Fermi-liquid.⁶ At higher

⁶This holds at zero temperature. At finite temperature a black hole horizon would form, causing inevitably some dissipation even in the presence of the confinement.

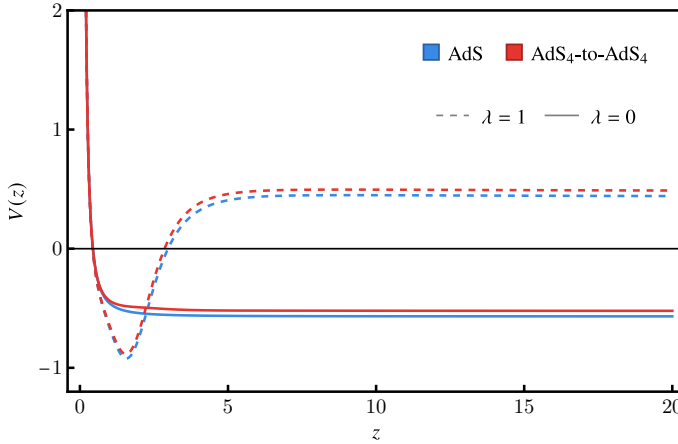


Figure 5.12: Comparison of the Schrödinger potential for the AdS₄ (blue) and AdS₄-to-AdS₄ (red) solutions with (dashed) and without (solid) regulator, for $\{m, \mu q, k, \omega\} = \{0.1, 1.05, 0, -0.027\}$.

energies, the spectrum switches to the featureless continuum inherited from the UV conformal field theory (though it is not conformally invariant due to the presence of the confining potential).

The regulated quantum electron star is the thermodynamically preferred solution over the Reissner-Nordström background for $\mu q/m > (\mu q/m)_{\text{critical}}$. The transition is first order, which means that there is no continuous exchange of charge from the RN solution to the bulk Fermi sea. Instead all the charge is carried by the infinitesimally small rQES. This is somewhat different from the conundrum that we mention in the Introduction: the onset of a log-oscillatory signal in the spectral function signaling a putative instability and the presence of normalizable solutions. The first order transition is essentially unrelated to the RN horizon instability.

Although it is not yet clear how the rQES is related to the final state after the conjectured continuous quantum phase transition which destroys the Reissner-Nordström black hole horizon signalled by the log-oscillatory instability, we nevertheless feel it is a step in the right direction, bringing us closer to the full unregulated quantum electron star. The reasons are the following:

1. It is now much clearer what a healthy Fermi liquid should do on the gravity side: it should self-consistently form a geometry which yields such an effective potential for the Dirac fermion that it is just confined enough not to diverge in far IR but not so much that the bulk Fermi sea dies out in the far IR, failing to influence the low-energy physics.
2. We have inspected in some detail the spectrum and the phenomenology of the dual confined Fermi liquid. Although our confining bulk construction is somewhat more natural in holography – it just uses a non-dynamical rather than

a dynamical scalar — than the hard-wall model [47], and it now allows us to compute the backreaction, qualitatively the field-theory side description is only marginally improved. Similar to the hard-wall model, the occupied fermions have vanishing self-energy. The main effect of the backreaction is to understand how this confined Fermi gas emerges in an RG flow from the UV conformal field theory. In the likely event that an unregulated (confining) quantum electron star — supported for instance by a dynamical rather than a non-dynamical scalar (such as the fluid electron star in [45]) — has a Lifshitz IR rather than an AdS_4 IR, possible decay into the Lifshitz horizon could provide a finite lifetime and an honest Fermi liquid.

3. Unlike the global AdS radius regulator of [50] which cannot be easily be sent to infinity, our scalar can at least in principle be made dynamical. That would be a perfectly natural holographic model, given the ubiquity of non-minimally coupled scalars in top-down holographic actions. Therefore, a very natural line of further research is to turn this construction into a fully dynamical Einstein-Maxwell-Dirac-scalar system, similar to the fluid approach of [45].

Apart from the natural next step – making the dilaton dynamic – a number of other directions of work open up. It would be useful to understand the relation of our work to the AdS/QCD studies, some of which employ a similar type of scalar (soft wall) to impose confinement. The role of the Fock correction (the one-loop exchange diagram) is also not clear yet, and may be important for a fully self-regulating solution and/or a finite self-energy. Finally, the most characteristic property of rQES – the domain-wall-type solution with an infrared AdS_4 , is analogous to the domain-wall holographic superconductor solutions of Horowitz-Roberts-Gubser-Rocha [41, 217, 229]. Based on those results and the macroscopic electron star with dynamical dilaton studied in [45], it strongly suggests that Lifshitz IR quantum electron stars must also exist.

Acknowledgements

We thank Jan Zaanen for discussions. This research was supported in part by the Netherlands Organization for Scientific Research (NWO), the Netherlands Organization for Scientific Research/Ministry of Science and Education (NWO/OCW), Ministry of Education, Science and Technological Development of the Republic of Serbia and Science Fund of the Republic of Serbia, under the Key2SM project (PROMIS program, Grant No. 6066160).

Chapter 6

Complexity for conformal field theories

Attribution

This chapter was published as a journal article under the title “Complexity for Conformal Field Theories in General Dimensions” in the journal *Physical Review Letters* (PRL), volume 128, issue 5 (2022), together with Shira Chapman, Jan de Boer and Claire Zukowski.

6.1 Introduction

The peculiarity of quantum systems is rooted in their entanglement pattern. Hence, there is increasing interest in studying measures characterizing entanglement in quantum states. The most famous of these measures is the entanglement entropy, which estimates the knowledge a given subsystem has about the full quantum state. In recent years, it became apparent that entanglement entropy is not enough to capture the full information about quantum correlations in a state. As a consequence, a new measure from quantum information became prominent in studies of quantum states. This measure, known as quantum computational complexity (QCC), estimates how hard it is to construct a given state from a set of elementary operations [230, 231, 56]. QCC is also of clear interest in recent efforts to construct quantum computers.

QCC has attracted a lot of attention in high energy theory due to its proposed relation to black holes [232, 54]. This relation was explicitly formulated within the holographic (or AdS/CFT) correspondence [25]. It turns out that the growth of black hole interiors behaves in a very similar way to the growth of complexity during Hamiltonian

evolution in quantum systems, see, *e.g.*, [233, 234, 235, 236, 237, 238, 239]. These ideas suggest a promising avenue to address puzzles related to black hole spacetimes and their interior geometry.

However, the lack of a complete framework for studying QCC within quantum field theory (QFT) has been a stumbling block towards rigorously establishing the connection between black hole interiors and QCC. Significant progress was made for free and weakly coupled QFTs [240, 241, 242, 243, 244, 245, 246] and for strongly coupled two-dimensional conformal field theories (CFTs) [247, 248, 249, 250, 251]. Yet, no results exist at present for circuit complexity in CFTs in $d > 2$ and further, its precise connection with holography has not been established in any dimension. The importance of studying complexity in $d > 2$ becomes evident when noting that holographic complexity behaves very differently in $d = 2$ and in $d > 2$, in particular when studying the complexity of formation of thermofield double states [252] or its sensitivity to defects [253, 254]. The goal of this letter is to bridge these gaps by studying complexity of CFTs in $d > 2$ and further by establishing a rigorous connection between complexity and geometry in holography.

We employ the symmetry generators to construct circuits in unitary representations of the Lorentzian conformal group and present explicit results for state-dependent distance functions along these circuits. Our circuits live in a phase space which is a coadjoint orbit of the conformal group and the various cost functions take the form of simple geometric notions on these orbits. Using symmetry generators to construct circuits restricts the circuits to move in the space of generalized coherent states. We use this fact to generalize our results to general symmetry groups. We illustrate our methods by focusing on circuits starting from a scalar primary state whose coadjoint orbit can be identified with the coset space $SO(d, 2)/(SO(2) \times SO(d))$, but our techniques are also applicable to more general spinning states. We derive bounds on the complexity and its rate of change.

We explicitly relate our unitary circuits to timelike geodesics in anti-de Sitter spacetimes. We find that the line element in the complexity metric admits a very simple interpretation as the average of the minimal and maximal squared distances between two nearby geodesics. This provides a novel bulk description for complexity which is rigorously derived from the CFT and opens new possibilities for testing the holographic complexity proposals.

This paper is organized as follows: in Sec. 6.2, we introduce the relevant complexity distance functions. In Sec. 6.3 we present the result for the complexity of CFT states in general dimensions. In Sec. 6.4-6.5, we connect our results to the notions of coadjoint orbits and generalized coherent states. In Sec. 6.6 we connect our results to holography. We conclude in Sec. 6.7 with a summary and outlook.

6.2 Preliminaries

Explicitly, QCC is defined as the minimal number of gates required to reach a desired *target state*, starting from a (typically simpler) *reference state*. For several applications, it is advantageous to focus on continuous notions of complexity rather than a discrete gate counting. Such ideas were put forward by Nielsen [58, 57, 255] who translated the problem of studying minimal gate complexity to that of studying geodesics on the space of unitary transformations. In a very similar way, we can study notions of continuous complexity using geodesics through the space of quantum states.

Continuous complexity is defined using a cost function $\mathcal{F}(\sigma)$, with circuit parameter σ . The complexity is the minimal cost among all possible trajectories moving from the reference state to the target state: $\mathcal{C} \equiv \min \int d\sigma \mathcal{F}(\sigma)$. Past attempts to study state complexity in CFTs (e.g., [247]) focused on two cost functions: the \mathcal{F}_1 cost function and the Fubini-Study (FS) norm defined as

$$\mathcal{F}_1(\sigma)d\sigma = \left| \langle \psi | \partial_\sigma \psi \rangle \right| d\sigma = \left| \langle \psi_R | U^\dagger dU | \psi_R \rangle \right|, \quad (6.1a)$$

$$\mathcal{F}_{FS}(\sigma)d\sigma = \sqrt{\langle \psi_R | dU^\dagger dU | \psi_R \rangle - \left| \langle \psi_R | U^\dagger dU | \psi_R \rangle \right|^2}, \quad (6.1b)$$

where $|\psi(\sigma)\rangle \equiv U(\sigma)|\psi_R\rangle$ are the states along the unitary circuit, $|\psi_R\rangle$ is the reference state and $ds_{FS}^2 = \mathcal{F}_{FS}^2(\sigma)d\sigma^2$ is the well known FS-metric. Our analysis in the next section demonstrates that the \mathcal{F}_1 cost function assigns zero cost to certain gates and has therefore disadvantages as a complexity measure.

The FS-metric along straight-line trajectories $e^{itH}|\psi_R\rangle$ is proportional to the variance $\Delta E = \sqrt{\langle H^2 \rangle - \langle H \rangle^2}$. We can interpret H as the Hamiltonian and t as the time. This variance was shown by [256] to bound the time required to reach an orthogonal state $\tau_{\text{orth.}} \geq \pi\hbar/(2\Delta E)$ on compact spaces. Inspired by these bounds on orthogonality time, Lloyd conjectured a bound on the rate of computation [257] (see also [234]). Unlike [256], our state manifold is non-compact and our states never become orthogonal. Nonetheless, we will derive bounds on the complexity and its rate of change by other means. Deriving bounds on the state overlap in our setup is an interesting question for future study.

6.3 Complexity in General Dimensions

Consider the Euclidean conformal algebra in $d \geq 2$ with $D, P_\mu, K_\mu, L_{\mu\nu}$ the Euclidean conformal generators (used to construct unitary representations of the Lorentzian conformal group in Sec. 6.A) satisfying

$$D^\dagger = D, \quad K_\mu^\dagger = P_\mu, \quad L_{\mu\nu}^\dagger = -L_{\mu\nu}, \quad (6.2)$$

in radial quantization.

As the reference state, we consider a scalar primary state $|\psi_R\rangle = |\Delta\rangle$ satisfying $D|\Delta\rangle = \Delta|\Delta\rangle$ and $K_\mu|\Delta\rangle = L_{\mu\nu}|\Delta\rangle = 0$ and focus on circuits generated by the unitary

$$U(\sigma) \equiv e^{i\alpha(\sigma)\cdot P} e^{i\gamma_D(\sigma)D} \left(\prod_{\mu<\nu} e^{i\lambda_{\mu\nu}(\sigma)L_{\mu\nu}} \right) e^{i\beta(\sigma)\cdot K}, \quad (6.3)$$

with σ a circuit parameter and $\alpha_\mu, \beta_\mu, \gamma_D$ and $\lambda_{\mu\nu}$ a priori complex parameters, further constrained by the restriction that $U(\sigma)$ be unitary. The circuits take the form $|\alpha(\sigma)\rangle \equiv U(\sigma)|\Delta\rangle \equiv \mathcal{N}(\sigma)e^{i\alpha(\sigma)\cdot P}|\Delta\rangle$ where $\mathcal{N}(\sigma) \equiv \exp(i\gamma_D(\sigma)\Delta)$ is a normalization factor and $\gamma_D(\sigma) \equiv \gamma_D^R(\sigma) + i\gamma_D^I(\sigma)$, with R/I indicating the real/imaginary part. Unitarity of $U(\sigma)$ implies $\gamma_D^I(\sigma) = -\frac{1}{2}\log A(\alpha, \alpha^*)$ (see Sec. 6.B) where

$$A(\alpha, \alpha^*) \equiv 1 - 2\alpha \cdot \alpha^* + \alpha^2 \alpha^{*2} > 0, \quad (6.4)$$

and requiring a positive spectrum for the Hamiltonian D along the circuit implies $\alpha^* \cdot \alpha < 1$ (equivalently $\alpha^2 \alpha^{*2} < 1$).

Substituting $|\alpha(\sigma)\rangle$ into the cost-functions (6.1a)-(6.1b) and using the expectation values of $\{P_\mu, K_\mu, K_\mu P_\nu\}$ (see Sec. 6.B), we find for the \mathcal{F}_1 cost function

$$\frac{\mathcal{F}_1}{\Delta} = \left| \frac{\dot{\alpha} \cdot \alpha^* - \dot{\alpha}^* \cdot \alpha + \alpha^2 (\dot{\alpha}^* \cdot \alpha^*) - \alpha^{*2} (\dot{\alpha} \cdot \alpha)}{A(\alpha, \alpha^*)} + i\dot{\gamma}_D^R \right|, \quad (6.5)$$

while for the FS-metric we obtain

$$\frac{ds_{FS}^2}{d\sigma^2} = 2\Delta \left[\frac{\dot{\alpha} \cdot \dot{\alpha}^* - 2|\dot{\alpha} \cdot \alpha|^2}{A(\alpha, \alpha^*)} + 2 \frac{|\dot{\alpha} \cdot \alpha^* - \alpha^{*2} \alpha \cdot \dot{\alpha}|^2}{A(\alpha, \alpha^*)^2} \right]. \quad (6.6)$$

The FS-metric (6.6) is a positive-definite Einstein-Kähler metric on the complex manifold of states with d complex coordinates α bounded inside the domain (6.4). It satisfies $ds_{FS}^2 = \partial_\alpha \partial_{\alpha^*} K(\alpha, \alpha^*) d\alpha d\alpha^*$, where the associated Kähler potential is defined as $K(\alpha, \alpha^*) = -\Delta \log A(\alpha, \alpha^*)$. Denoting collectively the indices of α and α^* by capital Latin letters, one finds that $R_{AB} = -\frac{2d}{\Delta} g_{AB}$ and $R = -\frac{4d^2}{\Delta}$ and that all sectional curvatures are negative. This means that geodesics will deviate from each other.

In fact, (6.6) is a natural metric on the following quotient space of the conformal group

$$\mathcal{M} = \frac{SO(d, 2)}{SO(2) \times SO(d)}, \quad (6.7)$$

which can also be identified with the space of timelike geodesics in AdS_{d+1} [258, 259], see §6.6. This is similar to the relation between the metric on kinematic space

and spacelike geodesics in AdS_{d+1} , [260, 261, 262, 263] where the relevant orbit is $SO(d, 2)/SO(1, 1) \times SO(1, d - 1)$ [264]. While some of the above observations are well known in the context of geometry of Lie groups [265, 266], here they find a novel role in the context of circuit complexity.

Since the coset space (6.7) is a negatively curved symmetric space, its geodesics passing through $|\psi_R\rangle$ take the form [267]

$$|\psi(\sigma)\rangle = \exp\left[i\sigma(\tilde{\alpha}P_\mu + \tilde{\alpha}^*K_\mu)\right]|\psi_R\rangle, \quad (6.8)$$

and do not reconnect, *i.e.*, (6.7) has no conjugate points [266]. Here, we parametrized our geodesics in terms of the straight-line-trajectory-parameter $\tilde{\alpha}$ rather than α . Explicitly, in terms of the α parametrization, the complexity of a target state $|\alpha(\sigma = 1)\rangle \equiv |\alpha_T\rangle$ is

$$\begin{aligned} C[\tilde{\alpha}] &= \sqrt{2\Delta \tilde{\alpha}^* \cdot \tilde{\alpha}}, \\ 2\tilde{\alpha} \cdot \tilde{\alpha}^* &= \left[\left(\tanh^{-1}\Omega_T^S \right)^2 + \left(\tanh^{-1}\Omega_T^A \right)^2 \right], \end{aligned} \quad (6.9)$$

where $\Omega_T^\pm \equiv \Omega_T^S \pm \Omega_T^A \equiv \sqrt{2\alpha_T \cdot \alpha_T^* \pm 2|\alpha_T^2|}$ (see Sec. 6.C and Sec. 6.D). Earlier, we chose to parametrize the states with $\alpha(\sigma)$ rather than $\tilde{\alpha}$ since this facilitates the evaluation of correlation functions in the state and therefore provides its more natural characterization. We will see later that the relation to holography is also done using the parameter α . The complexity (6.9) can be bounded by employing the inequalities around (6.4)

$$\frac{\Delta}{E_T + \Delta} \sqrt{(E_T - \Delta)} \leq C[\alpha_T] \leq \sqrt{E_T - \Delta} \quad (6.10)$$

where $E_T \equiv \langle \alpha_T | D | \alpha_T \rangle = \Delta(1 - \alpha_T^2 \alpha_T^{*2})/A(\alpha_T, \alpha_T^*)$ is the energy of the target state in radial quantization (see Sec. 6.E).

A substantial difference between the \mathcal{F}_1 cost function and the FS metric is that the former depends on γ_D^R which induces an overall phase in the states through which our circuits pass. In fact, the \mathcal{F}_1 cost function (6.5) without absolute values vanishes on-shell except for its part associated with the overall phase γ_D^R and is simply proportional to the Berry gauge field, cf. [268, 269, 248].

We close by observing that the FS distance along time evolved states $e^{i\tau D}|\alpha_0\rangle$ satisfies a Lloyd-like bound [257]

$$\frac{ds_{\text{FS}}}{d\tau} \leq \frac{E}{\sqrt{\Delta}} \leq \sqrt{\frac{2}{d-2}} E. \quad (6.11)$$

where $E \equiv \langle \alpha_0 | D | \alpha_0 \rangle$ is the energy, $|\alpha_0\rangle$ an arbitrary initial state, and we used the unitarity bound $\Delta \geq d/2 - 1$ [270].

We compare our results to the existing literature for $d = 2$ CFTs in Sec. 6.F. In that case, holomorphic factorization allows us to also treat spinning states (see Sec. 6.G).

6.4 Geometric Action and Coadjoint Orbits

Our results for the cost functions (6.5)-(6.6) can be understood in terms of the geometry of coadjoint orbits, see, e.g., [271, 272]. A similar connection was pointed out in two dimensions in [247, 248].

Let us start by briefly describing the coadjoint orbit method in representation theory. Consider a Lie group G with Lie algebra \mathfrak{g} , a dual space \mathfrak{g}^* consisting of linear maps on \mathfrak{g} , and a pairing $\langle \cdot, \cdot \rangle$ between the Lie algebra and dual space. For matrix groups, the adjoint action of $u \in G$ on $X \in \mathfrak{g}$ is defined as $\text{Ad}_u(X) = uXu^{-1}$. At the level of the algebra, the adjoint action is simply the commutator $\text{ad}_Y(X) = [Y, X]$ where $X, Y \in \mathfrak{g}$. The Maurer-Cartan (MC) form on the full group is $\Theta \equiv u^{-1}du$ where $u \in G$ and it satisfies $d\Theta = -\Theta \wedge \Theta$.

The coadjoint action on the dual space is defined implicitly by

$$\langle \text{Ad}_u^* \xi, X \rangle = \langle \xi, \text{Ad}_{u^{-1}} X \rangle, \quad \xi \in \mathfrak{g}^*, X \in \mathfrak{g}, u \in G, \quad (6.12)$$

from which one can build the coadjoint orbit $\mathcal{O}_\lambda \equiv \{\text{Ad}_u^* \lambda | u \in G\} \subset \mathfrak{g}^*$ of a given dual algebra element $\lambda \in \mathfrak{g}^*$. \mathcal{O}_λ can be identified with the coset space G/H_λ , where the subgroup $H_\lambda = \text{Stab}(\lambda) \equiv \{u \in G | \text{Ad}_u^* \lambda = \lambda\}$ is the stabilizer and the corresponding algebra is $\mathfrak{h}_\lambda \equiv \text{stab}(\lambda)$.

Each coadjoint orbit corresponds to a symplectic manifold with a local pre-symplectic form \mathcal{A}_λ and the Kirillov-Kostant symplectic form ω_λ defined as

$$\mathcal{A}_\lambda = \langle \lambda, \Theta \rangle, \quad \omega_\lambda = \langle \lambda, d\Theta \rangle. \quad (6.13)$$

The geometric action associated to the coadjoint orbit is $S_\lambda = \int \mathcal{A}_\lambda$ [273, 274].

The symplectic form ω_λ is compatible with a complex structure J_λ satisfying $J_\lambda^2 = -1$ if $\omega_\lambda(J_\lambda x, J_\lambda y) = \omega_\lambda(x, y)$. In this case it is possible to define a Kähler metric $ds_{G/H_\lambda}^2(x, y) = \omega_\lambda(x, J_\lambda y)$ on the coadjoint orbit \mathcal{O}_λ .

In Sec. 6.H, we apply the above definitions in the fundamental (matrix) representation of the conformal algebra $\mathfrak{so}(d, 2)$ with representative λ taken to be proportional to the dilatation matrix with stabilizer group $\mathfrak{h}_\lambda = \mathfrak{so}(2) \times \mathfrak{so}(d)$ and orbit corresponding to the quotient space G/H_λ from Eq. (6.7). This yields an agreement with Eqs. (6.5)-(6.6), i.e.,

$$\mathcal{F}_1 d\sigma = |\mathcal{A}_\lambda|, \quad ds_{FS}^2 = ds_{G/H_\lambda}^2. \quad (6.14)$$

As alluded to above, \mathcal{A}_λ can also be interpreted as a Berry gauge field, and the Berry curvature is simply the symplectic form ω_λ . Circuits starting from spinning primary states in $d > 2$ amount to a different choice of representative to match with the relevant reduced stabilizer group.

6.5 Coherent State Generalization

The equivalence of the FS-metric and the \mathcal{F}_1 cost function with their geometric counterparts on the coadjoint orbit is also valid within infinite dimensional Hilbert spaces obtained via geometric quantization of the orbits of arbitrary Lie groups [247, 251, 275]. This can be understood using a group theoretical generalization of the notion of coherent states, see *e.g.*, [276, 277, 278, 279]. The existence of these states is intrinsically connected to the representation theory of the symmetry in question. In this section we explain how the coadjoint orbit perspective leads to the complexity functionals of (6.5)-(6.6) for general Lie groups.

As before, we consider some real Lie group G with Lie algebra \mathfrak{g} . The corresponding complex algebra admits a decomposition $\mathfrak{g}_{\mathbb{C}} = \mathfrak{n}_+ + \mathfrak{h}_{\mathbb{C}} + \mathfrak{n}_-$ with a real structure (a dagger) which maps $\mathfrak{h}_{\mathbb{C}}$ to itself and \mathfrak{n}_+ to \mathfrak{n}_- . For a detailed account of this decomposition, see Sec. 6.I. The generators of the real Lie algebra are anti-Hermitian. We denote the real subalgebra of $\mathfrak{h}_{\mathbb{C}}$ by \mathfrak{h} and its associated Lie group H . We also assume that $[\mathfrak{n}_+, \mathfrak{n}_+] \subset \mathfrak{n}_+$ and similarly for \mathfrak{n}_- and that $[\mathfrak{h}_{\mathbb{C}}, \mathfrak{n}_{\pm}] \subset \mathfrak{n}_{\pm}$. We take a basis of raising operators E_{α} for \mathfrak{n}_+ and lowering operators $E_{-\alpha}$ for \mathfrak{n}_- with $E_{\alpha}^{\dagger} = E_{-\alpha}$ and a basis h_i for \mathfrak{h} .

We consider a unitary highest weight representation generated by a one-dimensional base state $|\psi_R\rangle$ satisfying $\mathcal{D}(E_{\alpha})|\psi_R\rangle = 0$ and $\mathcal{D}(h_i)|\psi_R\rangle = \chi_i|\psi_R\rangle$ with χ_i constants and where \mathcal{D} is the representation on the Hilbert space. In other words, the base state is invariant up to a phase under the action of the stabilizer subgroup $H \subset G$. This includes the possibility of spinning highest weight representations, cf. [280, 281, 282, 283], in which case the stabilizer subgroup will be smaller compared to the spinless case.

We act on our base state with a unitary transformation $U = \exp\left(\sum_{\alpha}(\lambda_{\alpha}E_{\alpha} - \lambda_{\alpha}^*E_{-\alpha}) + \sum_i x_i h_i\right)$ in order to produce generalized coherent states

$$|u\rangle \equiv U|\psi_R\rangle = \mathcal{N}_H(z, z^*, x) \exp\{z_{\alpha} \mathcal{D}(E_{-\alpha})\} |\psi_R\rangle, \quad (6.15)$$

with \mathcal{N}_H a normalization factor (including possibly an overall phase). x are real coordinates on the stabilizer and z, z^* are holomorphic coordinates on the orbit. The relation between the coordinates which appear in U and the coordinates z can be quite complicated in general. Of course, multiplying U from the right by an element of H does not modify $|u\rangle$ (up to an overall phase) and therefore U can be thought of as an element of $\mathcal{D}(G/H)$.

Generalized coherent states can be understood in terms of coadjoint orbits. Consider the dual element

$$\lambda(\mathcal{O}) = i \text{Tr} \left[|\psi_R\rangle \langle \psi_R| \mathcal{D}(\mathcal{O}) \right], \quad (6.16)$$

where the trace is taken in the infinite dimensional representation space. The coadjoint action (6.12) on λ is simply $\langle \text{Ad}_U^* \lambda, \mathcal{O} \rangle = i \text{Tr} \left(|\psi_R\rangle \langle \psi_R| U^{-1} \mathcal{D}(\mathcal{O}) U \right) = i \langle u | \mathcal{D}(\mathcal{O}) | u \rangle$,

which indeed remains unmodified by the stabilizing elements $U \in \mathcal{D}(H)$. Thus we can view λ as a representative that selects the orbit G/H .

The MC form of the unitary U in Eq. (6.15) can be decomposed as $\Theta \equiv U^\dagger dU \equiv \Theta^- + \Theta^{(H)} + \Theta^+$ with $\Theta_\pm \in \mathfrak{n}_\pm$, $\Theta^{(H)} \in \mathfrak{h}_\mathbb{C}$. When acting with it on the base state we obtain

$$\Theta|\psi_R\rangle = U^{-1} \left[\frac{d\mathcal{N}_H}{\mathcal{N}_H} U + \mathcal{N}_H d \left(e^{z_\alpha \mathcal{D}(E-\alpha)} \right) \right] |\psi_R\rangle. \quad (6.17)$$

So $\Theta_-|\psi\rangle = (U^{-1}\mathcal{N}_H d e^{z_\alpha \mathcal{D}(E-\alpha)})_-|\psi\rangle$ and this only depends on dz_α and not on dz_α^* . Therefore $\Theta^-|\psi_R\rangle = \Theta^-_\mu dz^\mu|\psi_R\rangle$ and by conjugation $\langle\psi_R|\Theta^+ = \langle\psi_R|\Theta^+_\mu dz^{*\mu}$. Notice also that $\Theta^\dagger = -\Theta$ and therefore the FS-metric (6.1b) becomes $ds_{FS}^2 = -\langle\psi_R|\Theta^+_\mu \Theta^-_\nu|\psi_R\rangle dz^{*\mu} dz^\nu$.

The metric has a manifest complex structure \mathcal{J} compatible with the dagger which maps z to $-iz$ and z^* to iz^* . Together, the metric and the complex structure define a closed 2-form according to $\omega(X, Y) = -g(X, \mathcal{J}Y)$, *i.e.*,

$$\begin{aligned} \omega &= -i\langle\psi_R|\Theta^+_\mu \Theta^-_\nu|\psi_R\rangle dz^{*\mu} \wedge dz^\nu \\ &= -i\langle\psi_R|\Theta \wedge \Theta|\psi_R\rangle = i\langle\psi_R|d\Theta|\psi_R\rangle. \end{aligned} \quad (6.18)$$

We recognize this as the Kirillov-Kostant symplectic form (6.13) through the representative (6.16).

Finally, the geometric action of the coadjoint orbit associated with the representative (6.16) relates to the \mathcal{F}_1 cost function (6.1a)

$$\mathcal{F}_1 d\sigma = |\langle\psi_R|U^\dagger dU|\psi_R\rangle| = |\langle\lambda, \Theta\rangle| = |\mathcal{A}_\lambda|. \quad (6.19)$$

For the specific case of the conformal algebra considered in §6.3, we can take as base states the scalar primary states, $|\psi_R\rangle = |\Delta\rangle$. The stabilizing subalgebra is $\mathfrak{h} = \mathfrak{so}(2) \times \mathfrak{so}(d)$, generated by D and $L_{\mu\nu}$. The raising operators $\mathfrak{n}_+ = \{K_\mu\}$ annihilate highest weight states and the lowering operators are their conjugates $\mathfrak{n}_- = \{P_\mu\}$. Together these parametrize the coset (6.7).

6.6 Holography

The symplectic geometry we found equally describes the space of timelike geodesics in AdS, and this allows us to rigorously derive a bulk description of complexity. Explicitly, our circuits (6.3) starting from a scalar primary are mapped to the following particle trajectory in embedding coordinates in AdS_{d+1} of curvature radius R (following [284]'s conventions)

$$\begin{aligned} X_0 &= r(t) \cos(t/R), & X_{0'} &= r(t) \sin(t/R), \\ X_\mu &= \frac{E_0 r(t)}{EA(\alpha, \alpha^*)} \left(\alpha_\mu B^*(t, \alpha^*) + \alpha_\mu^* B(t, \alpha) \right) \end{aligned} \quad (6.20)$$

where

$$r(t) = \frac{RE}{E_0} \frac{\sqrt{A(\alpha, \alpha^*)}}{|B(t, \alpha)|}, \quad E = E_0 \frac{(1 - \alpha^2 \alpha^{*2})}{A(\alpha, \alpha^*)} \quad (6.21)$$

$$B(t, \alpha) = e^{it/R} \alpha^2 - e^{-it/R}.$$

Here, α parametrizes the phase space of the geodesics, and $A(\alpha, \alpha^*) > 0$ and $\alpha^2 \alpha^{*2} < 1$. E is the energy of the massive particle, which is minimal at rest and equal to $E_0 = mR(1 + O(1/mR))$, with m the mass of the particle. The phase space is identical to that of the CFT_d with the identification $\Delta = E_0$. Time evolution $e^{itD} |\alpha\rangle = |\alpha e^{it}\rangle$ amounts to translating the geodesic in time in AdS_{d+1} and fixed radius geodesics correspond to $\alpha^2 = 0$. The complexity (6.9) is expressed in terms of the energy E and the angular momentum J of the massive particle through $\Omega_T^{S/A} = \sqrt{\frac{E \pm J - \Delta}{E \pm J + \Delta}}$ (see Sec. 6.J). For a circuit of circular geodesics starting at the origin and ending at a radius $r_T = R^2/\delta$ close to the boundary, the complexity diverges as $\mathcal{C}[\delta] \sim \sqrt{\Delta} \log[2R/\delta]$.

The FS-metric over the space of circuits receives a surprisingly simple interpretation in terms of the maximal and minimal perpendicular distance between two infinitesimally nearby geodesics (as illustrated in figure 6.1, see Sec. 6.J)

$$ds_{\text{FS}}^2 = \frac{\Delta}{2R^2} \left(\delta X_{\text{perp, min}}^2 + \delta X_{\text{perp, max}}^2 \right). \quad (6.22)$$

6.7 Summary and Outlook

We studied the circuit complexity of trajectories associated to unitary representations of the conformal group in general dimensions. We considered primary states as reference states. Boundary states which are disentangled [285] could be an interesting alternative. Our gates, consisting of global conformal transformations, are non-local similarly to the gates relevant for holographic complexity [286]. We explained how our results can be understood using the geometry of coadjoint orbits. We presented general proofs relating the FS-metric and \mathcal{F}_1 cost function to a coadjoint orbit metric and geometric action in the context of generalized coherent states. These proofs are also applicable to circuits starting from spinning primaries and to other symmetry groups.

Our complexity geometry does not provide a notion of distance between any two states in the CFT Hilbert space. It is an important question for the future to describe the complexity for circuits moving across different conformal families. Furthermore, considering more general states formed by non-local insertions could reveal the role of OPE coefficients in studying complexity.

Considering the complexity of mixed states in CFT, *e.g.*, thermal states or subregions of the vacuum is another important question. For example, coherent states

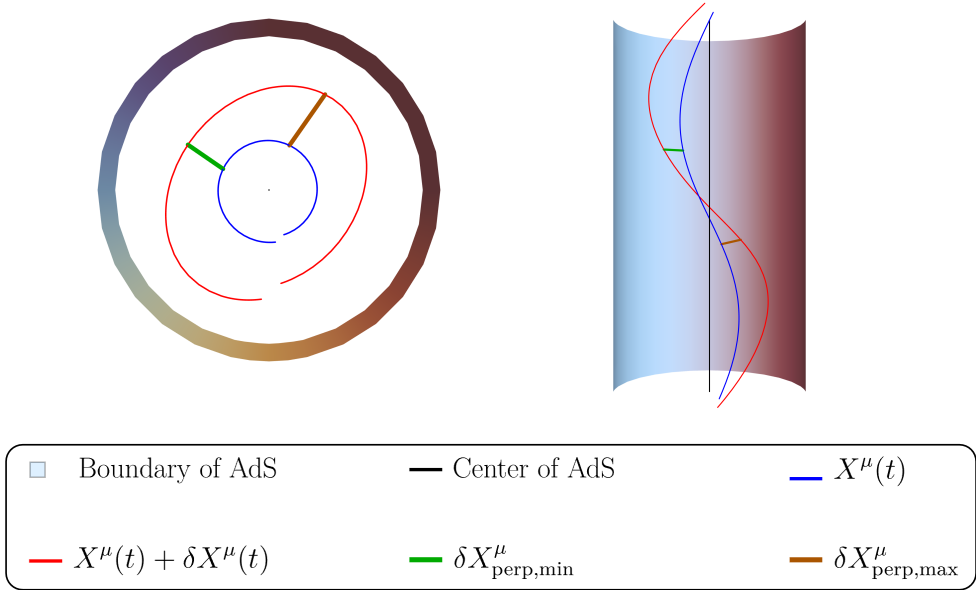


Figure 6.1: Illustration of two nearby timelike geodesics in AdS_3 (blue, red) corresponding to two boundary circuits and the minimal (green) and maximal (brown) perpendicular distance between them. The infinitesimal variation was exaggerated to improve the visualization.

can be used as a starting point for the ensemble approach to mixed state complexity [287]. It is also interesting to explore the complexity of states with a conformal timelike defect/boundary and compare to holography [253, 254, 288].

The path-integral approach to complexity [289, 290, 291, 292, 293, 294] involves the two-dimensional Liouville action and central charge. Hence, it relates to circuits going beyond the global conformal group. It is therefore compelling to study the $d > 2$ complexity of circuits constructed from general smearings of the stress tensor and tie the result to a higher-dimensional Liouville action [289, 295].

Our complexity geometry is highly symmetric. It is interesting to break some of the symmetry by adding penalty factors – effectively favoring certain directions through the manifold of conformal unitaries. Our \mathcal{F}_1 cost function (6.1a) (also considered in [289]) vanishes along certain non-trivial trajectories and differs from the \mathcal{F}_1 norm used when studying the complexity of Gaussian states (*e.g.*, [240]). The difference is reminiscent of exchanging the order of the absolute value in the complexity definition and the sum over circuit generators. We intend to compare these two different definitions in the future.

We rigorously derived a bulk description of our circuits as trajectories between timelike geodesics in AdS. We could connect this picture to the holographic complexity

proposals for instance by exploring the influence of massive particles on the action. It is valuable to study generalizations of our circuit-geodesic duality in other spacetimes and for more than one (possibly spinning) particle. Further, it is important to explore the relation of our bulk picture to the phase space of Euclidean sources [296, 297, 298, 299] and hence possibly to the complexity=volume proposal (see also [300]). Another compelling possibility is to connect our bulk picture to a parallel transport problem of timelike geodesics similarly to what was done for spacelike geodesics [301, 302] in the context of kinematic space [260, 261, 262, 263].

Complexity provides us with a new measure of entanglement in CFTs and it is interesting to probe its potential in diagnosing phase transitions. Some inspiration can be drawn from [303, 304, 305, 306, 307]. We hope to come back to this question in the future.

6.A Relating the Euclidean and Lorentzian Conformal Generators

The Euclidean conformal generators

$$\begin{aligned}
 [D, P_\mu] &= P_\mu, & [L_{\mu\nu}, P_\rho] &= \delta_{\nu\rho} P_\mu - \delta_{\mu\rho} P_\nu, \\
 [D, K_\mu] &= -K_\mu, & [L_{\mu\nu}, K_\rho] &= \delta_{\nu\rho} K_\mu - \delta_{\mu\rho} K_\nu, \\
 [K_\mu, P_\nu] &= 2\left(\delta_{\mu\nu} D - L_{\mu\nu}\right), \\
 [L_{\mu\nu}, L_{\rho\sigma}] &= -L_{\mu\rho} \delta_{\nu\sigma} + L_{\mu\sigma} \delta_{\nu\rho} - (\mu \leftrightarrow \nu),
 \end{aligned} \tag{6.23}$$

used in our analysis obey an $SO(d+1, 1)$ algebra. This might seem confusing since we are interested in studying unitary circuits of the Lorentzian conformal group $SO(d, 2)$. However, the choice of Hermiticity conditions (6.2) ensures that we are building unitary circuits of the Lorentzian conformal group. We present below the explicit relation between the Euclidean conformal generators on \mathbb{R}^d and the Lorentzian conformal generators on $\mathbb{R}^{1, d-1}$. The Euclidean generators are then used to construct unitary representations of the Lorentzian conformal group and in fact play a role analogous to that of the ladder operators J_\pm in the quantum mechanical treatment of angular momentum. Although this idea is very commonly used in defining the Hilbert space in CFTs with respect to constant time slices on the Lorentzian cylinder, it is not always explicitly addressed. We found that it was most clearly explained in [308, 309], see also [310]. Since here the generators play an essential role in constructing the circuits for defining complexity, we found it worthwhile to present some of the details of this construction here for completeness.

The idea is to construct the Hilbert space with respect to constant time slices on the Lorentzian cylinder, using the cylinder translation generator as the Hamiltonian in quantizing the theory. This means that as a starting point for our circuits, we will consider states which are eigenstates of this generator. Since we are constructing

unitary Lorentzian representations, all the Lorentzian generators are taken to be anti-Hermitian. The generator of time translations on the cylinder is mapped via a hyperbolic map $\tan(t_{cyl}) = \frac{2t}{1+|\vec{x}|^2-t^2}$ to the generator $P_L^0 - K_L^0$ on the Lorentzian plane, which plays the role of the Hamiltonian when quantizing the theory on the Lorentzian plane. The relevant time slices are illustrated in figure 6.2. Here and throughout the following, we will use a subscript L to denote Lorentzian generators on $\mathbb{R}^{1,d-1}$ and E to denote Euclidean generators on \mathbb{R}^d . To go to the Euclidean picture one has to Wick rotate with respect to the time direction on the Lorentzian cylinder $\tau_{cyl} = it_{cyl}$, in such a way as to obtain a Euclidean cylinder, and finally map radially to the Euclidean plane $\tau_{cyl} = \log(r)$. The Hermiticity conditions of the Euclidean generators follow from this mapping procedure and are as given in Eq. (6.2).

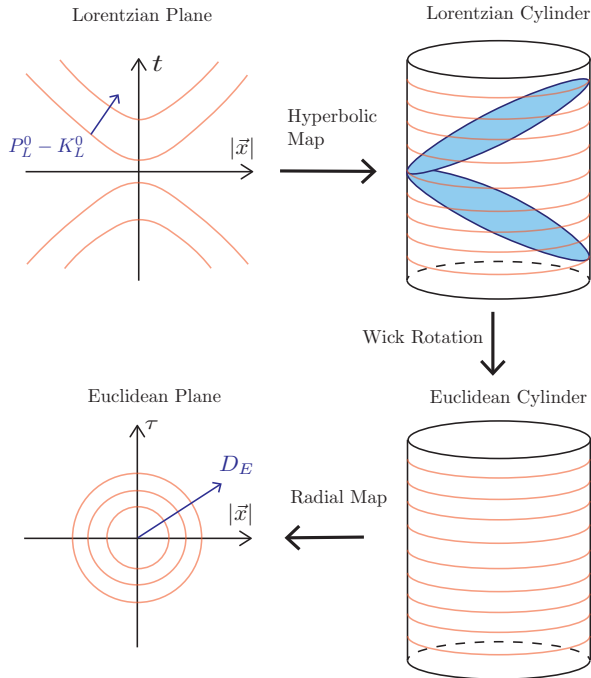


Figure 6.2: Illustration of the process of mapping the Lorentzian generators to the Euclidean generators. We start with quantizing the theory with respect to constant $P^0 - K^0$ slices on the Lorentzian plane. Those are mapped to constant time slices on the Lorentzian cylinder. The Wick rotation maps those to constant time slices on the Euclidean cylinder. Finally we map the Euclidean cylinder to the Euclidean plane via a radial map.

The explicit relations between the generators are given by [309]:

$$L_{pq}^E = \begin{cases} L_{pq}^L & 1 \leq p \leq d-1 \quad \text{and} \quad 1 \leq q \leq d-1, \\ -\frac{1}{2}(P_p^L + K_p^L) & q = d \quad \text{and} \quad 1 \leq p \leq d-1, \\ \frac{1}{2}(P_q^L + K_q^L) & p = d \quad \text{and} \quad 1 \leq q \leq d-1, \\ 0 & p = d \quad \text{and} \quad q = d, \end{cases} \quad (6.24a)$$

$$P_p^E = \begin{cases} \frac{1}{2}(P_p^L - K_p^L) - iL_{p0}^L & 1 \leq p \leq d-1, \\ D^L - \frac{i}{2}(P_0^L + K_0^L) & p = d, \end{cases} \quad (6.24b)$$

$$K_p^E = \begin{cases} -\frac{1}{2}(P_p^L - K_p^L) - iL_{p0}^L & 1 \leq p \leq d-1, \\ -D^L - \frac{i}{2}(P_0^L + K_0^L) & p = d, \end{cases} \quad (6.24c)$$

$$D^E = \frac{i}{2}(P_0^L - K_0^L), \quad (6.24d)$$

where the index p takes values between 1 and d . The Lorentzian generators are the usual anti-Hermitian ones. In terms of the differential representation for example:

$$\begin{aligned} L_{\mu\nu}^L &= x_\mu \partial_\nu - x_\nu \partial_\mu, \\ P_\mu^L &= -\partial_\mu, \\ K_\mu^L &= x^2 \partial_\mu - 2x_\mu x^\nu \partial_\nu, \\ D^L &= -x^\mu \partial_\mu, \end{aligned} \quad (6.25)$$

where $\mu = 0 \dots d-1$. It then follows straightforwardly that the Euclidean generators satisfy the algebra (6.23) and the Hermiticity conditions (6.2).

6.B Expectation Values of the Conformal Generators in $d \geq 2$

Here, we present additional details about the derivation of the expectation values of the symmetry generators in the state $|\alpha(\sigma)\rangle$. We start by considering the following conjugation relations

$$g(\alpha M, N) \equiv e^{-i\alpha M} N e^{i\alpha M}, \quad (6.26)$$

where M and N are two generators of a given algebra. The conjugation functions obey a system of differential equations

$$\frac{d}{d\alpha} g(\alpha M, N) = -i e^{-i\alpha M} [M, N] e^{i\alpha M}, \quad g(0, N) = N, \quad (6.27)$$

which can then be solved to obtain the conjugation relations for the generators of the algebra. Specifying to the case of the conformal group (6.23) in $d \geq 2$ we obtain

$$g(\alpha \cdot P, D) = D + i\alpha \cdot P, \quad (6.28a)$$

$$g(\alpha \cdot K, D) = D - i\alpha \cdot K, \quad (6.28b)$$

$$g(\alpha \cdot P, L_{\mu\nu}) = L_{\mu\nu} - i\alpha_\mu P_\nu + i\alpha_\nu P_\mu, \quad (6.28c)$$

$$g(\alpha \cdot K, L_{\mu\nu}) = L_{\mu\nu} - i\alpha_\mu K_\nu + i\alpha_\nu K_\mu, \quad (6.28d)$$

$$g(\alpha \cdot P, K_\mu) = K_\mu + 2i\alpha_\mu D - 2i\alpha^\rho L_{\mu\rho} - \left(2\alpha_\mu \alpha^\rho - \alpha^2 \delta_\mu^\rho\right) P_\rho, \quad (6.28e)$$

$$g(\alpha \cdot K, P_\mu) = P_\mu - 2i\alpha_\mu D - 2i\alpha^\rho L_{\mu\rho} - (2\alpha_\mu \alpha^\rho - \alpha^2 \delta_\mu^\rho) K_\rho. \quad (6.28f)$$

Next, we explain how to evaluate the expectation values required to get Eq. (6.5)-(6.6). The one point functions are evaluated as follows:

$$\langle \alpha | K_\mu | \alpha \rangle = 2i\alpha_\mu \Delta - \left(2\alpha_\mu \alpha^\rho - \alpha^2 \delta_\mu^\rho\right) \langle \alpha | P_\rho | \alpha \rangle, \quad (6.29)$$

where we have used the conjugation (6.28e) to derive this equality. We further make the ansatz $\langle \alpha | K_\mu | \alpha \rangle = (\langle \alpha | P_\mu | \alpha \rangle)^* = A\alpha_\mu + B^* \alpha_\mu^*$ with A and B two complex coefficients. Solving for the coefficients leads to

$$\langle \alpha | P_\mu | \alpha \rangle = \left(\langle \alpha | K_\mu | \alpha \rangle \right)^* = -2i\Delta \frac{\alpha_\mu^* - \alpha^{*2} \alpha_\mu}{A(\alpha, \alpha^*)}, \quad (6.30)$$

where $A(\alpha, \alpha^*)$ was defined in Eq. (6.4). Next, we evaluate the expectation value

$$\langle \alpha | K_\mu P_\nu | \alpha \rangle = \langle \alpha | [K_\mu, P_\nu] | \alpha \rangle + \langle \alpha | P_\nu K_\mu | \alpha \rangle = 2\delta_{\mu\nu} \langle \alpha | D | \alpha \rangle - 2\langle \alpha | L_{\mu\nu} | \alpha \rangle + \langle \alpha | P_\nu K_\mu | \alpha \rangle, \quad (6.31)$$

where in the last equality, we have used the algebra (6.23). The expectation values $\langle \alpha | D | \alpha \rangle$ and $\langle \alpha | L_{\mu\nu} | \alpha \rangle$ can be related to those calculated in Eq. (6.30) by using the conjugation relations (6.28a) and (6.28c), respectively. The conjugations (6.28e) and (6.28f) can then be used to relate the expectation value $\langle \alpha | P_\nu K_\mu | \alpha \rangle$ to the unknown $\langle \alpha | K_\mu P_\nu | \alpha \rangle$. Finally we solve the entire relation by using the ansatz $\langle \alpha | K_\mu P_\nu | \alpha \rangle = A\delta_{\mu\nu} + B\alpha_\mu \alpha_\nu + B^* \alpha_\mu^* \alpha_\nu^* + C\alpha_\mu^* \alpha_\nu + D\alpha_\mu \alpha_\nu^*$ with A, C and D real coefficients and B a complex coefficient. In making this ansatz we have taken into account that $\langle \alpha | K_\mu P_\nu | \alpha \rangle$ is invariant under complex conjugation and the exchange of its indices. Finally, solving for the coefficients leads to

$$\langle \alpha | K_\mu P_\nu | \alpha \rangle = \frac{2\Delta}{A(\alpha, \alpha^*)^2} \left[\delta_{\mu\nu} A(\alpha, \alpha^*) - 2(\Delta + 1) \left(\alpha^{*2} \alpha_\mu \alpha_\nu + \alpha^2 \alpha_\mu^* \alpha_\nu^* - \alpha_\mu \alpha_\nu^* \right) - 2 \left(1 - 2\alpha \cdot \alpha^* - \Delta \alpha^2 \alpha^{*2} \right) \alpha_\mu^* \alpha_\nu \right]. \quad (6.32)$$

The expectation value of the dilatation generator is derived in a very similar manner

$$\langle \alpha | D | \alpha \rangle = \Delta \frac{1 - \alpha^2 \alpha^{*2}}{A(\alpha, \alpha^*)}. \quad (6.33)$$

Positivity of this expectation value together with the condition $A(\alpha, \alpha^*) > 0$ implies $\alpha \cdot \alpha^* < 1$ (or equivalently $\alpha^2 \alpha^{*2} < 1$). Similarly, we derive the expectation value of $L_{\mu\nu}$ through

$$\langle \alpha | L_{\mu\nu} | \alpha \rangle = i\alpha_\nu \langle \alpha | P_\mu | \alpha \rangle - i\alpha_\mu \langle \alpha | P_\nu | \alpha \rangle = 2\Delta \frac{\alpha_\mu^* \alpha_\nu - \alpha_\mu \alpha_\nu^*}{A(\alpha, \alpha^*)}, \quad (6.34)$$

such that its contraction yields

$$\frac{1}{2} \langle \alpha | iL_{\mu\nu} | \alpha \rangle \langle \alpha | iL_{\mu\nu} | \alpha \rangle = 4\Delta^2 \frac{(\alpha \cdot \alpha^*)^2 - \alpha^2 \alpha^{*2}}{A(\alpha, \alpha^*)^2}. \quad (6.35)$$

When we introduce the bulk picture, $\langle \alpha | D | \alpha \rangle$ and $\frac{1}{2} \langle \alpha | iL_{\mu\nu} | \alpha \rangle \langle \alpha | iL_{\mu\nu} | \alpha \rangle$ will be the energy and the squared angular momentum of the particle, respectively.

Constraints from unitarity: Using the above one- and two-point functions we can now explain how the requirement that Eq. (6.3) encodes a unitary transformation leads to the constraint

$$\gamma_D^I = -\frac{1}{2} \log A(\alpha, \alpha^*), \quad (6.36)$$

where $A(\alpha, \alpha^*)$ was defined in Eq. (6.4). In our derivation below, we use similar techniques to those often used in the context of coherent states, see, *e.g.*, [311]. The requirement that U in Eq. (6.3) be unitary implies

$$1 = \langle \alpha | \alpha \rangle = e^{-2\gamma_D^I \Delta} \langle \Delta | e^{-i\alpha^* \cdot K} e^{i\alpha \cdot P} | \Delta \rangle \equiv e^{-2\gamma_D^I \Delta} \langle \hat{\alpha} | \hat{\alpha} \rangle, \quad (6.37)$$

where in the last equality, we have defined the un-normalized coherent state

$$|\hat{\alpha}\rangle \equiv e^{i\alpha \cdot P} |\Delta\rangle. \quad (6.38)$$

In order to evaluate the overlap $\langle \hat{\alpha} | \hat{\alpha} \rangle$, let us apply successive derivatives to this expression

$$\begin{aligned} \partial_{\alpha^* \mu} \log \langle \hat{\alpha} | \hat{\alpha} \rangle &= \frac{\langle \hat{\alpha} | -iK_\mu | \hat{\alpha} \rangle}{\langle \hat{\alpha} | \hat{\alpha} \rangle} = \langle \alpha | -iK_\mu | \alpha \rangle, \\ \partial_{\alpha \mu} \log \langle \hat{\alpha} | \hat{\alpha} \rangle &= \frac{\langle \hat{\alpha} | iP_\mu | \hat{\alpha} \rangle}{\langle \hat{\alpha} | \hat{\alpha} \rangle} = \langle \alpha | iP_\mu | \alpha \rangle. \end{aligned} \quad (6.39)$$

Using the explicit expectation values in Eq. (6.30) and integrating these equations, we find

$$\log \langle \hat{\alpha} | \hat{\alpha} \rangle = -\Delta \log A(\alpha, \alpha^*) + c_1, \quad (6.40)$$

with c_1 an arbitrary constant. The trivial solution for $\alpha = \alpha^* = 0$ can then be used to fix $c_1 = 0$. Finally, substituting the overlap $\langle \hat{\alpha} | \hat{\alpha} \rangle$ into Eq. (6.37), we obtain Eq. (6.36).

6.C Geodesic Trajectories in the Complexity Metric

As mentioned in §6.3, the geodesics on the coset space (6.7) take the form

$$|\alpha(\sigma)\rangle \equiv \mathcal{N}(\sigma) e^{i\alpha(\sigma) \cdot P} |\Delta\rangle \equiv e^{i\sigma(\tilde{\alpha} \cdot P + \tilde{\alpha}^* \cdot K)} |\Delta\rangle \equiv e^{i\sigma X} |\Delta\rangle, \quad (6.41)$$

where the relation between $\alpha(\sigma)$ and $\{\tilde{\alpha}, \sigma\}$ is yet to be determined. We choose a convention in which the trajectory will reach its end point (the target state) at $\sigma = 1$ where $\alpha(\sigma = 1) \equiv \alpha_T$. We will explain in Sec. 6.D how to relate α_T and $\tilde{\alpha}$. For the moment, we will only need the relation

$$2\tilde{\alpha} \cdot \tilde{\alpha}^* = \left(\tanh^{-1} \Omega_T^S \right)^2 + \left(\tanh^{-1} \Omega_T^A \right)^2 \quad (6.42)$$

where $\Omega_T^{S/A} = (\Omega_T^+ \pm \Omega_T^-)/2$ and $\Omega_T^\pm = \sqrt{2} \sqrt{\alpha_T \cdot \alpha_T^* \pm \sqrt{\alpha_T^2 \alpha_T^{*2}}}$. A useful simplification is $(\Omega^{S/A})^2 = \alpha_T \cdot \alpha_T^* \pm \sqrt{(\alpha_T \cdot \alpha_T^*)^2 - \alpha_T^2 \alpha_T^{*2}}$. The Fubini-Study metric associated to the trajectory (6.41) is

$$\frac{ds^2}{d\sigma^2} = \langle \Delta | X^\dagger X | \Delta \rangle - \left| \langle \Delta | X | \Delta \rangle \right|^2 = \tilde{\alpha}^{*\mu} \tilde{\alpha}^\nu \langle \Delta | K_\mu P_\nu | \Delta \rangle = 2\Delta \tilde{\alpha} \cdot \tilde{\alpha}^*, \quad (6.43)$$

so the complexity of the state $|\alpha_T\rangle$ is given by

$$\mathcal{C}[\tilde{\alpha}] = \sqrt{2\Delta \tilde{\alpha}^* \cdot \tilde{\alpha}}, \quad (6.44)$$

where it remains to substitute the relation (6.42). We can see from this result that \mathcal{C} admits no non-trivial null directions since $\mathcal{C} = 0$ would require $\Omega_T^+ = \Omega_T^- = 0$ which in turn implies that $\alpha_T \cdot \alpha_T^* = \alpha_T^2 = 0$. Therefore, $\alpha_T = 0$. In the bulk of the paper we insisted on parametrizing the state in terms of $\alpha(\sigma)$ rather than $\tilde{\alpha}$ since, as we saw in Sec. 6.B, this facilitates the evaluation of correlation functions in the state. We therefore regard it as a more explicit characterization of the state throughout the paper. We will also see later that the description in terms of $\alpha(\sigma)$ lends itself to a more natural holographic interpretation.

As an example, let us consider the one-dimensional case for which we have

$$|\alpha(\sigma)\rangle = e^{i\alpha(\sigma)P} e^{i\gamma(\sigma)D} e^{i\beta(\sigma)K} |\Delta\rangle = e^{i\sigma(\tilde{\alpha}P + \tilde{\alpha}^*K)} |\Delta\rangle. \quad (6.45)$$

In this case the relation between $\alpha(\sigma)$ and $\{\tilde{\alpha}, \sigma\}$ is straightforward to derive and we obtain

$$\alpha(\sigma) = \frac{\tilde{\alpha}}{|\tilde{\alpha}|} \tanh(\sigma|\tilde{\alpha}|) \quad (6.46)$$

(see, e.g., Sec. 11.3.3 of [312] or appendix C of [241] for this recombination formula). It is possible to verify that this function solves the affinely parametrized geodesic equations $\alpha''(\sigma) = \frac{2\alpha^*(\sigma)\alpha'(\sigma)^2}{\alpha(\sigma)\alpha^*(\sigma)-1}$ (and its complex conjugate) for the $d = 1$ metric $ds_{FS}^2 =$

$2\Delta \left[\frac{d\alpha d\alpha^*}{(1-|\alpha|^2)^2} \right]$ cf. Eq. (6.6). The target state obtained at $\sigma = 1$, i.e., $\alpha(1) = \alpha_T$ satisfies $\tanh(|\tilde{\alpha}|) = |\alpha_T|$. This leads to the complexity

$$\mathcal{C}[\alpha_T] = \sqrt{2\Delta} \tanh^{-1}(|\alpha_T|), \quad (6.47)$$

which is indeed consistent with Eqs. (6.42), (6.44).

In two dimensions, we can use holomorphic factorization to decompose the metric as $ds^2 = ds_H^2 + ds_{AH}^2$ where H stands for holomorphic and AH stands for anti-holomorphic, see Eq. (6.98) below. The geodesic trajectories take the form of a direct product of two elements of the form (6.45) with parameters $\{\zeta(\sigma), \tilde{\zeta}\}$ for the holomorphic part and $\{\bar{\zeta}(\sigma), \tilde{\bar{\zeta}}\}$ for the anti-holomorphic part (cf. Eq. (6.83) below). The metric along these (straight-line trajectories) reads

$$ds^2 = 2d\sigma^2 \left[h|\tilde{\zeta}|^2 + \bar{h}|\tilde{\bar{\zeta}}|^2 \right]. \quad (6.48)$$

Due to the holomorphic factorization we have that

$$\zeta(\sigma) = \frac{\tilde{\zeta}}{|\tilde{\zeta}|} \tanh\left(\sigma|\tilde{\zeta}|\right), \quad \bar{\zeta}(\sigma) = \frac{\tilde{\bar{\zeta}}}{|\tilde{\bar{\zeta}}|} \tanh\left(\sigma|\tilde{\bar{\zeta}}|\right). \quad (6.49)$$

Using the same logic as before, we can compute the complexity for the end state $\{\zeta_T, \bar{\zeta}_T\}$ and obtain

$$C[\zeta_T, \bar{\zeta}_T] = \sqrt{2h (\tanh^{-1}|\zeta_T|)^2 + 2\bar{h} (\tanh^{-1}|\bar{\zeta}_T|)^2}. \quad (6.50)$$

Note that this equation is consistent with the result Eqs. (6.42), (6.44) in general dimensions (using the relation (6.100) below).

6.D Canonical Variables and Recombination Formula

In this part of the supplementary material, we will explain how to establish the relation $\alpha(\tilde{\alpha})$ in general dimensions, see Sec. 6.C. This method will be based on reference [313] which explains how to use the matrix representation of the algebra to find the coset representative of an arbitrary group element.

We will work in the fundamental representation of the conformal group corresponding to the matrix algebra $\mathfrak{so}(d, 2)$ spanned by

$$(M_{AB})^C{}_D \equiv \delta_A^C g_{BD} - \delta_B^C g_{AD}, \quad (6.51)$$

where $g = \text{Diag}(-, -, +, \dots, +)$ is the flat metric over $\mathbb{R}^{d,2}$, δ_{AB} is the Kronecker delta, and $A, B, C, D \in \{-1, 0, \dots, d-1, d\}$. These matrices obey the commutation relations

$$[M_{AB}, M_{CD}] = -g_{BD}M_{AC} + g_{BC}M_{AD} + g_{AD}M_{BC} - g_{AC}M_{BD}, \quad (6.52)$$

and the orthogonality condition

$$gM^T = -Mg. \quad (6.53)$$

The Euclidean conformal generators are given in the fundamental representation (denoted by R) by

$$\begin{aligned} R(D) &\equiv -iM_{-1,0}, & R(L_{\mu\nu}) &\equiv M_{\mu,\nu}, \\ R(P_\mu) &\equiv M_{-1,\mu} - iM_{0,\mu}, & R(K_\mu) &\equiv -(M_{-1,\mu} + iM_{0,\mu}), \end{aligned} \quad (6.54)$$

where $\mu, \nu \in \{1, \dots, d\}$. Note that this representation obeys the algebra (6.23), and is consistent with the Hermiticity conditions (6.2) through

$$R(\mathcal{O}^\dagger) = g^{-1} R(\mathcal{O})^\dagger g \quad (6.55)$$

for any operator \mathcal{O} in the conformal algebra.

We can define a vacuum vector $\Omega \in \mathbb{R}^{d,2}$ as

$$\Omega = (1, i, 0 \dots), \quad R(D) \cdot \Omega = -\Omega, \quad R(K_\mu) \cdot \Omega = 0, \quad R(L_{\mu\nu}) \cdot \Omega = 0. \quad (6.56)$$

Note that the D eigenvalue for the vector Ω above is not generic. However, in the following equation, the result of exponentiating D is absorbed in the normalization constant \mathcal{N} and hence changing it amounts to changing the overall phase of the coherent state. This phase eventually cancels out in Eq. (6.58) and hence this choice does not influence our results. The action of a coherent element on the vacuum vector takes the form

$$\mathcal{N} e^{i\alpha \cdot R(P)} \cdot \Omega = \mathcal{N} \begin{bmatrix} 1 - \alpha^2 \\ i(1 + \alpha^2) \\ 2i\alpha_1 \\ \vdots \\ 2i\alpha_d \end{bmatrix}, \quad (6.57)$$

which means that we can find the coset representative α associated to an arbitrary group element g from the vector $v = g \cdot \Omega$ through

$$\alpha_\mu = -i \frac{v_\mu}{v_{-1} - i v_0}. \quad (6.58)$$

Choosing now a geodesic path $g(\sigma) = e^{i\sigma(\tilde{\alpha} \cdot R(P) + \tilde{\alpha}^* \cdot R(K))}$, we can use this method to find its associated coherent state parametrization $\alpha(\tilde{\alpha}, \sigma)$.

In $d = 1$, this method confirms the recombination formula (6.46). In that case, the vector v associated with the group element $g(\sigma)$ is

$$v = \begin{bmatrix} \cosh(|\tilde{\alpha}|\sigma)^2 - \frac{\tilde{\alpha}}{\tilde{\alpha}^*} \sinh(|\tilde{\alpha}|\sigma)^2 \\ \frac{i}{2} \left(\left(1 + \frac{\tilde{\alpha}}{\tilde{\alpha}^*}\right) \cosh(2\sigma|\tilde{\alpha}|) + 1 - \frac{\tilde{\alpha}}{\tilde{\alpha}^*} \right) \\ i \sqrt{\frac{\tilde{\alpha}}{\tilde{\alpha}^*}} \sinh(2\sigma|\tilde{\alpha}|) \end{bmatrix}, \quad (6.59)$$

and $\alpha(\tilde{\alpha}, \sigma)$ is given by

$$\alpha(\tilde{\alpha}, \sigma) = \frac{\tilde{\alpha}}{|\tilde{\alpha}|} \tanh(|\tilde{\alpha}|\sigma). \quad (6.60)$$

This equation can be inverted as follows

$$\tilde{\alpha}(\alpha) = \frac{\alpha}{|\alpha|} \tanh^{-1}(|\alpha|/\sigma). \quad (6.61)$$

In $d \geq 2$, we find that

$$\alpha_\mu = \frac{\sinh(\tilde{\omega}_+\sigma)}{\cosh(\tilde{\omega}_+\sigma) + \cosh(\tilde{\omega}_-\sigma)} \frac{\tilde{\alpha}_\mu^* e^{i\tilde{\beta}} + \tilde{\alpha}_\mu}{\tilde{\omega}_+} - \frac{\sinh(\tilde{\omega}_-\sigma)}{\cosh(\tilde{\omega}_+\sigma) + \cosh(\tilde{\omega}_-\sigma)} \frac{\tilde{\alpha}_\mu^* e^{i\tilde{\beta}} - \tilde{\alpha}_\mu}{\tilde{\omega}_-} \quad (6.62)$$

where $\tilde{\omega}_\pm = \sqrt{2} \sqrt{\tilde{\alpha} \cdot \tilde{\alpha}^* \pm \sqrt{\tilde{\alpha}^2 \tilde{\alpha}^{*2}}}$ and $e^{2i\tilde{\beta}} = \tilde{\alpha}^2 / \tilde{\alpha}^{*2}$. This method is applicable for any dimension d . As a consistency check, we note that in $d = 2$, the above formula is consistent with holomorphic factorization, *i.e.*, using it together with the relation (6.100) below, we simply obtain a double copy of the relation (6.60)

$$\zeta = \frac{\tilde{\zeta}}{|\tilde{\zeta}|} \tanh(\sigma |\tilde{\zeta}|), \quad \bar{\zeta} = \frac{\tilde{\bar{\zeta}}}{|\tilde{\bar{\zeta}}|} \tanh(\sigma |\tilde{\bar{\zeta}}|). \quad (6.63)$$

The inversion (finding $\tilde{\alpha}$ in terms of α) can be translated to the problem of solving three equations (for $\alpha \cdot \alpha$, $\alpha^* \cdot \alpha^*$ and $\alpha \cdot \alpha^*$) in terms of three variables ($\tilde{\alpha} \cdot \tilde{\alpha}$, $\tilde{\alpha}^* \cdot \tilde{\alpha}^*$ and $\tilde{\alpha} \cdot \tilde{\alpha}^*$) using the above relations. This system of equations can be solved analytically. To start, note that

$$\alpha(\sigma)^2 = \sqrt{\frac{\tilde{\alpha}^2 \cosh(\tilde{\omega}_+\sigma) - \cosh(\tilde{\omega}_-\sigma)}{\tilde{\alpha}^{*2} \cosh(\tilde{\omega}_+\sigma) + \cosh(\tilde{\omega}_-\sigma)}}, \quad \alpha(\sigma) \cdot \alpha(\sigma)^* = \frac{\sinh(\tilde{\omega}_+\sigma)^2 + \sinh(\tilde{\omega}_-\sigma)^2}{(\cosh(\tilde{\omega}_+\sigma) + \cosh(\tilde{\omega}_-\sigma))^2}, \quad (6.64)$$

and $\alpha^2 / \alpha^{*2} = \tilde{\alpha}^2 / \tilde{\alpha}^{*2}$. It is useful to consider the following combinations:

$$\Omega_\pm(\sigma) = \frac{2 \sinh(\tilde{\omega}_\pm \sigma)}{\cosh(\tilde{\omega}_+\sigma) + \cosh(\tilde{\omega}_-\sigma)} \quad \text{where } \Omega_\pm(\sigma) \equiv \sqrt{2} \sqrt{\alpha(\sigma) \cdot \alpha^*(\sigma) \pm \sqrt{\alpha(\sigma)^2 \alpha^*(\sigma)^2}}, \quad (6.65)$$

which can be inverted as

$$\tilde{\omega}_\pm = \frac{1}{\sigma} \tanh^{-1} \left(\frac{4 \Omega_\pm(\sigma)}{4 \pm (\Omega_+^2(\sigma) - \Omega_-^2(\sigma))} \right) = \frac{1}{\sigma} \left(\tanh^{-1} [\Omega^S(\sigma)] \pm \tanh^{-1} [\Omega^A(\sigma)] \right) \quad (6.66)$$

where we have introduced the variables $\Omega^{S/A}(\sigma) \equiv (\Omega^+(\sigma) \pm \Omega^-(\sigma))/2$ and used the identity $\tanh^{-1}(x) = \frac{1}{2} \log \left[\frac{1+x}{1-x} \right]$. Noting that $\tilde{\alpha} \cdot \tilde{\alpha}^* = (\tilde{\omega}_+^2 + \tilde{\omega}_-^2)/4$ and using the previous formula leads to

$$\tilde{\alpha} \cdot \tilde{\alpha}^* = \frac{1}{2\sigma^2} \left[\left(\tanh^{-1} \Omega^S(\sigma) \right)^2 + \left(\tanh^{-1} \Omega^A(\sigma) \right)^2 \right]. \quad (6.67)$$

This is true for all σ and so in particular for $\sigma = 1$ we find

$$2 \tilde{\alpha} \cdot \tilde{\alpha}^* = \left(\tanh^{-1} \left[\frac{\Omega_T^+ + \Omega_T^-}{2} \right] \right)^2 + \left(\tanh^{-1} \left[\frac{\Omega_T^+ - \Omega_T^-}{2} \right] \right)^2, \quad (6.68)$$

with $\Omega_T^\pm \equiv \sqrt{2} \sqrt{\alpha_T \cdot \alpha_T^* \pm \sqrt{\alpha_T^2 \alpha_T^{*2}}}$ where we have defined $\alpha(\sigma = 1) \equiv \alpha_T$. Similarly using $\tilde{\alpha}^2 = \sqrt{\alpha^2/\alpha^{*2}} (\tilde{\omega}_+^2 - \tilde{\omega}_-^2)/4$ we obtain

$$\tilde{\alpha}^2 = \frac{1}{\sigma^2} \sqrt{\frac{\alpha^2}{\alpha^{*2}}} \tanh^{-1}[\Omega^A(\sigma)] \tanh^{-1}[\Omega^S(\sigma)]. \quad (6.69)$$

Using the above, the full inversion of (6.62) is straightforwardly obtained

$$\begin{aligned} \sigma \tilde{\alpha}_\mu &= \tanh^{-1}(\Omega^S(\sigma)) \frac{\Omega^S(\sigma) \alpha_\mu(\sigma) - \Omega^A(\sigma) \sqrt{\frac{\alpha^2}{\alpha^{*2}} \alpha_\mu^*(\sigma)}}{\Omega^+(\sigma) \Omega^-(\sigma)} \\ &\quad - \tanh^{-1}(\Omega^A(\sigma)) \frac{\Omega^A(\sigma) \alpha_\mu(\sigma) - \Omega^S(\sigma) \sqrt{\frac{\alpha^2}{\alpha^{*2}} \alpha_\mu^*(\sigma)}}{\Omega^+(\sigma) \Omega^-(\sigma)}. \end{aligned} \quad (6.70)$$

6.E Bounds on Complexity and its Time Evolution

Here, we derive bounds on the complexity and its rate of change.

6.E.1 Bounds on Complexity

We consider bounds on the complexity (6.9) of a final state α_T with energy E_T . We will use the following bounds on log

$$\frac{y-1}{y+1} \leq \log(y) \leq \frac{y-1}{\sqrt{y}}, \quad y \geq 1, \quad (6.71)$$

which lead to the following bounds on $\tanh^{-1}(x)^2$

$$\frac{x^2}{4} \leq \tanh^{-1}(x)^2 \leq \frac{x^2}{1-x^2}, \quad -1 < x < 1. \quad (6.72)$$

We therefore have

$$\frac{\sqrt{\Delta}}{2} \sqrt{(\Omega_T^S)^2 + (\Omega_T^A)^2} \leq \mathcal{C}[\alpha_T] \leq \sqrt{\Delta} \sqrt{\frac{(\Omega_T^S)^2}{1 - (\Omega_T^S)^2} + \frac{(\Omega_T^A)^2}{1 - (\Omega_T^A)^2}} \quad (6.73)$$

$$\text{i.e., } \sqrt{\frac{\Delta}{2}} \alpha_T \cdot \alpha_T^* \leq \mathcal{C}[\alpha_T] \leq \sqrt{E_T - \Delta}$$

where we used $(\Omega^{S/A})^2 = \alpha_T \cdot \alpha_T^* \pm \sqrt{(\alpha_T \cdot \alpha_T^*)^2 - \alpha_T^2 \alpha_T^{*2}} = \frac{E_T \pm J_T - \Delta}{E_T \pm J_T + \Delta}$ with the energy E_T and the angular momentum J_T given by

$$\begin{aligned} E_T &\equiv \langle \alpha_T | D | \alpha_T \rangle = \Delta (1 - \alpha_T^2 \alpha_T^{*2}) / A(\alpha_T, \alpha_T^*), \\ J_T &\equiv \sqrt{\langle \alpha_T | i L_{\mu\nu} | \alpha_T \rangle \langle \alpha_T | i L_{\mu\nu} | \alpha_T \rangle} / 2 = 2\Delta \sqrt{(\alpha_T \cdot \alpha_T^*)^2 - \alpha_T^2 \alpha_T^{*2}} / A(\alpha_T, \alpha_T^*). \end{aligned} \quad (6.74)$$

The lower bound can be expressed in terms of E_T by using the inequalities

$$0 \leq J_T \leq E_T - \Delta \quad \Rightarrow \quad \alpha_T \cdot \alpha_T^* = \frac{E_T^2 - J_T^2 - \Delta^2}{(E_T + \Delta)^2 - J_T^2} \geq \frac{2\Delta(E_T - \Delta)}{(E_T + \Delta)^2}, \quad (6.75)$$

leading to

$$\frac{\Delta}{E_T + \Delta} \sqrt{(E_T - \Delta)} \leq C[\alpha_T] \leq \sqrt{E_T - \Delta}. \quad (6.76)$$

The above bound uses the inequality $J_T + \Delta \leq E_T$ which can be proven using the definitions of E_T and J_T above (these will actually have a nice interpretation in holography, see (6.144) below). For this note that

$$(E_T - \Delta)^2 - J_T^2 = \frac{4\Delta^2 \alpha^2 \alpha^{*2}}{A(\alpha, \alpha^*)} > 0. \quad (6.77)$$

We then see indeed that $J_T + \Delta \leq E_T$ when $\Delta \leq E_T$ which in turn follows from positivity of the spectrum, see comment below Eq. (6.4).

6.E.2 Complexity of Time Evolved States

Let us now consider the time evolution of a coherent state $e^{i\tau D} |\alpha_0\rangle = |\alpha_0 e^{i\tau}\rangle$, for which the FS-metric reduces to

$$ds_{FS}^2 = 2\Delta d\tau^2 \left(\frac{\alpha_0 \cdot \alpha_0^*}{A(\alpha_0, \alpha_0^*)} + 2 \frac{(\alpha_0 \cdot \alpha_0^*)^2 - \alpha_0^2 \alpha_0^{*2}}{A(\alpha_0, \alpha_0^*)^2} \right). \quad (6.78)$$

This can be simplified and bounded as follows

$$\begin{aligned} \frac{ds_{FS}^2}{d\tau^2} &= 2\Delta \frac{\alpha_0 \cdot \alpha_0^* + (\alpha_0 \cdot \alpha_0^* - 2)\alpha_0^2 \alpha_0^{*2}}{A(\alpha_0, \alpha_0^*)^2}, \\ &= \frac{\langle \alpha_0 | D | \alpha_0 \rangle^2}{\Delta} \frac{2\alpha_0^2 \alpha_0^{*2} (\alpha_0 \cdot \alpha_0^* - 2) + 2\alpha_0 \cdot \alpha_0^*}{(1 - \alpha_0^2 \alpha_0^{*2})^2} \\ &= \frac{\langle \alpha_0 | D | \alpha_0 \rangle^2}{\Delta} \left(1 - \frac{(1 + \alpha_0^2 \alpha_0^{*2})A(\alpha_0, \alpha_0^*)}{(1 - \alpha_0^2 \alpha_0^{*2})^2} \right) \\ &\leq \frac{\langle \alpha_0 | D | \alpha_0 \rangle^2}{\Delta} \equiv \frac{E^2}{\Delta}. \end{aligned} \quad (6.79)$$

Unitarity further constrains Δ for $d \geq 3$ [270]

$$\Delta \geq d/2 - 1. \quad (6.80)$$

Therefore, the rate of change of the FS-distance along this trajectory in the space of states is bounded by

$$\frac{ds_{FS}}{d\tau} \leq \frac{E}{\sqrt{\Delta}} \leq E \sqrt{\frac{2}{d-2}}. \quad (6.81)$$

6.F Comparison with Previous Results in $d = 2$

In this part of the supplementary material, we will focus on conformal circuits in two dimensions. In this case, the global conformal group can be extended to (two copies of) the full Virasoro group. The discussion is often phrased in terms of holomorphic and anti-holomorphic coordinates $z = x + i\tau$ ($\bar{z} = x - i\tau$). The global conformal algebra $\mathfrak{so}(2, 2) \simeq \mathfrak{sl}(2, \mathbb{R}) \times \mathfrak{sl}(2, \mathbb{R})$ is generated by holomorphic generators L_{-1}, L_0, L_1 satisfying

$$[L_{\pm 1}, L_0] = \pm L_{\pm 1}, \quad [L_1, L_{-1}] = 2L_0, \quad (6.82)$$

and anti-holomorphic generators $\bar{L}_{-1}, \bar{L}_0, \bar{L}_1$ satisfying similar relations. In radial quantization, the generators satisfy the Hermiticity conditions $L_1^\dagger = L_{-1}$ (and $\bar{L}_1^\dagger = \bar{L}_{-1}$). Working in this language will allow us to compare our results with the previous complexity literature in $2d$ CFTs [247, 248, 249, 250].

For the reference state we again select a spinless highest weight state $|\psi_R\rangle = |h, \bar{h} = h\rangle \equiv |\mathbf{h}\rangle$, satisfying $\bar{L}_0|\mathbf{h}\rangle = L_0|\mathbf{h}\rangle = h|\mathbf{h}\rangle$, $\bar{L}_1|\mathbf{h}\rangle = L_1|\mathbf{h}\rangle = 0$. As expected, the cost functions (6.1) factorize into holomorphic and anti-holomorphic parts, which can be treated separately. We will focus on holomorphic unitary circuits within the $2d$ global conformal group

$$U(\sigma) \equiv e^{i\zeta(\sigma)L_{-1}} e^{i\gamma(\sigma)L_0} e^{i\zeta_1(\sigma)L_1}, \quad (6.83)$$

$$|\zeta\rangle \equiv U(\sigma)|\mathbf{h}\rangle = \mathcal{N}(\sigma) e^{i\zeta(\sigma)L_{-1}} |\mathbf{h}\rangle,$$

where $\gamma \equiv \gamma_R + i\gamma_I$ is decomposed into its real and imaginary parts and unitarity restricts $\gamma_I = -\log(1 - |\zeta|^2)$ with $|\zeta|^2 < 1$ and $\zeta_1 = \zeta^* e^{i\gamma_R}$. These relations can be derived using an explicit recombination formula, see Sec. 11.3.3 of [312]. Following the same logic as in §6.3 (see the expectation values of the conformal generators below) we can derive the \mathcal{F}_1 cost (6.1a)

$$\frac{\mathcal{F}_1}{h} = \left| \frac{\zeta\zeta^* - \zeta^*\zeta}{1 - |\zeta|^2} + i\gamma_R + (\zeta \leftrightarrow \bar{\zeta}) \right|, \quad (6.84)$$

and the Fubini-Study metric (6.1b)

$$ds_{FS}^2 = 2h \left[\frac{d\zeta d\zeta^*}{(1 - |\zeta|^2)^2} + \frac{d\bar{\zeta} d\bar{\zeta}^*}{(1 - |\bar{\zeta}|^2)^2} \right], \quad (6.85)$$

which corresponds to the hyperbolic geometry on (two copies of) the Poincaré unit disk. These cost functions are obtained from those in the §6.3 by the substitutions $\alpha^\mu \partial_\mu = \left(\frac{\zeta - \bar{\zeta}}{2i}\right) \partial_\tau + \left(\frac{\zeta + \bar{\zeta}}{2}\right) \partial_x$ and $\gamma_D^R = (\gamma_R + \bar{\gamma}_R)/2$. It is worth noting that holomorphic factorization implies that in the case with spin $s = h - \bar{h} \neq 0$ in $2d$ the result is straightforwardly

obtained by replacing the coefficient in front of the anti-holomorphic part of the metric by \tilde{h} .

There are a number of existing results in the literature for the circuit complexity of the Virasoro group on the cylinder [247, 248, 249, 250]. However, in those papers the circuit complexity is given in terms of the diffeomorphism $f(z = e^{i\theta}) \in \text{Diff}(S^1)$ associated to the holomorphic part of the circuit. We find it insightful to explicitly relate our approach to the previous literature for $d = 2$. In addition to providing a consistency check for our results, this also provides a clear interpretation of the circuits and gates associated with the diffeomorphisms of [247, 248, 249, 250]. Restricting to the holomorphic copy, [247] have shown that the \mathcal{F}_1 cost is given by

$$\mathcal{F}_1 = \left| \int_0^{2\pi} \frac{d\theta}{2\pi} \frac{\partial_\sigma f(\sigma, \theta)}{\partial_\theta f(\sigma, \theta)} \left[-\tilde{h} + \frac{c}{12} \{f, \theta\} \right] \right|, \quad (6.86)$$

where c is the central charge, $\tilde{h} \equiv h - c/24$ is the shifted eigenvalue of the generator L_0 on the cylinder and $\{f, \theta\}$ is the Schwarzian derivative. Denoting $\varepsilon_i = \frac{\partial_\sigma f(\sigma, \theta_i)}{\partial_{\theta_i} f(\sigma, \theta_i)}$, the FS-metric is [249, 250]

$$\frac{ds_{FS}^2}{d\sigma^2} = \int_0^{2\pi} \frac{d\theta_1}{2\pi} \frac{d\theta_2}{2\pi} \varepsilon_1 \varepsilon_2 \left[\frac{c}{32 \sin^4[(\theta_1 - \theta_2)/2]} - \frac{h}{2 \sin^2[(\theta_1 - \theta_2)/2]} \right]. \quad (6.87)$$

As explained in section §3.3 of [250], this expression must be regularized and thus we have

$$\frac{ds_{FS}^2}{d\sigma^2} = \int_0^{2\pi} d\theta_1 d\theta_2 \log \left[\sin \left(\frac{\theta_1 - \theta_2}{2} \right)^2 \right] \left[-\frac{c}{24} \partial_{\theta_1}^2 \varepsilon_1 \partial_{\theta_2}^2 \varepsilon_2 - \tilde{h} \partial_{\theta_1} \varepsilon_1 \partial_{\theta_2} \varepsilon_2 \right]. \quad (6.88)$$

The diffeomorphism associated with the circuit (6.83) is a Möbius transformation on the circle parametrized by the coordinate θ , *i.e.*, $z = e^{i\theta}$

$$f(\sigma): e^{i\theta} \rightarrow \frac{A(\sigma)e^{i\theta} + B(\sigma)}{B^*(\sigma)e^{i\theta} + A^*(\sigma)} \text{ with } |A|^2 - |B|^2 = 1, \quad (6.89)$$

which maps the unit circle in the complex plane to itself. Acting with our unitary (6.83) expressed in terms of the differential generators $L_n = -z^{n+1} \partial_z$ ($n = 0, \pm 1$) straightforwardly leads to

$$f(\sigma): e^{i\theta} \rightarrow \frac{e^{i\theta} \left(e^{i\gamma/2} + \zeta \zeta_1 e^{-i\gamma/2} \right) + i\zeta e^{-i\gamma/2}}{-i\zeta_1 e^{i\theta} e^{-i\gamma/2} + e^{-i\gamma/2}}, \quad (6.90)$$

where the flip in the signs of the parameters is due to the usual active/passive transformation conversion. Constraining this transformation to be Möbius yields

$$\zeta_1 = \zeta^* e^{i\gamma_R}, \quad \gamma_I = -\log(1 - |\zeta|^2). \quad (6.91)$$

Note that these are precisely the relations we obtained by requiring that the circuit (6.83) is a unitary. Finally, substituting the relations (6.91) into the unitary (6.90) we obtain

$$f(\sigma, e^{i\theta}) = \frac{e^{i\gamma^*/2} e^{i\theta} + i\zeta(\sigma) e^{-i\gamma/2}}{-i\zeta^*(\sigma) e^{i\gamma^*/2} e^{i\theta} + e^{-i\gamma/2}}. \quad (6.92)$$

As expected for a global transformation in $d = 2$ we have $\{f, z\} = 0$, while the mapping to the cylinder creates a non-zero Schwarzian $\{f, \theta\} = 1/2$. Substituting this diffeomorphism into Eqs. (6.86) and (6.88), we immediately recover our results (6.84)-(6.85) upon the addition of the second copy.

6.F.1 Expectation Values of the Conformal Generators in $d = 2$

We here derive the conjugation relations and expectation values of the conformal generators in the special case of $d = 2$ required for the derivation of Eqs. (6.84)-(6.85). For the conjugation relations (6.26) we obtain using the algebra (6.82)

$$g(\zeta L_1, L_0) = L_0 - i\zeta L_1, \quad (6.93a)$$

$$g(\zeta L_{-1}, L_0) = L_0 + i\zeta L_{-1}, \quad (6.93b)$$

$$g(\zeta L_1, L_{-1}) = L_{-1} - 2i\zeta L_0 - \zeta^2 L_1, \quad (6.93c)$$

$$g(\zeta L_{-1}, L_1) = L_1 + 2i\zeta L_0 - \zeta^2 L_{-1}. \quad (6.93d)$$

Next, we explain how to evaluate the one- and two-point functions of the 2d conformal generators in the states (6.83) along the circuit. The one point functions are evaluated as follows:

$$\langle \zeta | L_1 | \zeta \rangle = 2i\zeta h - \zeta^2 \langle \zeta | L_{-1} | \zeta \rangle, \quad (6.94)$$

where in this equality we used the relation (6.93d). The Hermiticity relations for the radial quantization further imply $\langle \zeta | L_1 | \zeta \rangle = (\langle \zeta | L_{-1} | \zeta \rangle)^*$. This then allows us to solve the relation (6.94) and obtain the one-point functions of the conformal generators

$$\langle \zeta | L_{-1} | \zeta \rangle = (\langle \zeta | L_1 | \zeta \rangle)^* = -2ih \frac{\zeta^*}{1 - |\zeta|^2}. \quad (6.95)$$

Finally, the two point function can be computed as follows

$$\langle \zeta | L_1 L_{-1} | \zeta \rangle = \langle \zeta | [L_1, L_{-1}] | \zeta \rangle + \langle \zeta | L_{-1} L_1 | \zeta \rangle = 2\langle \zeta | L_0 | \zeta \rangle + \langle \zeta | L_{-1} L_1 | \zeta \rangle, \quad (6.96)$$

where in the last equality, we have used the algebra (6.82). The expectation value $\langle \zeta | L_0 | \zeta \rangle$ can be related to those calculated in Eq. (6.95) by using the conjugation relation (6.93b). The conjugations (6.93c) and (6.93d) can then be used to relate the expectation value $\langle \zeta | L_{-1} L_1 | \zeta \rangle$ to the unknown $\langle \zeta | L_1 L_{-1} | \zeta \rangle$. Note that $\langle \zeta | L_1 L_{-1} | \zeta \rangle$ should be real due to the Hermiticity conditions. Finally we solve the entire relation, which leads to

$$\langle \zeta | L_1 L_{-1} | \zeta \rangle = 2h \frac{1 + 2h|\zeta|^2}{(1 - |\zeta|^2)^2}. \quad (6.97)$$

6.G Comments about Spinning States

In this part of the supplementary material we make use of holomorphic factorization in $2d$ to present extensions of the results (6.84)-(6.85) for the case with non-zero spin $s = h - \bar{h}$. We translate these results to the higher dimensional language in terms of the circuit parameter α^μ in an attempt to reveal the structure of the result for the case with spin. However, let us emphasize that the results of this section are only valid in two dimensions and that this case is special in that spinning representations are one dimensional (*i.e.*, they consist of a single component state $|h, \bar{h}\rangle \equiv |\Delta, s\rangle$, with the scaling dimension $\Delta = h + \bar{h}$). We leave a detailed analysis of spinning states in general dimensions for future work.

Let us begin with the generalized version of Eqs. (6.84)-(6.85) when $h \neq \bar{h}$

$$\mathcal{F}_1 = \left| h \left(\frac{\dot{\zeta}\zeta^* - \dot{\zeta}^*\zeta}{1-|\zeta|^2} + i\dot{\gamma}_R \right) + \bar{h} \left(\frac{\dot{\bar{\zeta}}\bar{\zeta}^* - \dot{\bar{\zeta}}^*\bar{\zeta}}{1-|\bar{\zeta}|^2} + i\dot{\gamma}_R \right) \right|, \quad (6.98)$$

$$ds_{FS}^2 = 2h \left[\frac{d\zeta d\zeta^*}{(1-|\zeta|^2)^2} \right] + 2\bar{h} \left[\frac{d\bar{\zeta} d\bar{\zeta}^*}{(1-|\bar{\zeta}|^2)^2} \right].$$

Using the relation between the conformal generators

$$\begin{aligned} L_{-1} &= \frac{1}{2}(P_x - iP_\tau), & L_0 &= \frac{1}{2}(D - iL_{\tau x}), & L_1 &= \frac{1}{2}(K_x + iK_\tau), \\ \bar{L}_{-1} &= \frac{1}{2}(P_x + iP_\tau), & \bar{L}_0 &= \frac{1}{2}(D + iL_{\tau x}), & \bar{L}_1 &= \frac{1}{2}(K_x - iK_\tau), \end{aligned} \quad (6.99)$$

allows us to identify the relation between the circuit parameters in two-dimensions (6.83) and those in higher dimensions (6.3). We obtain

$$\begin{aligned} \alpha_x &= \frac{\zeta + \bar{\zeta}}{2}, & \alpha_\tau &= \frac{\zeta - \bar{\zeta}}{2i}, & \gamma_D &= \frac{\gamma + \bar{\gamma}}{2}, & \lambda_{\tau x} &= \frac{\gamma - \bar{\gamma}}{2i}, \\ \beta_x &= \frac{\zeta_1 + \bar{\zeta}_1}{2}, & \beta_\tau &= -\frac{\zeta_1 - \bar{\zeta}_1}{2i}, \end{aligned} \quad (6.100)$$

which yields for the various costs

$$\begin{aligned} \mathcal{F}_1 &= \left| \Delta \left(\frac{\dot{\alpha} \cdot \alpha^* - \dot{\alpha}^* \cdot \alpha + \alpha^2(\dot{\alpha}^* \cdot \alpha^*) - \alpha^{*2}(\dot{\alpha} \cdot \alpha)}{A(\alpha, \alpha^*)} + i\dot{\gamma}_D^R \right) \right. \\ &\quad \left. + is \frac{\dot{\alpha} \cdot M \cdot \alpha^* - \alpha \cdot M \cdot \dot{\alpha}^* + \alpha^2(\alpha^* \cdot M \cdot \dot{\alpha}^*) - \alpha^{*2}(\dot{\alpha} \cdot M \cdot \alpha)}{A(\alpha, \alpha^*)} - is \dot{\lambda}_{\tau x}^I \right| \end{aligned} \quad (6.101)$$

and

$$\begin{aligned}
 ds_{FS}^2 = 2\Delta & \left[\frac{\dot{\alpha} \cdot \dot{\alpha}^* - 2|\dot{\alpha} \cdot \alpha|^2}{A(\alpha, \alpha^*)} + 2 \frac{|\dot{\alpha} \cdot \alpha^* - \alpha^{*2} \alpha \cdot \dot{\alpha}|^2}{A(\alpha, \alpha^*)^2} \right] \\
 & + 2is \frac{2(1 - |\alpha|^2)(\dot{\alpha} \cdot \dot{\alpha}^*)(\alpha \cdot M \cdot \alpha^*) + \dot{\alpha} \cdot M \cdot \dot{\alpha}^* \left[2(1 - |\alpha|^2)^2 - A(\alpha, \alpha^*) \right]}{A(\alpha, \alpha^*)^2}
 \end{aligned} \tag{6.102}$$

where $A(\alpha, \alpha^*)$ was defined in Eq. (6.4), $M \equiv \begin{pmatrix} 0 & 1 \\ -1 & 0 \end{pmatrix}$, $\alpha = (\alpha_\tau, \alpha_x)$ and we have used superscripts to denote the real part of γ_D and the imaginary part of $\lambda_{\tau x}$ (which remain unfixed by the unitarity constraint). Similar to the result in section 6.3, the curvature of this metric is $R = -16 \frac{\Delta}{\Delta^2 - s^2} = -\frac{4}{\hbar} - \frac{4}{\bar{\hbar}} = R_h + R_{\bar{h}}$ where $R_h, R_{\bar{h}}$ are the curvatures of the holomorphic and anti-holomorphic parts, as expected from the holomorphic factorization. Of course, setting $s = 0$ recovers Eqs. (6.5)-(6.6).

6.H Metric and Geometric Action in the Fundamental Representation of the Conformal Group

Here we will evaluate various quantities related to coadjoint orbits in the fundamental representation of the conformal group (see Sec. 6.D for our conventions of the fundamental representation of the conformal algebra $\mathfrak{so}(d, 2)$). In this case, the Lie algebra and the dual space are isomorphic since the algebra admits a non-degenerate bilinear form $(X, Y) \equiv \frac{1}{2} \text{Tr}[X \cdot Y]$. Therefore each algebra element can be identified with a dual algebra element according to $\langle \lambda, \cdot \rangle \equiv (\lambda, \cdot)$. It is then straightforward to build $R(U)$, the matrix representation associated to the unitary U in Eq. (6.3). The field theory unitarity conditions is imposed by requiring that we have

$$R(U^\dagger) = g^{-1} R(U)^\dagger g = R(U)^{-1}. \tag{6.103}$$

This condition fixes the parameters $\{\beta^\mu, \gamma_D^I, \lambda_{\mu\nu}^R\}$ in the definition of U in Eq. (6.3) as a function of the remaining parameters $\{\alpha, \gamma_D^R, \lambda_{\mu\nu}^I\}$ where the superscripts R and I indicate the real and imaginary parts, respectively. In particular, one of those constraints $\gamma_D^I = -\frac{1}{2} \log(1 - 2\alpha \cdot \alpha^* + \alpha^2 \alpha^{*2})$ should be familiar from the discussion in section 6.3. We were able to solve the constraints explicitly for $d = 1$ and $d = 2$ and order by order in a perturbative expansion in $|\alpha|$ in $d > 2$, however the explicit expressions are cumbersome and not particularly illuminating, and so we do not include them here. One can then compute the MC form associated to the trajectory implemented by the unitary U in terms of the coordinates $\{\alpha, \gamma_D^R, \lambda_{\mu\nu}^I\}$ by evaluating

$$R(\Theta) \equiv R(U)^{-1} dR(U). \tag{6.104}$$

To make the connection to our previous results we consider a representative in the dual space $\lambda(\mathcal{O}) \equiv (i\Delta R(D), \mathcal{O}) = \frac{1}{2} \text{Tr}(\Delta M_{-1,0} \cdot \mathcal{O})$. This element of the dual algebra is of course identified via the bilinear form with the algebra element $\lambda = i\Delta R(D)$ (here we slightly abuse the notation since we give the same name to the dual algebra element and the corresponding algebra element, but since the bilinear form is non-degenerate indeed the two can be identified). The stabilizer algebra is $\mathfrak{h}_\lambda = \mathfrak{so}(2) \times \mathfrak{so}(d)$ and it naturally leads to an orbit which can be identified with the coset space in Eq. (6.7). In the $d = 2$ spinning case, where $\bar{h} \neq h$ (see Sec. 6.G), the relevant representative is identified with the algebra element $\lambda = i\Delta R(D) + sR(L_{Tx})$ where $\Delta = h + \bar{h}$ and $s = h - \bar{h}$.

In order to evaluate the metric along the orbit associated with the representative (6.16), we compute the symplectic form

$$\omega = \frac{1}{2} \text{Tr} [\lambda \cdot dR(\Theta)] \quad (6.105)$$

and then obtain the components

$$\omega = \omega_{\bar{\mu}\nu} d\alpha^{*\bar{\mu}} \wedge d\alpha^\nu, \quad (6.106)$$

where we have introduced barred indices to formally distinguish between α and α^* . The wedge product is canonically identified with the tensor product through $x \wedge y \equiv \frac{1}{2}(x \otimes y - y \otimes x)$ hence

$$\omega = \frac{1}{2} \omega_{\bar{\mu}\nu} (d\alpha^{*\bar{\mu}} \otimes d\alpha^\nu - d\alpha^\nu \otimes d\alpha^{*\bar{\mu}}). \quad (6.107)$$

The metric is then obtained by contracting with the complex structure J given by

$$J^\mu{}_\rho d\alpha^\rho = -i d\alpha^\mu, \quad J^{\bar{\nu}}{}_{\bar{\rho}} d\alpha^{*\bar{\rho}} = i d\alpha^{*\bar{\nu}}, \quad (6.108)$$

such that

$$ds_{G/H_\lambda}^2 = \frac{1}{2} \omega_{\bar{\mu}\rho} d\alpha^{*\bar{\mu}} \otimes J^\rho{}_\nu d\alpha^\nu - \frac{1}{2} \omega_{\bar{\rho}\nu} d\alpha^\nu \otimes J^{\bar{\rho}}{}_{\bar{\mu}} d\alpha^{*\bar{\mu}} \quad (6.109)$$

leading to

$$ds_{G/H_\lambda}^2 = -i \omega_{\bar{\mu}\nu} d\alpha^{*\bar{\mu}} d\alpha^\nu. \quad (6.110)$$

Finally, the pre-symplectic form (6.13) is given by

$$\mathcal{A}_\lambda = \frac{1}{2} \text{Tr} [\lambda \cdot R(\Theta)]. \quad (6.111)$$

Our results for the metric on the coset space coincide with the Fubini-Study metric in Eq. (6.6) and those for the pre-symplectic potential becomes the \mathcal{F}_1 cost function in Eq. (6.5) up to an absolute value, *i.e.*,

$$\mathcal{F}_1 d\sigma = |\mathcal{A}_\lambda|, \quad ds_{FS}^2 = ds_{G/H_\lambda}^2. \quad (6.112)$$

We have verified this analytically in $d = 2$ and in a perturbative expansion in $d > 2$.

Explicit Example – $\text{SO}(2,1)$: Let us demonstrate how all this works for the simplest example of the $\mathfrak{so}(2,1)$ algebra. This algebra is locally isomorphic to $\mathfrak{sl}(2, \mathbb{R})$, which represents (for example) the holomorphic copy in two dimensions. The relevant generators are

$$P_1 \simeq L_{-1} = \begin{bmatrix} 0 & 0 & 1 \\ 0 & 0 & -i \\ 1 & -i & 0 \end{bmatrix} \quad D \simeq L_0 = \begin{bmatrix} 0 & i & 0 \\ -i & 0 & 0 \\ 0 & 0 & 0 \end{bmatrix} \quad K_1 \simeq L_1 = \begin{bmatrix} 0 & 0 & -1 \\ 0 & 0 & -i \\ -1 & -i & 0 \end{bmatrix}. \quad (6.113)$$

The unitary is given by

$$R(U) \equiv e^{i\zeta L_{-1}} e^{i(\gamma_R + i\gamma_I)L_0} e^{i\zeta_1 L_1}. \quad (6.114)$$

Requiring the unitarity condition (6.103) imposes

$$\gamma_I = -\log(1 - |\zeta|^2), \quad \zeta_1 = e^{i\gamma_R} \zeta^*. \quad (6.115)$$

The MC form is

$$\Theta = L_{-1} \frac{(ie^{-i\gamma_R} d\zeta)}{1 - |\zeta|^2} + L_0 \left(\frac{\zeta^* d\zeta - \zeta d\zeta^*}{1 - |\zeta|^2} + i d\gamma_R \right) + L_1 \frac{(ie^{i\gamma_R} d\zeta^*)}{1 - |\zeta|^2}. \quad (6.116)$$

The representative is $\lambda = i\hbar L_0$ whose stabilizer is spanned by the generator L_0 . The exterior derivative of the MC form is given by

$$\begin{aligned} d\Theta &= \frac{i}{(1 - |\zeta|^2)^2} \left[\zeta^* e^{i\gamma_R} L_1 - \zeta e^{-i\gamma_R} L_{-1} + 2iL_0 \right] d\zeta \wedge d\zeta^* \\ &+ \frac{d\gamma_R}{1 - |\zeta|^2} \wedge \left[e^{-i\gamma_R} d\zeta L_{-1} - e^{i\gamma_R} d\zeta^* L_1 \right]. \end{aligned} \quad (6.117)$$

The metric on the coset space (6.110) and the pre-symplectic form (6.111) read

$$ds_{G/H_\lambda}^2 = 2\hbar \frac{d\zeta d\zeta^*}{(1 - |\zeta|^2)^2}, \quad \mathcal{A}_\lambda = i\hbar \left(\frac{\zeta^* d\zeta - \zeta d\zeta^*}{1 - |\zeta|^2} + i d\gamma_R \right), \quad (6.118)$$

which matches our results in Eqs. (6.84)-(6.85) (up to an absolute value for \mathcal{F}_1) when focusing on a single $\mathfrak{sl}(2, \mathbb{R})$ copy.

6.I Root Space Decomposition

The assumptions used in section 6.5 to equate the Fubini-Study metric with the metric compatible with the symplectic form on a coadjoint orbit follow naturally from the structure of a root space decomposition (for a summary of how this works

for other coherent state symmetry groups, which use a slightly different root space decomposition, see [311]). For the conformal algebra, the relevant decomposition is known as the minimal Bruhat decomposition [314], see [315, 316] for applications to conformal field theory in the context of parabolic Verma modules. In this part of the supplementary material we will both motivate the assumptions of the proof and explain how to construct the representations of interest using a more mathematical language.

Consider a unitarily represented semisimple group G with Lie algebra \mathfrak{g} , with \mathcal{D} a highest-weight representation on the Hilbert space. For our purposes we have in mind the Euclidean conformal group, but for now we keep the group arbitrary. The group theoretic generalization of a coherent state is often defined in terms of a base state $|\psi_R\rangle$ left invariant up to a phase by a subgroup $H \subset G$, or equivalently one that is an eigenstate of the corresponding subalgebra \mathfrak{h} ,

$$x|\psi_R\rangle = \chi|\psi_R\rangle, \quad \forall x \in \mathcal{D}(\mathfrak{h}). \quad (6.119)$$

In the case of vector coherent states [280, 281, 282, 283] (relevant to circuits constructed from a spinning primary in the conformal algebra in $d > 2$), one often considers instead a collection of base states that transform into each other under the action of a subgroup, much like primaries with spin transform among each other under the action of the $L_{\mu\nu}$'s. We will explain how the subalgebra \mathfrak{h} relates to a portion of a root space decomposition, and also indicate how this works for the vector coherent states.

Any semisimple algebra admits some Cartan decomposition $\mathfrak{g} = \mathfrak{s} + \mathfrak{t}$ where $[\mathfrak{s}, \mathfrak{s}] \subset \mathfrak{s}$, $[\mathfrak{s}, \mathfrak{t}] \subset \mathfrak{t}$ and $[\mathfrak{t}, \mathfrak{t}] \subset \mathfrak{s}$. Let $\mathfrak{a} \subset \mathfrak{t}$ be a maximal Abelian subalgebra for \mathfrak{t} , and $\mathfrak{m} \subset \mathfrak{s}$ be the centralizer of \mathfrak{a} in \mathfrak{s} , in other words the elements $X \in \mathfrak{s}$ such that $[X, h] = 0$ for all $h \in \mathfrak{a}$. The adjoint action with respect to \mathfrak{a} can be diagonalized, with the eigenspaces known as the restricted root spaces \mathfrak{g}_α :

$$\mathfrak{g}_\alpha = \{X \in \mathfrak{g} : [h, X] = \alpha(h)X \quad \forall h \in \mathfrak{a}\}. \quad (6.120)$$

The linear functionals $\alpha(h)$ are the roots. A root is called positive with respect to a given basis of the dual space if its coefficients in the expansion over this basis are positive. We denote the set of all roots as Φ and the set of positive and negative roots as Φ^\pm . Unlike for the standard semisimple Lie algebra root space decomposition, these roots are defined with respect to an Abelian algebra \mathfrak{a} that is not maximal.

The minimal Bruhat decomposition is the resulting root space decomposition:

$$\mathfrak{g} = \mathfrak{n}^- \oplus \mathfrak{m} \oplus \mathfrak{a} \oplus \mathfrak{n}^+, \quad \mathfrak{n}^\pm = \bigoplus_{\alpha \in \Phi^\pm} \mathfrak{g}_\alpha. \quad (6.121)$$

Here $\mathfrak{g}_0 \equiv \mathfrak{m} \oplus \mathfrak{a}$ is the centralizer of \mathfrak{a} , since \mathfrak{m} is the centralizer of \mathfrak{a} in \mathfrak{s} and \mathfrak{a} is maximal in \mathfrak{t} . \mathfrak{n}^\pm are the positive and negative root spaces.

Pick a basis $E_{\alpha,p} \in \mathfrak{g}_\alpha$. The label p here accounts for any root degeneracy, which is possible given that the Abelian algebra \mathfrak{a} used in the root space decomposition (6.121)

is not the full maximal Abelian algebra (the Cartan subalgebra) for \mathfrak{g} . By Eq. (6.120) these satisfy

$$[h_i, E_{\alpha,p}] = \alpha_i E_{\alpha,p}, \quad \forall h_i \in \mathfrak{a}. \quad (6.122)$$

For an inner product with $h_i^\dagger = h_i$, applying the dagger to Eq. (6.122) gives $E_{\alpha,p}^\dagger = E_{-\alpha,p}$.

Using the Jacobi relation applied to Eq. (6.122), we can prove inclusions for the commutation relations for the root spaces,

$$[\mathfrak{g}_\alpha, \mathfrak{g}_\beta] \subset \mathfrak{g}_{\alpha+\beta}, \quad \alpha + \beta \in \Phi \text{ or } \alpha + \beta = 0, \quad (6.123)$$

and for the part of the centralizer not in the Abelian algebra \mathfrak{a} ,

$$[\mathfrak{m}, \mathfrak{g}_\alpha] \subset \mathfrak{g}_\alpha, \quad [\mathfrak{m}, \mathfrak{m}] \subset \mathfrak{m}. \quad (6.124)$$

For an ordinary root space decomposition, the commutator of a root vector with its Hermitian conjugate would take values in the Cartan subalgebra. Notice that here, it instead takes values in the centralizer \mathfrak{g}_0 of the Abelian algebra \mathfrak{a} defining the root decomposition.

Consider a highest-weight representation for this root decomposition. This consists of states $|\lambda\rangle$ labelled by their eigenvalues λ under the h_i ,

$$h_i |\lambda\rangle = \lambda_i |\lambda\rangle, \quad (6.125)$$

where a highest-weight state $|\lambda_0\rangle$ is annihilated by all the raising operators,

$$E_{\alpha,p} |\lambda_0\rangle = 0, \quad \forall \alpha, p. \quad (6.126)$$

By Eq. (6.122), $E_{\alpha,p}$ raises the eigenvalue under h_i by α_i , thus it can be interpreted as a ladder operator. Likewise, $E_{\alpha,p}^\dagger = E_{-\alpha,p}$ is a ladder operator that lowers the eigenvalue. We build the representation by applying the lowering operators successively starting from the highest weight state. Note that here, in order to match with the standard CFT literature, we use opposite conventions to those used in the definition of coherent states for the Heisenberg group in quantum mechanics where one typically starts with a lowest weight state.

Now consider an element $x \in \mathfrak{m}$ (in the centralizer but not in \mathfrak{a}). Then $[\mathfrak{m}, \mathfrak{g}_\alpha] \subset \mathfrak{g}_\alpha$ by Eq. (6.124), and acting the commutator on $|\lambda_0\rangle$ and applying the highest weight condition (6.126) gives $\mathfrak{g}_\alpha x |\lambda_0\rangle = 0$. So $x |\lambda_0\rangle$ must be a highest-weight state. If there is a *single* state satisfying Eq. (6.126), then $x |\lambda_0\rangle$ is proportional to $|\lambda_0\rangle$. Thus the eigenvalue condition (6.125) extends from \mathfrak{a} to \mathfrak{g}_0 ,

$$x |\lambda_0\rangle = \chi |\lambda_0\rangle, \quad \forall x \in \mathfrak{g}_0. \quad (6.127)$$

Recalling Eq. (6.119), this means that the highest weight state of a root space representation using the Bruhat decomposition is a natural candidate for our base state in

the coherent state construction, with an invariance group $H \subset G$ whose algebra \mathfrak{h} is just the stabilizer \mathfrak{g}_0 of α :

$$|\psi_R\rangle = |\lambda_0\rangle, \quad \mathfrak{h} = \mathfrak{g}_0. \quad (6.128)$$

The orthogonal complements to \mathfrak{h} are \mathfrak{n}^\pm . These consist of raising and lowering operators that are related by Hermitian conjugation and build the representation starting from $|\lambda_0\rangle$.

In the spinning case, a highest-weight representation can still be built from a preferred highest weight state, with a highest weight condition (6.126) that includes ladder operators in \mathfrak{m} . Thus, $|\lambda_0\rangle$ satisfying only Eq. (6.126) is not unique and $x|\lambda_0\rangle$ defines a subspace of states. This subset of states will participate in the generalization of the eigenvalue condition (6.119) to vector coherent states. Imposing Eq. (6.127) applied to the preferred highest weight state results in an invariance subalgebra that is smaller than the centralizer.

We now return to consider how this structure ties to the proof in section 6.5. We saw that we could identify $\mathfrak{g}_0 \supseteq \mathfrak{h}$. In other words, the centralizer for α is either equal to the stabilizing subalgebra in the spinless case, or contains it in the spinning case. Thus the commutation relations (6.122), (6.123) and (6.124) are simply the assumptions that $[\mathfrak{n}_\pm, \mathfrak{n}_\pm] \subset \mathfrak{n}_\pm$ and $[\mathfrak{h}, \mathfrak{n}_\pm] \subset \mathfrak{n}_\pm$. The Hermiticity condition $E_{\alpha,p}^\dagger = E_{-\alpha,p}$ is also natural for the root space decomposition. These were the starting points for the proof in section 6.5.

Conformal algebra: Now we will be more explicit about how these abstract ingredients apply to the specific case of the conformal algebra as considered in section 6.3. Recall that we are considering the real Euclidean conformal algebra, a semisimple real algebra that can be expressed in terms of its complexification as $\mathfrak{so}(d+1, 1) = \{X \in \mathfrak{so}(d+2, \mathbb{C}) \mid X \text{ real}, X^T \eta + \eta X = 0\}$, where $\eta = \text{diag}(-1, 1, \dots, 1)$ is the flat metric on $\mathbb{R}^{d+1,1}$. Note that the real matrices obeying these conditions differ from our choice of complex generators in Eq. (6.54), however the algebras are isomorphic. The starting point for the Bruhat decomposition is a Cartan decomposition of $\mathfrak{so}(d+1, 1)$, which is not unique and can be specified by an involution. A natural choice is

$$\theta(X) = \eta X \eta. \quad (6.129)$$

The Cartan splitting $\theta(X) = X$ for $X \in \mathfrak{s}$, $\theta(X) = -X$ for $x \in \mathfrak{t}$ implies that $\mathfrak{s} = \{L_{\mu\nu}, P_\mu + K_\mu\}$ and $\mathfrak{t} = \{D, P_\mu - K_\mu\}$. The maximal Abelian subalgebra for \mathfrak{t} is $\mathfrak{a}_0 = \{-D\}$, with centralizer $\mathfrak{m}_0 = \{L_{\mu\nu}\}$ in \mathfrak{s} . Note that we have chosen \mathfrak{a}_0 to be generated by $-D$ instead of D to match with the usual conventions for CFT representations.

The positive and negative root spaces with respect to \mathfrak{a}_0 are $\mathfrak{n}^- = \{P_\mu\}$, $\mathfrak{n}^+ = \{K_\mu\}$, which are related through the involution as $\theta(\mathfrak{n}^\pm) = \mathfrak{n}^\mp$. The positive and negative roots

are all degenerate with $\alpha = \pm 1$. The minimal Bruhat decomposition (6.121) for the Euclidean conformal group is

$$\mathfrak{g} = \{P_\mu\} \oplus \{L_{\mu\nu}\} \oplus \{D\} \oplus \{K_\mu\}. \quad (6.130)$$

The usual highest-weight representation for the conformal algebra consists of a conformal primary state $|\Delta\rangle$ annihilated by K_μ , with the remaining descendant states built by acting with P_μ . Both the primary and its descendants are eigenstates of $-D$, with P_μ acting as a lowering operator since it decreases the $-D$ -eigenvalue. But this is precisely a highest-weight representation for the Bruhat decomposition described above. $-D$ generates the Abelian algebra \mathfrak{a} . The condition (6.127) that the stabilizer algebra for the highest weight state is the centralizer of \mathfrak{a} is just the statement that the primary state is also an eigenstate under $L_{\mu\nu}$:

$$D|\Delta\rangle = \Delta|\Delta\rangle, \quad L_{\mu\nu}|\Delta\rangle = 0. \quad (6.131)$$

We end by summarizing how our assumptions in section 6.5 apply to the case of the conformal algebra. The condition $[\mathfrak{h}, \mathfrak{n}_\pm] \subset \mathfrak{n}_\pm$ is satisfied by the algebra (6.23) and $[\mathfrak{n}_\pm, \mathfrak{n}_\pm] \subset \mathfrak{n}_\pm$ is trivially satisfied since for the conformal algebra, the P_μ 's and K_μ 's commute so \mathfrak{n}_\pm is Abelian. With respect to the field theory dagger (6.103), the generators of \mathfrak{n}_\pm obey the Hermiticity conditions $P_\mu^\dagger = K_\mu$. These are just the conditions $E_{\alpha,p}^\dagger = E_{-\alpha,p}$ taken above for the root space decomposition and used in the proof in section 6.5.

6.J Holographic Interpretation

In this part of the supplemental material, we present further details on the relation of our coherent states in CFT_d and the trajectories of massive particles in AdS_{d+1} . In particular we explain the geometric interpretation of the Fubini-Study metric and the complexity of states in terms of the bulk geometry and present an interesting example of geodesics with fixed radius.

6.J.1 Background

Here, we review our conventions for the embedding space and trajectories of massive particles in AdS_{d+1} following [284] (up to a modification of the signature). Let us start with the action of a massive particle of mass m in an embedding space description of AdS_{d+1} of radius R consisting of a hyperbola of radius R in flat space $\mathbb{R}^{d,2}$ with metric $g_{AB} = \text{diag}(-, -, +, \dots, +)$. The coordinates of the flat space will be denoted X^A with $A \in \{0, 0', 1, \dots, d\}$ and we will use Greek indices to denote the space directions $\mu \in \{1, \dots, d\}$. The action for the massive particle reads

$$S = - \int d\tau \left[-\frac{\dot{X}(\tau)^2}{2e(\tau)} + \frac{e(\tau)m^2}{2} - \frac{\mu(\tau)}{2} (X(\tau)^2 + R^2) \right]. \quad (6.132)$$

In this action, $e(\tau)$ is the einbein and $\mu(\tau)$ is a Lagrange multiplier enforcing the hyperbola condition $X(\tau)^2 = -R^2$. The equations of motion derived from this action fix

$$e(\tau)^2 = -\dot{X}(\tau)^2/m^2, \quad \mu(\tau) = -\frac{m}{R^2} \sqrt{-\dot{X}(\tau)^2}. \quad (6.133)$$

Solutions will be timelike geodesics in AdS_{d+1} with

$$X_0(t) = r(t) \cos(t/R), \quad X_{0'}(t) = r(t) \sin(t/R), \quad (6.134)$$

where t is the AdS_{d+1} time coordinate and the restriction to the hyperbola fixes

$$-R^2 = X^2(t) = -r(t)^2 + X_\mu(t)X^\mu(t). \quad (6.135)$$

The action (6.132) is $\text{SO}(d, 2)$ invariant and the associated conserved charges read

$$J_{AB} = P_B(t)X_A(t) - P_A(t)X_B(t) = P_B(0)X_A(0) - P_A(0)X_B(0), \quad (6.136)$$

where $P_A(t) \equiv \dot{X}_A(t)/e(t) = m\dot{X}^A(t)/\sqrt{-\dot{X}^2(t)}$ is the canonical momentum associated with $X_A(t)$. The charges corresponding to the compact subgroup $\text{SO}(2) \times \text{SO}(d)$ are the energy $E \equiv J_{0,0'}$ and angular momentum $J_{\mu\nu}$, with $J^2 = J_{\mu\nu}J_{\mu\nu}/2$ the squared angular momentum of the trajectory. We selected our geodesics to be future oriented, *i.e.*, $X_0\dot{X}_{0'} - X_{0'}\dot{X}_0 > 0$ and this simply tells us that the energy is positive $E > 0$. The remaining conserved charges are $J_{0,\mu}$ and $J_{0',\mu}$ which can be reorganized into a pair of complex coordinates describing (without redundancy) the phase space of timelike geodesics

$$z_\mu \equiv J_{0',\mu} - iJ_{0,\mu}, \quad z_\mu^* \equiv J_{0,\mu} + iJ_{0',\mu}. \quad (6.137)$$

Using (6.136), we can write d equations for the coordinates X_μ

$$EX_\mu = J_{0,\mu}X_{0'} - J_{0',\mu}X_0 \quad (6.138)$$

which yield

$$X_\mu(t) = -\frac{r(t)}{2E} \left(z_\mu^* e^{it/R} + z_\mu e^{-it/R} \right), \quad \text{with } r(t) = \frac{2ER}{\sqrt{4E^2 - z^{*2}e^{2it/R} - z^2e^{-2it/R} - 2z \cdot z^*}}. \quad (6.139)$$

(z, z^*) are complex coordinates on the phase space of the particle which can be used to evaluate its symplectic form

$$\omega_{\text{bulk}} = dP_A \wedge dX^A. \quad (6.140)$$

The energy is minimal when the particle is at rest and equal to $E_0 = mR$. Quantizing the classical system canonically by promoting the observables $\{E, J_{\mu\nu}, z_\mu, z_\mu^*\}$ to operators leads to a unitary reducible representation of $\text{SO}(d, 2)$. We introduce the following change of coordinates

$$z_\mu = 2E_0 \frac{\alpha_\mu^* - \alpha^{*2} \alpha_\mu}{A(\alpha, \alpha^*)}, \quad z_\mu^* = 2E_0 \frac{\alpha_\mu - \alpha^2 \alpha_\mu^*}{A(\alpha, \alpha^*)}. \quad (6.141)$$

As shown by [284], an irreducible representation can be obtained upon imposing that α is in the domain (6.4) together with the condition $\alpha \cdot \alpha^* < 1$. Furthermore, we can find that

$$\omega_{\text{bulk}} = \omega_{\text{CFT}_d}, \quad (6.142)$$

provided that we identify $\Delta = E_0$, where the symplectic form of the CFT can be easily read from the metric (6.6) via the relations (6.107) and (6.110). Starting with the action (6.132), the classical geodesic trajectory in the bulk is based on a saddle point approximation with large mass. The mass of the dual quantum particle is related to the field theory operator dimension as $m^2 R^2 = \Delta(\Delta - d)$ which can be inverted as

$$\Delta = mR \left(\sqrt{1 + \frac{d^2}{4m^2 R^2}} + \frac{d}{2mR} \right). \quad (6.143)$$

In the limit of large mass we simply have $mR = \Delta$. Therefore, we have an exact duality between CFT_d states and timelike geodesics in AdS_{d+1} . It is interesting to notice that due to canonical quantization, the conserved charges associated with the isometries in the bulk map to the expectation values of algebra elements in the CFT_d . For example, we find that $z_\mu = \langle \alpha | i P_\mu | \alpha \rangle$ and the energy and angular momentum of the particle are given by

$$E = \Delta \frac{1 - \alpha^2 \alpha^{*2}}{A(\alpha, \alpha^*)} = \langle \alpha | D | \alpha \rangle, \quad J = 2\Delta \frac{\sqrt{(\alpha \cdot \alpha^*)^2 - \alpha^2 \alpha^{*2}}}{A(\alpha, \alpha^*)} = \sqrt{\frac{1}{2} \langle \alpha | i L_{\mu\nu} | \alpha \rangle \langle \alpha | i L_{\mu\nu} | \alpha \rangle}, \quad (6.144)$$

which can be inverted as

$$\alpha \cdot \alpha^* = \frac{E^2 - J^2 - \Delta^2}{(E + \Delta)^2 - J^2}, \quad \alpha^2 \alpha^{*2} = \frac{(E - \Delta)^2 - J^2}{(E + \Delta)^2 - J^2}. \quad (6.145)$$

In this coordinate system, $r(t)$ can be simplified into

$$r(t) = \frac{R E \sqrt{A(\alpha, \alpha^*)}}{\Delta |B(t, \alpha)|}, \quad B(t, \alpha) \equiv e^{it/R} \alpha^2 - e^{-it/R}. \quad (6.146)$$

6.J.2 Complexity in Holography

We have established an explicit connection between states in the CFT_d and timelike geodesics in AdS_{d+1} (or particle states). We can now re-express the complexity (6.42)-(6.44) of a target state $|\alpha_T\rangle$ in the field theory in terms of the energy E_T and angular momentum J_T of the associated target particle state in AdS_{d+1} as

$$\mathcal{C}[E_T, J_T] = \sqrt{\Delta} \sqrt{\left(\tanh^{-1} \sqrt{\frac{E_T + J_T - \Delta}{E_T + J_T + \Delta}} \right)^2 + \left(\tanh^{-1} \sqrt{\frac{E_T - J_T - \Delta}{E_T - J_T + \Delta}} \right)^2}, \quad (6.147)$$

where we used that

$$\Omega_T^S = \sqrt{\frac{E_T + J_T - \Delta}{E_T + J_T + \Delta}}, \quad \Omega_T^A = \sqrt{\frac{E_T - J_T - \Delta}{E_T - J_T + \Delta}}. \quad (6.148)$$

6.J.3 Geometric Interpretation of the Fubini-Study Metric

We have argued that states $|\alpha\rangle$ are related to timelike geodesics in AdS_{d+1} according to (6.20)-(6.21). The question that remains to be answered is what is the gravitational dual of the Fubini-Study line element between two infinitesimally close states.

Consider two nearby geodesics $X^\mu(t)$ and $X^\mu(t) + \delta X^\mu(t)$ corresponding to two nearby states $|\alpha\rangle$ and $|\alpha + \delta\alpha\rangle$, respectively. We can expand $\delta X^\mu(t)$ as follows

$$\delta X^\mu(t) = d\alpha \cdot \partial_\alpha X^\mu(t) + d\alpha^* \cdot \partial_{\alpha^*} X^\mu(t) + dt \dot{X}^\mu(t). \quad (6.149)$$

The relation (6.20) implies that both X^μ and $X^\mu + \delta X^\mu$ are geodesics in AdS_{d+1} corresponding to the parameters α, α^* and $\alpha + d\alpha, \alpha^* + d\alpha^*$. We further impose a requirement that $\delta X \cdot \dot{X} = 0$ which can be used to solve for dt as follows

$$dt = -\frac{1}{\dot{X}^2(t)} \left(\dot{X}_\mu(t) d\alpha^\nu \frac{\partial X^\mu(t)}{\partial \alpha^\nu} + \dot{X}_\mu(t) d\alpha^{*\nu} \frac{\partial X^\mu(t)}{\partial \alpha^{*\nu}} \right). \quad (6.150)$$

This requirement can be understood as looking at the hyperplane orthogonal to $\dot{X}^\mu(t)$ and finding the intersection of this hyperplane with the second geodesic at every time t . We will measure the perpendicular distance between the two geodesics along this hyperplane. The perpendicular distance $\delta X_{\text{perp}}^2(t)$ can be related to ds_{FS}^2 in (6.6) as follows. We begin by separating $\delta X_{\text{perp}}^2(t)$ into three contributions

$$\delta X_{\text{perp}}^2(t) = \frac{R^2}{\Delta} ds_{\text{FS}}^2 + g_{\alpha\alpha}(t) d\alpha^2 + g_{\alpha\alpha}^*(t) d\alpha^{*2}, \quad \text{with } g_{\alpha\alpha}(t) = \frac{R^2}{A(\alpha, \alpha^*)} \frac{e^{2it/R} - \alpha^{*2}}{1 - e^{2it/R} \alpha^2}. \quad (6.151)$$

Note that only the last two terms in $\delta X_{\text{perp}}^2(t)$ are time dependent. Next, we look for times at which $\delta X_{\text{perp}}^2(t)$ is extremal, *i.e.*, $\partial_t \delta X_{\text{perp}}^2(t) = 0$. This leads to two solutions t_+ and t_- corresponding to a maximum (with $\partial_t^2 \delta X_{\text{perp}}^2(t_+) < 0$) and a minimum (with $\partial_t^2 \delta X_{\text{perp}}^2(t_-) > 0$) perpendicular distance, respectively, which are given by

$$e^{2it_\pm/R} = \frac{\alpha^{*2} \sqrt{d\alpha \cdot d\alpha} \pm \sqrt{d\alpha^* \cdot d\alpha^*}}{\sqrt{d\alpha \cdot d\alpha} \pm \alpha^2 \sqrt{d\alpha^* \cdot d\alpha^*}}, \quad (6.152)$$

where

$$\delta X_{\text{perp,max/min}}^2 \equiv \delta X^2(t_\pm) = \frac{R^2}{\Delta} ds_{\text{FS}}^2 \pm \frac{2R^2 \sqrt{d\alpha^2 d\alpha^{*2}}}{A(\alpha, \alpha^*)}. \quad (6.153)$$

Using the above relations, we finally recover the equivalence (6.22)

$$ds_{\text{FS}}^2 = \frac{\Delta}{2R^2} \left(\delta X_{\text{perp,min}}^2 + \delta X_{\text{perp,max}}^2 \right). \quad (6.154)$$

6.J.4 Example: Timelike Geodesics with Fixed Radius

We will now work out an explicit case for which much of the previous calculations simplify. The goal of this presentation is to give an intuition of how to use our holographic results. We will therefore focus on states for which we have $\alpha(\sigma)^2 = 0$. The condition (6.4) then implies $\alpha(\sigma) \cdot \alpha^*(\sigma) < 1/2$ and for these values, we have, from Eq. (6.20)-(6.21)

$$E(\sigma) = \frac{\Delta}{1 - 2\alpha(\sigma) \cdot \alpha^*(\sigma)}, \quad r(t; \sigma) = \frac{R}{\sqrt{1 - 2\alpha(\sigma) \cdot \alpha^*(\sigma)}} \equiv r_0(\sigma), \quad (6.155)$$

where $\rho(t) = R \operatorname{arccosh}(r(t)/R)$ is the global AdS radial coordinate. The fact that $r(t; \sigma)$ does not depend on t means that the associated timelike geodesics have fixed radius which we will define as circular geodesics. This choice of $\alpha(\sigma)$ leads to a path within the subset of fixed radius geodesics for which (6.9) simplifies into

$$\begin{aligned} \Omega_T^S &= \sqrt{2 \alpha_T \cdot \alpha_T^*}, \quad \Omega_T^A = 0, \\ C[\alpha_T] &= \sqrt{\Delta} \tanh^{-1} \left(\sqrt{2 \alpha_T \cdot \alpha_T^*} \right). \end{aligned} \quad (6.156)$$

In the holographic formulation, $J_T = E_T - \Delta$ for such states so the complexity can be expressed using the energy of the particle

$$C_{\text{circular}}[E_T] = \sqrt{\Delta} \tanh^{-1} \left(\sqrt{1 - \frac{\Delta}{E_T}} \right) = \sqrt{\Delta} \tanh^{-1} \left(\sqrt{1 - \frac{R^2}{r_T^2}} \right), \quad (6.157)$$

where $r_T \equiv r_0(\sigma = 1)$ is the radius of the outermost geodesic in the circuit. Considering the AdS metric in a Fefferman-Graham expansion $ds^2 = \frac{1}{z^2} (dz^2 + dx_\mu dx^\mu)$, we have near the boundary ($\rho \rightarrow \infty$) the relation $z \simeq R/\sinh(\rho/R) \simeq \frac{R^2}{r}$. Close to the boundary $z \sim \delta$ and this means $r_T \sim R^2/\delta$ such that

$$C_{\text{circular}}[\delta] \sim \sqrt{\Delta} \log [2R/\delta]. \quad (6.158)$$

This result captures the divergent behavior of complexity as we go to states (represented by circular geodesics) which are very far from our reference state (very close to the boundary in AdS_{d+1}). Note that this is different from asking what is the vacuum divergence of complexity evaluated using the holographic proposals as in, *e.g.*, [317, 318].

Bibliography

- [1] S. A. Hartnoll, A. Lucas, and S. Sachdev. *Holographic Quantum Matter*. MIT Press, 2018. ISBN: 9780262038430.
- [2] J. A. Hertz. “Quantum Critical Phenomena”. *Phys. Rev. B* 14 (1976). DOI: 10.1103/PhysRevB.14.1165.
- [3] A. J. Millis. “Effect of a Nonzero Temperature on Quantum Critical Points in Itinerant Fermion Systems”. *Phys. Rev. B* 48 (1993). DOI: 10.1103/PhysRevB.48.7183.
- [4] K. Yang. “Ferromagnetic Transition in One-Dimensional Itinerant Electron Systems”. *Phys. Rev. Lett.* 93 (2004). DOI: 10.1103/PhysRevLett.93.066401.
- [5] T. R. Kirkpatrick and D. Belitz. “Nature of the quantum phase transition in clean itinerant Heisenberg ferromagnets”. *Phys. Rev. B* 67 (2003). DOI: 10.1103/PhysRevB.67.024419.
- [6] A. V. Chubukov, C. Pépin, and J. Rech. “Instability of the Quantum-Critical Point of Itinerant Ferromagnets”. *Phys. Rev. Lett.* 92 (2004). DOI: 10.1103/PhysRevLett.92.147003.
- [7] K. F. Quader, K. S. Bedell, and G. E. Brown. “Strongly interacting fermions”. *Phys. Rev. B* 36 (1987). DOI: 10.1103/PhysRevB.36.156.
- [8] J. G. Bednorz and K. A. Müller. “Possible high T_c superconductivity in the Ba-La-Cu-O system”. *Zeitschrift für Physik B Condensed Matter* 64 (1986). DOI: 10.1007/BF01303701.
- [9] C. J. Pickard, I. Errea, and M. I. Eremets. “Superconducting Hydrides Under Pressure”. *Annual Review of Condensed Matter Physics* 11 (2020). DOI: 10.1146/annurev-conmatphys-031218-013413.
- [10] B. Keimer, S. A. Kivelson, M. R. Norman, S. Uchida, and J. Zaanen. “From Quantum Matter to High-Temperature Superconductivity in Copper Oxides”. *Nature* 518 (2015). DOI: 10.1038/nature14165.

- [11] P. Giraldo-Gallo, J. A. Galvis, Z. Stegen, K. A. Modic, F. F. Balakirev, J. B. Betts, X. Lian, C. Moir, S. C. Riggs, J. Wu, A. T. Bollinger, X. He, I. Božović, B. J. Ramshaw, R. D. McDonald, G. S. Boebinger, and A. Shekhter. “Scale-Invariant Magnetoresistance in a Cuprate Superconductor”. *Science* 361 (2018). DOI: 10.1126/science.aan3178.
- [12] P. W. Phillips, N. E. Hussey, and P. Abbamonte. “Stranger than Metals”. *Science* 377 (2022). DOI: 10.1126/science.abh4273.
- [13] R. A. Cooper, Y. Wang, B. Vignolle, O. J. Lipscombe, S. M. Hayden, Y. Tanabe, T. Adachi, Y. Koike, M. Nohara, H. Takagi, C. Proust, and N. E. Hussey. “Anomalous Criticality in the Electrical Resistivity of $\text{La}_{2-x}\text{Sr}_x\text{CuO}_4$ ”. *Science* 323 (2009). DOI: 10.1126/science.1165015.
- [14] S. Martin, A. T. Fiory, R. M. Fleming, L. F. Schneemeyer, and J. V. Waszczak. “Normal-State Transport Properties of $\text{Bi}_{2+x}\text{Sr}_{2-y}\text{CuO}_{6+\delta}$ Crystals”. *Phys. Rev. B* 41 (1990). DOI: 10.1103/PhysRevB.41.846.
- [15] N. E. Hussey, K. Takenaka, and H. Takagi. “Universality of the Mott–Ioffe–Regel Limit in Metals”. *Philosophical Magazine* 84 (2004). DOI: 10.1080/14786430410001716944.
- [16] S. Sachdev and J. Ye. “Universal Quantum-Critical Dynamics of Two-Dimensional Antiferromagnets”. *Phys. Rev. Lett.* 69 (1992). DOI: 10.1103/PhysRevLett.69.2411.
- [17] T. J. Reber, X. Zhou, N. C. Plumb, S. Parham, J. A. Waugh, Y. Cao, Z. Sun, H. Li, Q. Wang, J. S. Wen, Z. J. Xu, G. Gu, Y. Yoshida, H. Eisaki, G. B. Arnold, and D. S. Dessau. “A Unified Form of Low-Energy Nodal Electronic Interactions in Hole-Doped Cuprate Superconductors”. *Nature Communications* 10 (2019). DOI: 10.1038/s41467-019-13497-4.
- [18] S. A. Hartnoll. “Horizons, Holography and Condensed Matter” (2012). arXiv: 1106.4324 [hep-th].
- [19] J. Zaanen, Y. Liu, Y.-W. Sun, and K. Schalm. *Holographic Duality in Condensed Matter Physics*. Cambridge University Press, 2015. ISBN: 9781139942492.
- [20] S. A. Hartnoll. “Lectures on Holographic Methods for Condensed Matter Physics”. *Class. Quant. Grav.* 26 (2009). DOI: 10.1088/0264-9381/26/22/224002.
- [21] M. Ammon and J. Erdmenger. *Gauge/Gravity Duality*. Cambridge University Press, 2015. ISBN: 9780511846373.
- [22] J. M. Maldacena. “The Large N Limit of Superconformal Field Theories and Supergravity”. *Int. J. Theor. Phys.* 38 (1999). DOI: 10.4310/ATMP.1998.v2.n2.a1.
- [23] E. Fradkin. *Quantum Field Theory: An Integrated Approach*. Princeton University Press, 2021. ISBN: 9780691189550.
- [24] G. 't Hooft. “A Planar Diagram Theory for Strong Interactions”. *Nucl. Phys. B* 72 (1974). DOI: 10.1016/0550-3213(74)90154-0.

-
- [25] O. Aharony, S. S. Gubser, J. M. Maldacena, H. Ooguri, and Y. Oz. “Large N Field Theories, String Theory and Gravity”. *Physics Reports* 323 (2000). DOI: 10.1016/S0370-1573(99)00083-6.
- [26] S. S. Gubser, I. R. Klebanov, and A. M. Polyakov. “Gauge Theory Correlators from Noncritical String Theory”. *Phys. Lett. B* 428 (1998). DOI: 10.1016/S0370-2693(98)00377-3.
- [27] E. Witten. “Anti-de Sitter Space and Holography”. *Adv. Theor. Math. Phys.* 2 (1998). DOI: 10.4310/ATMP.1998.v2.n2.a2.
- [28] S. W. Hawking. “Particle Creation by Black Holes”. *Commun. Math. Phys.* 43 (1975). DOI: 10.1007/BF02345020.
- [29] J. D. Bekenstein. “Black Holes and Entropy”. *Phys. Rev. D* 7 (1973). DOI: 10.1103/PhysRevD.7.2333.
- [30] S. S. Gubser, I. R. Klebanov, and A. A. Tseytlin. “Coupling constant dependence in the thermodynamics of N=4 supersymmetric Yang-Mills theory”. *Nucl. Phys. B* 534 (1998). DOI: 10.1016/S0550-3213(98)00514-8.
- [31] I. Papadimitriou. “Holographic Renormalization as a Canonical Transformation”. *JHEP* 11 (2010). DOI: 10.1007/JHEP11(2010)014.
- [32] T. Faulkner, H. Liu, J. McGreevy, and D. Vegh. “Emergent Quantum Criticality, Fermi Surfaces, and AdS₂”. *Phys. Rev. D* 83 (2011). DOI: 10.1103/PhysRevD.83.125002.
- [33] N. Iqbal, H. Liu, and M. Mezei. “Semi-Local Quantum Liquids”. *JHEP* 04 (2012). DOI: 10.1007/JHEP04(2012)086.
- [34] C. Charmousis, B. Goutéraux, B. Soo Kim, E. Kiritsis, and R. Meyer. “Effective Holographic Theories for Low-Temperature Condensed Matter Systems”. *JHEP* 11 (2010). DOI: 10.1007/JHEP11(2010)151.
- [35] B. Goutéraux and E. Kiritsis. “Generalized Holographic Quantum Criticality at Finite Density”. *JHEP* 12 (2011). DOI: 10.1007/JHEP12(2011)036.
- [36] L. Huijse, S. Sachdev, and B. Swingle. “Hidden Fermi Surfaces in Compressible States of Gauge-Gravity Duality”. *Phys. Rev. B* 85 (2012). DOI: 10.1103/PhysRevB.85.035121.
- [37] S. A. Hartnoll and E. Shaghoulian. “Spectral weight in holographic scaling geometries”. *JHEP* 07 (2012). DOI: 10.1007/JHEP07(2012)078.
- [38] S. S. Gubser and F. D. Rocha. “Peculiar Properties of a Charged Dilatonic Black Hole in AdS₅”. *Phys. Rev. D* 81 (2010). DOI: 10.1103/PhysRevD.81.046001.
- [39] S. A. Hartnoll, C. P. Herzog, and G. T. Horowitz. “Building a Holographic Superconductor”. *Phys. Rev. Lett.* 101 (2008). DOI: 10.1103/PhysRevLett.101.031601.
- [40] S. A. Hartnoll, C. P. Herzog, and G. T. Horowitz. “Holographic Superconductors”. *JHEP* 12 (2008). DOI: 10.1088/1126-6708/2008/12/015.

- [41] S. S. Gubser and A. Nellore. “Ground States of Holographic Superconductors”. *Phys. Rev. D* 80 (2009). DOI: 10.1103/PhysRevD.80.105007.
- [42] S. A. Hartnoll and A. Tavanfar. “Electron Stars for Holographic Metallic Criticality”. *Phys. Rev. D* 83 (2011). DOI: 10.1103/PhysRevD.83.046003.
- [43] S. A. Hartnoll and P. Petrov. “Electron Star Birth: A Continuous Phase Transition at Nonzero Density”. *Phys. Rev. Lett.* 106 (2011). DOI: 10.1103/PhysRevLett.106.121601.
- [44] S. A. Hartnoll, D. M. Hofman, and D. Vegh. “Stellar Spectroscopy: Fermions and Holographic Lifshitz Criticality”. *JHEP* 08 (2011). DOI: 10.1007/JHEP08(2011)096.
- [45] S. A. Hartnoll and L. Huijse. “Fractionalization of Holographic Fermi Surfaces”. *Class. Quant. Grav.* 29 (2012). DOI: 10.1088/0264-9381/29/19/194001.
- [46] M. V. Medvedyeva, E. Gubankova, M. Čubrović, K. Schalm, and J. Zaanen. “Quantum Corrected Phase Diagram of Holographic Fermions”. *JHEP* 12 (2013). DOI: 10.1007/JHEP12(2013)025.
- [47] S. Sachdev. “A Model of a Fermi Liquid Using Gauge-Gravity Duality”. *Phys. Rev. D* 84 (2011). DOI: 10.1103/PhysRevD.84.066009.
- [48] M. Čubrović, Y. Liu, K. Schalm, Y.-W. Sun, and J. Zaanen. “Spectral Probes of the Holographic Fermi Groundstate: Dialing between the Electron Star and AdS Dirac Hair”. *Phys. Rev. D* 84 (2011). DOI: 10.1103/PhysRevD.84.086002.
- [49] A. Allais, J. McGreevy, and S. J. Suh. “A Quantum Electron Star”. *Phys. Rev. Lett.* 108 (2012). DOI: 10.1103/PhysRevLett.108.231602.
- [50] A. Allais and J. McGreevy. “How to Construct a Gravitating Quantum Electron Star”. *Phys. Rev. D* 88 (2013). DOI: 10.1103/PhysRevD.88.066006.
- [51] T. J. Osborne and M. A. Nielsen. “Entanglement, Quantum Phase Transitions, and Density Matrix Renormalization”. *Quantum Information Processing* 1 (2002). DOI: 10.1023/A:1019601218492.
- [52] G. Vidal, J. I. Latorre, E. Rico, and A. Kitaev. “Entanglement in Quantum Critical Phenomena”. *Phys. Rev. Lett.* 90 (2003). DOI: 10.1103/PhysRevLett.90.227902.
- [53] S. Ryu and T. Takayanagi. “Holographic Derivation of Entanglement Entropy from AdS/CFT”. *Phys. Rev. Lett.* 96 (2006). DOI: 10.1103/PhysRevLett.96.181602.
- [54] L. Susskind. “Entanglement Is Not Enough”. *Fortsch. Phys.* 64 (2016). DOI: 10.1002/prop.201500095.
- [55] S. Chapman and G. Policastro. “Quantum Computational Complexity from Quantum Information to Black Holes and Back”. *Eur. Phys. J. C* 82 (2022). DOI: 10.1140/epjc/s10052-022-10037-1.

- [56] M. Nielsen and I. Chuang. *Quantum Computation and Quantum Information*. Cambridge University Press, 2000. ISBN: 9780521635035.
- [57] M. Nielsen. “A Geometric Approach to Quantum Circuit Lower Bounds”. *Quantum Inf. Comput.* 6 (2006).
- [58] M. A. Nielsen, M. R. Dowling, M. Gu, and A. C. Doherty. “Quantum Computation as Geometry”. *Science* 311 (2006). DOI: 10.1126/science.1121541.
- [59] R. T. Collins, Z. Schlesinger, F. Holtzberg, P. Chaudhari, and C. Feild. “Reflectivity and Conductivity of $\text{YBa}_2\text{Cu}_3\text{O}_7$ ”. *Phys. Rev. B* 39 (1989). DOI: 10.1103/PhysRevB.39.6571.
- [60] J. Orenstein, G. A. Thomas, A. J. Millis, S. L. Cooper, D. H. Rapkine, T. Timusk, L. F. Schneemeyer, and J. V. Waszczak. “Frequency- and Temperature-Dependent Conductivity in $\text{YBa}_2\text{Cu}_3\text{O}_{6+x}$ Crystals”. *Phys. Rev. B* 42 (1990). DOI: 10.1103/PhysRevB.42.6342.
- [61] D. van der Marel, H. J. A. Molegraaf, J. Zaanen, Z. Nussinov, F. Carbone, A. Damascelli, H. Eisaki, M. Greven, P. H. Kes, and M. Li. “Quantum Critical Behaviour in a High-Tc Superconductor”. *Nature* 425 (2003). DOI: 10.1038/nature01978.
- [62] E. van Heumen, X. Feng, S. Cassanelli, L. Neubrand, L. de Jager, M. Berben, Y. Huang, T. Kondo, T. Takeuchi, and J. Zaanen. “Strange Metal Electrodynamics across the Phase Diagram of $\text{Bi}2-x\text{Pb}x\text{Sr}2-y\text{La}y\text{CuO}6+d$ Cuprates”. *Phys. Rev. B* 106 (2022). DOI: 10.1103/PhysRevB.106.054515.
- [63] J. Zaanen. “Why the Temperature Is High”. *Nature* 430 (2004). DOI: 10.1038/30512a.
- [64] S. A. Hartnoll. “Theory of Universal Incoherent Metallic Transport”. *Nature Phys.* 11 (2015). DOI: 10.1038/nphys3174.
- [65] J. A. N. Bruin, H. Sakai, R. S. Perry, and A. P. Mackenzie. “Similarity of Scattering Rates in Metals Showing T-Linear Resistivity”. *Science* 339 (2013). DOI: 10.1126/science.1227612.
- [66] A. Legros, S. Benhabib, W. Tabis, F. Laliberté, M. Dion, M. Lizaire, B. Vignolle, D. Vignolles, H. Raffy, Z. Z. Li, P. Auban-Senzier, N. Doiron-Leyraud, P. Fournier, D. Colson, L. Taillefer, and C. Proust. “Universal T-linear Resistivity and Planckian Dissipation in Overdoped Cuprates”. *Nature Phys* 15 (2019). DOI: 10.1038/s41567-018-0334-2.
- [67] L. Delacrétaz, B. Goutéraux, S. A. Hartnoll, and A. Karlsson. “Bad Metals from Fluctuating Density Waves”. *SciPost Phys.* 3 (2017). DOI: 10.21468/SciPostPhys.3.3.025.
- [68] L. D’Alessio, Y. Kafri, A. Polkovnikov, and M. Rigol. “From Quantum Chaos and Eigenstate Thermalization to Statistical Mechanics and Thermodynamics”. *Adv. Phys.* 65 (2016). DOI: 10.1080/00018732.2016.1198134.

- [69] J. Zaanen. “Lectures on Quantum Supreme Matter” (2021). arXiv: 2110.00961 [cond-mat.str-el].
- [70] S. Chakravarty, B. I. Halperin, and D. R. Nelson. “Two-Dimensional Quantum Heisenberg Antiferromagnet at Low Temperatures”. *Phys. Rev. B* 39 (1989). DOI: 10.1103/PhysRevB.39.2344.
- [71] S. Sachdev. *Quantum Phase Transitions*. 2nd edition. Cambridge University Press, 2011. ISBN: 9780521514682.
- [72] M. Blake. “Universal Charge Diffusion and the Butterfly Effect in Holographic Theories”. *Phys. Rev. Lett.* 117 (2016). DOI: 10.1103/PhysRevLett.117.091601.
- [73] M. Blake. “Universal Diffusion in Incoherent Black Holes”. *Phys. Rev. D* 94 (2016). DOI: 10.1103/PhysRevD.94.086014.
- [74] M. Blake, R. A. Davison, and S. Sachdev. “Thermal Diffusivity and Chaos in Metals without Quasiparticles”. *Phys. Rev. D* 96 (2017). DOI: 10.1103/PhysRevD.96.106008.
- [75] J. Zaanen. “Planckian Dissipation, Minimal Viscosity and the Transport in Cuprate Strange Metals”. *SciPost Phys.* 6 (2019). DOI: 10.21468/SciPostPhys.6.5.061.
- [76] C. Murthy, A. Pandey, I. Esterlis, and S. A. Kivelson. “A Stability Bound on the T-linear Resistivity of Conventional Metals”. *PNAS* 120 (2023). DOI: 10.1073/pnas.2216241120.
- [77] M. Ammon and J. Erdmenger. *Gauge/Gravity Duality: Foundations and Applications*. Cambridge University Press, 2015. ISBN: 9781107010345.
- [78] J. Zaanen, G. A. Sawatzky, and J. W. Allen. “Band Gaps and Electronic Structure of Transition-Metal Compounds”. *Phys. Rev. Lett.* 55 (1985). DOI: 10.1103/PhysRevLett.55.418.
- [79] P. A. Lee, N. Nagaosa, and X.-G. Wen. “Doping a Mott Insulator: Physics of High-Temperature Superconductivity”. *Rev. Mod. Phys.* 78 (2006). DOI: 10.1103/RevModPhys.78.17.
- [80] P. Phillips. “Motttness” (2007). arXiv: cond-mat/0702348.
- [81] G. T. Horowitz, J. E. Santos, and D. Tong. “Optical Conductivity with Holographic Lattices”. *JHEP* 07 (2012). DOI: 10.1007/JHEP07(2012)168.
- [82] G. T. Horowitz, J. E. Santos, and D. Tong. “Further Evidence for Lattice-Induced Scaling”. *JHEP* 11 (2012). DOI: 10.1007/JHEP11(2012)102.
- [83] J. P. Gauntlett, J. Sonner, and T. Wiseman. “Quantum Criticality and Holographic Superconductors in M-theory”. *JHEP* 02 (2010). DOI: 10.1007/JHEP02(2010)060.
- [84] A. Donos and J. P. Gauntlett. “The Thermoelectric Properties of Inhomogeneous Holographic Lattices”. *JHEP* 01 (2015). DOI: 10.1007/JHEP01(2015)035.

-
- [85] B. Withers. “Holographic Checkerboards”. *JHEP* 09 (2014). DOI: 10.1007/JHEP09(2014)102.
- [86] R. A. Davison, K. Schalm, and J. Zaanen. “Holographic Duality and the Resistivity of Strange Metals”. *Phys. Rev. B* 89 (2014). DOI: 10.1103/PhysRevB.89.245116.
- [87] S. A. Hartnoll and D. M. Hofman. “Locally Critical Resistivities from Umklapp Scattering”. *Phys. Rev. Lett.* 108 (2012). DOI: 10.1103/PhysRevLett.108.241601.
- [88] L. V. Delacrétaz, B. Goutéraux, and V. Ziogas. “Damping of Pseudo-Goldstone Fields”. *Phys. Rev. Lett.* 128 (2022). DOI: 10.1103/PhysRevLett.128.141601.
- [89] A. Amoretti, D. Areán, B. Goutéraux, and D. Musso. “Universal Relaxation in a Holographic Metallic Density Wave Phase”. *Phys. Rev. Lett.* 123 (2019). DOI: 10.1103/PhysRevLett.123.211602.
- [90] C. Niu and K.-Y. Kim. “Diffusion and Butterfly Velocity at Finite Density”. *JHEP* 06 (2017). DOI: 10.1007/JHEP06(2017)030.
- [91] D. S. Ageev and I. Y. Aref’eva. “When Things Stop Falling, Chaos Is Suppressed”. *JHEP* 01 (2019). DOI: 10.1007/JHEP01(2019)100.
- [92] N. Sorokhaibam. “Phase Transition and Chaos in Charged SYK Model”. *JHEP* 07 (2020). DOI: 10.1007/JHEP07(2020)055.
- [93] P. Colangelo, F. De Fazio, and N. Losacco. “Chaos in a $Q\bar{Q}$ System at Finite Temperature and Baryon Density”. *Phys. Rev. D* 102 (2020). DOI: 10.1103/PhysRevD.102.074016.
- [94] X. Chen, Y. Gu, and A. Lucas. “Many-Body Quantum Dynamics Slows down at Low Density”. *SciPost Phys.* 9 (2020). DOI: 10.21468/SciPostPhys.9.5.071.
- [95] C. M. Varma, P. B. Littlewood, S. Schmitt-Rink, E. Abrahams, and A. E. Ruckenstein. “Phenomenology of the Normal State of Cu-O High-Temperature Superconductors”. *Phys. Rev. Lett.* 63 (1989). DOI: 10.1103/PhysRevLett.63.1996.
- [96] C. M. Varma. “Colloquium: Linear in Temperature Resistivity and Associated Mysteries Including High Temperature Superconductivity”. *Rev. Mod. Phys.* 92 (2020). DOI: 10.1103/RevModPhys.92.031001.
- [97] M. Mitrano, A. A. Husain, S. Vig, A. Kogar, M. S. Rak, S. I. Rubeck, J. Schmalian, B. Uchoa, J. Schneeloch, R. Zhong, G. D. Gu, and P. Abbamonte. “Anomalous Density Fluctuations in a Strange Metal”. *PNAS* 115 (2018). DOI: 10.1073/pnas.1721495115.
- [98] J. W. Loram, K. A. Mirza, J. M. Wade, J. R. Cooper, and W. Y. Liang. “The Electronic Specific Heat of Cuprate Superconductors”. *Physica C: Superconductivity* 235–240 (1994). DOI: 10.1016/0921-4534(94)91331-5.
- [99] T. Faulkner, N. Iqbal, H. Liu, J. McGreevy, and D. Vegh. “Holographic Non-Fermi-liquid Fixed Points”. *Phil. Trans. Roy. Soc. A* 369 (2011). DOI: 10.1098/rsta.2010.0354.

- [100] A. Krikun. “Numerical Solution of the Boundary Value Problems for Partial Differential Equations. Crash Course for Holographer” (2018). arXiv: 1801.01483 [hep-th].
- [101] M. Headrick, S. Kitchen, and T. Wiseman. “A New Approach to Static Numerical Relativity and Its Application to Kaluza–Klein Black Holes”. *Class. Quant. Grav.* 27 (2010). DOI: 10.1088/0264-9381/27/3/035002.
- [102] A. Adam, S. Kitchen, and T. Wiseman. “A Numerical Approach to Finding General Stationary Vacuum Black Holes”. *Class. Quant. Grav.* 29 (2012). DOI: 10.1088/0264-9381/29/16/165002.
- [103] A. Donos and J. P. Gauntlett. “Thermoelectric DC Conductivities from Black Hole Horizons”. *JHEP* 11 (2014). DOI: 10.1007/JHEP11(2014)081.
- [104] E. Banks, A. Donos, and J. P. Gauntlett. “Thermoelectric DC Conductivities and Stokes Flows on Black Hole Horizons”. *JHEP* 10 (2015). DOI: 10.1007/JHEP10(2015)103.
- [105] A. Donos, J. P. Gauntlett, T. Griffin, and L. Melgar. “DC Conductivity of Magnetised Holographic Matter”. *JHEP* 01 (2016). DOI: 10.1007/JHEP01(2016)113.
- [106] A. Donos, J. P. Gauntlett, T. Griffin, N. Lohitsiri, and L. Melgar. “Holographic DC Conductivity and Onsager Relations”. *JHEP* 07 (2017). DOI: 10.1007/JHEP07(2017)006.
- [107] M. Baggioli and B. Goutéraux. “Colloquium: Hydrodynamics and Holography of Charge Density Wave Phases”. *Rev. Mod. Phys.* 95 (2023). DOI: 10.1103/RevModPhys.95.011001.
- [108] R. A. Davison and B. Goutéraux. “Dissecting Holographic Conductivities”. *JHEP* 09 (2015). DOI: 10.1007/JHEP09(2015)090.
- [109] A. Lucas and S. D. Sarma. “Electronic Hydrodynamics and the Breakdown of the Wiedemann-Franz and Mott Laws in Interacting Metals”. *Phys. Rev. B* 97 (2018). DOI: 10.1103/PhysRevB.97.245128.
- [110] S. A. Hartnoll, R. Mahajan, M. Punk, and S. Sachdev. “Transport near the Ising-nematic Quantum Critical Point of Metals in Two Dimensions”. *Phys. Rev. B* 89 (2014). DOI: 10.1103/PhysRevB.89.155130.
- [111] A. Lucas, S. Sachdev, and K. Schalm. “Scale-Invariant Hyperscaling-Violating Holographic Theories and the Resistivity of Strange Metals with Random-Field Disorder”. *Phys. Rev. D* 89 (2014). DOI: 10.1103/PhysRevD.89.066018.
- [112] J. Erdmenger, B. Herwerth, S. Klug, R. Meyer, and K. Schalm. “S-Wave Superconductivity in Anisotropic Holographic Insulators”. *JHEP* 05 (2015). DOI: 10.1007/JHEP05(2015)094.
- [113] S. Bhattacharyya, V. E. Hubeny, S. Minwalla, and M. Rangamani. “Nonlinear Fluid Dynamics from Gravity”. *JHEP* 02 (2008). DOI: 10.1088/1126-6708/2008/02/045.

-
- [114] A. Lucas. “Conductivity of a Strange Metal: From Holography to Memory Functions”. *JHEP* 03 (2015). DOI: 10.1007/JHEP03(2015)071.
- [115] A. Lucas. “Hydrodynamic Transport in Strongly Coupled Disordered Quantum Field Theories”. *New J. Phys.* 17 (2015). DOI: 10.1088/1367-2630/17/11/113007.
- [116] A. Lucas, J. Crossno, K. C. Fong, P. Kim, and S. Sachdev. “Transport in Inhomogeneous Quantum Critical Fluids and in the Dirac Fluid in Graphene”. *Phys. Rev. B* 93 (2016). DOI: 10.1103/PhysRevB.93.075426.
- [117] A. Donos, J. P. Gauntlett, and V. Ziogas. “Diffusion in Inhomogeneous Media”. *Phys. Rev. D* 96 (2017). DOI: 10.1103/PhysRevD.96.125003.
- [118] Y. Ling, C. Niu, J.-P. Wu, and Z.-Y. Xian. “Holographic Lattice in Einstein-Maxwell-dilaton Gravity”. *JHEP* 11 (2013). DOI: 10.1007/JHEP11(2013)006.
- [119] P. Kovtun. “Lectures on Hydrodynamic Fluctuations in Relativistic Theories”. *J. Phys. A* 45 (2012). DOI: 10.1088/1751-8113/45/47/473001.
- [120] N. Chagnet and K. Schalm. “Hydrodynamics of a relativistic charged fluid in the presence of a periodically modulated chemical potential”. *SciPost Phys.* 16 (2024). DOI: 10.21468/SciPostPhys.16.1.028.
- [121] L. V. Delacrétaz, B. Goutéraux, S. A. Hartnoll, and A. Karlsson. “Theory of Hydrodynamic Transport in Fluctuating Electronic Charge Density Wave States”. *Phys. Rev. B* 96 (2017). DOI: 10.1103/PhysRevB.96.195128.
- [122] A. Amoretti, D. Areán, B. Goutéraux, and D. Musso. “Dc Resistivity of Quantum Critical, Charge Density Wave States from Gauge-Gravity Duality”. *Phys. Rev. Lett.* 120 (2018). DOI: 10.1103/PhysRevLett.120.171603.
- [123] J. Armas and A. Jain. “Hydrodynamics for Charge Density Waves and Their Holographic Duals”. *Phys. Rev. D* 101 (2020). DOI: 10.1103/PhysRevD.101.121901.
- [124] M. Ammon, D. Arean, M. Baggioli, S. Gray, and S. Griener. “Pseudo-Spontaneous U(1) Symmetry Breaking in Hydrodynamics and Holography”. *JHEP* 03 (2022). DOI: 10.1007/JHEP03(2022)015.
- [125] J. Armas, A. Jain, and R. Lier. “Approximate Symmetries, Pseudo-Goldstones, and the Second Law of Thermodynamics”. *Phys. Rev. D* (2022). DOI: 10.1103/PhysRevD.108.086011.
- [126] D. Areán, R. A. Davison, B. Goutéraux, and K. Suzuki. “Hydrodynamic Diffusion and Its Breakdown near AdS₂ Quantum Critical Points”. *Phys. Rev. X* 11 (2021). DOI: 10.1103/PhysRevX.11.031024.
- [127] M. P. Heller, A. Serantes, M. Spalinski, V. Svensson, and B. Withers. “Convergence of Hydrodynamic Modes: Insights from Kinetic Theory and Holography”. *SciPost Phys.* 10 (2021). DOI: 10.21468/SciPostPhys.10.6.123.
- [128] N. Wu, M. Baggioli, and W.-J. Li. “On the Universality of AdS₂ Diffusion Bounds and the Breakdown of Linearized Hydrodynamics”. *JHEP* 05 (2021). DOI: 10.1007/JHEP05(2021)014.

- [129] H.-S. Jeong, K.-Y. Kim, and Y.-W. Sun. “The Breakdown of Magneto-Hydrodynamics near AdS₂ Fixed Point and Energy Diffusion Bound”. *JHEP* 02 (2022). DOI: 10.1007/JHEP02(2022)006.
- [130] Y. Liu and X.-M. Wu. “Breakdown of Hydrodynamics from Holographic Pole Collision”. *JHEP* 01 (2022). DOI: 10.1007/JHEP01(2022)155.
- [131] R. J. Anantua, S. A. Hartnoll, V. L. Martin, and D. M. Ramirez. “The Pauli Exclusion Principle at Strong Coupling: Holographic Matter and Momentum Space”. *JHEP* 03 (2013). DOI: 10.1007/JHEP03(2013)104.
- [132] R. A. Davison and A. Parnachev. “Hydrodynamics of Cold Holographic Matter”. *JHEP* 06 (2013). DOI: 10.1007/JHEP06(2013)100.
- [133] D. Forster. *Hydrodynamic Fluctuations, Broken Symmetry, and Correlation Functions*. CRC Press, 2019. 352 pp. ISBN: 9780429493683.
- [134] M. Blake and A. Donos. “Diffusion and Chaos from near AdS₂ Horizons”. *JHEP* 02 (2017). DOI: 10.1007/JHEP02(2017)013.
- [135] S. Grozdanov, K. Schalm, and V. Scopelliti. “Black Hole Scrambling from Hydrodynamics”. *Phys. Rev. Lett.* 120 (2018). DOI: 10.1103/PhysRevLett.120.231601.
- [136] Y. Ling and Z.-Y. Xian. “Holographic Butterfly Effect and Diffusion in Quantum Critical Region”. *JHEP* 09 (2017). DOI: 10.1007/JHEP09(2017)003.
- [137] D. Ahn, Y. Ahn, H.-S. Jeong, K.-Y. Kim, W.-J. Li, and C. Niu. “Thermal Diffusivity and Butterfly Velocity in Anisotropic Q-Lattice Models”. *JHEP* 01 (2018). DOI: 10.1007/JHEP01(2018)140.
- [138] A. Lucas. “Operator Size at Finite Temperature and Planckian Bounds on Quantum Dynamics”. *Phys. Rev. Lett.* 122 (2019). DOI: 10.1103/PhysRevLett.122.216601.
- [139] B. W. Langley and P. W. Phillips. “Quantum Critical Diffusion and Thermodynamics in Lifshitz Holography”. *Phys. Rev. D* 103 (2021). DOI: 10.1103/PhysRevD.103.026016.
- [140] W. Li, S. Lin, and J. Mei. “Thermal Diffusion and Quantum Chaos in Neutral Magnetized Plasma”. *Phys. Rev. D* 100 (2019). DOI: 10.1103/PhysRevD.100.046012.
- [141] G. A. Inkof, J. M. C. Kupper, J. M. Link, B. Goutéraux, and J. Schmalian. “Quantum Critical Scaling and Holographic Bound for Transport Coefficients near Lifshitz Points”. *JHEP* 11 (2020). DOI: 10.1007/JHEP11(2020)088.
- [142] M. Baggioli and W.-J. Li. “Universal Bounds on Transport in Holographic Systems with Broken Translations”. *SciPost Phys.* 9 (2020). DOI: 10.21468/SciPostPhys.9.1.007.
- [143] H.-S. Jeong, K.-Y. Kim, and Y.-W. Sun. “Bound of Diffusion Constants from Pole-Skipping Points: Spontaneous Symmetry Breaking and Magnetic Field”. *JHEP* 07 (2021). DOI: 10.1007/JHEP07(2021)105.

-
- [144] H.-S. Jeong, K.-Y. Kim, and Y.-W. Sun. “Quasi-Normal Modes of Dyonic Black Holes and Magneto-Hydrodynamics”. *JHEP* 07 (2022). DOI: 10.1007/JHEP07(2022)065.
- [145] A. A. Patel and S. Sachdev. “Quantum Chaos on a Critical Fermi Surface”. *PNAS* 114 (2017). DOI: 10.1073/pnas.1618185114.
- [146] A. A. Patel, D. Chowdhury, S. Sachdev, and B. Swingle. “Quantum Butterfly Effect in Weakly Interacting Diffusive Metals”. *Phys. Rev. X* 7 (2017). DOI: 10.1103/PhysRevX.7.031047.
- [147] Y. Werman, S. A. Kivelson, and E. Berg. “Quantum Chaos in an Electron-Phonon Bad Metal” (2017). arXiv: 1705.07895 [cond-mat.str-el].
- [148] M. Blake and H. Liu. “On Systems of Maximal Quantum Chaos”. *JHEP* 05 (2021). DOI: 10.1007/JHEP05(2021)229.
- [149] A. Lucas and J. Steinberg. “Charge Diffusion and the Butterfly Effect in Striped Holographic Matter”. *JHEP* 10 (2016). DOI: 10.1007/JHEP10(2016)143.
- [150] Y. Gu, A. Lucas, and X.-L. Qi. “Energy Diffusion and the Butterfly Effect in Inhomogeneous Sachdev-Ye-Kitaev Chains”. *SciPost Phys.* 2 (2017). DOI: 10.21468/SciPostPhys.2.3.018.
- [151] R. A. Davison, S. A. Gentle, and B. Goutéraux. “Slow Relaxation and Diffusion in Holographic Quantum Critical Phases”. *Phys. Rev. Lett.* 123 (2019). DOI: 10.1103/PhysRevLett.123.141601.
- [152] H.-K. Wu and J. Sau. “A Classical Model for Sub-Planckian Thermal Diffusivity in Complex Crystals”. *Phys. Rev. B* 103 (2021). DOI: 10.1103/PhysRevB.103.184305.
- [153] J. Maldacena, S. H. Shenker, and D. Stanford. “A Bound on Chaos”. *JHEP* 08 (2016). DOI: 10.1007/JHEP08(2016)106.
- [154] P. Chesler, A. Lucas, and S. Sachdev. “Conformal Field Theories in a Periodic Potential: Results from Holography and Field Theory”. *Phys. Rev. D* 89 (2014). DOI: 10.1103/PhysRevD.89.026005.
- [155] J. A. Sulpizio, L. Ella, A. Rozen, J. Birkbeck, D. J. Perello, D. Dutta, M. Ben-Shalom, T. Taniguchi, K. Watanabe, T. Holder, R. Queiroz, A. Principi, A. Stern, T. Scaffidi, A. K. Geim, and S. Ilani. “Visualizing Poiseuille Flow of Hydrodynamic Electrons”. *Nature* 576 (2019). DOI: 10.1038/s41586-019-1788-9.
- [156] B. Michon, C. Berthod, C. W. Rischau, A. Ataei, L. Chen, S. Komiyama, S. Ono, L. Taillefer, D. van der Marel, and A. Georges. “Reconciling scaling of the optical conductivity of cuprate superconductors with Planckian resistivity and specific heat”. *Nature Communications* 14 (2023). DOI: 10.1038/s41467-023-38762-5.
- [157] A. A. Husain, M. Mitrano, M. S. Rak, S. Rubeck, B. Uchoa, K. March, C. Dwyer, J. Schneeloch, R. Zhong, G. D. Gu, and P. Abbamonte. “Crossover of Charge Fluctuations across the Strange Metal Phase Diagram”. *Phys. Rev. X* 9 (2019). DOI: 10.1103/physrevx.9.041062.

- [158] U. Gran, M. Tornsö, and T. Zingg. “Holographic Plasmons”. *JHEP* 11 (2018). DOI: 10.1007/JHEP11(2018)176.
- [159] E. Mauri and H. T. C. Stoof. “Screening of Coulomb Interactions in Holography”. *JHEP* 04 (2019). DOI: 10.1007/JHEP04(2019)035.
- [160] A. Romero-Bermúdez, A. Krikun, K. Schalm, and J. Zaanen. “Anomalous Attenuation of Plasmons in Strange Metals and Holography”. *Phys. Rev. B* 99 (2019). DOI: 10.1103/PhysRevB.99.235149.
- [161] T. Andrade, A. Krikun, and A. Romero-Bermúdez. “Charge Density Response and Fake Plasmons in Holographic Models with Strong Translation Symmetry Breaking”. *JHEP* 12 (2019). DOI: 10.1007/JHEP12(2019)159.
- [162] E. W. Huang, R. Sheppard, B. Moritz, and T. P. Devereaux. “Strange Metallicity in the Doped Hubbard Model”. *Science* 366 (2019). DOI: 10.1126/science.aau7063.
- [163] S. Xu and B. Swingle. “Scrambling Dynamics and Out-of-Time-Ordered Correlators in Quantum Many-Body Systems”. *PRX Quantum* 5 (2024). DOI: 10.1103/prxquantum.5.010201.
- [164] N. Tsuji and P. Werner. “Out-of-Time-Ordered Correlators of the Hubbard Model: Sachdev-Ye-Kitaev Strange Metal in the Spin-Freezing Crossover Region”. *Phys. Rev. B* 99 (2019). DOI: 10.1103/PhysRevB.99.115132.
- [165] M. Christos, D. G. Joshi, S. Sachdev, and M. Tikhonovskaya. “Critical Metallic Phase in the Overdoped Random T-J Model”. *Proc. Nat. Acad. Sci.* 119 (2022). DOI: 10.1073/pnas.2206921119.
- [166] A. A. Abrikosov and I. M. Khalatnikov. “The Theory of a Fermi Liquid (the Properties of Liquid ^3He at Low Temperatures)”. *Reports on Progress in Physics* 22 (1959). DOI: 10.1088/0034-4885/22/1/310.
- [167] C. Collignon, A. Ataei, A. Gourgout, S. Badoux, M. Lizaire, A. Legros, S. Licciardello, S. Wiedmann, J.-Q. Yan, J.-S. Zhou, Q. Ma, B. D. Gaulin, N. Doiron-Leyraud, and L. Taillefer. “Thermopower across the Phase Diagram of the Cuprate $\text{La}_{1.6-x}\text{Nd}_{0.4}\text{Sr}_x\text{CuO}_4$: Signatures of the Pseudogap and Charge Density Wave Phases”. *Phys. Rev. B* 103 (2021). DOI: 10.1103/PhysRevB.103.155102.
- [168] A. Gourgout, G. Grissonnanche, F. Laliberté, A. Ataei, L. Chen, S. Verret, J.-S. Zhou, J. Mravlje, A. Georges, N. Doiron-Leyraud, and L. Taillefer. “Seebeck Coefficient in a Cuprate Superconductor: Particle-Hole Asymmetry in the Strange Metal Phase and Fermi Surface Transformation in the Pseudogap Phase”. *Phys. Rev. X* 12 (2022). DOI: 10.1103/physrevx.12.011037.
- [169] A. Donos and J. P. Gauntlett. “Minimally Packed Phases in Holography”. *JHEP* 03 (2016). DOI: 10.1007/JHEP03(2016)148.

- [170] N. Chagnet, F. Balm, and K. Schalm. “Quantization and Variational Problem of the Gubser-Rocha Einstein-Maxwell-Dilaton Model, Conformal and Non-Conformal Deformations, and Its Proper Thermodynamics”. *JHEP* 03 (2023). DOI: 10.1007/JHEP03(2023)081.
- [171] S. Balay, W. D. Gropp, L. C. McInnes, and B. F. Smith. “Efficient Management of Parallelism in Object-Oriented Numerical Software Libraries”. *Modern Software Tools for Scientific Computing*. Birkhäuser, 1997, pp. 163–202. ISBN: 9781461219866.
- [172] S. Balay, S. Abhyankar, M. F. Adams, S. Benson, J. Brown, P. Brune, K. Buschelman, E. M. Constantinescu, L. Dalcin, A. Dener, V. Eijkhout, W. D. Gropp, V. Hapla, T. Isaac, P. Jolivet, D. Karpeev, D. Kaushik, M. G. Knepley, F. Kong, S. Kruger, D. A. May, L. C. McInnes, R. T. Mills, L. Mitchell, T. Munson, J. E. Roman, K. Rupp, P. Sanan, J. Sarich, B. F. Smith, S. Zampini, H. Zhang, H. Zhang, and J. Zhang. *PETSc/TAO Users Manual 3.16*. 2021.
- [173] F. Balm. *FlorisBalm/HoloLattices*. Version v0.1.0. Zenodo, 2022. DOI: 10.5281/zenodo.7284816.
- [174] F. Balm. *FlorisBalm/HoloLattices-2D*. Version v0.0.1. Zenodo, 2022. DOI: 10.5281/zenodo.7305480.
- [175] R. A. Davison, B. Goutéraux, and S. A. Hartnoll. “Incoherent Transport in Clean Quantum Critical Metals”. *JHEP* 10 (2015). DOI: 10.1007/JHEP10(2015)112.
- [176] L. Brillouin. *Wave Propagation in Periodic Structures: Electric Filters and Crystal Lattices*. Dover Books on Engineering and Engineering Physics. McGraw-Hill Book Company, Incorporated, 1946.
- [177] C. Elachi. “Waves in active and passive periodic structures: A review”. *Proceedings of the IEEE* 64 (1976). DOI: 10.1109/PROC.1976.10409.
- [178] L. Schächter. *Beam-Wave Interaction in Periodic and Quasi-Periodic Structures*. Particle Acceleration and Detection. Springer Berlin Heidelberg, 2013. ISBN: 9783662033982.
- [179] *Acoustic Waves in Periodic Structures, Metamaterials, and Porous Media*. Springer International Publishing, 2021. ISBN: 9783030843007.
- [180] A. Lucas and S. Sachdev. “Memory Matrix Theory of Magnetotransport in Strange Metals”. *Phys. Rev. B* 91 (2015). DOI: 10.1103/PhysRevB.91.195122.
- [181] A. Lucas and K. C. Fong. “Hydrodynamics of Electrons in Graphene”. *J. Phys. Condens. Matter* 30 (2018). DOI: 10.1088/1361-648X/aaa274.
- [182] A. Aharon-Steinberg, T. Völkl, A. Kaplan, A. K. Pariari, I. Roy, T. Holder, Y. Wolf, A. Y. Meltzer, Y. Myasoedov, M. E. Huber, B. Yan, G. Falkovich, L. S. Levitov, M. Hücker, and E. Zeldov. “Direct Observation of Vortices in an Electron Fluid”. *Nature* 607 (2022). DOI: 10.1038/s41586-022-04794-y.
- [183] L. Fritz and T. Scaffidi. “Hydrodynamic Electronic Transport” (2023). arXiv: 2303.14205 [cond-mat].

- [184] F. Balm, N. Chagnet, S. Arend, J. Aretz, K. Grosvenor, M. Janse, O. Moors, J. Post, V. Ohanesjan, D. Rodriguez-Fernandez, K. Schalm, and J. Zaanen. “T-Linear Resistivity, Optical Conductivity and Planckian Transport for a Holographic Local Quantum Critical Metal in a Periodic Potential”. *Phys. Rev. B* 108 (2023). DOI: 10.1103/PhysRevB.108.125145.
- [185] V. Scopelliti, K. Schalm, and A. Lucas. “Hydrodynamic Charge and Heat Transport on Inhomogeneous Curved Spaces”. *Phys. Rev. B* 96 (2017). DOI: 10.1103/PhysRevB.96.075150.
- [186] K. Jensen, M. Kaminski, P. Kovtun, R. Meyer, A. Ritz, and A. Yarom. “Parity-Violating Hydrodynamics in 2+1 Dimensions”. *JHEP* 05 (2012). DOI: 10.1007/JHEP05(2012)102.
- [187] K. Pongsangangan, T. Ludwig, H. T. C. Stoof, and L. Fritz. *Hydrodynamics of Charged Two-Dimensional Dirac Systems II: The Role of Collective Modes*. 2022. DOI: 10.48550/arXiv.2206.09694. arXiv: 2206.09694 [cond-mat].
- [188] K. Pongsangangan, T. Ludwig, H. T. C. Stoof, and L. Fritz. “Hydrodynamics of Charged Two-Dimensional Dirac Systems I: Thermo-Electric Transport”. *Physical Review B* 106 (2022). DOI: 10.1103/PhysRevB.106.205126.
- [189] L. P. Kadanoff and P. C. Martin. “Hydrodynamic equations and correlation functions”. *Annals of Physics* 24 (1963). DOI: 10.1016/0003-4916(63)90078-2.
- [190] T. Andrade and A. Krikun. “Commensurate lock-in in holographic non-homogeneous lattices”. *JHEP* 03 (2017). DOI: 10.1007/JHEP03(2017)168
- [191] J. Casalderrey-Solana, H. Liu, D. Mateos, K. Rajagopal, and U. A. Wiedemann. *Gauge/String Duality, Hot QCD and Heavy Ion Collisions*. Cambridge University Press, 2014. ISBN: 9781107022461.
- [192] P. K. Kovtun and A. O. Starinets. “Quasinormal modes and holography”. *Phys. Rev. D* 72 (2005). DOI: 10.1103/PhysRevD.72.086009.
- [193] M. Edalati, J. I. Jottar, and R. G. Leigh. “Shear Modes, Criticality and Extremal Black Holes”. *JHEP* 04 (2010). DOI: 10.1007/JHEP04(2010)075.
- [194] M. Edalati, J. I. Jottar, and R. G. Leigh. “Holography and the sound of criticality”. *JHEP* 10 (2010). DOI: 10.1007/JHEP10(2010)058.
- [195] D. K. Brattan and S. A. Gentle. “Shear channel correlators from hot charged black holes”. *JHEP* 04 (2011). DOI: 10.1007/JHEP04(2011)082.
- [196] J. Hwang, T. Timusk, and G. Gu. “Doping dependent optical properties of $\text{Bi}_2\text{Sr}_2\text{CaCu}_2\text{O}_{8+\delta}$ ”. *Journal of Physics: Condensed Matter* 19 (2007).
- [197] N. Abbasi and S. Tahery. “Complexified Quasinormal Modes and the Pole-Skipping in a Holographic System at Finite Chemical Potential”. *JHEP* 2020 (2020). DOI: 10.1007/JHEP10(2020)076.
- [198] N. Abbasi, M. Kaminski, and O. Tavakol. “Ultraviolet-Regulated Theory of Non-Linear Diffusion” (2022). arXiv: 2212.11499 [hep-th].

-
- [199] P. K. Kovtun, D. T. Son, and A. O. Starinets. “Viscosity in Strongly Interacting Quantum Field Theories from Black Hole Physics”. *Phys. Rev. Lett.* 94 (2005). DOI: 10.1103/PhysRevLett.94.111601.
- [200] Q. Si, S. Rabello, K. Ingersent, and J. L. Smith. “Locally critical quantum phase transitions in strongly correlated metals”. *Nature* 413 (2001).
- [201] K. Goldstein, S. Kachru, S. Prakash, and S. P. Trivedi. “Holography of Charged Dilaton Black Holes”. *JHEP* 08 (2010). DOI: 10.1007/JHEP08(2010)078.
- [202] B. S. Kim. “Holographic Renormalization of Einstein-Maxwell-Dilaton Theories”. *JHEP* 11 (2016). DOI: 10.1007/JHEP11(2016)044.
- [203] M. M. Caldarelli, A. Christodoulou, I. Papadimitriou, and K. Skenderis. “Phases of Planar AdS Black Holes with Axionic Charge”. *JHEP* 04 (2017). DOI: 10.1007/JHEP04(2017)001.
- [204] E. Witten. “Multitrace Operators, Boundary Conditions, and AdS / CFT Correspondence” (2001). arXiv: hep-th/0112258.
- [205] W. Mück. “An Improved Correspondence Formula for AdS/CFT with Multi-Trace Operators”. *Phys. Lett. B* 531 (2002). DOI: 10.1016/S0370-2693(02)01487-9.
- [206] L. Li. “On Thermodynamics of AdS Black Holes with Scalar Hair”. *Phys. Lett. B* 815 (2021). DOI: 10.1016/j.physletb.2021.136123.
- [207] I. Papadimitriou. “Multi-Trace Deformations in AdS/CFT: Exploring the Vacuum Structure of the Deformed CFT”. *JHEP* 05 (2007). DOI: 10.1088/1126-6708/2007/05/075.
- [208] V. Balasubramanian and P. Kraus. “A Stress Tensor for Anti-de Sitter Gravity”. *Commun. Math. Phys.* 208 (1999). DOI: 10.1007/s002200050764.
- [209] L. Vecchi. “Multitrace Deformations, Gamow States, and Stability of AdS/CFT”. *JHEP* 04 (2011). DOI: 10.1007/JHEP04(2011)056.
- [210] A. Bernamonti and B. Craps. “D-Brane Potentials from Multi-Trace Deformations in AdS/CFT”. *JHEP* 08 (2009). DOI: 10.1088/1126-6708/2009/08/112.
- [211] J. Ren. “Analytic Solutions of Neutral Hyperbolic Black Holes with Scalar Hair”. *Phys. Rev. D* 106 (2022). DOI: 10.1103/PhysRevD.106.086023.
- [212] E. Dyer and K. Hinterbichler. “Boundary Terms, Variational Principles, and Higher Derivative Modified Gravity”. *Phys. Rev. D* 79 (2009). DOI: 10.1103/PhysRevD.79.024028.
- [213] L. Huijse and S. Sachdev. “Fermi Surfaces and Gauge-Gravity Duality”. *Phys. Rev. D* 84 (2011). DOI: 10.1103/PhysRevD.84.026001.
- [214] H. Liu, J. McGreevy, and D. Vegh. “Non-Fermi Liquids from Holography”. *Phys. Rev. D* 83 (2011). DOI: 10.1103/PhysRevD.83.065029.
- [215] M. Cubrovic, J. Zaanen, and K. Schalm. “String Theory, Quantum Phase Transitions and the Emergent Fermi-Liquid”. *Science* 325 (2009). DOI: 10.1126/science.1174962.

- [216] V. G. M. Puletti, S. Nowling, L. Thorlacius, and T. Zingg. “Holographic Metals at Finite Temperature”. *JHEP* 01 (2011). DOI: 10.1007/JHEP01(2011)117.
- [217] G. T. Horowitz and M. M. Roberts. “Zero Temperature Limit of Holographic Superconductors”. *JHEP* 11 (2009). DOI: 10.1088/1126-6708/2009/11/015.
- [218] S. S. Gubser and F. D. Rocha. “The Gravity Dual to a Quantum Critical Point with Spontaneous Symmetry Breaking”. *Phys. Rev. Lett.* 102 (2009). DOI: 10.1103/PhysRevLett.102.061601.
- [219] C. P. Herzog. “A Holographic Prediction of the Deconfinement Temperature”. *Phys. Rev. Lett.* 98 (2007). DOI: 10.1103/PhysRevLett.98.091601.
- [220] G. F. de Teramond and S. J. Brodsky. “Excited Baryons in Holographic QCD”. *AIP Conf. Proc.* 1432 (2012). DOI: 10.1063/1.3701207.
- [221] A. Karch, E. Katz, D. T. Son, and M. A. Stephanov. “Linear Confinement and AdS/QCD”. *Phys. Rev. D* 74 (2006). DOI: 10.1103/PhysRevD.74.015005.
- [222] Z. Fang, D. Li, and Y.-L. Wu. “IR-improved Soft-Wall AdS/QCD Model for Baryons”. *Phys. Lett. B* 754 (2016). DOI: 10.1016/j.physletb.2016.01.045.
- [223] N. Iizuka, N. Kundu, P. Narayan, and S. P. Trivedi. “Holographic Fermi and Non-Fermi Liquids with Transitions in Dilaton Gravity”. *JHEP* 01 (2012). DOI: 10.1007/JHEP01(2012)094.
- [224] L. D. Landau and E. M. Lifshitz. *Statistical Physics, Part 2: Theory of the Condensed State*. Fizmatlit, 2004. ISBN: 5020138509.
- [225] S. S. Gubser, F. D. Rocha, and P. Talavera. “Normalizable Fermion Modes in a Holographic Superconductor”. *JHEP* 10 (2010). DOI: 10.1007/JHEP10(2010)087.
- [226] F. Denef, S. A. Hartnoll, and S. Sachdev. “Quantum Oscillations and Black Hole Ringing”. *Phys. Rev. D* 80 (2009). DOI: 10.1103/PhysRevD.80.126016.
- [227] K. Hashimoto and N. Iizuka. “A Comment on Holographic Luttinger Theorem”. *JHEP* 07 (2012). DOI: 10.1007/JHEP07(2012)064.
- [228] N. Iqbal and H. Liu. “Real-Time Response in AdS/CFT with Application to Spinors”. *Fortsch. Phys.* 57 (2009). DOI: 10.1002/prop.200900057.
- [229] G. Horowitz, A. Lawrence, and E. Silverstein. “Insightful D-branes”. *JHEP* 07 (2009). DOI: 10.1088/1126-6708/2009/07/057.
- [230] J. Watrous. “Quantum Computational Complexity” (2008). arXiv: 0804.3401 [quant-ph].
- [231] S. Aaronson. “The Complexity of Quantum States and Transformations: From Quantum Money to Black Holes” (2016). arXiv: 1607.05256 [quant-ph].
- [232] L. Susskind. “Three Lectures on Complexity and Black Holes”. SpringerBriefs in Physics. Springer, 2020. ISBN: 9783030451097. DOI: 10.1007/978-3-030-45109-7. arXiv: 1810.11563 [hep-th].

-
- [233] L. Susskind. “Computational Complexity and Black Hole Horizons”. *Fortsch. Phys.* 64 (2016). [Addendum: *Fortsch.Phys.* 64, 44–48 (2016)]. DOI: 10.1002/prop.201500092.
- [234] A. R. Brown, D. A. Roberts, L. Susskind, B. Swingle, and Y. Zhao. “Complexity, Action, and Black Holes”. *Phys. Rev. D* 93 (2016). DOI: 10.1103/PhysRevD.93.086006.
- [235] A. R. Brown, D. A. Roberts, L. Susskind, B. Swingle, and Y. Zhao. “Complexity Equals Action”. *Phys. Rev. Lett.* 116 (2016). DOI: 10.1103/PhysRevLett.116.191301.
- [236] D. Carmi, S. Chapman, H. Marrochio, R. C. Myers, and S. Sugishita. “On the Time Dependence of Holographic Complexity”. *JHEP* 11 (2017). DOI: 10.1007/JHEP11(2017)188.
- [237] D. Stanford and L. Susskind. “Complexity and Shock Wave Geometries”. *Phys. Rev. D* 90 (2014). DOI: 10.1103/PhysRevD.90.126007.
- [238] S. Chapman, H. Marrochio, and R. C. Myers. “Holographic Complexity in Vaidya Spacetimes. Part I”. *JHEP* 06 (2018). DOI: 10.1007/JHEP06(2018)046.
- [239] S. Chapman, H. Marrochio, and R. C. Myers. “Holographic Complexity in Vaidya Spacetimes. Part II”. *JHEP* 06 (2018). DOI: 10.1007/JHEP06(2018)114.
- [240] R. Jefferson and R. C. Myers. “Circuit Complexity in Quantum Field Theory”. *JHEP* 10 (2017). DOI: 10.1007/JHEP10(2017)107.
- [241] S. Chapman, M. P. Heller, H. Marrochio, and F. Pastawski. “Towards Complexity for Quantum Field Theory States”. *Phys. Rev. Lett.* 120 (2018). DOI: 10.1103/PhysRevLett.120.121602.
- [242] R. Khan, C. Krishnan, and S. Sharma. “Circuit Complexity in Fermionic Field Theory”. *Phys. Rev. D* 98 (2018). DOI: 10.1103/PhysRevD.98.126001.
- [243] L. Hackl and R. C. Myers. “Circuit Complexity for Free Fermions”. *JHEP* 07 (2018). DOI: 10.1007/JHEP07(2018)139.
- [244] S. Chapman, J. Eisert, L. Hackl, M. P. Heller, R. Jefferson, H. Marrochio, and R. C. Myers. “Complexity and Entanglement for Thermofield Double States”. *SciPost Phys.* 6 (2019). DOI: 10.21468/SciPostPhys.6.3.034.
- [245] S. Chapman and H. Z. Chen. “Complexity for Charged Thermofield Double States”. *JHEP* 02 (2021). DOI: 10.1007/JHEP02(2021)187.
- [246] A. Bhattacharyya, A. Shekar, and A. Sinha. “Circuit Complexity in Interacting QFTs and RG Flows”. *JHEP* 10 (2018). DOI: 10.1007/JHEP10(2018)140.
- [247] P. Caputa and J. M. Magan. “Quantum Computation as Gravity”. *Phys. Rev. Lett.* 122 (2019). DOI: 10.1103/PhysRevLett.122.231302.
- [248] J. Erdmenger, M. Gerbershagen, and A.-L. Weigel. “Complexity Measures from Geometric Actions on Virasoro and Kac-Moody Orbits”. *JHEP* 11 (2020). DOI: 10.1007/JHEP11(2020)003.

- [249] M. Flory and M. P. Heller. “Geometry of Complexity in Conformal Field Theory”. *Phys. Rev. Res.* 2 (2020). DOI: 10.1103/PhysRevResearch.2.043438.
- [250] M. Flory and M. P. Heller. “Conformal Field Theory Complexity from Euler-Arnold Equations”. *JHEP* 12 (2020). DOI: 10.1007/JHEP12(2020)091.
- [251] P. Bueno, J. M. Magan, and C. S. Shahbazi. “Complexity Measures in QFT and Constrained Geometric Actions”. *JHEP* 09 (2021). DOI: 10.1007/JHEP09(2021)200.
- [252] S. Chapman, H. Marrochio, and R. C. Myers. “Complexity of Formation in Holography”. *JHEP* 01 (2017). DOI: 10.1007/JHEP01(2017)062.
- [253] S. Chapman, D. Ge, and G. Policastro. “Holographic Complexity for Defects Distinguishes Action from Volume”. *JHEP* 05 (2019). DOI: 10.1007/JHEP05(2019)049.
- [254] Y. Sato and K. Watanabe. “Does Boundary Distinguish Complexities?” *JHEP* 11 (2019). DOI: 10.1007/JHEP11(2019)132.
- [255] M. R. Dowling and M. A. Nielsen. “The Geometry of Quantum Computation”. *Quantum Information & Computation* 8 (2008). DOI: 10.26421/QIC8.10-1.
- [256] J. Anandan and Y. Aharonov. “Geometry of Quantum Evolution”. *Phys. Rev. Lett.* 65 (1990). DOI: 10.1103/PhysRevLett.65.1697.
- [257] S. Lloyd. “Ultimate Physical Limits to Computation”. *Nature* 406 (2000). DOI: 10.1038/35023282.
- [258] G. W. Gibbons. “Holography and the Future Tube”. *Class. Quant. Grav.* 17 (2000). DOI: 10.1088/0264-9381/17/5/316.
- [259] L. Andrianopoli, S. Ferrara, M. A. Lledo, and O. Macia. “Integration of Massive States as Contractions of Non Linear Sigma-Models”. *J. Math. Phys.* 46 (2005). DOI: 10.1063/1.1960719.
- [260] B. Czech, L. Lamprou, S. McCandlish, and J. Sully. “Integral Geometry and Holography”. *JHEP* 10 (2015). DOI: 10.1007/JHEP10(2015)175.
- [261] J. de Boer, M. P. Heller, R. C. Myers, and Y. Neiman. “Holographic de Sitter Geometry from Entanglement in Conformal Field Theory”. *Phys. Rev. Lett.* 116 (2016). DOI: 10.1103/PhysRevLett.116.061602.
- [262] B. Czech, L. Lamprou, S. McCandlish, B. Mosk, and J. Sully. “A Stereoscopic Look into the Bulk”. *JHEP* 07 (2016). DOI: 10.1007/JHEP07(2016)129.
- [263] J. de Boer, F. M. Haehl, M. P. Heller, and R. C. Myers. “Entanglement, Holography and Causal Diamonds”. *JHEP* 08 (2016). DOI: 10.1007/JHEP08(2016)162.
- [264] R. F. Penna and C. Zukowski. “Kinematic Space and the Orbit Method”. *JHEP* 07 (2019). DOI: 10.1007/JHEP07(2019)045.
- [265] J. Gallier and J. Quaintance. *Differential Geometry and Lie Groups*. Springer, 2019. ISBN: 9783030460402.

- [266] S. Helgason. *Differential Geometry, Lie Groups, and Symmetric Spaces*. Elsevier Science, 1979. ISBN: 9780080873961.
- [267] B. O'Neill. *Semi-Riemannian Geometry with Applications to Relativity*. Elsevier Science, 1983. ISBN: 9780080570570.
- [268] B. Oblak. "Berry Phases on Virasoro Orbits". *JHEP* 10 (2017). DOI: 10.1007/JHEP10(2017)114.
- [269] I. Akal. "Reflections on Virasoro Circuit Complexity and Berry Phase". *Phys. Rev. D* 105 (2022). DOI: 10.1103/PhysRevD.105.025012.
- [270] S. Rychkov. *EPFL Lectures on Conformal Field Theory in $D \geq 3$ Dimensions*. 2017. ISBN: 9783319436265.
- [271] E. Witten. "Coadjoint Orbits of the Virasoro Group". *Commun. Math. Phys.* 114 (1988). DOI: 10.1007/BF01218287.
- [272] A. A. Kirillov. *Lectures on the orbit method*. en. Graduate studies in mathematics. American Mathematical Society, 2004. ISBN: 0821835300.
- [273] A. Alekseev and S. Shatashvili. "Path Integral Quantization of the Coadjoint Orbits of the Virasoro Group and 2-d Gravity". *Nucl. Phys. B* 323 (1989). DOI: 10.1016/0550-3213(89)90130-2.
- [274] A. Alekseev and S. L. Shatashvili. "Coadjoint Orbits, Cocycles and Gravitational Wess-Zumino". *Reviews in Mathematical Physics* 30 (2018). DOI: 10.1142/9789813233867_0007.
- [275] W. Taylor. "Coadjoint Orbits and Conformal Field Theory". PhD Thesis. University of California, Berkeley, 1993. DOI: 10.48550/arXiv.hep-th/9310040.
- [276] A. M. Perelomov. "Coherent States for Arbitrary Lie Group". *Commun. Math. Phys.* 26 (1972).
- [277] R. Gilmore. "On the Properties of Coherent States". *Revista Mexicana de Física* 23 (1974).
- [278] L. G. Yaffe. "Large N Limits as Classical Mechanics". *Rev. Mod. Phys.* 54 (1982). DOI: 10.1103/RevModPhys.54.407.
- [279] J. P. Provost and G. Vallee. "Riemannian Structure on Manifolds of Quantum States". *Commun. Math. Phys.* 76 (1980). DOI: 10.1007/BF02193559.
- [280] D. J. Rowe, G. Rosensteel, and R. Gilmore. "Vector Coherent State Representation Theory". *J. Math. Phys.* 26 (1985). DOI: 10.1063/1.526702.
- [281] D. J. Rowe, R. Le Blanc, and K. T. Hecht. "Vector Coherent State Theory and Its Application to the Orthogonal Groups". *J. Math. Phys.* 29 (1988). DOI: 10.1063/1.528066.
- [282] D. J. Rowe. "Vector Coherent State Representations and Their Inner Products". *J. Phys. A* 45 (2012). DOI: 10.1088/1751-8113/45/24/244003.

- [283] S. D. Bartlett, D. J. Rowe, and J. Repka. “Vector Coherent State Representations, Induced Representations and Geometric Quantization: II. Vector Coherent State Representations”. *J. Phys. A: Math. Gen.* 35 (2002). DOI: 10.1088/0305-4470/35/27/307.
- [284] H. Dorn and G. Jorjadze. “On Particle Dynamics in AdS_{N+1} Space-Time”. *Fortsch. Phys.* 53 (2005). DOI: 10.1002/prop.200510208.
- [285] M. Miyaji, S. Ryu, T. Takayanagi, and X. Wen. “Boundary States as Holographic Duals of Trivial Spacetimes”. *JHEP* 05 (2015). DOI: 10.1007/JHEP05(2015)152.
- [286] Z. Fu, A. Maloney, D. Marolf, H. Maxfield, and Z. Wang. “Holographic Complexity Is Nonlocal”. *JHEP* 02 (2018). DOI: 10.1007/JHEP02(2018)072.
- [287] C. A. Agón, M. Headrick, and B. Swingle. “Subsystem Complexity and Holography”. *JHEP* 02 (2019). DOI: 10.1007/JHEP02(2019)145.
- [288] P. Braccia, A. L. Cotrone, and E. Tonni. “Complexity in the Presence of a Boundary”. *JHEP* 02 (2020). DOI: 10.1007/JHEP02(2020)051.
- [289] P. Caputa, N. Kundu, M. Miyaji, T. Takayanagi, and K. Watanabe. “Liouville Action as Path-Integral Complexity: From Continuous Tensor Networks to AdS/CFT”. *JHEP* 11 (2017). DOI: 10.1007/JHEP11(2017)097.
- [290] H. A. Camargo, M. P. Heller, R. Jefferson, and J. Knaute. “Path Integral Optimization as Circuit Complexity”. *Phys. Rev. Lett.* 123 (2019). DOI: 10.1103/PhysRevLett.123.011601.
- [291] A. Milsted and G. Vidal. “Tensor Networks as Path Integral Geometry” (2018). arXiv: 1807.02501 [cond-mat.str-el].
- [292] A. Milsted and G. Vidal. “Geometric Interpretation of the Multi-Scale Entanglement Renormalization Ansatz” (2018). arXiv: 1812.00529 [hep-th].
- [293] B. Czech. “Einstein Equations from Varying Complexity”. *Phys. Rev. Lett.* 120 (2018). DOI: 10.1103/PhysRevLett.120.031601.
- [294] A. R. Chandra, J. de Boer, M. Flory, M. P. Heller, S. Hörtnner, and A. Rolph. “Spacetime as a Quantum Circuit”. *JHEP* 21 (2021). DOI: 10.1007/JHEP04(2021)207.
- [295] T. Levy and Y. Oz. “Liouville Conformal Field Theories in Higher Dimensions”. *JHEP* 06 (2018). DOI: 10.1007/JHEP06(2018)119.
- [296] D. Marolf, O. Parrikar, C. Rabideau, A. I. Rad, and M. Van Raamsdonk. “From Euclidean Sources to Lorentzian Spacetimes in Holographic Conformal Field Theories”. *JHEP* 06 (2018). DOI: 10.1007/JHEP06(2018)077.
- [297] A. Belin, A. Lewkowycz, and G. Sárosi. “The Boundary Dual of the Bulk Symplectic Form”. *Phys. Lett. B* 789 (2019). DOI: 10.1016/j.physletb.2018.10.071.
- [298] A. Belin, A. Lewkowycz, and G. Sarosi. “Complexity and the Bulk Volume, a New York Time Story”. *JHEP* 03 (2019). DOI: 10.1007/JHEP03(2019)044.

-
- [299] M. Miyaji, T. Numasawa, N. Shiba, T. Takayanagi, and K. Watanabe. “Gravity Dual of Quantum Information Metric”. *Phys. Rev. Lett.* 115 (2015). DOI: 10.1103/PhysRevLett.115.261602.
- [300] R. Abt, J. Erdmenger, M. Gerbershagen, C. M. Melby-Thompson, and C. Northe. “Holographic Subregion Complexity from Kinematic Space”. *JHEP* 01 (2019). DOI: 10.1007/JHEP01(2019)012.
- [301] B. Czech, L. Lamprou, S. McCandlish, and J. Sully. “Modular Berry Connection for Entangled Subregions in AdS/CFT”. *Phys. Rev. Lett.* 120 (2018). DOI: 10.1103/PhysRevLett.120.091601.
- [302] B. Czech, J. De Boer, D. Ge, and L. Lamprou. “A Modular Sewing Kit for Entanglement Wedges”. *JHEP* 11 (2019). DOI: 10.1007/JHEP11(2019)094.
- [303] L. Campos Venuti and P. Zanardi. “Quantum Critical Scaling of the Geometric Tensors”. *Phys. Rev. Lett.* 99 (2007). DOI: 10.1103/PhysRevLett.99.095701.
- [304] M. Kolodrubetz, V. Gritsev, and A. Polkovnikov. “Classifying and Measuring the Geometry of the Quantum Ground State Manifold”. *Phys. Rev. B* 88 (2013). DOI: 10.1103/PhysRevB.88.064304.
- [305] V. Gritsev and A. Polkovnikov. “Integrable Floquet Dynamics”. *SciPost Phys.* 2 (2017). DOI: 10.21468/SciPostPhys.2.3.021.
- [306] G. Camilo and D. Teixeira. “Complexity and Floquet Dynamics: Non-Equilibrium Ising Phase Transitions”. *Phys. Rev. B* 102 (2020). DOI: 10.1103/PhysRevB.102.174304.
- [307] F. Liu, S. Whitsitt, J. B. Curtis, R. Lundgren, P. Titum, Z.-C. Yang, J. R. Garrison, and A. V. Gorshkov. “Circuit Complexity across a Topological Phase Transition”. *Phys. Rev. Res.* 2 (2020). DOI: 10.1103/PhysRevResearch.2.013323.
- [308] D. Mazac. *Bootstrap Introduction*. Bootstrap Collaboration. 2018. URL: <https://youtu.be/pCh3Gznf0vY>.
- [309] S. Minwalla. “Restrictions imposed by superconformal invariance on quantum field theories”. *Adv. Theor. Math. Phys.* 2 (1998). DOI: 10.4310/ATMP.1998.v2.n4.a4.
- [310] M. Luscher and G. Mack. “Global Conformal Invariance in Quantum Field Theory”. *Commun. Math. Phys.* 41 (1975). DOI: 10.1007/BF01608988.
- [311] W.-M. Zhang, D. H. Feng, and R. Gilmore. “Coherent States: Theory and Some Applications”. *Rev. Mod. Phys.* 62 (1990). DOI: 10.1103/RevModPhys.62.867.
- [312] A. Klimov and S. Chumakov. *A Group-Theoretical Approach to Quantum Optics: Models of Atom-Field Interactions*. Wiley, 2009. ISBN: 9783527624010.
- [313] P. Feinsilver, J. Kocik, and M. Giering. “Canonical Variables and Analysis on $so(n, 2)$ ”. *Journal of Physics A: Mathematical and General* 34 (2001).
- [314] V. K. Dobrev. *Noncompact Semisimple Lie Algebras and Groups*. De Gruyter, 2016. ISBN: 9783110435429.

- [315] J. Penedones, E. Trevisani, and M. Yamazaki. “Recursion Relations for Conformal Blocks”. *JHEP* 09 (2016). DOI: 10.1007/JHEP09(2016)070.
- [316] M. Yamazaki. “Comments on Determinant Formulas for General CFTs”. *JHEP* 10 (2016). DOI: 10.1007/JHEP10(2016)035.
- [317] D. Carmi, R. C. Myers, and P. Rath. “Comments on Holographic Complexity”. *JHEP* 03 (2017). DOI: 10.1007/JHEP03(2017)118.
- [318] A. Reynolds and S. F. Ross. “Divergences in Holographic Complexity”. *Class. Quant. Grav.* 34 (2017). DOI: 10.1088/1361-6382/aa6925.

Summary

By their very nature, strongly coupled systems are both some of the most interesting while simultaneously being some of the least understood systems in physics. Without the help of perturbation theory and other common tools, physicists have had to be creative in order to probe and learn more about strongly coupled systems. To that end, the AdS/CFT correspondence, which is at the heart of this thesis, has shown tremendous promise and success in helping elucidate the physics of various systems such as the quark gluon plasma or strongly correlated electronic metals found for instance in cuprate high- T_c superconductors.

This thesis brings about new numerical insights on this type of system in chapter 2, using complex black hole models and high-performance computing. The results of such simulations demonstrate a rich variety of behaviors; the black holes with a spatially undulating horizon are shown to behave like a relativistic fluid in a periodic potential for which a universal effective hydrodynamic theory is presented in chapter 3. The extent to which this model can explain the transport properties of such strongly-coupled system dual to these black holes is an indicator that electrons in cuprates might behave more like a fluid than like billiard balls in a traditional metal. Such black hole models require extreme care and analysis in order to be properly defined as we discuss in chapter 4.

As a general mathematical duality, AdS/CFT can be applied to a wide range of theories and models. Among the most intriguing questions it can help answer, the problem of finding a configuration of fermions in a stable gravitational and electromagnetic potential in AdS space has remained elusive for the better part of a decade. In chapter 5, we improve on the previous models and make some significant progress towards a final resolution to this question. Another recent burning question has been to understand the entanglement patterns of such strongly coupled systems, as it has been theorized that measuring their long-range entanglement properties could be a meaningful probe of their unique physics. One such measure which has garnered a lot of interest is complexity, a continuum generalization of the ubiquitous computer science notion. In chapter 6, we expand on the proper definition of such notion for conformal field theories and bring about a direct connection to the geometry of the dual Anti-de Sitter spacetime.

The common theme between these results is the predictive power of seemingly unrelated computations of gravitational solutions when interpreted through the lens of a dual lower-dimensional strongly coupled quantum system. These *holographic* theories provide generic examples of computationally tractable strongly-interacting systems which are otherwise unreachable with conventional methods.

Samenvatting

Inherent aan hun aard zijn sterk gekoppelde systemen zowel de meest interessante als tegelijkertijd de minst begrepen systemen in de natuurkunde. Zonder de hulp van de storingstheorie en andere veelgebruikte hulpmiddelen hebben natuurkundigen creatief moeten zijn om deze systemen te onderzoeken en er meer over te leren. Met dat doel voor ogen heeft de AdS/CFT-correspondentie, die de kern vormt van dit proefschrift, enorme beloftes en succes getoond bij het helpen ophelderen van de fysica van verschillende sterk gekoppelde systemen, zoals quark-gluon-plasma's of sterk gecorreleerde elektronische metalen die bijvoorbeeld worden gevonden in hoge temperatuur supergeleidende cupraten.

Dit proefschrift brengt nieuwe numerieke inzichten over dit type systeem naar voren in hoofdstuk 2, waarbij gebruik wordt gemaakt van complexe modellen van zwarte gaten en high-performance computing. De resultaten van dergelijke simulaties laten een rijke verscheidenheid aan gedrag zien; zwarte gaten met een ruimtelijke op-en-neer dijende horizon blijken zich te gedragen als een relativistische vloeistof in een periodiek potentiaal waarvoor in hoofdstuk 3 een universeel effectieve hydrodynamische theorie wordt gepresenteerd. De mate waarin dit model de transporteigenschappen van een dergelijk sterk gekoppeld systeem dual aan deze zwarte gaten kan verklaren, is een indicator dat elektronen in cupraten zich misschien meer als een vloeistof gedragen dan als biljartballen in een traditioneel metaal. Dergelijke modellen voor zwarte gaten vereisen uiterste zorgvuldigheid en analyse om goed te kunnen worden gedefinieerd, zoals we in hoofdstuk 4 bespreken.

Als algemene wiskundige dualiteit kan AdS/CFT worden toegepast op een breed scala aan theorieën en modellen. Eén van de meest intrigerende vragen die het kan helpen beantwoorden, is het probleem van het vinden van een configuratie van fermionen in een stabiele zwaartekracht- en elektromagnetische potentiaal in de AdS-ruimte, die al ruim tien jaar ongreepbaar is gebleven. In hoofdstuk 5 verbeteren we de voorgaande modellen en laten we aanzienlijke vooruitgang zien in de richting van een definitieve oplossing voor deze vraag. Een andere recente brandende vraag is het begrijpen van de verstrengelingspatronen van dergelijke sterk gekoppelde systemen, omdat er wordt gespeculeerd dat het meten van hun verstrengelingseigenschappen over lange afstanden een betekenisvolle toets zou kunnen zijn van hun unieke fysica.

Eén van die maatstaven, die veel belangstelling heeft gewekt, is complexiteit, een continuüm-generalisatie van een welbekend computerwetenschappelijke begrip. In hoofdstuk 6 breiden we de juiste definitie van een dergelijk begrip voor conforme veldtheorieën uit en brengen we een directe verbinding tot stand met de geometrie van de duale Anti-de Sitter-ruimtetijd.

Het gemeenschappelijke thema van deze resultaten is de voorspellingskracht van op het oog ongerelateerde berekeningen aan zwaartekracht oplossingen wanneer deze door de lens van een dual lager dimensionaal sterk gekoppeld quantum system worden geïnterpreteerd. Deze holografische theorieën geven generieke voorbeelden van rekentechnisch navolgbare sterk interagerende systemen die anders onbegrijpbaar zouden zijn met conventionele methoden.

Résumé

De par leur nature, les systèmes fortement couplés font à la fois partie des systèmes les plus intéressants, mais aussi partie des systèmes les moins compris de la physique. Sans l'appui de la théorie des perturbations ainsi que des autres outils usuels, les physiciens ont dû être créatifs afin de pouvoir sonder et étudier ces systèmes dans la limite de fort couplage. La correspondance AdS/CFT, qui est au cœur de cette thèse, s'est montrée très prometteuse dans l'étude de la physique de plusieurs systèmes de ce type, comme le plasma de quarks et de gluons ou encore les électrons fortement corrélés présents dans les phases métalliques des supraconducteurs à haute température de transition (ou cuprates).

La présente thèse apporte de nouveaux résultats issus de simulations numériques sur ce type de systèmes au chapitre 2, utilisant des modèles de trous noirs complexes et s'appuyant sur des algorithmes à haute performance. Les résultats de ces simulations illustrent une grande diversité de phénomènes ; les trous noirs avec un horizon des événements ondulatoire se comportent comme des fluides relativistes dans un potentiel périodique pour lesquels une description universelle hydrodynamique est présentée au chapitre 3. La précision avec laquelle ces modèles peuvent expliquer les propriétés de transport de ces systèmes à fort couplage, en dualité avec ces trous noirs, est une preuve que les électrons dans les cuprates se comporteraient plus comme un fluide que comme des boules de billard dans un métal traditionnel. Ce type de modèle de trous noirs demande une attention particulière afin d'être correctement définis, comme cela est expliqué au chapitre 4.

En tant que dualité mathématique, la correspondance AdS/CFT peut être appliquée à une vaste gamme de théories et de systèmes. Parmi les plus intéressants se trouve la question de l'existence d'une configuration de fermions dans un potentiel gravitationnel et électromagnétique stable dans un espace-temps AdS. Cette question reste sans réponse après une décennie de recherche. Au chapitre 5, nous présentons une amélioration des modèles précédents et nous nous rapprochons ainsi d'une solution à ce problème. Une autre problématique d'un intérêt notable est la question de la configuration d'intrication quantique de ces systèmes à fort couplage, pour lesquels il a été théorisé que la mesure de leurs propriétés d'intrication à longue distance pourrait être une source de leurs propriétés uniques. Une des quantités possibles pour cette mesure

qui a attiré beaucoup d'attention dans la communauté est la complexité, une analogie continue de la notion de complexité en informatique. Au chapitre 6, nous présentons une définition possible de cette notion pour les théories conformes des champs et nous mettons en évidence une connexion directe avec la géométrie de l'espace-temps Anti-de Sitter.

Le fil conducteur des résultats présentés dans cette dissertation est le pouvoir de prédiction des modèles gravitationnels vraisemblablement sans rapport avec les théories des champs quantiques à fort couplage et en dimension réduite. Ces théories *holographiques* fournissent des exemples numériques résolubles de systèmes à fortes interactions qui sont autrement hors d'atteinte des méthodes conventionnelles.

Curriculum Vitae

I was born on August 17th, 1996 in Beaumont-Sur-Oise, a small town in the region of Paris, France, although my family quickly moved to Porticcio in Corsica, where I spent my childhood years. I then went to high school at *Lycées Vauvenargues* in Aix-en-Provence, France. After high school, I entered the French system of *Classes Préparatoires aux Grandes Écoles* at *Lycée du Parc* in Lyon, a two-year intensive program in Mathematics, Physics, Computer Science and Engineering culminating in national competitive exams. I was successfully admitted as *Élève Normalien* at *École Normale Supérieure de Lyon* where I obtained my Bachelor's and Master's degrees.

During those years, I did an internship on Tokamak fusion reactors at the Swiss Plasma Center of *École Polytechnique Fédérale de Lausanne*, Switzerland. This path led me to the more theoretical side of physics and to Leiden University, where I first arrived as an Erasmus exchange student doing a Master's project with the late Prof.dr. Jan Zaanen and under the guidance of Dr. Aurelio Romero-Bermúdez. After a brief return to Lyon, I executed a series of research projects back in the Leiden group with Prof.dr. Koenraad Schalm and Prof. Mihailo Čubrović (from the University of Belgrade) but also at the University of Amsterdam with Prof.dr. Jan de Boer, Prof. Shira Chapman (now senior lecturer at the Ben-Gurion University, Israel) and Prof. Claire Zukowski (now assistant professor at the University of Minnesota Duluth).

I finally started my PhD in September 2020 in the Quantum Matter group of Leiden University with Prof. Dr. Koenraad Schalm. During my PhD, I had duties of teacher assistant in the course Complex Networks with Prof.dr. Diego Garlaschelli (for a total duration of four semesters) and attended the 2022 DRSTP Summer School in Condensed Matter physics held in Callantsoog. Alongside my research, I also presented my work at various international conferences such as “Hydrodynamics at all scales” organized at the Nordita institute in Stockholm, Sweden, “Workshop on String Theory, Holography, and Black Holes” organized at ICTP in Trieste, Italy and “Physics@Veldhoven” organized at Veldhoven, The Netherlands.

I will remain at Leiden University as a Postdoctoral researcher until August 31st, 2025.

Acknowledgements

This thesis would not have been possible without all those who helped and supported me over the years, and I would like to thank all of them. I would like to start with the late Jan Zaanen for taking a chance on me and inviting me to Leiden University. I would then like to thank Koenraad Schalm, my PhD supervisor, for your guidance, mentoring and invaluable insights. Thank you for making these years so interesting, and for putting up with me knocking on your door every day. It has truly been a great pleasure.

I would also like to thank my collaborators Floris Balm, Mihailo Čubrović, Jan de Boer, Claire Zukowski, for their patience and their help in publishing the chapters of this thesis. I would like to give special thanks to another collaborator, Shira Chapman, for being a great sparring partner for ideas and for never taking my results for granted, you always pushed me to improve. I would also like to extend thanks to Jay Armas, Blaise Goutéraux, Richard Davison, and Sašo Grozdanov for all the help and advice you have given me over the years.

I want to thank all the people I have had the chance to work with at Leiden University and remotely, Joost Aretz, Luca Barbera, Vladan Djukić, Kevin Grosvenor, Sasha Krikun, David Rodríguez Fernández, Akash Jain, Ruben Lier, Aurelio Romero-Bermúdez, Philippe Sabella-Garnier, Joshua Saldi, Osher Shoval, Ashish Shukla, Tereza Vakhtel, Vaios Ziogas. I also want to thank Aravindh Swaminathan Shankar, Floris Balm, Aleksandar Bukva, Tim Fuchs, Vladimir Ohanesjan for not only being great colleagues but also for being great friends, you have made these years great ones.

I would like to thank the support staff, secretariat (especially Fran Ouwerkerk for all your help) and IT support of the Lorentz Institute, as well as Leiden University as a whole for welcoming me and supporting me during this PhD. I would like to acknowledge the Dutch national Cartesius and Snellius National Supercomputing Facilities and the SURF Cooperative for their support.

Dad, Fanny, Grandpa, Grandma, thank you for supporting me and pushing me all my life, I would not be here without you. Louis, thank you for being a great friend and for being there whenever I needed you. Antonio, Germana, Yann, thank you for your

support and Zoé, my niece, your arrival in this world in the later stages of this work was a true ray of sunshine.

Finally, I am eternally grateful to my wife, Martina. You were there and supported me through all of it, good and bad. None of this would have been possible if it weren't for you, your presence by my side has made every single day much better.

List of publications

- [1] N. Chagnet, S. Chapman, J. de Boer, and C. Zukowski. “Complexity for Conformal Field Theories in General Dimensions”. *Phys. Rev. Lett.* 128 (2022). DOI: 10.1103/PhysRevLett.128.051601.
- [2] N. Chagnet, V. Đukić, M. Čubrović, and K. Schalm. “Emerging Fermi Liquids from Regulated Quantum Electron Stars”. *JHEP* 08 (2022). DOI: 10.1007/JHEP08(2022)222.
- [3] N. Chagnet, F. Balm, and K. Schalm. “Quantization and Variational Problem of the Gubser-Rocha Einstein-Maxwell-Dilaton Model, Conformal and Non-Conformal Deformations, and Its Proper Thermodynamics”. *JHEP* 03 (2023). DOI: 10.1007/JHEP03(2023)081.
- [4] F. Balm, N. Chagnet, S. Arend, J. Aretz, K. Grosvenor, M. Janse, O. Moors, J. Post, V. Ohanesjan, D. Rodriguez-Fernandez, K. Schalm, and J. Zaanen. “T-Linear Resistivity, Optical Conductivity and Planckian Transport for a Holographic Local Quantum Critical Metal in a Periodic Potential”. *Phys. Rev. B* 108 (2023). DOI: 10.1103/PhysRevB.108.125145.
- [5] N. Chagnet and K. Schalm. “Hydrodynamics of a relativistic charged fluid in the presence of a periodically modulated chemical potential”. *SciPost Phys.* 16 (2024). DOI: 10.21468/SciPostPhys.16.1.028.